CORA Cork Open Research Archive
Cartlann Taighde Oscailte Chorcaí

| | |
|---|---|
| Title | An exploration of open coupled-cavity lasers: from exceptional points to dynamics |
| Authors | O'Connor, Christopher P.J. |
| Publication date | 2020-12-24 |
| Original Citation | O'Connor, C. P. J. 2020. An exploration of open coupled-cavity lasers: from exceptional points to dynamics. PhD Thesis, University College Cork. |
| Type of publication | Doctoral thesis |
| Rights | © 2020, Christopher P.J. O'Connor. - https://creativecommons.org/licenses/by-nc-nd/4.0/ |
| Download date | 2026-11-15 18:02:33 |
| Item downloaded from | https://hdl.handle.net/10468/11886 |

UCC
University College Cork, Ireland
Coláiste na hOllscoile Corcaigh

# An Exploration of Open Coupled-Cavity Lasers: From Exceptional Points to Dynamics

**Christopher P.J. O'Connor**
*Críostoir P.S. O'Concobhair*




**National University of Ireland, Cork**
*Ollscoil na hÉireann, Corcaigh*

Department of Applied Mathematics

Thesis submitted for the degree of
**Doctor of Philosophy**

$24^{th}$ December 2020

Head of Department: Prof. Sebastian Wieczorek

Supervisors: Dr. Andreas Amann
Prof. Sebastian Wieczorek

# Contents


**1 Introduction** **1**

**2 Semiclassical Laser Theory and Background** **6**
2.1 Quantum Mechanics . . . . . 6
2.1.1 The Hamiltonian and the State Vector . . . . . 7
2.1.2 Density Operator . . . . . 8
2.1.3 Electric-Dipole Light-Matter Interactions . . . . . 9
2.2 Two-Level Atom . . . . . 12
2.2.1 Population Matrix and Pumping . . . . . 14
2.3 Gain Polarisation and Population Inversion Dynamical Equations for Semiconductors . . . . . 15
2.3.1 Semiconductor Two-level Model . . . . . 15
2.3.2 Gain Polarisation and Population Inversion . . . . . 16
2.4 Maxwell's Equations . . . . . 18
2.4.1 Electric Field and Gain Polarisation Decomposition . . . . . 20
2.5 Gain Polarisation and Population Inversion Dynamics . . . . . 21
2.5.1 Gain Polarisation Equation Approximation and Rotating Wave Approximation for Gain Polarisation . . . . . 21
2.5.2 Population Inversion Approximations . . . . . 23
2.6 Dynamics and Coupled-Cavity Lasers . . . . . 24
2.6.1 Closed Single Cavity Lasers . . . . . 25
2.6.2 Composite Cavity Modes . . . . . 27
2.6.3 Optical Injection . . . . . 28
2.6.4 Mutually-Coupled Lasers . . . . . 28
2.7 Conclusions . . . . . 30

**3 Coupled Mode Theory** **31**
3.1 Exceptional Points in a Linearly Coupled System . . . . . 31
3.1.1 Two-Dimensional Eigenvalue Problem . . . . . 32
3.1.2 Matrix Transformation . . . . . 32
3.2 Coupled Resonators with Losses . . . . . 33
3.3 Frequencies, Losses and Exceptional Points . . . . . 37
3.3.1 Analysis of Frequencies corresponding to Eigenvalues . . . . . 37
3.3.2 Analysis of Losses corresponding to Eigenvalues . . . . . 38
3.3.3 Analysis of Eigenvalue Branches and EPs . . . . . 39

3.4 Restrictions of non-gain coupled resonators using Coupled Mode Theory 42
3.4.1 Losses Restriction . . . . . 42
3.4.2 Dynamical scenarios of coupled non-gain cavities . . . . . 45
3.5 Conclusions . . . . . 47

**4 $q$-Basis and Exceptional Points using the Steady-state *ab-initio* Laser Theory 48**
4.1 $q$-Basis and the Electromagnetic Field . . . . . 49
4.1.1 Steady-State Maxwell's Equations . . . . . 50
4.1.2 Power Flow and Poynting's Theorem . . . . . 52
4.1.3 $q$-basis . . . . . 53
4.2 Steady-State *ab-initio* Laser Theory . . . . . 55
4.2.1 Electric Field Equation Close to Threshold . . . . . 56
4.2.2 Threshold Constant Flux States (TCFs) . . . . . 57
4.3 Coupled-Cavities and Exceptional Points using the $q$-basis . . . . . 60
4.3.1 Transfer Matrix using the $q$-basis . . . . . 60
4.3.2 Interface Conditions in terms of the $q$-Basis . . . . . 63
4.3.3 Boundary Conditions in terms of the $q$-Basis . . . . . 64
4.3.4 Transfer Matrix Condition using the $q$-basis . . . . . 65
4.4 Analysis of Coupled-Cavity Laser Modes and Exceptional Points . . . 67
4.4.1 Intensity of Coupled Cavities at Exceptional Points . . . . . 67
4.4.2 Exceptional Points with different Gap lengths . . . . . 74
4.4.3 The second condition for Threshold . . . . . 75
4.5 Unequal Pumping and the $q$-Basis . . . . . 77
4.5.1 Power Outflow and Exceptional Points . . . . . 78
4.5.2 Changes in Refractive Index at an EP . . . . . 80
4.5.3 Eigenvalue Branches with varying $\eta$ . . . . . 81
4.6 Conclusions . . . . . 81

**5 The $\mathcal{Z}$-Basis and Threshold EPs for Open Coupled Cavities 85**
5.1 The $\mathcal{Z}$-basis . . . . . 86
5.1.1 Permittivity of a Laser Medium . . . . . 87
5.1.2 $\mathcal{Z}$-Basis Spatial Fixed Points . . . . . 88
5.2 Analytical Solution and the $\mathcal{Z}$-basis . . . . . 88
5.2.1 Möbius Transformation . . . . . 89
5.2.2 Solving $\mathcal{Z}(z)$ using the Möbius Transformation . . . . . 91
5.2.3 Electric field Intensity . . . . . 92
5.2.4 Power Flow with the $\mathcal{Z}$-basis . . . . . 92
5.3 Fabry-Perot with the $\mathcal{Z}$-Basis . . . . . 93
5.3.1 Threshold Condition for Fabry-Perot . . . . . 93
5.3.2 Loxodrome and the Fabry-Perot . . . . . 94
5.3.3 Power Flow for Fabry-Perot . . . . . 96
5.3.4 Permittivity and the Fabry-Perot Laser . . . . . 97
5.4 Coupled-Cavities at Threshold and TEPs . . . . . 98
5.4.1 Coupled-Cavity Lasers with the $\mathcal{Z}$-basis . . . . . 98

5.4.2 Exceptional Points at Threshold . . . 99
5.4.3 Loxodromes and Coupled-Cavity Lasers . . . 100
5.4.4 Power Flow for Coupled-Cavities . . . 105
5.4.5 Permittivities of Coupled-Cavities with the $\mathcal{Z}$-basis . . . 106
5.4.6 Comparison to the Fabry-Perot Laser . . . 110
5.5 Analysis of Coupled-Cavities with no gap . . . 110
5.6 Conclusion . . . 115

**6 Open Coupled Cavity Dynamics 116**
6.1 Scaling Dynamics for the Electromagnetic field . . . 117
6.1.1 Maxwell's Equations . . . 118
6.1.2 $Q$-time Basis . . . 119
6.1.3 Dynamics for Scaling and Population Inversion . . . 119
6.2 Power Flow Dynamics for a Single Cavity Open Laser . . . 120
6.2.1 Power Flow Equation . . . 120
6.2.2 Population Inversion Dynamical Equation . . . 122
6.3 Spatial Variation of Cavity and the $q$-basis . . . 123
6.3.1 Dynamics of $A(t)$ with $x_n$ . . . 124
6.3.2 Single-Cavity Dynamical Equations . . . 125
6.4 Coupled-Cavity Open Laser . . . 126
6.4.1 Dynamics of Population Inversion . . . 127
6.4.2 Power Balance Equation . . . 128
6.4.3 Steady-state solution and scaling with $x_n$ . . . 129
6.5 Coupled-Cavity Dynamical Equations . . . 130
6.5.1 Dynamics of $N_1$ and $N_2$ when $\dot{A} = 0$ . . . 132
6.5.2 Approximation of modes above and below threshold . . . 133
6.5.3 Variation of $F_{12}(N_1, N_2)$, $H_1(N_1, N_2)$ and $H_2(N_1, N_2)$ . . . 135
6.6 Conclusion . . . 138

**7 Conclusion and Future Work 139**

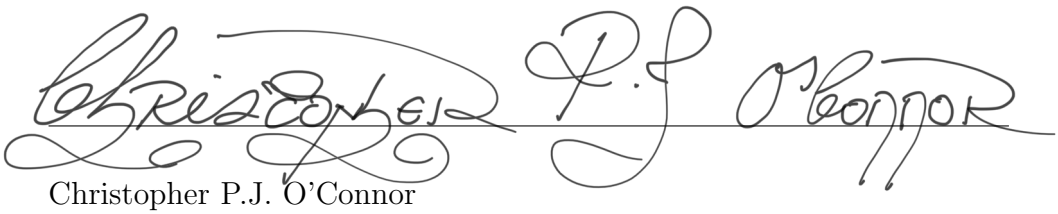
**List of Abbreviations 143**

**List of Symbols 144**

**List of Figures 151**

**Bibliography 157**

This is to certify that the work I am submitting is my own and has not been submitted for another degree, either at University College Cork or elsewhere. All external references and sources are clearly acknowledged and identified within the contents. I have read and understood the regulations of University College Cork concerning plagiarism.



Christopher P.J. O'Connor
*Críostoir P.S. O'Concobhair*

# Abstract

In optical communications, there is an increase in demand for investigation of multi-section laser cavities, which are involved in the development of Photonic Integrated Circuits or PICs. The requirement for such circuits results from, for example, the increase in demand for faster internet devices, which means improving the infrastructure involved. PICs are useful for such advancements as instead of an electrical circuit, these use optical devices such as lasers. Furthermore, these laser cavities are closely interacting or strongly coupled as they are of millimetre to submillimetre scales. Due to the size and complexity of these devices, they are not yet fully understood. Previous work has shown some interesting behaviour with these strongly coupled cavities. For example, the existence of exceptional points, where two modes coalesce, and also the possibility for a laser mode to go below threshold with increasing population inversion in a cavity, all in the steady state. However, for these types of devices, there is currently no full dynamical model that considers the complexity of strongly coupled cavities, with only outgoing light at the boundary of the laser.

Thus, the aim of this thesis is to investigate three important areas. The first is to understand the steady state situation further and improve upon what is known already. We introduce a new basis to do this and create a threshold condition, which is used to explore the complexities of coupled cavities. With this, we further address the occurrence of these exceptional points and give a more in-depth insight into the interesting effects that occur. The second area is to introduce a new, elegant approach in solving the electromagnetic field equation for the steady state, while still considering the geometrical features of a multisection laser. We introduce a second formalism for laser equations at threshold, which is shown to be a projection of a loxodromic spiral on a Riemann sphere with the use of Möbius transformations. With this, we investigate the threshold branches of multisection laser devices and discover a different type of exceptional point, where instead, the branches merge rather than modes. Furthermore, this new approach removes the need for unnecessary information while retaining the important physical characteristics to explain a coupled cavity laser. Lastly, a dynamical model that represents a strongly coupled laser with outgoing boundary conditions is introduced by connecting the classical electromagnetic field to the quantum mechanical description for the active medium. We go beyond the steady state by introducing a time-dependent scaling term for the electromagnetic field, which scales with the population inversion equations to provide a physically explained self-consistent set of dynamical equations. This model confirms results seen in the steady state situation. It also expands upon the steady state to show

possible dynamical properties which are a result of the close interactions between both cavities, while crucially considering open boundary conditions while using the spatial profile for the active medium.

# Acknowledgements

To start off, I would like to give thanks to my supervisors Andreas and Sebastian. I give my utmost gratitude and respect firstly to Andreas. You were always available when I needed a chat about my project and did so much to help me solve any problems I encountered. You showed so much patience, care and understanding which I am grateful for. Any general advice was always given for any aspect of the PhD. Thank you! I also want to thank my second supervisor Sebastian. Whenever I needed a little inspiration or some physics book which solved any issue I had, you were there. Thank you for your help. I would also like to recognise my examiners for the viva, Lucas Illing and Kieran Mulchrone for taking time to read this. It was nice to have an interesting discussion on this topic which you both provided.

I would like to extend my thanks and appreciation to my family. Without them, I would not have been able to complete this thesis. Firstly, my fiancé Liam. You were always there to listen and gave me the confidence to complete my thesis. You have always been there to support me and listened to me whenever I needed you. Next is my mam, Marion, you have given me so much throughout my life and gave me the confidence to achieve what I wanted and without you, this would have not been possible. There is also my brother James, sister Theresa and her partner Andrew who all were there for me whenever I needed them, with advice when I wanted it and showed genuine curiosity in what I am doing. Thanks to you all. There is one person who I give my thanks to that is no longer with us and that is my father James (Jim). You gave me so much inspiration and wanted me to achieve my dreams while teaching me how understand the world around me, which led to my love of physics. I would like to thank Thady too who was there anytime I needed him, always with some useful words of wisdom. Moreover, I am grateful to my extended family of aunties, uncles and cousins in particular aunty Pauline & Vincent, uncle Mark & Ellen, aunty Sheila, uncle John & Josephine, uncle Dan, aunty Mary & Paddy, aunty Nan & Charlie, aunty Margaret & Des and uncle Bill & Nuala. I am thankful to all my neighbours back home who were always steering me towards success! I would like to thank my Welsh family whom I have come to know during my PhD, in particular Avril, Julie, Joel, Ella & Kailan, Connie, Pam and Darren & Tamsyn's family, who always had a keen interest in what I was doing.

Next I would like to thank the friends I have who have always been there when I needed them. Firstly, I give my gratitude to my friends from Maynooth who made sure I was grounded during my PhD and made sure I always had a laugh too, mostly at my expense! Thanks in particular to Adrian (Sparky) & Niamh, Paddy, Kevin

(Ken), Diarmuid (JOAM), Catriona, Steve, Aidan and Rob. There are friends and colleagues in UCC who I owe so much thanks to as well. They made my PhD more entertaining, funny and enlightening throughout. In particular, I am so grateful to 'Master' Justin, Andrew, Edu (Eddie) and Adrian who mostly had to endure my ramblings! I would also like to thank Tony, Paula, Chun, Andy, Mat, Paul, Eoin, Rory, Pierce and all the others I encountered in the WGB office. I am indebted to all my colleagues and friends I made in Cork who made the journey from Meath worthwhile!

*"Blank pages are just ideas waiting to happen."*

*For my family*

# Chapter 1

# Introduction

The LASER (Light Amplification by Stimulated Emission of Radiation) was one of the foremost discoveries in mid 1900s. It is now one of the most commonly known and used devices today. The main idea of a laser is to produce a coherent monochromatic beam of light which can travel large distances, in contrast to more elementary devices such as lightbulbs and flashlights which are incoherent where the light is made up of multiple frequencies. The most simplistic version of a laser that can be thought of is the Fabry-Perot [1] type cavity with an external pumping mechanism which can be electrical or optical. The cavity has two highly reflective surfaces, such as mirrors, on both ends and an active medium with excited atoms that can generate light of a certain frequency $\omega$ as shown in Figure 1.1. Lasers are typically smaller than popularly imagined, without the characteristic "ZAP!" sound of laser gun fire seen in movies. The applications of lasers appear to be endless, especially in the most modern devices. We see new uses for lasers such as in medicine [2] for both therapeutic and diagnostic purposes and in optical communications [3] to name but a few. To achieve such a device, many years have been spent theorising and developing the technology and understanding required.

Our journey starts off with the well-known physicist Einstein in 1917 [4] and one of his most famous contributions which presented a theoretical understanding for emission of radiation, more particularly, stimulated emission. From here, it would take a considerable amount of time to design a device which amplifies light using an active medium such that stimulated emission occurs to produce light. In 1953, Gordan, Zeiger and Townes [5] successfully designed an amonia MASER (Microwave Amplification by Stimulated Emission of Radiation) for microwave radiation. From there, Townes, along with Schawlow proposed the possibility of designing devices for both infrared and visible light radiation in 1958 [6]. Only a few years later this

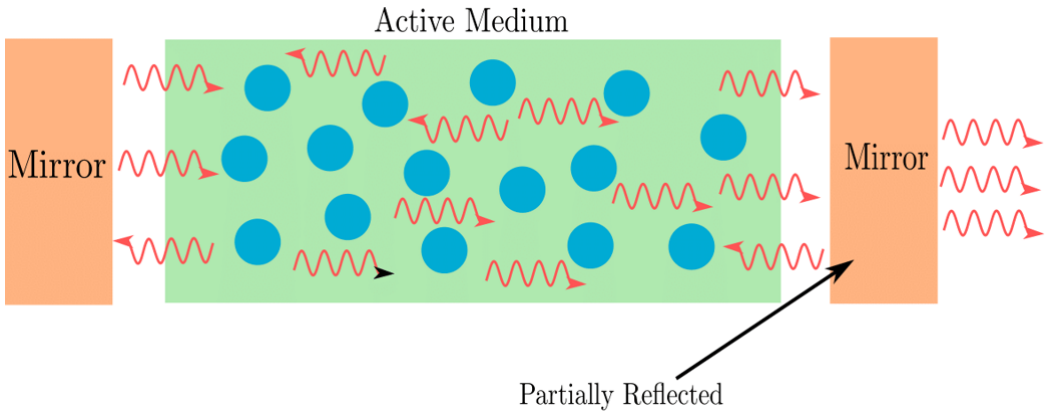



Figure 1.1: Setup of a simplistic single-cavity laser with an external pump, and excited atoms (blue) in an active medium (green). This example has a fully reflective mirror on the left and a partially reflective one on the right which allows photons to escape.

theoretical idea became reality as Maiman [7] produced a ruby laser in 1960 and thus one of the most useful devices in the world was created.

Of course the mass production of lasers did not come about straight way, as more theoretical and experimental understanding was required. Along with solid state lasers, the production of a gaseous active medium was also successful in late 1960s with Javen and Bennett [8] and the use of a He-Ne medium. Subsequently, dye lasers [9, 10],where the medium is an optically pumped dilute solution of organic dye [1], were created. However, the most efficient and inexpensive laser medium is made of semiconductor material. It can produce small, effective lasers that require little external power.

Vast amounts of research has been carried out to try to model lasers effectively since their inception. This research has yielded a large amount of knowledge regarding laser theory, leading to some interesting dynamical properties. One way to describe the active medium is Semiclassical Laser Theory (SLT) [11]. This describes the electromagnetic field by using Maxwell's equations and connecting them to the quantum mechanical description of the gain medium and the overall laser structure as a whole. SLT can be used as a good theoretical model for a single cavity laser. It can simulate the dynamics of the electromagnetic field and its interaction with the gain medium to a high level of proficiency for a simple laser structure [12]. SLT is a good model for single cavity lasers with closed boundaries but further theoretical work would be required to model lasers with a more difficult geometrical structure and open boundaries. Increased demand for smaller laser devices prompts further investigation in the area of optical communications which require increasingly more

complex laser designs.

With an increase in demand for faster internet and the ability to watch higher quality video content, scientists are working on how to send information faster, by improving the infrastructure that connects people to the internet. One area where lasers are beneficial is Fiber-optic communications. This involves sending information through an optical fiber in the visible or infrared parts of the electromagnetic spectrum. This means the design of such devices to send this amount information must be small with the use of chips like Photonic Integrated Circuits (PICs) [13] which would have multiple lasers closely interacting with each other. In terms of scale, laser cavities on PICs would typically be of millimetre size and gaps between them are on a micrometre to millimetre scale. PICs also would be comprised of semiconductor material such as GaAs (Gallium Arsenide) or InP (Indium Phosphide).Considering this information, we need to understand small coupled-cavity laser devices to be able to use PICs for optical communications.

With more complex laser structures on PICs, where we have coupled cavities with leaking boundaries, it is quite difficult to simulate both the geometry of the laser and dynamics together. For coupled cavities, there are two paths to consider, whether they are strongly or weakly coupled. For weakly coupled cavities, we can think of them as two separate lasers with separate electromagnetic fields with a physical connection such as an optical fibre. A model for the dynamics of weak coupling is Coupled Mode Theory (CMT) [14] for non-gain resonators with loss. Moreover, there exist more complicated dynamical models for delayed coupled semiconductor lasers with the use of delay differential equations (DDEs) [15]. While these models are good for dynamics of weakly coupled systems, we investigate further models to help describe the close interaction between cavities. Unfortunately, given the design of PICs, which have cavities at a close distance and strong coupling, it is quite difficult to use weak coupling theory to effectively describe such a structure. For these lasers though, recent models try to employ the idea of closely interacting cavities. One model is optical injection from one cavity into another [16] which is quite effective for these type of injection lasers. Where both cavities interact, we use the idea of composite cavity modes which considers the spatial variation of the electromagnetic field over the entire structure but for passive cavities [17].

The problem with such theories mentioned is the fact that the geometry of the mode is not accurately described and does not use the open boundary conditions for modes in an active medium with cavities that are open to the outside world and are strongly coupled. A solution to this problem was addressed for the steady-state

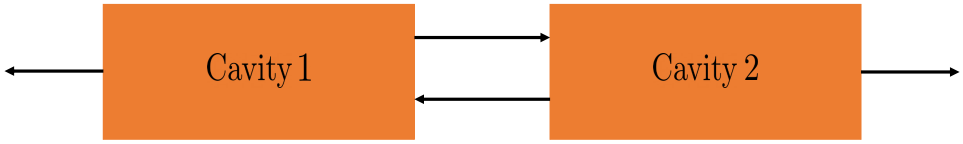



Figure 1.2: Setup of the coupled cavity system with open boundaries separated by a gap.

regime with the Steady-state *ab-initio* Laser Theory (SALT) [18, 19]. It provides a spatial description of the electromagnetic field over a complex geometric structure such as a many cavity laser, but at steady-state. A sample structure that SALT can simulate and what we will use throughout this thesis is shown in Figure 1.2.

With two strongly coupled cavities, interesting phenomena have been theoretically and experimentally shown. A significant conundrum which has arisen that is counter intutitive is the idea of suppression of laser output even with increasing, yet unequal pumping. [20]. This gives rise to the mathematical concept of Exceptional Points (EPs) which is when two eigenvalues coalesce with the variation of the parameters of the system [21]. However in the case of the EPs in coupled cavities similar to [20], not much is known on how they exist and under what conditions.

Thus we arrive at the major questions which are addressed in this thesis. The first being how can we further understand the conditions on which these EPs occur in the strongly coupled cavities. Another point to investigate the threshold regions of these coupled cavities in detail and how they change with different types of laser structures. From there, the next question we would like to answer is that if it is possible to derive dynamical equations for strongly coupled cavities with open boundaries which correctly takes into account the geometrical structure and active medium of the laser. These questions are useful in the context of understanding how devices in the communications industry such as PICs with laser cavities that are strongly interacting work. The main idea to answer these questions will be the use of the power balance equation. Using Poynting's theorem [22, 23], we obtain a relation between the power at the boundaries to the energy density of the laser. As a result, we can see how an EP affects the power inside the cavities. We explore the idea of power balance and power flow and how the threshold of a laser changes with the variation of parameters. Moreover, we use this relation to obtain effective dynamical equations for the electromagnetic field.

This thesis is comprised of the following chapters:

- In chapter 2, we introduce the background to the problems addressed and also derive the Maxwell-Bloch equations from SLT which will be used throughout to describe the gain medium. We further address previous models used to describe coupled cavities for both weak and strong coupling theory.

- Chapter 3 is where we start to explore the openness of the laser with weak coupling and investigate EPs in CMT. We also show the limits in the model for coupled resonators with loss and no gain.

- In the fourth chapter, we introduce what is termed the "$q$-basis" for the electric and magnetic fields, in a similar format to Stokes parameters [24]. From there, using the $q$-basis, we can replicate results from SALT and also obtain EPs. We will also derive the power balance equation, from Poynting's theorem, which is the critical piece in deriving the dynamical equations in later chapters used for describing the electromagnetic field. We extended the knowledge of coupled cavities and EPs using this $q$-basis such as how threshold and EPs change with the variation of parameters. We further determine how the power flow can effect threshold.

- Chapter 5 looks into the threshold regions in the steady-state scenario in detail using a new mathematical approach, with the use of Möbius transformations, named the $\mathcal{Z}$-basis. With this, we can determine a new type of EP and also provide a clear understanding on how strongly coupled cavities behave.

- Finally in chapter 6, we use the previously mentioned $q$-basis to derive dynamical self-consistent equations for the electromagnetic field and gain medium that takes into account the spatial geometry of the laser along with open boundary conditions.

# Chapter 2

# Semiclassical Laser Theory and Background

In this chapter, we would like to introduce the background to the problems we are trying to solve. The fundamental theory which is mentioned in the introduction that will be used to derive the dynamical equations for the electromagnetic field and active medium is Semiclassical Laser Theory (SLT). Haken [12, 25, 26] and Lamb [11, 27–29] have written numerous literature to provide a clear understanding of SLT which we will use as an aid throughout the thesis. In SLT, we consider the classical electromagnetic field where we are able to use Maxwell's equations as a starting point. However, when dealing with the active or gain medium, we will in fact use quantum theory to understand the motions of electrons. With the introduction of the density matrix formalism [30], we can relate the quantum mechanical description of the active medium to macroscopic variables that are population inversion and gain polarisation. The first part of this chapter focuses on SLT. The second part explores the work that has been carried out to model coupled cavities effectively. This includes weakly coupled lasers modelled by DDEs and optically injecting lasers, and also strongly coupled cavities with composite cavity modes.

## 2.1 Quantum Mechanics

Before we derive the dynamical equations for the gain medium, we will start by explaining some of the fundamental quantum mechanics required.

### 2.1.1 The Hamiltonian and the State Vector

One of the most important aspects of quantum mechanics we are using is the quantum mechanical description of an electron. To understand this, we can write electrons in terms of a complex probability function $\psi(\mathbf{R}, t)$ which is space and time dependent where $\mathbf{R}$ is the displacement of the electron from the nucleus [12]. $\psi(\mathbf{R}, t)$ is called the wave function and satisfies the time dependent Schrödinger equation. We can also write any wave function in Dirac notation, given by the state vector $|\psi(t)\rangle$, referred to as a 'ket' in bra-ket notation. For each $|\psi(t)\rangle$, there exists a 'bra' denoted as $\langle\psi(t)|$ which is the adjoint of the 'ket'. In terms of matrices, one can think of the adjoint of a matrix as its transpose complex conjugate.

The Hamiltonian operator is first seen in the sixth postulate of quantum mechanics [30]. For a given state vector $|\psi(t)\rangle$, it is governed by the Schrödinger equation:

$$i\hbar\frac{d\,|\psi(t)\rangle}{dt} = \hat{H}(t)\,|\psi(t)\rangle\,, \tag{2.1}$$

where the operator $\hat{H}(t)$ is the Hamiltonian and represents the total energy in the system. The composition of the time-dependent Hamiltonian is as follows,

$$\hat{H}(t) = \hat{H}_0 + \hat{W}(t). \tag{2.2}$$

where $\hat{H}_0$ is the time independent operator such that that, applying $\hat{H}_0$ to the state vector will result in the eigenvalues $\hbar\omega_n$ that correspond to the eigenstates $|\phi_n\rangle$,

$$\hat{H}_0\,|\psi(t)\rangle = \sum_n \hbar\omega_n c_n(t)\,|\phi_n\rangle\,. \tag{2.3}$$

The $\hat{W}(t)$ term is a time-dependent perturbation which we relate to the electric dipole light-matter interaction terms which will be further explained in later subsections.

Thus the state vector can be written in terms of a linear combination of eigenstates $\{|\phi_n\rangle\}$ such that [30],

$$|\psi(t)\rangle = \sum_n c_n(t)\,|\phi_n\rangle \tag{2.4}$$

with time dependent coefficients $c_n(t)$ such that, the probability of the electron having eigenstate $|\phi_n\rangle$ is $|c_n(t)|^2$ where $\sum_n |c_n(t)|^2 = 1$. In fact, the eigenstates are

orthonormal and satisfy the orthonormal condition that,

$$\langle \phi_m | \phi_n \rangle = \int \phi_m^*(\mathbf{R}) \phi_n(\mathbf{R}) d\mathbf{R} = \delta_{mn} \tag{2.5}$$

where $\phi_i(\mathbf{R})$ are eigenfunctions that are the decomposition of the wave function $\psi(\mathbf{R}, t)$. Mathematically, $\langle \phi_m | \phi_n \rangle$ can be thought of as the inner product between the two eigenfunctions $\phi_m$ and $\phi_n$ where the solution is Kronecker's delta given by [30],

$$\delta_{mn} = \begin{cases} 1 & \text{if} m = n, \\ 0 & \text{if} m \neq n. \end{cases} \tag{2.6}$$

Thus the inner product between an eigenstate $|\phi_m\rangle$ and the state vector obtains $c_m(t)$. These time-varying amplitudes are extremely important for the density operator which will be used to describe the the dynamics of the active medium.

### 2.1.2 Density Operator

While the state vector is quite a useful tool for giving information on the quantum mechanical state of the electron, another way is to represent the quantum system is the density operator (in matrix representation, density matrix). The operator used with the eigenstates mentioned previously, can determine the probability of an electron having such state. The density operator $\hat{\rho}(t)$ can be written in terms of pure states or mixed states. The pure state can be written in terms of $|\psi(t)\rangle$ and is written as [30],

$$\hat{\rho}(t) = |\psi(t)\rangle \langle \psi(t)| = \sum_{n,m} \rho_{nm}(t) |\phi_n\rangle \langle \phi_m| \tag{2.7}$$

where $\rho_{nm}(t) = c_n(t) c_m(t)^*$. Moreover, we can introduce a density matrix, $\hat{\rho}(t)$ which is the representation of the density operator with individual elements $\rho_{ij}(t)$ which is given by,

$$\rho(t) = \begin{pmatrix} \rho_{11}(t) & \rho_{12}(t) \\ \rho_{21}(t) & \rho_{22}(t) \end{pmatrix} = \begin{pmatrix} |c_1(t)|^2 & c_1(t) c_2(t)^* \\ c_1(t)^* c_2(t) & |c_2(t)|^2 \end{pmatrix} \tag{2.8}$$

for a two level system. Mixed states require a more complex decomposition. Instead of a single $|\psi(t)\rangle$, a mix state density matrix considers a statistical ensemble of state vectors $|\psi_i(t)\rangle$ attached to a probability $p_i$. The mixed state density operator is

written as [30],

$$\hat{\rho}(t) = \sum_i p_i \left|\psi_i(t)\right\rangle \left\langle\psi_i(t)\right| \tag{2.9}$$

where $p_i$ is the probability for the $i^{th}$ component with the condition that $\sum_i p_i = 1$.

Using the components of the density matrix, $\rho_{mn}$, we can write the dynamical equation for the density matrix elements in terms of $c_n(t)$ and $c_m(t)^*$,

$$\frac{d\rho_{nm}}{dt} = \frac{dc_n(t)}{dt}c_m^*(t) + c_n(t)\frac{dc_m^*(t)}{dt}. \tag{2.10}$$

### 2.1.3 Electric-Dipole Light-Matter Interactions

The second term of (2.2), $\hat{W}(t)$ is the result of effects on the atom due to an induced electric field. To understand the effect on the atom, we will consider a simplistic version with a central nucleus surrounded by a cloud of electrons. Without an electric field, the charge density is located in the centre of the atom. However, inducing an electric field results in a shift of electrons away from the positively charged nucleus which creates an electric dipole. Classically, this dipole will oscillate in a similar way to an electron on a spring governed by an equation of motion similar to [12],

$$m_e\ddot{\mathbf{R}} + \omega_A^2\mathbf{R} = -e\mathbf{E}(\mathbf{r}, t). \tag{2.11}$$

where $m_e$ is the mass of the electron, $\omega_A$, the damping constant and $-e$ (where $e > 0$) is the charge of an electron. Note that $\mathbf{r}$ is the laboratory co-ordinate system [27]. As such, the electric field varies slowly over $\mathbf{R}$, so on the scale of the atom, the electric field can be considered to be constant. We will denote this spatially constant electric field by $\mathbf{E}_\mathbf{r}(t)$. In this classical interpretation, the Hamiltonian, labelled $\mathcal{H}$ is given by,

$$\mathcal{H} = \mathcal{K} + \mathcal{V} \tag{2.12}$$

where $\mathcal{K}$ is the kinetic energy while $\mathcal{V}$ is the potential. In the context of (2.11), the kinetic energy is given by $\mathcal{K} = \frac{1}{2}m_e\dot{\mathbf{R}}^2$ while the potential is the result of the forces due to Hooke's law and the force due to the electric field, $-e\mathbf{E}_\mathbf{r}(t)$. The Hamiltonian is thus written as,

$$\mathcal{H} = \frac{1}{2}m_e\dot{\mathbf{R}}^2 + \frac{1}{2}\gamma_D\mathbf{R}^2 + e\mathbf{E}_\mathbf{r}(t)\cdot\mathbf{R}. \tag{2.13}$$

The last term is the one we are interested in as we can write an operator that has the same effect as this electric field term. In terms of the quantum mechanical Hamiltonian, we can replace the position $\mathbf{R}$ with the operator $\hat{\mathbf{R}}$. Thus we can write $\hat{W}(t)$ as [27],

$$\hat{W}(t) = e\hat{\mathbf{R}} \cdot \mathbf{E_r}(t), \tag{2.14}$$

where $\hat{\mathbf{R}}$ is the position operator. Moreover, we are using the classical electric field in (2.14) instead of an operator.

Using the result from the time independent Hamiltonian,(2.3) with the Schrödinger equation given by (2.1), results in the following,

$$\sum_n i\hbar \frac{dc_n(t)}{dt} |\phi_n\rangle = \sum_n c_n(t) \left(\hbar\omega_n + \hat{W}(t)\right) |\phi_n\rangle . \tag{2.15}$$

If we take some eigenstate, $\langle\phi_m|$, and obtain the inner product, the result is given by,

$$i\hbar \frac{dc_m(t)}{dt} = c_m(t)\hbar\omega_m + \sum_n c_n(t) W_{mn}(t) \tag{2.16}$$

where $W_{mn}(t) = \langle\phi_m|\hat{W}(t)|\phi_n\rangle$. Using the physics behind the perturbation operator, we can get a clearer understanding of (2.16). Each component of $W_{mn}(t)$ is thus given by,

$$W_{mn}(t) = e\mathbf{R}_{mn} \cdot \mathbf{E_r}(t), \tag{2.17}$$

where $\mathbf{R}_{mn} = \langle\phi_m|\hat{\mathbf{R}}|\phi_n\rangle$ [27] and $-e\mathbf{R}_{mn}$ refers to the dipole matrix element. Moreover, $W_{nn} = 0$ [12, 30] as a static dipole is not a possible situation here.

To obtain the rate equations for each element of the density matrix, we need to use Schrödinger's equation with the Hamiltonian $\hat{H}(t)$ as described previously. For two operators $\hat{A}$ and $\hat{B}$, the following is the commutator for both,

$$[\hat{A}, \hat{B}] = \hat{A}\hat{B} - \hat{B}\hat{A}. \tag{2.18}$$

Also given the Hamiltonian is self-ajoint, Schrödinger's equation can be written for $\langle\psi_i|$ as follows,

$$i\hbar \frac{d}{dt} \langle\psi_i| = - \langle\psi_i| \hat{H}(t). \tag{2.19}$$

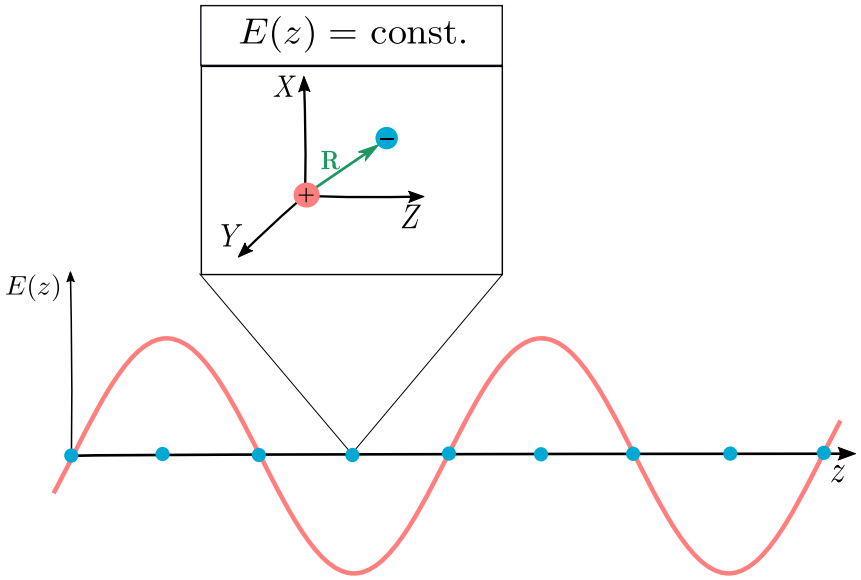



Figure 2.1: Classical constant in time electric field amplitude in the $x$ direction, $E(z)$ (red line) with atoms (in blue) along the $z$ axis. Each atom contains a separate coordinate system with position vector $\mathbf{R}$ which measures the distance from the nucleus to electrons of an atom (subset of figure).

Using these two properties, we can obtain a relation between the Hamiltonian and the density matrix,

$$\begin{aligned} i\hbar\frac{d\hat{\rho}(t)}{dt} &= \left(\hat{H}(t)\left|\psi(t)\right\rangle\left\langle\psi(t)\right| - \left|\psi(t)\right\rangle\left\langle\psi(t)\right|\hat{H}(t)\right) \\ &= \hat{H}(t)\hat{\rho}(t) - \hat{\rho}(t)\hat{H}(t) \\ &= [\hat{H}(t), \hat{\rho}(t)], \end{aligned} \tag{2.20}$$

We have now obtained a relation between the Hamiltonian and density operator. To get an equation for each individual component of $\hat{\rho}(t)$, we use both (2.10) and (2.16) to obtain,

$$\begin{aligned} \frac{d\rho_{nm}(t)}{dt} &= -\frac{i}{\hbar}\sum_l \left[H_{nl}(t)c_l(t)c_m(t)^* - c_n(t)c_l(t)^* H_{lm}(t)\right] \\ &= -\frac{i}{\hbar}\sum_l \left[H_{ml}(t)\rho_{ln}(t) - \rho_{ml}(t)H_{ln}(t)\right], \end{aligned} \tag{2.21}$$

where $H_{nm}(t) = \hbar\omega_m\delta_{nm} + W_{mn}(t)$ such that $H_{nm}(t) = H_{mn}(t)^*$.

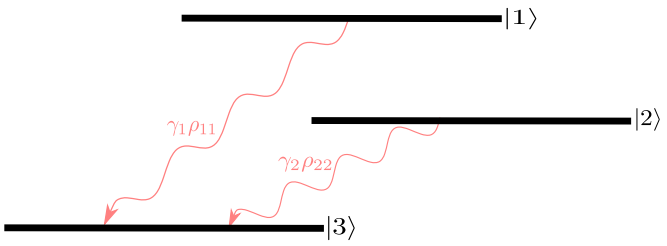



Figure 2.2: Two-level atom with the excited state $|1\rangle$ and lower state $|2\rangle$. Both decay to a level $|3\rangle$ at decay rates $\gamma_1$ and $\gamma_2$ from levels $|1\rangle$ and $|2\rangle$ respectively.

## 2.2 Two-Level Atom

So far, we have introduced the quantum mechanical ideas required for SLT. In this section, we would like to focus on deriving the equations of motion for each component of the density matrix for the two level atom. Moreover, we will make a few assumptions for the electromagnetic field which interacts with the atom. First, we will assume that the electromagnetic field varies only in the $z$ direction. Added to this, we will assume that the field amplitude is one dimensional which is transverse to the direction of propagation such that the amplitude is given by $\mathbf{E}(z,t) = E(z,t)\hat{\mathbf{i}}$, where $\hat{\mathbf{i}}$ is the unit vector in the $x$ direction. For an individual atom, we will denote $E_z(t)$ as the electric field for an individual atom at position $z$ which is constant in space over this atom. Moreover the vector $\mathbf{R}_{mn}$ in the direction of the electric field amplitude is $X_{mn}$ such that,

$$X_{mn} = \langle \phi_m | \hat{X} | \phi_n \rangle \tag{2.22}$$

where $\hat{X}$ is the position operator that corresponds to the $X$ co-ordinate (atomic co-ordinate system) shown in Figure 2.1. Thus the electric field term of the Hamiltonian is given by,

$$W_{mn}(t) \approx eX_{mn}E_z(t). \tag{2.23}$$

Note that $X_{mn} = X^*_{nm}$. As the electric field is real, $W_{mn}(t) = W_{nm}(t)^*$.

Given all this, we will now introduce the idea of the two level atom. We will consider two levels which we will denote by the excited state $|1\rangle$, and lower level $|2\rangle$. Both of these states have complex probability amplitudes $c_1(t)$ and $c_2(t)$ which correspond to the eigenstates $|\phi_1\rangle$ and $|\phi_2\rangle$ respectively given by the composition of (2.4). While the dynamical equations for each of these levels are given by (2.16), it

does not describe what happens to an atom completely. The main problem is the decay on an atom from the excited state is not accounted for. Thus we must add decay terms $\gamma_1$ and $\gamma_2$ which corresponds to the decay of atoms from levels $|1\rangle$ and $|2\rangle$ respectively to some ground state $|3\rangle$ as shown in Figure 2.2. Adding these terms into our system and using (2.16), we obtain [27],

$$\frac{dc_1(t)}{dt} = -\left(\frac{\gamma_1}{2} + i\omega_1\right) c_1(t) - \frac{i}{\hbar} W_{12}(t) c_2(t), \tag{2.24}$$

$$\frac{dc_2(t)}{dt} = -\left(\frac{\gamma_2}{2} + i\omega_2\right) c_2(t) - \frac{i}{\hbar} W_{21}(t) c_1(t). \tag{2.25}$$

Using (2.10), the rate equations for the density matrix elements, for the two level atom are,

$$\dot{\rho}_{11}(t) = -\gamma_1 \rho_{11}(t) - \frac{i}{\hbar}\left[W_{12}(t)\rho_{21}(t) - W_{21}(t)\rho_{12}(t)\right] \tag{2.26}$$

$$\dot{\rho}_{22}(t) = -\gamma_2 \rho_{22}(t) - \frac{i}{\hbar}\left[W_{21}(t)\rho_{12}(t) - W_{12}(t)\rho_{21}(t)\right] \tag{2.27}$$

$$\dot{\rho}_{12}(t) = -\left(\frac{1}{2}\left[\gamma_1 + \gamma_2\right] + i\omega_0\right) \rho_{12}(t) - \frac{i}{\hbar} W_{12}(t)\left[\rho_{22}(t) - \rho_{11}(t)\right] \tag{2.28}$$

$$\dot{\rho}_{21}(t) = -\left(\frac{1}{2}\left[\gamma_1 + \gamma_2\right] - i\omega_0\right) \rho_{21}(t) - \frac{i}{\hbar} W_{21}(t)\left[\rho_{11}(t) - \rho_{22}(t)\right] \tag{2.29}$$

where $\omega_0 = (\omega_1 - \omega_2)$ which is the atomic transition frequency. The lower, non-interacting level $|3\rangle$, we write the following dynamical equation,

$$\dot{\rho}_{33}(t) = \gamma_1 \rho_{11}(t) + \gamma_2 \rho_{22}(t). \tag{2.30}$$

We will assume, where $m \neq 3$, that $\rho_{m3}(t) = \rho_{3m}(t) = 0$ such that off diagonal terms of the density matrix including the third level are zero. This is using an assumption that these terms decay quickly and can be taken to be zero.

We also include an addition to the off-diagonal elements which is a result of elastic atomic collisions [27,31]. To account for this phenomenon, we will add a further decay rate for both the dynamical equations $\rho_{12}(t)$ and $\rho_{21}(t)$, which is denoted by $\gamma_{ph}$. Thus the total decay rate in these off diagonal elements is given by the decay rate [11], $\gamma_a$ such that $\gamma_a = \gamma_{ph} + \frac{1}{2}(\gamma_1 + \gamma_2)$. As a result,

$$\dot{\rho}_{12}(t) = -\left(\gamma_a + i\omega_0\right) \rho_{12}(t) - \frac{i}{\hbar} W_{12}(t)\left[\rho_{22}(t) - \rho_{11}(t)\right], \tag{2.31}$$

$$\dot{\rho}_{21}(t) = -\left(\gamma_a - i\omega_0\right) \rho_{21}(t) - \frac{i}{\hbar} W_{21}(t)\left[\rho_{11}(t) - \rho_{22}(t)\right]. \tag{2.32}$$

### 2.2.1 Population Matrix and Pumping

So far we have derived the density matrix equations for individual atoms with phenomenologically introducing decays. We will now consider multiple atoms such that $\rho(z,t,t_0)$, the density matrix for the individual atoms located at $z$ and $t_0$. $t_0$ is the time at which the atom is excited to either $|1\rangle$ or $|2\rangle$ [27]. At a time $t = t_0$, or the excitation time, the density matrix is written as [32],

$$\rho(z,t_0,t_0) = \sum_n \rho_{nn}^{(0)}(z,t_0,t_0)\,|n\rangle\,\langle n| \tag{2.33}$$

where at the time $t_0$, the off-diagonal terms of this mixed state density matrix are zero. The composition of $\rho(z,t,t_0)$ is written as [32],

$$\rho(z,t,t_0) = \sum_{m,n} \rho_{mn}(z,t,t_0)\,|m\rangle\,\langle n| \tag{2.34}$$

where $m,n = 1,2$ and $\rho_{mn}(z,t,t_0)$ represents all elements in the density matrix of a two level atom. Instead of thinking of atoms in this way, we will introduce the idea of a population matrix instead. This matrix will sum over the initial times where the atoms will be pumped at a rate of $r(z,t_0)$. With all this in mind, the population matrix is given by [32],

$$\rho(z,t) = \sum_{m,n} \int_{-\infty}^{t} r(z,t_0)\rho_{mn}(z,t,t_0)dt_0\,|m\rangle\,\langle n|\,. \tag{2.35}$$

Taking the derivative of the population matrix will obtain the following equations of motion [27],

$$\dot{\rho}(z,t) = \sum_{m,n} \left( r(z,t)\rho_{mn}(z,t,t) + \int_{-\infty}^{t} r(z,t_0)\dot{\rho}_{mn}(z,t,t_0)dt_0 \right) |m\rangle\,\langle n|\,. \tag{2.36}$$

where $\rho_{mn}(z,t,t) = \delta_{mn}\rho_{mn}^{(0)}(z,t,t)$ given by (2.33). As a result, the cross off-diagonal terms are zero, $\rho_{12}^{(0)}(z,t,t) = \rho_{21}^{(0)}(z,t,t) = 0$. Furthermore we will label the pumping terms as $\lambda_1(z,t) = r(z,t)\rho_{11}^{(0)}(z,t,t)$ and $\lambda_2(z,t) = r(z,t)\rho_{22}^{(0)}(z,t,t)$. Then using (2.26), (2.27), (2.31) and (2.32), we can obtain the population dynamical equations

for $\rho_{11}(z,t)$, $\rho_{22}(z,t)$, $\rho_{12}(z,t)$ and $\rho_{21}(z,t)$,

$$\dot{\rho}_{11}(z,t) = \lambda_1(z,t) - \gamma_1\rho_{11}(z,t) - \frac{i}{\hbar}\left[W_{12}(z,t)\rho_{21}(z,t) - W_{21}(z,t)\rho_{12}(z,t)\right], \quad (2.37)$$

$$\dot{\rho}_{22}(z,t) = \lambda_2(z,t) - \gamma_2\rho_{22}(z,t) - \frac{i}{\hbar}\left[W_{21}(z,t)\rho_{12}(z,t) - W_{12}(z,t)\rho_{21}(z,t)\right], \quad (2.38)$$

$$\dot{\rho}_{12}(z,t) = -\left(\gamma_a + i\omega_0\right)\rho_{12}(z,t) - \frac{i}{\hbar}W_{12}(z,t)\left[\rho_{22}(z,t) - \rho_{11}(z,t)\right], \quad (2.39)$$

$$\dot{\rho}_{21}(z,t) = -\left(\gamma_a - i\omega_0\right)\rho_{21}(z,t) - \frac{i}{\hbar}W_{21}(z,t)\left[\rho_{11}(z,t) - \rho_{22}(z,t)\right]. \quad (2.40)$$

Given the introduction of the population matrix which represents multiple atoms over both space and time and thus the electric field is no longer constant. As a result, we have re-introduced the spatial dependence of the electric field which we denoted by $E(z,t)$. Moreover, introducing the pumping terms to the third level gives the following population dynamical equation,

$$\dot{\rho}_{33}(z,t) = \gamma_1\rho_{11}(z,t) + \gamma_2\rho_{22}(z,t) - \lambda_1(z,t) - \lambda_2(z,t). \quad (2.41)$$

Now we have obtained dynamical equations for each term in the population matrix. This is valid for solid state lasers but it can be used to approximate a semiconductor active medium as we will see in the next section.

## 2.3 Gain Polarisation and Population Inversion Dynamical Equations for Semiconductors

### 2.3.1 Semiconductor Two-level Model

In this section, we will relate the two-level atom model to semiconductors. We can still use the idea of the excited state $|1\rangle$ and we will now call the ground state $|2\rangle$. In terms of semiconductors, $|1\rangle$ refers to the existence of an electron-hole pair while $|2\rangle$ is the absence of such a pair. This is a good model for the most part however not perfect. There are two levels not taken into consideration, when there is only an electron and only a hole. However, this is derived in [33] with a four level model. For what is required here, the two level model is sufficient.

To achieve this, we remove the level $|3\rangle$ from the previous sections and create a self-consistent model for $|1\rangle$ and $|2\rangle$ only. The decays from level $|1\rangle$ will go to the ground state $|2\rangle$ while there are no decays from level $|2\rangle$. Instead the losses from $|2\rangle$ will result from the excitation of electrons into the conduction band, creating an electron-hole

pair. Thus the pumping term $\lambda_1(z,t) = \Lambda\rho_{22}(z,t)$ which arises from losses in the ground state and thus we call $-\gamma_2\rho_{22}(z,t) = -\Lambda\rho_{22}(z,t)$. We will similarly call the decay from the excited state $-\gamma_1\rho_{11}(z,t) = -\Gamma\rho_{11}(z,t)$ which results to an increase in the population of the ground state where $\lambda_2(z,t) = \Gamma\rho_{11}(z,t)$ Thus the population matrix equations for $\rho_{11}(z,t)$ and $\rho_{22}(z,t)$ become [33],

$$\dot{\rho}_{11}(z,t) = \Lambda\rho_{22}(z,t) - \Gamma\rho_{11}(z,t) - \frac{i}{\hbar}\left[W_{12}(z,t)\rho_{21}(z,t) - W_{21}(z,t)\rho_{12}(z,t)\right], \quad (2.42)$$

$$\dot{\rho}_{22}(z,t) = \Gamma\rho_{11}(z,t) - \Lambda\rho_{22}(z,t) - \frac{i}{\hbar}\left[W_{21}(z,t)\rho_{12}(z,t) - W_{12}(z,t)\rho_{21}(z,t)\right]. \quad (2.43)$$

Moreover, the gain polarisation decay time, $\gamma_P$, comprised of the carrier-carrier interactions (charge carriers like electrons and holes). It is introduced in a similar way to (2.39) and (2.40) with $\gamma_a$,

$$\dot{\rho}_{12}(z,t) = -\left(\gamma_P + i\omega_0\right)\rho_{12}(z,t) - \frac{i}{\hbar}W_{12}(z,t)\left[\rho_{22}(z,t) - \rho_{11}(z,t)\right], \quad (2.44)$$

$$\dot{\rho}_{21}(z,t) = -\left(\gamma_P - i\omega_0\right)\rho_{21}(z,t) - \frac{i}{\hbar}W_{21}(z,t)\left[\rho_{11}(z,t) - \rho_{22}(z,t)\right]. \quad (2.45)$$

### 2.3.2 Gain Polarisation and Population Inversion

So far we have derived the dynamical equations for each element of the population matrix. Now it is time to connect these equations of motion to the electromagnetic field via the macroscopic gain polarisation and population inversion. Firstly we will assume as with previous sections that the gain polarisation and population inversion vary only in the $z$ direction and the amplitude for gain polarisation is in the same one dimensional direction as the electric field $E(z,t)$. Thus we write $P_g(z,t)$ as the gain polarisation and $N(z,t)$ as the population inversion.

Gain polarisation, $P_g(z,t)$ is the measure of the dipole moment per unit volume as a result of the interaction of the active medium with the electric field. Thus we can write gain polarisation in terms of the population matrix, $\rho_{12}(z,t)$ and $\rho_{21}(z,t)$, which are the off diagonal elements of $\rho(z,t)$ which is written as [32],

$$P_g(z,t) = -e(X_{21}\rho_{12}(z,t) + X_{12}\rho_{21}(z,t)). \quad (2.46)$$

With this composition, we can write the positive frequency component, $P_g^+(z,t)$ as,

$$P_g^+(z,t) = -2eX_{21}\rho_{12}(z,t). \quad (2.47)$$

where $P_g(z,t) = \mathrm{Re}(P_g^+(z,t))$.

Next we turn our attention to the population inversion. In a semiconductor laser, we must have a large number of electrons in the conduction band, while a large number of holes are also present in the valance band, to allow stimulated emission to occur. This is the principle of population inversion, $N(z,t)$. We can write $N(z,t)$ in terms of $\rho_{11}(z,t)$ and $\rho_{22}(z,t)$ [11],

$$N(z,t) = \rho_{11}(z,t) - \rho_{22}(z,t). \tag{2.48}$$

With this in mind, we can obtain dynamical equations for gain polarisation and population inversion. Firstly, we will note the perturbation term $W_{21} = eX_{21}E(z,t)$ is written in terms of the electric field, and as a result the dynamical equation for $P_g^+(z,t)$ is gotten from (2.39) and using the composition of $N(z,t)$ [12],

$$\frac{\partial P_g^+(z,t)}{\partial t} = -(\gamma_P + i\omega_0)P_g^+(z,t) - \frac{2i\wp^2}{\hbar}N(z,t)E(z,t), \tag{2.49}$$

where $\wp^2 = e^2 X_{12}X_{21} = e^2\left|X_{12}\right|^2$.

Now we turn our attention to the population inversion, $N(z,t)$. Firstly, let $A(z,t)$ be the total population of both levels such that $A(z,t) = \rho_{11}(z,t) + \rho_{22}(z,t)$. If we subtract (2.43) from (2.42) [33],

$$\begin{aligned}
\frac{\partial N(z,t)}{\partial t} =& 2\Lambda\rho_{22}(z,t) - 2\Gamma\rho_{11}(z,t) - \frac{2i}{\hbar}W_{12}\left[\rho_{21}(z,t) - \rho_{12}(z,t)\right], \\
=& \Lambda(\rho_{22}(z,t) - \rho_{11}(z,t)) + \Lambda(\rho_{11}(z,t) + \rho_{22}(z,t)) - \Gamma(\rho_{11}(z,t) - \rho_{22}(z,t)) \\
& - \Gamma(\rho_{11}(z,t) + \rho_{22}(z,t)) + \frac{i}{\hbar}E(z,t)\left(P_g^+(z,t)^* - P_g^+(z,t)\right), \\
=& -\left(\Lambda + \Gamma\right)N(z,t) + \left(\Lambda - \Gamma\right)A(z,t) + \frac{i}{\hbar}E(z,t)\left(P_g^+(z,t)^* - P_g^+(z,t)\right),
\end{aligned}$$

where we have used the composition of $P^+(z,t)$ and $W_{12}$. We define the population inversion relaxation rate as $\gamma_N = \Lambda + \Gamma$ and the steady-state inversion as,

$$N_0(z,t) = \frac{\Lambda - \Gamma}{\gamma_N}A(z,t). \tag{2.50}$$

We will assume that $A(z,t)$ is constant in time which we will replace with $A(z)$ which results in a time-independent pump, $N_0(z)$. Putting all of these together, we get the

dynamical equation for $N(z,t)$ [12,33],

$$\frac{\partial N(z,t)}{\partial t} = -\gamma_N(N(z,t) - N_0(z)) + \frac{i}{\hbar}E(z,t)\left(P_g^+(z,t)^* - P_g^+(z,t)\right). \tag{2.51}$$

We have now obtained the equations connecting the ideas of quantum mechanics for the gain medium to the classical interpretation of the electromagnetic field. These are the dynamical equations for population inversion and gain polarisation. Now we can connect them to the classical electromagnetic field via Maxwell's equations.

## 2.4 Maxwell's Equations

In this section, we will connect the classical electromagnetic field to the equations obtained in the previous section for both the population inversion and gain polarisation. We introduce the electric field $\mathbf{E}(\mathbf{r},t)$, magnetic field $\mathbf{H}(\mathbf{r},t)$, magnetic induction $\mathbf{B}(\mathbf{r},t)$, electric displacement vector $\mathbf{D}(\mathbf{r},t)$ and the current and charge densities given by $\mathbf{J}(\mathbf{r},t)$ and $\rho_c(\mathbf{r},t)$ respectively. They are all related by Maxwell's equations which are given by [22],

$$\nabla \cdot \mathbf{D}(\mathbf{r},t) = \rho_c(\mathbf{r},t) \tag{2.52}$$

$$\nabla \cdot \mathbf{B}(\mathbf{r},t) = 0 \tag{2.53}$$

$$\nabla \times \mathbf{E}(\mathbf{r},t) = -\frac{\partial \mathbf{B}(\mathbf{r},t)}{\partial t} \tag{2.54}$$

$$\nabla \times \mathbf{H}(\mathbf{r},t) = \mathbf{J}(\mathbf{r},t) + \frac{\partial \mathbf{D}(\mathbf{r},t)}{\partial t} \tag{2.55}$$

We will make th assumption that the medium is electrically neutral which means the charge density is zero. Thus (2.52) becomes,

$$\nabla \cdot \mathbf{D}(\mathbf{r},t) = 0. \tag{2.56}$$

Like we have done in previous sections, which was to consider the electromagnetic field, along with the polarisation to be only varying in the $z$ direction and each variable has a one dimensional amplitude transverse to the direction of propagation.This means supposing that $\mathbf{E}(\mathbf{r},t) = E(z,t)\hat{\mathbf{i}}$, $\mathbf{D}(\mathbf{r},t) = D(z,t)\hat{\mathbf{i}}$, $\mathbf{P}_g(\mathbf{r},t) = P_g(z,t)\hat{\mathbf{i}}$, $\mathbf{P}_b(\mathbf{r},t) = P_b(z,t)\hat{\mathbf{i}}$ and $\mathbf{J}(\mathbf{r},t) = J(z,t)\hat{\mathbf{i}}$ where $\hat{\mathbf{i}}$ is the unit vector in the $x$ direction. Using the same principle, we write the magnetic induction and magnetic field as, $\mathbf{B}(\mathbf{r},t) = B(z,t)\hat{\mathbf{j}}$ and $\mathbf{H}(\mathbf{r},t) = H(z,t)\hat{\mathbf{j}}$ where $\hat{\mathbf{j}}$ is the unit vector in the $y$ direction.

As a result, we can write (2.54) and (2.55) in a similar way to [34],

$$\frac{\partial E(z,t)}{\partial z} = -\frac{\partial B(z,t)}{\partial t} \tag{2.57}$$

$$\frac{\partial H(z,t)}{\partial z} = -J(z,t) - \frac{\partial D(z,t)}{\partial t}. \tag{2.58}$$

The composition of the electric displacement vector is written as $D(z,t) = \epsilon_0 E(z,t) + P(z,t)$ where $\epsilon_0$ is the permittivity of free space and $P(z,t)$ is the polarisation and is a summation of the background ($P_b(z,t)$) and gain medium ($P_g(z,t)$) polarisations given by $P(z,t) = P_b(z,t) + P_g(z,t)$. We can write $D(z,t)$ as,

$$D(z,t) = \epsilon_0 E(z,t) + P_b(z,t) + P_g(z,t) \tag{2.59}$$

The magnetic induction is written as $B(z,t) = \mu_0(H(z,t) + M(z,t))$ where $\mu_0$ is the permeability of free space and $M(z,t)$ is the magnetisation ($M(z,t) = 0$ in Maxwell's equations above). The current density can also be written in terms of the electric field which is given by $J(z,t) = \sigma E(z,t)$, which is referred to as Ohm's law where $\sigma$ is the conductivity of the medium. Introducing the background electrical susceptibility, $\chi_b(z)$, we can relate $P_b(z,t)$ and $E(z,t)$,

$$P_b(z,t) = \epsilon_0 \chi_b(z) E(z,t). \tag{2.60}$$

Using all of this information, (2.57) and (2.58) become,

$$\frac{\partial E(z,t)}{\partial z} = -\frac{\partial B(z,t)}{\partial t}, \tag{2.61}$$

$$\frac{\partial B(z,t)}{\partial z} = -\sigma\mu_0 E(z,t) - \frac{n_b(z)^2}{c^2}\frac{\partial E(z,t)}{\partial t} - \mu_0 \frac{\partial P_g(z,t)}{\partial t}, \tag{2.62}$$

where we use the relation $c^2 = (\epsilon_0\mu_0)^{-1}$ and introduce the background refractive index as,

$$n_b(z)^2 = 1 + \chi_b(z). \tag{2.63}$$

From here we can obtain the electric field equation which can be obtained by taking the spatial derivative of (2.61) and relating it to (2.62) to eliminate the magnetic induction to obtain,

$$\frac{\partial^2 E(z,t)}{\partial z^2} = \sigma\mu_0 \frac{\partial E(z,t)}{\partial t} + \frac{n_b^2(z)}{c^2}\frac{\partial^2 E(z,t)}{\partial t^2} + \mu_0 \frac{\partial^2 P_g(z,t)}{\partial t^2}. \tag{2.64}$$

Thus we have obtained all the Maxwell-Bloch equations for the electric field, (2.64), gain polarisation, (2.49), and population inversion, (2.51). Note that the conductivity term, $\sigma$ can be thought of as losses in the laser [11].

### 2.4.1 Electric Field and Gain Polarisation Decomposition

For this chapter, we would like to decompose $E(z,t)$ and $P_g(z,t)$ as follows. The electric field and the gain polarisation can be written in terms of frequencies $\omega_n$ for the n$^{th}$ mode. Decomposing these terms can further be written in terms of spatial varying, $U_n(z)$ and introducing complex amplitudes $\mathcal{E}_n(t)$ and $\mathcal{P}_n(z,t)$ for the electric field and gain polarisation respectively. Thus the decomposition can be written as,

$$E(z,t) = \frac{1}{2}\sum_n \left(\mathcal{E}_n(t)U_n(z)e^{-i\omega_n t} + \mathcal{E}_n(t)^* U_n(z)^* e^{i\omega_n t}\right), \tag{2.65}$$

$$P_g(z,t) = \frac{1}{2}\sum_n \left(\mathcal{P}_n(z,t)e^{-i\omega_n t} + \mathcal{P}_n(z,t)^* e^{i\omega_n t}\right), \tag{2.66}$$

where we also define the positive frequency components for the electric field and gain polarisation, $E^+(z,t)$ and $P_g^+(z,t)$ respectively and are given by,

$$E^+(z,t) = \sum_n \mathcal{E}_n(t)U_n(z)e^{-i\omega_n t}, \tag{2.67}$$

$$P_g^+(z,t) = \sum_n \mathcal{P}_n(z,t)e^{-i\omega_n t}. \tag{2.68}$$

Note that we consider the time varying amplitudes, $\mathcal{E}(t)$ and $\mathcal{P}(z,t)$ and their complex conjugates to be slowly varying in time in comparison to the exponential terms in the above decompositions. The relation between the electric field and gain polarisation to (2.67) and (2.68) is given by,

$$E(z,t) = \mathrm{Re}(E^+(z,t)) = \frac{1}{2}\left(E^+(z,t) + E^+(z,t)^*\right), \tag{2.69}$$

$$P_g(z,t) = \mathrm{Re}(P_g^+(z,t)) = \frac{1}{2}\left(P_g^+(z,t) + P_g^+(z,t)^*\right). \tag{2.70}$$

Consider the electric field equation (2.64). Instead of seeking the solution with $E(z,t)$ and $P_g(z,t)$, we can instead use $E^+(z,t)$ and $P_g^+(z,t)$ to solve the following wave

equation,

$$\frac{\partial^2 E^+(z,t)}{\partial z^2} = \sigma\mu_0 \frac{\partial E^+(z,t)}{\partial t} + \frac{n_b^2(z)}{c^2}\frac{\partial^2 E^+(z,t)}{\partial t^2} + \mu_0 \frac{\partial^2 P_g^+(z,t)}{\partial t^2}. \tag{2.71}$$

## 2.5 Gain Polarisation and Population Inversion Dynamics

In this section, we will consider the dynamical equations for population inversion and gain polarisation. We can in fact make some approximations which will make some of the calculations later on in the thesis easier. First we can adiabatically eliminate the dynamics from gain polarisation and then use the rotating wave approximation (RWA). Then we can simplify the population inversion dynamical equation with the assumption that the dynamics of the population inversion is quite slow.

### 2.5.1 Gain Polarisation Equation Approximation and Rotating Wave Approximation for Gain Polarisation

The gain polarisation equation approximation, which we will consider throughout, which is used for modelling lasers to adiabatically eliminate the gain polarisation dynamical equation [16, 33, 35]. To see this approximation in action, consider the gain polarisation dynamical equation, (2.49) and using the decomposition of $E(z,t)$ and $P_g^+(z,t)$ ((2.65) and (2.68)) such that,

$$\begin{aligned}\sum_n \frac{\partial}{\partial t}\left(\mathcal{P}_n(z,t)e^{-i\omega_n t}\right) = -\sum_n \Bigg( &\left(\gamma_P + i\omega_0\right)\mathcal{P}_n(z,t)e^{-i\omega_n t} \\ &+ \frac{i\wp^2}{\hbar} N(z,t)\left(\mathcal{E}_n(t)U_n(z)e^{-i\omega_n t} + \mathcal{E}_n(t)^* U_n(z)^* e^{i\omega_n t}\right)\Bigg)\end{aligned} \tag{2.72}$$

If we multiply this equation by the exponential factor $e^{(i\omega_0+\gamma_p)t}$ and integrating through time, such that we can write the gain polarisation dynamical equation as,

$$\sum_n \mathcal{P}_n(z,t)e^{-i(\omega_n-\omega_0)t+\gamma_P t}$$
$$= -\frac{i\wp^2}{\hbar}\int_{-\infty}^{t}\Big(N(z,t')\sum_n\big(\mathcal{E}_n(t')U_n(z)e^{-i(\omega_n-\omega_0)t'+\gamma_P t'} + \mathcal{E}_n(t')^*U_n(z)^*e^{i(\omega_n+\omega_0)t'+\gamma_P t'}\big)\Big)dt' \tag{2.73}$$

Now we can use the gain polarisation equation approximation. If we consider the case where the population inversion term and electric field amplitudes, $\mathcal{E}_n(t)$ and $\mathcal{E}_n(t)^*$ vary slowly in comparison to the exponential terms, we can approximate the integral as follows,

$$\int_{-\infty}^{t}\Big(N(z,t')\big(\mathcal{E}_n(t')U_n(z)e^{-i(\omega_n-\omega_0)t'+\gamma_P t'} + \mathcal{E}_n(t')^*U_n(z)^*e^{i(\omega_n+\omega_0)t'+\gamma_P t'}\big)\Big)dt' \approx$$
$$N(z,t)\left(\mathcal{E}_n(t)U_n(z)\int_{-\infty}^{t}e^{-i(\omega_n-\omega_0)t'+\gamma_P t'}dt' + \mathcal{E}_n(t)^*U_n(z)^*\int_{-\infty}^{t}e^{i(\omega_n+\omega_0)t'+\gamma_P t'}dt'\right). \tag{2.74}$$

Thus we have adiabatically eliminated the dynamics for the gain polarisation and we obtain a function for $P_g^+(z,t)$ which is given by,

$$P_g^+(z,t) = -\frac{i\wp^2}{\hbar}N(z,t)\sum_n\left(\frac{\mathcal{E}_n(t)U_n(z)e^{-i\omega_n t}}{\gamma_P + i(\omega_0-\omega_n)} + \frac{\mathcal{E}_n(t)^*U_n(z)^*e^{i\omega_n t}}{\gamma_P + i(\omega_0+\omega_n)}\right). \tag{2.75}$$

The next approximation we will use is the RWA. This is a useful approximation to remove terms which are small in comparison to the others. We will apply this to the gain polarisation equation (2.75). Notice that we have two denominators, one with the frequencies summed up, $\omega_0+\omega_n$ and the other with the difference between the two frequencies, $\omega_0-\omega_n$. If we assume that $\gamma_P, |\omega_0-\omega_n| \ll \omega_0+\omega_n$, then the second term of (2.75) is much smaller than the first and as a result we can neglect it. This is an example of the RWA. Thus we can write,

$$P_g^+(z,t) \approx -\frac{i\wp^2}{\hbar} N(z,t) \sum_n \frac{\mathcal{E}_n(t) U_n(z) e^{-i\omega_n t}}{\gamma_P + i(\omega_0 - \omega_n)}. \tag{2.76}$$

$$= -\frac{\wp^2}{\gamma_P \hbar} N(z,t) \sum_n \frac{1}{1 + \left(\frac{\omega_0 - \omega_n}{\gamma_P}\right)^2} \left(\frac{\omega_0 - \omega_n}{\gamma_P} + i\right) \mathcal{E}_n(t) U_n(z) e^{-i\omega_n t} \tag{2.77}$$

$$= -\frac{\wp^2}{\gamma_P \hbar} N(z,t) \sum_n \mathscr{L}(\Delta_n)(\Delta_n + i) \mathcal{E}_n(t) U_n(z) e^{-i\omega_n t}, \tag{2.78}$$

where $\mathscr{L}(\Delta_n)$ is the Lorentzian distribution which given by,

$$\mathscr{L}(\Delta_n) = \frac{1}{1 + \Delta_n^2} \tag{2.79}$$

such that $\Delta_n$ is the frequency detuning term for the $n^{th}$ mode, $\Delta_n = \frac{\omega_0 - \omega_n}{\gamma_P}$.

The idea of the RWA is to do with the exponential terms containing $\omega_0 + \omega_n$ and $\omega_0 - \omega_n$. When we integrate over a time interval longer than $\frac{2\pi}{\omega_0}$ but small enough such that remaining time dependent quantities are slowly-varying, like we have done in (2.73), the exponential containing the sum of the frequencies oscillate rapidly and the result after integrating it is small compared to the terms oscillating at the frequency difference [12]. As a result we neglect the second term in (2.75).

### 2.5.2 Population Inversion Approximations

We will now simplify the dynamics for population inversion. The first approximation we will use is the RWA. Using the decomposition of the electric field, with (2.76) and noting (2.51), we can write the following,

$$\begin{aligned} E(z,t)(P^+(z,t)^* - P^+(z,t)) =& \frac{1}{2} \sum_{n,m} \Bigg( \frac{1}{\gamma_P - i(\omega_0 - \omega_m)} \times \\ & \Big( \mathcal{E}_n(t) \mathcal{E}_m(t)^* U_n(z) U_m(z)^* e^{-i(\omega_n - \omega_m)t} + \mathcal{E}_n(t)^* \mathcal{E}_m(t)^* U_n(z)^* U_m(z)^* e^{i(\omega_n + \omega_m)t} \Big) \\ & + \frac{1}{\gamma_P + i(\omega_0 - \omega_m)} \times \\ & \Big( \mathcal{E}_m(t) \mathcal{E}_n(t)^* U_m(z) U_n(z)^* e^{-i(\omega_m - \omega_n)t} + \mathcal{E}_m(t) \mathcal{E}_n(t) U_m(z) U_n(z) e^{-i(\omega_m + \omega_n)t} \Big) \Bigg). \end{aligned} \tag{2.80}$$

With the same methodology as used with the gain polarisation, we can use the RWA given the fact that the time dynamics for $N(z,t)$ is much smaller than the sum of

two modal frequencies $\omega_n + \omega_m$. If we assume that $\gamma_N, |\omega_n - \omega_m| \ll \omega_n + \omega_m$, we can write the above in terms of $E^+(z,t)$ and $P_g^+(z,t)$ such that,

$$E(z,t)(P_g^+(z,t)^* - P_g^+(z,t)^*) \approx \frac{1}{2}\left(E^+(z,t)P_g^+(z,t)^* - P_g^+(z,t)E^+(z,t)^*\right) \quad (2.81)$$

Thus (2.51) becomes,

$$\frac{\partial N(z,t)}{\partial t} = -\gamma_N(N(z,t) - N_0(z)) + \frac{i}{2\hbar}\left(E^+(z,t)P_g^+(z,t)^* - P_g^+(z,t)E^+(z,t)^*\right). \quad (2.82)$$

Now we turn our attention to the second assumption. In the population inversion equation (2.82), if we expand out $E^+(z,t)$ and $P_g^+(z,t)$, we take into account degenerate modes where the frequencies $\omega_n$ and $\omega_m$ are quite close and thus modes effect each other. However we would like to consider non-degenerate modes such that the for any two modal frequencies $\omega_n$ and $\omega_m$, that $|\omega_n - \omega_m|$ is large in comparison to the decay rate for $N(z,t)$, $\gamma_N$. If this is true we can take $\omega_n = \omega_m$ in (2.80). However to maintain the RWA as well, the sum of these frequencies must be significantly larger than both $|\omega_n - \omega_m|$, $\gamma_N$. Thus if $\gamma_N \ll |\omega_n - \omega_m| \ll \omega_n + \omega_m$,

$$\frac{\partial N(z,t)}{\partial t} = -\gamma_N(N(z,t) - N_0(z)) - \frac{\wp^2}{\gamma_P\hbar^2}N(z,t)\sum_n \mathscr{L}(\Delta_n)\,|\mathcal{E}_n(t)|^2|U_n(z)|^2 \quad (2.83)$$

where the homogeneous broadening term is a Lorentzian distribution, $\mathscr{L}(\Delta_n)$.

## 2.6 Dynamics and Coupled-Cavity Lasers

One of the main aims of this thesis is to investigate coupled cavities with open boundaries. In particular, we will focus on these coupled cavities with a gap in between them as shown in Figure 2.3. We will only consider outgoing waves that go to infinity at each boundary of the entire laser with no incoming light. Throughout, we will discuss various aspects of laser theory which can be used in conjunction with this setup from the steady-state, in Chapters 4 and 5, to the dynamical model we will derive in Chapter 6. Furthermore, we will compare this setup to other types of lasers such as a single cavity structure or two cavities with no gap. In later chapters, we see the effect the gap has on modes and how its changes the effect of EPs have on these devices. In this section, we will give an overview of the research previously carried out involving the dynamics of lasers and the advantages or disadvantages these ideas have

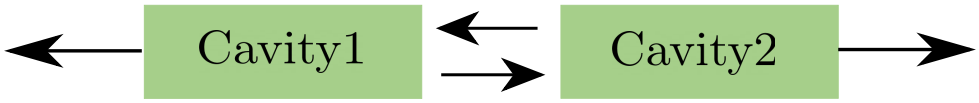



Figure 2.3: Open boundaries of a coupled-cavity laser system with two cavities with a gap in between.

for the structure shown in Figure 2.3. Firstly, we will provide a brief account of closed boundary single cavity lasers. From there, we will discuss when that is extended to a more complicated structure such as coupled cavities. The final two subsections deal with weakly-coupled cavities either using optical injection or mutually-coupled cavities which uses DDEs.

### 2.6.1 Closed Single Cavity Lasers

In this subsection, we will derive dynamical equations for a closed boundary, single cavity laser. This type of laser was the major focus for modelling with SLT when it was first used [11]. To see this, we will consider a laser with a single cavity of length $L$ with refractive index $n_s$ and with closed boundaries such that for any spatial modal profile $U_n(z)$, which comes from the electric field decomposition given by both (2.65) and (2.67), we have the following boundary conditions,

$$U_n(0) = U_n(L) = 0. \tag{2.84}$$

Moreover, given the closed boundary, two real spatial distributions $U_n(z)$ and $U_m(z)$ satisfy the orthogonality condition such that,

$$\int_0^L U_n(z)U_m(z)dz = \mathcal{G}\delta_{mn}, \tag{2.85}$$

where $\mathcal{G}$ is a normalisation constant. Furthermore we introduce the passive cavity frequency $\Omega_n$ such that $U_n(z)$ satisfies the following equation,

$$\left\{\frac{d^2}{dz^2} + \left(\frac{\Omega_n n_s}{c}\right)^2\right\} U_n(z) = 0. \tag{2.86}$$

In previous sections, we considered a spatially varying $N(z,t)$, however here we will spatially average over the length of the laser instead where $\bar{N}(t) = \frac{1}{L}\int_0^L N(z,t)dz$,

where $L$ is the length of the cavity, and approximate (2.76) as,

$$P_g^+(z,t) \approx -\frac{i\wp^2}{\hbar}\bar{N}(t)\sum_n \frac{\mathcal{E}_n(t)U_n(z)e^{-i\omega_n t}}{\gamma_P + i(\omega_0 - \omega_n)}. \tag{2.87}$$

Using the gain polarisation (2.87), the passive mode differential equation (2.86) and the positive frequency electric field decomposition (2.67), (2.71) becomes,

$$\sum_n \left( \frac{n_s^2\Omega_n^2}{c^2}\mathcal{E}_n(t) + \sigma\mu_0(\dot{\mathcal{E}}_n(t) - i\omega_n\mathcal{E}_n(t)) + \frac{n_s^2}{c^2}(\ddot{\mathcal{E}}_n(t) - 2i\omega_n\dot{\mathcal{E}}_n(t) - \omega_n^2\mathcal{E}_n(t)) \right.$$
$$\left. - \frac{i\wp^2\mu_0}{\hbar}\frac{\left(\frac{d^2}{dt^2}(\bar{N}(t)\mathcal{E}_n(t)) - 2i\omega_n\frac{d}{dt}(\bar{N}(t)\mathcal{E}_n(t)) - \omega_n^2(\bar{N}(t)\mathcal{E}_n(t))\right)}{\gamma_P + i(\omega_0 - \omega_n)} \right) U_n(z)e^{-i\omega_n t} = 0. \tag{2.88}$$

Given the fact that $\mathcal{E}_n(t)$ and $\bar{N}(t)$ is slowly varying in comparison to exponential factors $e^{i\omega_n t}$, we can use the Slowly Varying Amplitude Approximation (SVAA) [12](also known as the Slowly Varying Envelope Approximation). Using SVAA, $|\dot{\mathcal{E}}_n(t)| \ll \omega_n|\mathcal{E}_n(t)|$ and $|\ddot{\mathcal{E}}_n(t)| \ll \omega_n|\dot{\mathcal{E}}_n(t)|$. We can thus eliminate terms in a similar way to [27], such that $\sigma\mu_0\dot{\mathcal{E}}_n(t)$ and $\frac{n_s^2}{c^2}\ddot{\mathcal{E}}_n(t)$ are neglected. We can approximate,

$$\frac{d^2}{dt^2}(\bar{N}(t)\mathcal{E}_n(t)) - 2i\omega_n\frac{d}{dt}(\bar{N}(t)\mathcal{E}_n(t)) - \omega_n^2(\bar{N}(t)\mathcal{E}_n(t)) \approx -\omega_n^2(\bar{N}(t)\mathcal{E}_n(t)). \tag{2.89}$$

Using all this information, the electric field equation for the $n^{th}$ mode, (2.64), becomes

$$\dot{\mathcal{E}}_n(t) = -\left(i(\Omega_n - \omega_n) + \frac{1}{2}\frac{\sigma}{n_s^2\epsilon_0}\right)\mathcal{E}_n(t) + \frac{\omega_n\wp^2}{2n_s^2\epsilon_0\hbar}\frac{\bar{N}(t)\mathcal{E}_n(t)}{\gamma_P + i(\omega_0 - \omega_n)}. \tag{2.90}$$

by using the following approximation [27],

$$\frac{\Omega_n^2 - \omega_n^2}{2\omega_n} \approx \Omega_n - \omega_n. \tag{2.91}$$

In the case of (2.90), we used the rate equation approximation, however if this is not valid, we can put the electric field dynamical equation in terms of the gain polarisation. Given a spatially averaged population inversion, we can write the gain polarisation for the $n^{th}$ mode as $\mathcal{P}_n(z,t) = \tilde{\mathcal{P}}_n(t)U_n(z)$. We can similarly use the SVAA for $\tilde{\mathcal{P}}_n(t)$ as assuming $\omega_n^2|\tilde{\mathcal{P}}_n(t)| \gg \omega_n\left|\dot{\tilde{\mathcal{P}}}_n(t)\right| \gg \left|\ddot{\tilde{\mathcal{P}}}_n(t)\right|$, we can write the

dynamical equation for the electric field as,

$$\dot{\mathcal{E}}_n(t) = -\left(i(\Omega_n - \omega_n) + \frac{1}{2}\frac{\sigma}{n_s^2\epsilon_0}\right)\mathcal{E}_n(t) + \frac{i\omega_n}{2n_s^2\epsilon_0}\tilde{\mathcal{P}}_n(t). \tag{2.92}$$

We have thus formulated a dynamical equation for the electric field of a single cavity structure in a closed laser with passive cavity modal frequencies $\Omega_n$. There are two issues with using this formalisation in later chapters. The first is the boundary conditions at both ends are zero for each $U_n(z)$ as we are discussing the closed-cavity laser. This is not a realistic interpretation of the laser as it would need to have open boundaries for the light to escape. The second issue is the method is only for a single cavity and for a more complicated structure, the orthogonality condition, (2.85), is not satisfied as a result.

### 2.6.2 Composite Cavity Modes

The composite-cavity model approach is quite similar to the one used for a single cavity. A composite cavity is a multi-sectioned laser which can be made up of several components for example multiple active mediums with gaps. Taking this idea, we can look at a modal profile over the entire structure, which are referred to as composite-cavity modes [17, 36, 37]. The $n^{th}$ mode has an electric field amplitude of $\mathcal{E}_n(t)$ with $U_n(z)$, the spatial mode for the entire structure. Suppose the length of the whole laser is $L$. We consider modes $U_n(z)$ with a closed boundary such that,

$$U_n(0) = U_n(L) = 0, \tag{2.93}$$

where $U_n(z)$ is continuous at the boundaries at each section along with its derivative and is zero [17]. As a result of the boundary conditions, for real $n^2(z)$ spatially varying refractive index, the following weighted orthogonality relation holds for two modes $U_m(z)$ and $U_n(z)$ where,

$$\int_0^L n^2(z)U_n(z)U_m(z)dz = \mathcal{G}\delta_{mn} \tag{2.94}$$

where $\mathcal{G}$ is a normalisation constant. Consider a three section laser with two gain medium cavities separated by gap. In composite-cavity modes, each cavity would have a separate population inversion. In this instance we would have a set of three dynamical equations, one for the complex electric field amplitude and two for the time dependent inversions in a similar way to the single cavity SLT equations [38].

The dynamics has been thoroughly investigated with composite-cavity modes which provides a nice picture of the behaviour of strongly-coupled cavities [39–43]. However, while composite cavity modes are able to model a more complicated structure, the spatial distribution described by $U_n(z)$ is for the passive situation and does not provide the spatial distribution of the active medium. Furthermore, these modes represent a closed-cavity system, as with the previous subsection.

### 2.6.3 Optical Injection

For optical injection dynamics, investigations were carried out both theoretically [16, 44, 45] and experimentally [46, 47]. Consider two lasers which we will label A and B. Laser A will be the "Master" laser such that it injects light into laser B. In contrast to mutually-coupled laser, laser B has no effect on laser A. As a result of this injection process, the frequency of laser B will adjust to match the incoming frequency of laser A. This is only valid if the frequency of laser A is close to laser B before injection and if the power input from A to B is sufficient [44]. The dynamical equations which govern this process are given by [16],

$$\dot{\tilde{E}}(t) = \frac{1}{2}\xi(1+i\alpha)(\tilde{N}(t) - N_{thr})\tilde{E}(t) + K\tilde{E}_i(t), \tag{2.95}$$

$$\dot{\tilde{N}}(t) = J - \gamma_N - (\gamma_E + \xi(\tilde{N}(t) - N_{thr}))|\tilde{E}(t)|^2, \tag{2.96}$$

where $\tilde{E}(t)$ is the complex electric field, $\tilde{N}(t)$ is the carrier density, $\xi$ is the gain coefficient, $J$ is the pump, $\alpha$ is the linewidth enhancement factor [48], $N_{thr}$ is the carrier density at threshold, $K$ is the injection field rate and $\tilde{E}_i(t)$ is the injection signal. Note that $\gamma_N$ here is the carrier decay rate while $\gamma_E$ represents cavity losses. The difference between these equations and the equations derived in SLT is the inclusion of the injection term in the electric field dynamics $K\tilde{E}_i(t)$. From (2.95) and (2.96), autonomous equations have been derived and with those, interesting dynamics have been shown when varying the parameters for detuning and injection strength [49–53]. However, optical injection does not fulfil the requirements of the lasers we are dealing with in this thesis. As explained, optical injection cannot describe a mutually coupled scenario as one lasers feeds into the other and not vice versa.

### 2.6.4 Mutually-Coupled Lasers

The next interesting area of research in coupled laser dynamics is looking into mutually-coupled lasers with time delay using DDEs such as ones similar to the Lang-Kobayashi

equations [54]. In contrast to optical injection, here we consider the instance where two lasers interact with each other rather than being unidirectional. There is also a major difference between using time delay equations and the dynamics of composite cavity modes [17]. With the time delay mutually coupled equations, each section, or laser has a separate electric field amplitude while composite cavity mode equations calculate the electric field dynamics for the entire structure of multiple sections. As the electric field amplitudes are separate for each laser, it is good for use of weakly-coupled lasers.

If we consider two lasers with electric field amplitudes $\mathscr{E}_1(t)e^{i\omega_0 t}$ and $\mathscr{E}_2(t)e^{i\omega_0 t}$ where $\omega_0$ is the central frequency, with $\mathscr{E}_1(t)$ and $\mathscr{E}_2(t)$ being slowly-varying functions. Moreover, we will write $\mathscr{N}_1(t)$ and $\mathscr{N}_2(t)$ as the normalised inversion which correspond to each laser with amplitudes $\mathscr{E}_1(t)$ and $\mathscr{E}_2(t)$ respectively. The resulting dynamical equations are given by [55],

$$\frac{d\mathscr{E}_{1/2}(t)}{dt} = (1+i\alpha)\mathscr{N}_{1/2}(t)\mathscr{E}_{1/2}(t) + \tilde{\mathcal{K}}e^{-iC_p}\mathscr{E}_{2/1}(t-\tau) - \frac{i}{2}(\omega_{2/1}-\omega_{1/2})\mathscr{E}_{1/2}(t) \tag{2.97}$$

$$\frac{d\mathscr{N}_{1/2}(t)}{dt} = \gamma_N\left(J - \mathscr{N}_{1/2}(t) - (1+2\mathscr{N}_{1/2}(t))|\mathscr{E}_{1/2}(t)|^2\right) \tag{2.98}$$

where $\alpha$ is the linewidth enhancement factor, $C_p$ is the coupling phase, $J$ is the pump, $\gamma_N$ is the carrier decay rate, $\tilde{\mathcal{K}}$ is the coupling strength and $\omega_1$ and $\omega_2$ are the frequencies of each laser. Note that $\tau$ is the time delay as a result of the coupling. An analytical solution can be obtained, known as compound laser modes, with the frequency of each laser being the same $\omega_1 = \omega_2 = \omega_s$. The resulting solution is [55],

$$\mathscr{E}_1(t) = \mathscr{E}_1^s e^{i\omega_s t} \tag{2.99}$$

$$\mathscr{E}_2(t) = \mathscr{E}_2^s e^{i\omega_s t + i\hat{\sigma}} \tag{2.100}$$

$$\mathscr{N}_{1/2}(t) = \mathscr{N}_{1/2}^s \tag{2.101}$$

where $\mathscr{E}_{1/2}^s$, $\mathscr{N}_{1/2}^s$ and $\hat{\sigma}$ are real valued and $\hat{\sigma}$ is the phase shift between the lasers. This solution is also known as one-colour states. Interesting dynamical effects from numerical solutions to more analytical results such as one-colour (compound laser modes) and two-colour states have been shown [56–62] and shows weakly coupled lasers have been thoroughly investigated theoretically. While mutually-coupled lasers with weak coupling can be modelled using the above equations, unfortunately it does not cover the closely-coupled cavity situation we will explore. The main difference is

to achieve an electric field which represents the entire structure rather than having two separate fields for each cavity. This is because an overall electric field can replicate effects due to strong interactions between the cavities.

## 2.7 Conclusions

In this chapter, we have provided an overview of the background which is required for the work carried out in this thesis. We also provide a brief description of other models which have been derived to describe various laser structures such as single cavity and coupled cavity lasers. In particular, we have derived dynamical equations for the population inversion and gain polarisation. We arrived at these equations by considering a two-level model approach to describe the active medium. We also use this model as one possible description of a semiconductor medium. Thus these equations are valid for both a atom laser and for a simplistic description of a semiconductor laser. From there we connected these dynamical variables with the classical electromagnetic field using SLT. Thus we arrived at a set of three self-consistent dynamical equations for the electric field, gain polarisation and population inversion for a single cavity laser. However in later chapters, we will use the inversion and gain polarisation equations to describe the coupled-cavity case, although we will still adiabatically eliminate the dynamics of $P_g^+(z,t)$. In the final section, we compared models which use SLT for different laser structures stating the advantages and disadvantages of each model presented.

# Chapter 3

# Coupled Mode Theory

In this chapter, we will focus on the idea of linearly coupled oscillators that are described by Coupled Mode Theory (CMT) [14, 63, 64] which is a model that is particularly useful for optical devices [65–68]. Although the model we consider will have no gain and is linearly coupled, we still can obtain effective results which describe complex effects of coupled cavities namely EPs [21,69,70]. We are also able to deduce from this model similar behaviour that will be seen in later chapters, with more complicated theories, such as how the eigenvalues of the system change with the variation of physical parameters. With this in mind, the chapter is written as follows. In the first section, we will give an overview of EPs in a general two-dimensional format which we are able to link to CMT. From there we will introduce coupled cavities with losses and obtain eigenvalues which represent the frequencies and losses of the coupled system. We discuss how changing the parameters will effect these eigenvalues and can lead to EPs. In the final section, we derive the conditions we must impose on the model so that it describes the physics of a non-gain coupled system correctly.

## 3.1 Exceptional Points in a Linearly Coupled System

EPs, also referred to as non-hermitian degeneracies [71], are an interesting phenomenon which has been widely studied over the past few years [20, 70, 72–78]. As mentioned previously, the fundamental idea of an EP is that two eigenvalues (usually complex) coalesce by the varying of parameters. However, this is not the only criteria for EPs. The second condition concerns the eigenvectors which correspond to these eigenvalues. The eigenvectors must also coalesce. In the a simple case, we will

consider a $2 \times 2$ system and show generally the solution that arises at an EP. We will then use this general system and apply it to CMT in later sections.

### 3.1.1 Two-Dimensional Eigenvalue Problem

We will consider the following $2 \times 2$ matrix system given by the matrix $\mathcal{C}$ and some complex vector $\mathbf{v}(t) = \begin{pmatrix} v_1(t) \\ v_2(t) \end{pmatrix}$,

$$\frac{d\mathbf{v}(t)}{dt} = \mathcal{C}\mathbf{v}(t), \tag{3.1}$$

where $\mathcal{C}$ is made up of complex-valued terms $a_{ij}$ which is written as,

$$\mathcal{C} = \begin{pmatrix} a_{11} & a_{12} \\ a_{21} & a_{22} \end{pmatrix}. \tag{3.2}$$

We will now seek to find eigenvalues $\lambda_\pm$ for (3.1). They are given by the following,

$$\lambda_\pm = \frac{\mathrm{tr}(\mathcal{C}) \pm \sqrt{\mathrm{tr}(\mathcal{C})^2 - 4\mathrm{det}(\mathcal{C})}}{2}, \tag{3.3}$$

where $\mathrm{tr}(\mathcal{C}) = a_{11}+a_{22}$ is the trace of $\mathcal{C}$ and $\mathrm{det}(\mathcal{C}) = a_{11}a_{22}-a_{12}a_{21}$ is the determinant of $\mathcal{C}$. For the two eigenvalues $\lambda_+$ and $\lambda_-$ to equal, which is to have an EP, the terms in the square root of (3.3) equal. Thus $\mathrm{tr}(\mathcal{C})^2 = 4\mathrm{det}(\mathcal{C})$ and in terms of the matrix elements of $\mathcal{C}$,

$$a_{12} = -\frac{(a_{11} - a_{22})^2}{4a_{21}}. \tag{3.4}$$

Thus the matrix in a $2 \times 2$ system given by (3.1) is written as,

$$\mathcal{C} = \begin{pmatrix} a_{11} & -\frac{(a_{11}-a_{22})^2}{4a_{21}} \\ a_{21} & a_{22} \end{pmatrix}. \tag{3.5}$$

### 3.1.2 Matrix Transformation

In later sections when investigating EPs in CMT, we will use a matrix transformation to help us with our analysis of coupled modes. We will thus apply a suitable transformation to (3.1) that we can turn (3.5) into a similar matrix as the one we will derive later on. Thus we will consider a complex diagonal matrix which we will

denote by $\mathcal{Q}$. It is given by,

$$\mathcal{Q} = \begin{pmatrix} 1 & 0 \\ 0 & u \end{pmatrix} \tag{3.6}$$

where $u$ is some complex number. With this transformation matrix and $\mathcal{C}$, we define our new matrix $\mathcal{D}$ such that,

$$\mathcal{D} = \mathcal{Q}^{-1}\mathcal{C}\mathcal{Q} \tag{3.7}$$

$$= \begin{pmatrix} a_{11} & ua_{12} \\ \frac{a_{21}}{u} & a_{22} \end{pmatrix} \tag{3.8}$$

Choosing $u = \sqrt{\frac{a_{21}}{a_{12}}}$ and introducing the complex quantity $\tilde{a} = -i\sqrt{a_{12}a_{21}}$. Thus we obtain the following for the matrix $\mathcal{D}$ which is given by,

$$\mathcal{D} = \begin{pmatrix} a_{11} & i\tilde{a} \\ i\tilde{a} & a_{22} \end{pmatrix}. \tag{3.9}$$

Given the composition of $\mathcal{D}$, we can see that the eigenvalues for the coupled system with $\mathcal{C}$ are the same as the coupled system for $\mathcal{D}$ which is given by,

$$\frac{d\tilde{\mathbf{v}}(t)}{dt} = \mathcal{D}\tilde{\mathbf{v}}(t), \tag{3.10}$$

for $\tilde{\mathbf{v}}(t) = \begin{pmatrix} \tilde{v}_1(t) \\ \tilde{v}_2(t) \end{pmatrix}$ such that $\tilde{v}_1(t) = \frac{v_1(t)}{\sqrt{a_{12}}}$ and $\tilde{v}_2(t) = \frac{v_2(t)}{\sqrt{a_{21}}}$. Thus the eigenvalues at an EP are $\lambda_\pm = \frac{a_{11}+a_{22}}{2}$ which occurs at if

$$\tilde{a}^2 = \frac{(a_{11} - a_{22})^2}{4}. \tag{3.11}$$

We will be able to use these quantities in CMT to gain further understanding of EPs and other complex information which can be derived from a more simplistic model that apply to sophisticated methods in later chapters.

## 3.2 Coupled Resonators with Losses

We will now provide an overview of two linearly-coupled optical resonators similar to [14] with the addition of losses in each cavity. By linearly-coupled, we mean that

the change in the field amplitude of one mode through time is dependent linearly on the other amplitude up to a coupling constant. To write such equations, consider a system of two resonators with modal frequencies $\omega_1$ and $\omega_2$ that have corresponding field amplitudes $a_1(t)$ and $a_2(t)$ respectively. Given the fact there are losses present, we consider the coupling to also be complex-valued. Moreover, we will consider the case where both resonators have losses $\gamma_1$ and $\gamma_2$ for amplitudes $a_1(t)$ and $a_2(t)$ respectively. Considering the losses, the dynamical equations for $a_1(t)$ and $a_2(t)$, become,

$$\dot{a}_1(t) = (i\omega_1 - \gamma_1)a_1(t) + i\kappa_{12}a_2(t), \tag{3.12}$$

$$\dot{a}_2(t) = (i\omega_2 - \gamma_2)a_2(t) + i\kappa_{21}a_1(t), \tag{3.13}$$

where $\kappa_{12}$ and $\kappa_{21}$ are coupling constants which are complex-valued. Note that for weakly-coupled resonators, $|\kappa_{12}| \ll \omega_1$ and $|\kappa_{21}| \ll \omega_2$ [79]. However both $\kappa_{12}$ and $\kappa_{21}$ are limited in what values they can be to preserve the idea of cavities with no gain. Notice that this system corresponds to the one seen in (3.1) where $a_{11} = i\omega_1 - \gamma_1$, $a_{12} = i\kappa_{12}$, $a_{21} = i\kappa_{21}$ and $a_{22} = i\omega_2 - \gamma_2$. As a result we can calculate the value of eigenvalues of this system at an EP and under what condition that must be satisfied. Firstly the eigenvalues $\lambda_{\pm}^{EP}$ of (3.12) and (3.13) at an EP is given by,

$$\lambda_{\pm}^{EP} = -\frac{1}{2}(\gamma_1 + \gamma_2 - i(\omega_1 + \omega_2)). \tag{3.14}$$

To obtain such eigenvalues, we compare with (3.4) to obtain the condition,

$$\kappa_{12} = \frac{(i(\omega_1 - \omega_2) - (\gamma_1 - \gamma_2))^2}{4\kappa_{21}}. \tag{3.15}$$

To provide a better understanding of these equations, we will define two new quantities $\hat{a}_1(t)$ and $\hat{a}_2(t)$ such that,

$$\hat{a}_1(t) = \frac{a_1(t)}{\sqrt{\kappa_{12}}}, \tag{3.16}$$

$$\hat{a}_2(t) = \frac{a_2(t)}{\sqrt{\kappa_{21}}}. \tag{3.17}$$

and thus defining the coupling constant $\kappa = |\kappa|e^{i\theta}$ with real angle $\theta$, where $\kappa =$

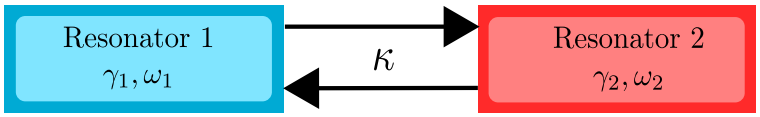



Figure 3.1: Two resonators coupled via the complex term $\kappa$ with decays present in each.

$\sqrt{\kappa_{12}\kappa_{21}}$, (3.12) and (3.13) can be rewritten as,

$$\dot{\hat{a}}_1(t) = (i\omega_1 - \gamma_1)\hat{a}_1(t) + i\kappa\hat{a}_2(t), \tag{3.18}$$

$$\dot{\hat{a}}_2(t) = (i\omega_2 - \gamma_2)\hat{a}_2(t) + i\kappa\hat{a}_1(t). \tag{3.19}$$

where $\omega_1$ and $\omega_2$ are the frequencies of resonator 1 and 2 respectively. Both $\gamma_1$ and $\gamma_2$ are strictly positive indicating that there is no gain in this system. Notice in this section, the coupling constant $\kappa$ is the exact same in (3.18) and (3.19).

CMT is a simple example of a resonating system which can help visualise some of the mysteries of more complex lasers. To achieve this, we examine the parameters presented in the above dynamical equations. Instead of having a dynamical system with six parameters (as the coupling term is complex), we will rewrite the coupled equations to make our analysis easier. We introduce new amplitudes $A_1(\tau)$ and $A_2(\tau)$ which correspond to the first and second mode respectively and are given by,

$$A_1(\tau) = \hat{a}_1\left(\frac{\tau}{\gamma_1}\right)e^{-i\omega_1\frac{\tau}{\gamma_1}} \tag{3.20}$$

$$A_2(\tau) = \hat{a}_2\left(\frac{\tau}{\gamma_1}\right)e^{-i\omega_1\frac{\tau}{\gamma_1}} \tag{3.21}$$

where we introduce $\tau$ as $\tau = \gamma_1 t$. Thus (3.18) and (3.19) become,

$$\frac{dA_1(\tau)}{d\tau} = -A_1(\tau) + i\tilde{\kappa}A_2(\tau), \tag{3.22}$$

$$\frac{dA_2(\tau)}{d\tau} = (-\tilde{\gamma} + i\Delta\tilde{\omega})A_2(\tau) + i\tilde{\kappa}A_1(\tau), \tag{3.23}$$

where $\tilde{\kappa} = \kappa/\gamma_1$, $\tilde{\gamma} = \gamma_2/\gamma_1$ and $\Delta\tilde{\omega} = (\omega_2 - \omega_1)/\gamma_1$ which will be referred to as the coupling, proportional loss and detuning respectively.

To obtain further insight into these equations and because (3.22) and (3.23) are

linear, we can turn them into a matrix equation as follows,

$$\frac{d}{d\tau}\begin{pmatrix} A_1(\tau) \\ A_2(\tau) \end{pmatrix} = \begin{pmatrix} -1 & i\tilde{\kappa} \\ i\tilde{\kappa} & -\tilde{\gamma} + i\Delta\tilde{\omega} \end{pmatrix}\begin{pmatrix} A_1(\tau) \\ A_2(\tau) \end{pmatrix}, \tag{3.24}$$

and define,

$$\mathrm{A} = \begin{pmatrix} -1 & i\tilde{\kappa} \\ i\tilde{\kappa} & -\tilde{\gamma} + i\Delta\tilde{\omega} \end{pmatrix}. \tag{3.25}$$

This system corresponds to the coupled set of equations which are shown in the previous section in (3.10). Comparing this system with (3.22), we see that $a_{11} = -1$, $a_{22} = -\tilde{\gamma} + i\Delta\tilde{\omega}$, $\tilde{a} = \tilde{\kappa}$. Consequently, we can find the eigenvalues of A which are given by,

$$\lambda_{\pm} = \frac{1}{2}\left(i\Delta\tilde{\omega} - (1+\tilde{\gamma}) \pm \sqrt{(1-\tilde{\gamma}+i\Delta\tilde{\omega})^2 - 4\tilde{\kappa}^2}\right). \tag{3.26}$$

Note that $\lambda_{\pm}$ are complex eigenvalues which is composed of losses $\Gamma_{\pm} = \mathrm{Re}(\lambda_{\pm})$ and frequencies $\Omega_{\pm} = \mathrm{Im}(\lambda_{\pm})$. To be more specific, when the two resonators are linearly coupled, there exists the possibility of two separate modes, with different frequencies and losses. To obtain these values, we first need to define,

$$z_{\lambda} = (1-\tilde{\gamma}+i\Delta\tilde{\omega})^2 - 4\tilde{\kappa}^2. \tag{3.27}$$

Then we also note the formulae [80]:

$$\mathrm{Re}(\sqrt{z_{\lambda}}) = \frac{1}{\sqrt{2}}\sqrt{\mathrm{Re}(z_{\lambda}) + \sqrt{\mathrm{Re}(z_{\lambda})^2 + \mathrm{Im}(z_{\lambda})^2}}, \tag{3.28}$$

$$\mathrm{Im}(\sqrt{z_{\lambda}}) = \frac{\mathrm{sgn}(\mathrm{Im}(z_{\lambda}))}{\sqrt{2}}\sqrt{-\mathrm{Re}(z_{\lambda}) + \sqrt{\mathrm{Re}(z_{\lambda})^2 + \mathrm{Im}(z_{\lambda})^2}}, \tag{3.29}$$

such that,

$$\mathrm{sgn}(\mathrm{Im}(z_{\lambda})) = \begin{cases} 1 & \text{if } \mathrm{Im}(z_{\lambda}) \geq 0, \\ -1 & \text{if } \mathrm{Im}(z_{\lambda}) < 0. \end{cases} \tag{3.30}$$

Using the above formulae, the frequencies are given by,

$$\Omega_{\pm} = \frac{\Delta\tilde{\omega}}{2} \pm \frac{\mathrm{sgn}(\mathrm{Im}(z_\lambda))}{2\sqrt{2}}\Big\{ - \left((1-\tilde{\gamma})^2 - \Delta\tilde{\omega}^2 - 4\mathrm{Re}\left(\tilde{\kappa}^2\right)\right) + \Big[ \left((1-\tilde{\gamma})^2 - \Delta\tilde{\omega}^2 - 4\mathrm{Re}\left(\tilde{\kappa}^2\right)\right)^2 + \left(2\Delta\tilde{\omega}(1-\tilde{\gamma}) - 4\mathrm{Im}\left(\tilde{\kappa}^2\right)\right)^2 \Big]^{\frac{1}{2}} \Big\}^{\frac{1}{2}}, \tag{3.31}$$

and the losses for each corresponding frequency being,

$$\Gamma_{\pm} = -\frac{1+\tilde{\gamma}}{2} \pm \frac{1}{2\sqrt{2}}\Big\{ (1-\tilde{\gamma})^2 - \Delta\tilde{\omega}^2 - 4\mathrm{Re}\left(\tilde{\kappa}^2\right) + \Big[ \left((1-\tilde{\gamma})^2 - \Delta\tilde{\omega}^2 - 4\mathrm{Re}\left(\tilde{\kappa}^2\right)\right)^2 + \left(2\Delta\tilde{\omega}(1-\tilde{\gamma}) - 4\mathrm{Im}\left(\tilde{\kappa}^2\right)\right)^2 \Big]^{\frac{1}{2}} \Big\}^{\frac{1}{2}}. \tag{3.32}$$

## 3.3 Frequencies, Losses and Exceptional Points

Now that we have found the eigenvalues and the corresponding frequencies and losses, we can study these in detail. First we will look into when the frequencies and losses of both eigenvalues are equal to each other. As we have discussed before, when two eigenvalues like $\lambda_{\pm}$ coalesce, we have an EP. To do this analysis, we will use the definition of coupling mentioned previously, $\tilde{\kappa} = |\kappa|e^{i\theta}$.

### 3.3.1 Analysis of Frequencies corresponding to Eigenvalues

However, we will first consider under what circumstances do the frequencies equal $\Omega_+ = \Omega_-$ and also the losses $\Gamma_+ = \Gamma_-$. Now we turn our attention to both frequencies $\Omega_+$ and $\Omega_-$ by taking into account (3.31). For $\Omega_+ = \Omega_-$, this means that $\mathrm{Im}(z_\lambda) = 0$ and we also have $\mathrm{Re}(z_\lambda) \geq 0$. In terms of the coupling, losses and detuning, $\mathrm{Im}(z_\lambda) = 0$ results in the following relation,

$$\mathrm{Im}\left(\tilde{\kappa}^2\right) = \frac{\Delta\tilde{\omega}(1-\tilde{\gamma})}{2}. \tag{3.33}$$

However the frequencies of the eigenvalues are only equal if the second condition $\mathrm{Re}(z_\lambda) \geq 0$ holds which is,

$$\frac{(1-\tilde{\gamma})^2 - \Delta\tilde{\omega}^2}{4} \geq \mathrm{Re}\left(\tilde{\kappa}^2\right). \tag{3.34}$$

Furthermore $\Omega_\pm$ can be analytically found given these two conditions which is,

$$\Omega_\pm = \frac{\Delta\tilde{\omega}}{2}. \tag{3.35}$$

These formulas are useful for finding when the frequency terms $\Omega_+$ and $\Omega_-$ are equivalent. Consider Figure 3.2 which shows the variation of both eigenvalue frequencies while varying the detuning. In Figure 3.2(a) we see that at very negative $\Delta\tilde{\omega}$, one of the frequency modes is at zero while the other comes from negative infinity. With increasing $\Delta\tilde{\omega}$, both eigenvalues frequencies then coalesce then one goes to infinity while the other goes back to zero. In Figure 3.2(b), instead of $\Omega_\pm$ crossing, we see them get closer together and deviate before meeting. Like before, at very negative $\Delta\tilde{\omega}$, one frequency comes from zero while the other comes from minus infinity. With increasing $\Delta\tilde{\omega}$, we see both frequency terms getting closer but then before meeting, one goes to infinity while the other goes to zero. The final case is shown in Figure 3.2(c), where instead of both frequency modes not meeting, they coalesce in the range $-1 \leq \Delta\tilde{\omega} \leq 1$.

### 3.3.2 Analysis of Losses corresponding to Eigenvalues

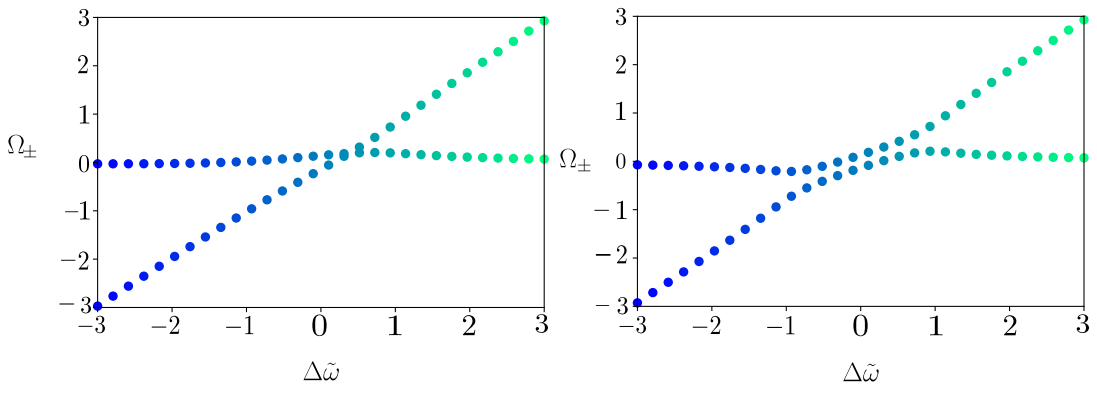
Let us now turn our attention to the real part of the eigenvalues $\lambda_\pm$ which correspond to loss terms $\Gamma_\pm$. We would like to determine when these loss terms are equivalent and how they change with varying $\Delta\tilde{\omega}$. In the case of the losses for each of the corresponding eigenvalues, $\Gamma_+ = \Gamma_-$, we consider (3.32). As with the frequencies equalling, (3.33) is also valid in this case however the condition involving $\mathrm{Re}(z_\lambda)$ becomes $\mathrm{Re}(z_\lambda) \leq 0$. Thus,

$$\frac{(1-\tilde{\gamma})^2 - \Delta\tilde{\omega}^2}{4} \leq \mathrm{Re}\left(\tilde{\kappa}^2\right). \tag{3.36}$$

These equivalent losses are seen for a range of detuning parameter values in Figure 3.3(c) for $|\Delta\tilde{\omega}| \geq 1$. When $\Gamma_\pm$ meet, this occurs at,

$$\Gamma_\pm = -\frac{1+\tilde{\gamma}}{2}. \tag{3.37}$$

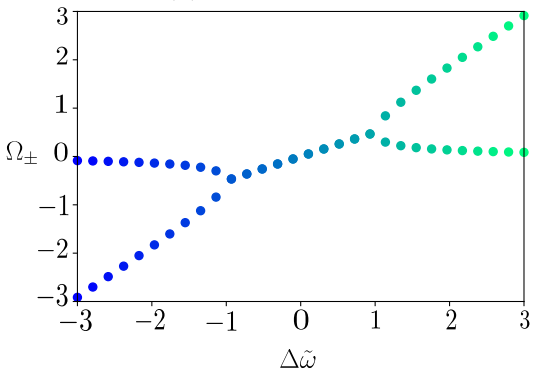
Let us consider Figure 3.3 which shows three examples of both $\Gamma_\pm$ varying over $\Delta\omega$. We see that in Figure 3.3(a) that both $\Gamma_\pm$ are symmetric to each other, and while they get closer with increasing $\Delta\tilde{\omega}$, they never meet. Comparing this with Figure 3.2(a), when $\Omega_\pm$ cross, $\Gamma_\pm$ do not. Thus the eigenvalues are not the same for these




(a) $\theta = 2$, $\tilde{\gamma} = 2$




(b) $\theta = 1.3$, $\tilde{\gamma} = 1$




(c) $\theta = \pi/2$, $\tilde{\gamma} = 1$

Figure 3.2: Frequency terms from eigenvalues $\lambda_\pm$ over the detuning $\Delta\tilde{\omega}$ where for all cases $|\tilde{\kappa}| = .5$.

parameters. In Figure 3.3(b), we see that both $\Gamma_\pm$ start off close together then diverge and get closer again for high $\Delta\tilde{\omega}$. In Figure 3.3(c), we see both $\Gamma_\pm$ coalesce at $\Gamma_\pm = -1$ and then diverge after $\Delta\tilde{\omega} = -1$. Then both $\Gamma_\pm$ meet again at $\Delta\tilde{\omega} = 1$. Comparing this to Figure 3.2(c), we see that $\Gamma_\pm$ meet and also $\Omega_\pm$ at $\Delta\tilde{\omega} = \pm 1$. This will become important in the next subsection with the introduction of EPs.

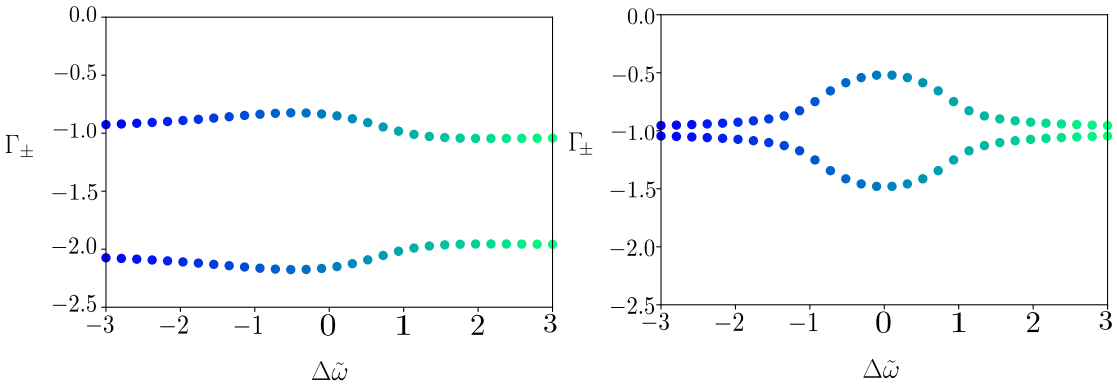
### 3.3.3 Analysis of Eigenvalue Branches and EPs

With our new basis, we can also write a condition for EPs to occur with CMT. If we consider (3.26) once again, we can see that an EP occurs when the terms underneath the square root sum up to zero. Hence the eigenvalues become,

$$\lambda_\pm^{EP} = \frac{i\Delta\tilde{\omega} - (1 + \tilde{\gamma})}{2} \tag{3.38}$$

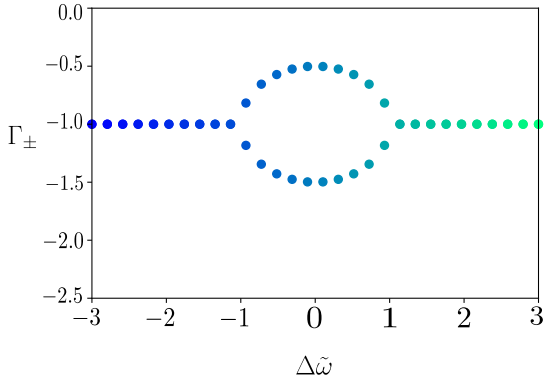
with the EP occurring if,

$$\tilde{\kappa}^2 = \frac{(1 - \tilde{\gamma} + i\Delta\tilde{\omega})^2}{4}, \tag{3.39}$$



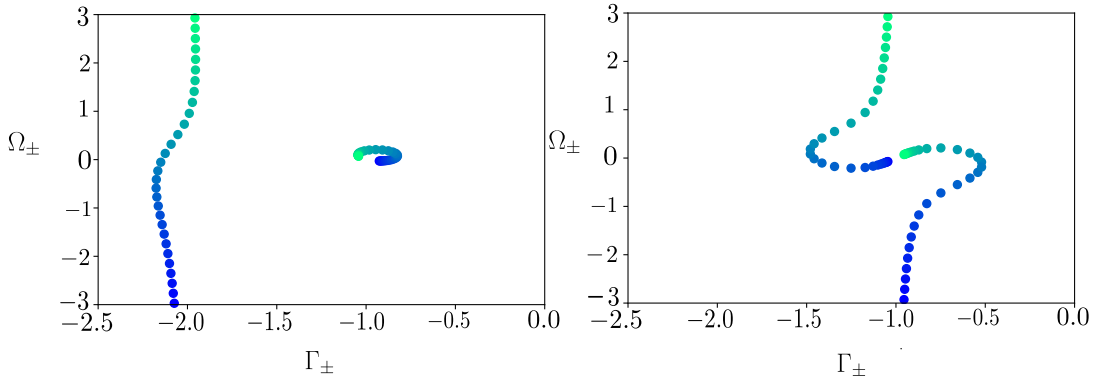

(a) $\theta = 2$, $\tilde{\gamma} = 2$

(b) $\theta = 1.3$, $\tilde{\gamma} = 1$



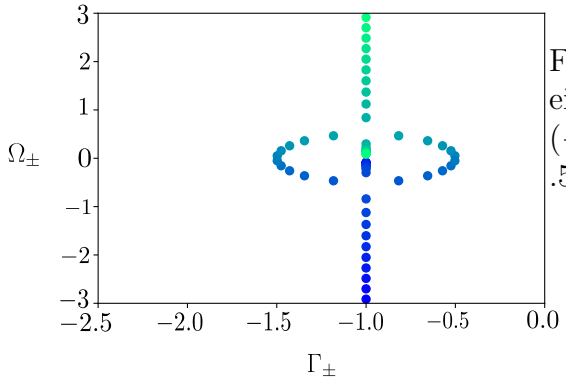

(c) $\theta = \pi/2$, $\tilde{\gamma} = 1$

Figure 3.3: Loss terms from eigenvalues $\lambda_\pm$ over the detuning $\Delta\tilde{\omega}$ where for all cases $|\tilde{\kappa}| = .5$.




(a) $\theta = 2$, $\tilde{\gamma} = 2$

(b) $\theta = 1.3$, $\tilde{\gamma} = 1$




(c) $\theta = \pi/2$, $\tilde{\gamma} = 1$

Figure 3.4: Real and imaginary parts of eigenvalues $\lambda_\pm$ over the detuning range $(-3, 3)$ for $\Delta\tilde{\omega}$ where for all cases $|\tilde{\kappa}| = .5$.

which are two equations as $\tilde{\kappa}$ is complex. This relates to the EP condition as seen in (3.11).

We will now consider three different scenarios for the eigenvalues $\lambda_\pm$ and how they change with the variation of parameters. While we vary the detuning term, $\Delta\tilde{\omega}$, the two eigenvalues create branches that have the potential to cross. If these branches cross at the same value of $\Delta\tilde{\omega}$, this is an EP. There are three different types eigenvalue movements we will be discussing and these are shown in Figure 3.4.

In Figure 3.4(a), we see that the branches do not cross and one branch does a slight orbit around zero while the other varies a little in the loss term while increasing in the frequency term. Note that in Figure 3.2(a), we see that the frequency terms $\Omega_\pm$ cross but this is not the case for $\lambda_\pm$ and thus these branches do not meet. In Figure 3.4(b), we see one eigenvalue branch increasing in frequency towards zero while the second branch starts at zero for the frequency and increases by increasing $\Delta\tilde{\omega}$. However, these branches never meet, even in frequency $\Omega_\pm$ or losses $\Gamma_\pm$ shown in Figures 3.2(b) and 3.3(b) respectively. Finally in Figure 3.4(c), the two branches meet twice when $\Delta\tilde{\omega} = \pm 1$. Where $\Delta\tilde{\omega} = -1$, using (3.35) and (3.37) we see that $\Omega_\pm = -0.5$ and $\Gamma_\pm = -1$. For $\Delta\tilde{\omega} = 1$, $\Omega_\pm = 0.5$ and $\Gamma_\pm = -1$. This is seen when one branch moves towards $-0.5$ and then the other branch moves from zero to meet it. Then both branches symmetrically increase in frequency until they meet at 0.5. Then one continues in frequency while the other moves towards zero.

## 3.4 Restrictions of non-gain coupled resonators using Coupled Mode Theory

In this section, we will look into the limitations CMT has to describe non-gain coupled cavities [17]. We will discuss how the change in parameters will effect what the permissible values coupling between both cavities are. We will also show what happens dynamically to both mode amplitudes in an allowed coupled regions and forbidden ones.

### 3.4.1 Losses Restriction

The restriction involves the values obtained from $\lambda_\pm$. In particular, the real part, $\Gamma_\pm$ must have the condition that $\Gamma_\pm \leq 0$ for all our choice of parameters. The fact that $\Gamma_\pm \leq 0$ is the result of the physical limitations we have imposed onto the system. From the beginning of the chapter, we have stated that there is no gain in each of

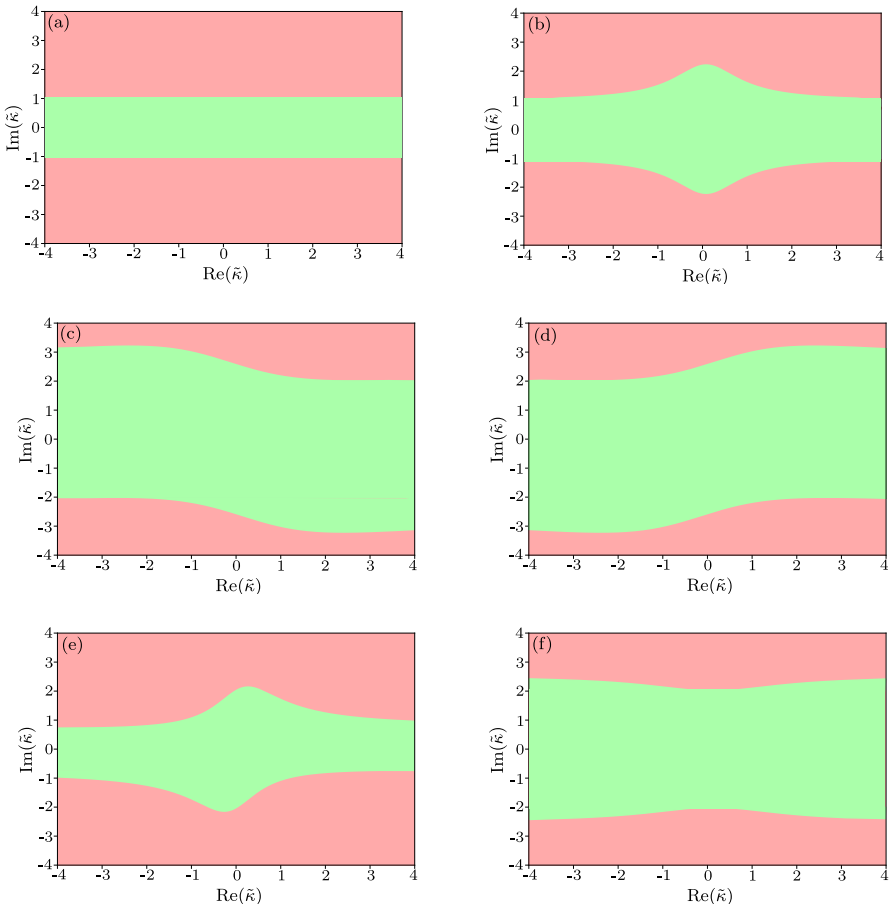



Figure 3.5: Illustration of allowed values (green) of coupling $\tilde{\kappa}$ where both $\Gamma_{\pm} \leq 0$. (a):$\tilde{\gamma} = 1, \Delta\tilde{\omega} = 0$, (b):$\tilde{\gamma} = 1, \Delta\tilde{\omega} = 4$, (c):$\tilde{\gamma} = 4, \Delta\tilde{\omega} = 4$, (d):$\tilde{\gamma} = 4, \Delta\tilde{\omega} = -4$, (e):$\tilde{\gamma} = \frac{1}{2}, \Delta\tilde{\omega} = 4$ and (f):$\tilde{\gamma} = 4, \Delta\tilde{\omega} = 0$.

the cavities. With this specification, $\Gamma_{\pm} \leq 0$ or else the coupled modes would grow in time due to active media. To see this condition, let us consider the case where the linearly coupled resonators have no overall loss i.e. $\Gamma_{\pm} = 0$. Using this with (3.26) and doing some algebra, we obtain the following condition,

$$\begin{aligned} |\tilde{\kappa}| = \pm\Bigg( \frac{1}{2\sin^2(2\theta)} \Big[ & \Delta\tilde{\omega}(1-\tilde{\gamma})\sin(2\theta) + \cos(2\theta)(1+\tilde{\gamma})^2 \\ & \pm \Big\{ (\Delta\tilde{\omega}(1-\tilde{\gamma})\sin(2\theta) + (1+\tilde{\gamma})^2\cos(2\theta))^2 \\ & + 4\tilde{\gamma}\sin^2(2\theta)((1+\tilde{\gamma})^2 + \Delta\tilde{\omega}^2) \Big\}^{\frac{1}{2}} \Big] \Bigg)^{\frac{1}{2}}. \end{aligned} \tag{3.40}$$

Given the fact $|\tilde{\kappa}|$ is real and positive, we can write the coupling magnitude as the following,

$$\begin{aligned} |\tilde{\kappa}| = \Bigg( \frac{1}{2\sin^2(2\theta)} \Big[ & \Delta\tilde{\omega}(1-\tilde{\gamma})\sin(2\theta) + \cos(2\theta)(1+\tilde{\gamma})^2 \\ & + \Big\{ (\Delta\tilde{\omega}(1-\tilde{\gamma})\sin(2\theta) + (1+\tilde{\gamma})^2\cos(2\theta))^2 \\ & + 4\tilde{\gamma}\sin^2(2\theta)((1+\tilde{\gamma})^2 + \Delta\tilde{\omega}^2) \Big\}^{\frac{1}{2}} \Big] \Bigg)^{\frac{1}{2}}. \end{aligned} \tag{3.41}$$

So any value of $|\tilde{\kappa}|$ less than (3.41) is valid under the restriction we have put in place given the values of parameters $\Delta\tilde{\omega}$, $\theta$ and $\tilde{\gamma}$. Figure 3.5 shows the allowed values for coupling and forbidden for given parameters $\tilde{\gamma}$ and $\Delta\tilde{\omega}$. The most simple solution is when the losses of each resonator are the same i.e. $\tilde{\gamma} = 1$ and zero detuning between them which is shown in Figure 3.5(a). In Figure 3.5(b), we allow for a positive detuning which increases the region of permissible values of $\tilde{\kappa}$ as shown. In Figures 3.5(c) and 3.5(d), we increase the proportional loss, $\tilde{\gamma}$, we see how the region changes where we still have more possible values of $\tilde{\kappa}$ than $\tilde{\gamma}$. Moreover, we see that 3.5(d) with $\Delta\tilde{\omega} = 4$ is antisymmetric to 3.5(c) with $\Delta\tilde{\omega} = -4$. The allowed regions shift slightly in Figure 3.5(e) in comparison to 3.5(b) where we have decreased the proportional loss. Finally with an increase in proportional loss, in Figure 3.5(f), we see even more allowed regions than in Figure 3.5(a). We will now explore some of these dynamical scenarios in detail to see how the mode amplitudes change over time.

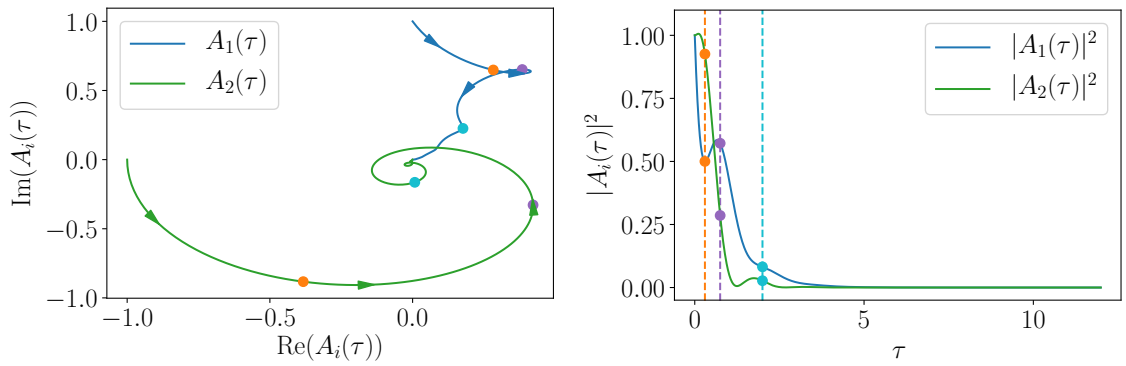



Figure 3.6: Dynamical picture where both $\Gamma_\pm < 0$ such that $\mathrm{Re}(\tilde{\kappa}) = 1$, $\mathrm{Im}(\tilde{\kappa}) = .7$, $\Delta\tilde{\omega} = 4$ and $\tilde{\gamma} = 1$.

### 3.4.2 Dynamical scenarios of coupled non-gain cavities

So far we have derived a condition that must be upheld so that our model can describe the scenario of two linearly-coupled cavities which have no gain. It was that the real part of the eigenvalue solutions, $\mathrm{Re}(\lambda_\pm)$ are always negative. This is valid no matter the initial conditions of the amplitudes $A_1(\tau)$ and $A_2(\tau)$. We can see by investigating the dynamics of $A_1(\tau)$ and $A_2(\tau)$ to see when the condition is broken. First we will find the fixed points of this coupled system which is given by,

$$A_1^{FP} = 0, \tag{3.42}$$

$$A_2^{FP} = 0, \tag{3.43}$$

where $A_1^{FP}$ and $A_2^{FP}$ correspond to the fixed point(FP) solution for the dynamical equations of $A_1(\tau)$ and $A_2(\tau)$ respectively. The fixed point is a stable spiral if both $\Gamma_\pm < 0$ and an unstable spiral where one of $\Gamma_\pm > 0$. For one of $\Gamma_\pm = 0$, the fixed point is a stable centre. As discussed in the previous section, we have explained how both $\Gamma_\pm \leq 0$ so that there is no gain in our dynamical equations. Thus we require the fixed point to be stable. Figures 3.6 and 3.7 show the stable fix points where both $\Gamma_\pm < 0$. They show the amplitudes and intensities that go to zero in both cases. In particular, as stated in the previous subsection, additional regions of coupling validity appear with a non-zero detuning as a result Figure 3.7 is a stable solution for coupling but would not be if $\Delta\tilde{\omega} = 0$. In contrast, Figure 3.8 shows the amplitudes and their intensities increasing where one of $\Gamma_\pm > 0$ and as a result is not a valid choice of coupling. All these figures are chosen in reference to Figure 3.5(b).

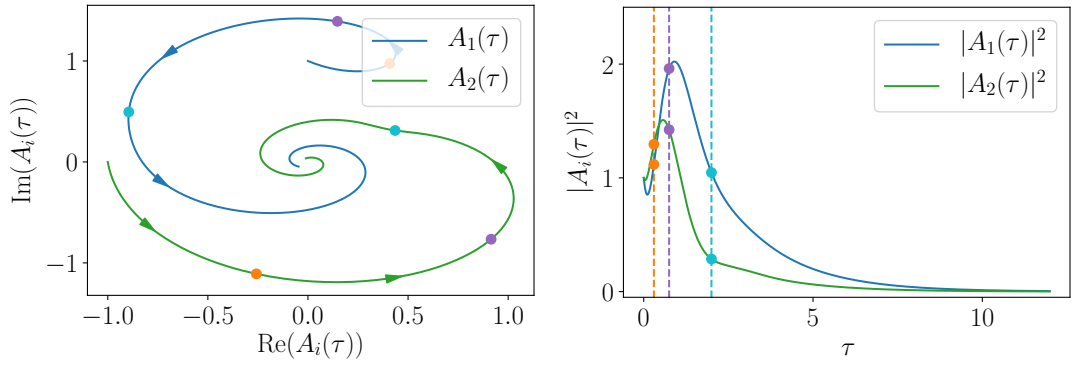



Figure 3.7: Dynamical picture where both $\Gamma_\pm < 0$ such that $\mathrm{Re}(\tilde{\kappa}) = .5$, $\mathrm{Im}(\tilde{\kappa}) = 1.8$, $\Delta\tilde{\omega} = 4$ and $\tilde{\gamma} = 1$.

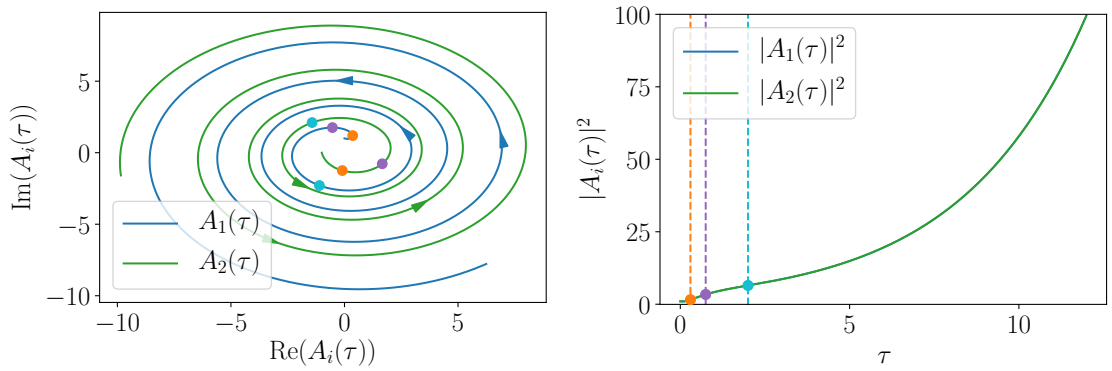



Figure 3.8: Dynamical picture where one of $\Gamma_\pm > 0$ such that $\mathrm{Re}(\tilde{\kappa}) = 0$, $\mathrm{Im}(\tilde{\kappa}) = 2.3$, $\Delta\tilde{\omega} = 4$ and $\tilde{\gamma} = 1$.

## 3.5 Conclusions

In this chapter, we have discussed the idea of a non-gain linearly coupled resonators with loss. We have analysed the dynamical equations that are associated with this system to determine the existence of EPs. We obtained an analytical formula in terms of the losses, detuning and coupling that shows when an EP occurs. In later chapters, we show the existence of these EPs in an open boundaries strongly coupled cavity laser. Moreover, we investigated the parameters of the system to determine the conditions necessary for the dynamical equations to make physical sense. This was carried out by obtaining an analytical expression for coupling in terms of the remaining parameters which allows the model to be used in a non-gain situation.

# Chapter 4

# $q$-Basis and Exceptional Points using the Steady-state *ab-initio* Laser Theory

In this chapter, we introduce a new basis, which is titled the $q$-basis, that represents a complex electromagnetic field in terms of real quantities. With this basis, we express the electric and magnetic field at a given point in terms of three real quantities. This can be used to investigate optical lasing modes in coupled cavities that have open boundaries. The $q$-basis is written in a similar way as the Stokes parameters [24] which have been widely used in representing the polarisation states of the electromagnetic field. The same formalisation is also used in quantum mechanics with the Bloch sphere where these parameters are used to represent the elements of the density matrix and also in mutually-delayed coupled laser systems [60, 81–83]. In all those cases, the absolute phase has no physical significance and the $q$-basis provides a way to express the electromagnetic field with less variables which produces the same results. This is given the fact that the complex amplitudes of the electric and magnetic fields make up four variables and the $q$-basis is made up of three. Thus the $q$-basis removes the unnecessary information in the description of strongly coupled cavities with open boundaries. Moreover, the $q$-basis also provides physical intuition where we introduce terms which represent the total energy and Poynting's vector.

In particular, we would like to use the $q$-basis to show the emergence of EPs in lasers. It has been shown in [20] that with the unequal pumping of two coupled cavities, close to where an EP is located, a laser can go below threshold with increasing pump, which is counter-intuitive. We would first like to replicate the work carried out in [20] using the $q$-basis. Moreover we would like to go beyond showing this effect

and provide a physical understanding of these EPs using the $q$-basis. As a result, we provide further analysis on these EPs to show under what conditions they exist and provide further understanding of what happens close to threshold.

In [20], EPs were first shown by using SALT(Steady-state *ab-initio* Laser Theory). In SALT, we consider the steady-state solution for the electromagnetic field along with a stationary population inversion [19]. While SALT is only valid in a steady-state regime, it is particularly useful to represent a complex laser structure, such as strongly-coupled cavities with open boundary conditions which we will explore in this chapter. SALT uses the quantum mechanical description of the active medium in Chapter 2 with this steady-state approach. Vast amounts of research has been carried out using SALT for coupled cavities which provide a detailed analysis on these laser structures in the steady-state regime [84–91].

With all of this in mind, the chapter is structured as follows. In the first section, we introduce the $q$-basis and provide a detailed derivation of steady-state differential equations that describes the spatial distribution of a complex laser design structure with gain. In the second section, we give a brief overview of SALT and show the conditions required to obtain EPs. We then use the $q$-basis, along with conditions provided in [20], to give further analysis of EPs. In this analysis, we provide an overview of how laser modes change with increasing pump, how the intensity and power flow change and what parameters are important for an EP to exist such as absorption and unequal pumping. From there, we discuss different laser structures and whether EPs exist in these scenarios and then look at the physical parameters of the modes in detail such as the atomic transition frequency, $\omega_0$ and polarisation relaxation rate, $\gamma_P$. In the final section, we provide a brief conclusion in our analysis with a discussion of how both pumps can be related by a single factor and how similar behaviour can be observed with our model as seen with CMT in the previous chapter.

## 4.1 $q$-Basis and the Electromagnetic Field

In this section, we will now introduce the $q$-basis for the steady-state electromagnetic field which will be used throughout this chapter and will become useful later when introducing the dynamical equations.

### 4.1.1 Steady-State Maxwell's Equations

We make the same proposal for the electromagnetic field as we have done in SLT, that the real amplitude of the electric field and magnetic induction are one-dimensional and vary in the $z$ direction. Let $E(z,t)$ and $B(z,t)$ be the electric field and magnetic induction respectively, and using the equations given in Chapter 2, (2.57) and (2.58),

$$\frac{\partial E(z,t)}{\partial z} = -\frac{\partial B(z,t)}{\partial t} \tag{4.1}$$

$$\frac{\partial B(z,t)}{\partial z} = -\mu_0 \frac{\partial D(z,t)}{\partial t}. \tag{4.2}$$

where we have used the relation between the magnetic induction and magnetic field $B(z,t) = \mu_0 H(z,t)$ and let the current density be zero $J(z,t) = 0$. Recall from Chapter 2, we discussed the composition of the electric displacement term $D(z,t)$ which is comprised of the electric field, background polarisation $P_b(z,t)$ and gain polarisation $P_g(z,t)$. With all this, we obtain (2.59), $D(z,t) = \epsilon_0 E(z,t) + P_b(z,t) + P_g(z,t)$.

In the steady-state regime, the electric field and magnetic induction have spatial amplitudes $E(z)$ and $B(z)$ respectively and the only time dependence is of the form $e^{-i\omega t}$. We will seek solutions to (4.1) and (4.2) for a single frequency $\omega$. Thus the decomposition, in terms of $\omega$, of $E(z,t)$ and $B(z,t)$ are given by,

$$E(z,t) = \frac{1}{2}\left(E(z)e^{-i\omega t} + E(z)^* e^{i\omega t}\right), \tag{4.3}$$

$$B(z,t) = \frac{1}{2}\left(B(z)e^{-i\omega t} + B(z)^* e^{i\omega t}\right), \tag{4.4}$$

where the electric field decomposition is the steady-state solution of (2.65). By steady-state, we mean that the only time dependence is in the form $e^{-i\omega t}$ with time independent variables $E(z)$ and $B(z)$. We further write the gain polarisation, $P_g(z,t)$ and $P_b(z,t)$ in a similar fashion and are as follows,

$$P_g(z,t) = \frac{1}{2}\left(P_g(z)e^{-i\omega t} + P_g(z)^* e^{i\omega t}\right), \tag{4.5}$$

$$P_b(z,t) = \frac{1}{2}\left(P_b(z)e^{-i\omega t} + P_b(z)^* e^{i\omega t}\right). \tag{4.6}$$

In this chapter, we introduce a complex background susceptibility where the imaginary term, $\tilde{\chi}_b(z)$ corresponds to the absorption of the medium. Thus the background

polarisation is given by,

$$P_b(z) = \epsilon_0 \tilde{\chi}_b(z) E(z). \tag{4.7}$$

From here, we can write the complex-valued refractive index, $\tilde{n}_b(z)$ in terms of $\tilde{\chi}_b(z)$, $\tilde{n}_b(z)^2 = 1 + \tilde{\chi}_b(z)$. Moreover, it can also be written in terms of the real refractive index $n_b(z)$ and the extinction coefficient $\kappa_a(z)$ such that,

$$\tilde{n}_b(z) = n_b(z)(1 + i\kappa_a(z)). \tag{4.8}$$

In most literature [92], one would typically write the extinction coefficient as $n_b(z)\kappa_a(z)$ but for our derivations throughout this thesis, we will call and denote the extinction coefficient as $\kappa_a(z)$.

For the gain polarisation, we assume that it can be adiabatically eliminated as in Chapter 2. As a result we can introduce the complex gain susceptibility $\chi_g(z)$ which is constant in time and thus we can write the gain polarisation for a single mode as,

$$P_g(z) = \epsilon_0 \chi_g(z) E(z). \tag{4.9}$$

In physical terms, the real component of the gain susceptibility contributes to the change in the refractive index. The imaginary component of $\chi_g(z)$ relates the gain of the laser which contributes to the light amplification. With all this in mind,

$$D(z,t) = \frac{1}{2}\left(\tilde{n}_b(z)^2 + \chi_g(z)\right)\epsilon_0 E(z) e^{-i\omega t} + \text{c.c} \tag{4.10}$$

Taking all of this into account, we can write (4.1) and (4.2) as,

$$\frac{dE(z)}{dz}e^{-i\omega t} + \frac{dE(z)^*}{dz}e^{i\omega t} = i\omega\left(B(z)e^{-i\omega t} - B(z)e^{i\omega t}\right), \tag{4.11}$$

$$\begin{aligned}\frac{dB(z)}{dz}e^{-i\omega t} + \frac{dB(z)^*}{dz}e^{i\omega t} =& \frac{i\omega}{c^2}\Big(\left(\tilde{n}_b(z)^2 + \chi_g(z)\right)E(z)e^{-i\omega t} \\ &- \left(\left(\tilde{n}_b(z)^*\right)^2 \chi_g(z)^*\right)E(z)^* e^{i\omega t}\Big).\end{aligned} \tag{4.12}$$

Differential equations are obtained in terms of $E(z)$ and $B(z)$ by multiplying by $e^{i\omega t}$ and integrating over one period (which is analogous to the rotating wave approximation [11, 12]), then the complex conjugate terms go to zero. The resulting equation

is,

$$\frac{dE(z)}{dz} = i\omega B(z), \tag{4.13}$$

$$\frac{dB(z)}{dz} = \frac{i\omega}{c^2}\left(\tilde{n}_b(z)^2 + \chi_g(z)\right)E(z). \tag{4.14}$$

### 4.1.2 Power Flow and Poynting's Theorem

Before we introduce the $q$-basis, we will give the physical reasoning behind it which arrives from deriving an equation for Poynting's vector, in a similar way to [22] for a steady-state solution using the complex representation for the electromagnetic field. We now introduce the Poynting vector as $\mathcal{S}(z,t)$ whose amplitude is in the perpendicular direction to the electromagnetic field. $\mathcal{S}(z,t)$ is given by,

$$\mathcal{S}(z,t) = \frac{1}{\mu_0}E(z,t)B(z,t). \tag{4.15}$$

Using the composition of the electric field and magnetic induction, we then can carry out the following,

$$\mathcal{S}(z,t) = \frac{1}{4\mu_0}\left(E(z)B(z)^* + E(z)^*B(z) + E(z)B(z)e^{2i\omega t} + E(z)^*B(z)^*e^{-2i\omega t}\right) \tag{4.16}$$

The next step is to time-average Poynting's vector by integrating over one period, $\frac{2\pi}{\omega}$. Denoting this time-averaged quantity by $\langle\mathcal{S}(z)\rangle$, we obtain,

$$\langle\mathcal{S}(z)\rangle = \frac{\omega}{2\pi}\int_0^{\frac{2\pi}{\omega}}\mathcal{S}(z,t)dt = \frac{1}{4\mu_0}\left(E(z)B(z)^* + E(z)^*B(z)\right). \tag{4.17}$$

As a result, we now can define a complex Poynting vector, $S(z)$ which is written as [22],

$$S(z) = \frac{1}{2\mu_0}E(z)B(z)^* \tag{4.18}$$

where $\langle\mathcal{S}(z)\rangle = \mathrm{Re}(S(z))$. We can calculate the derivative of $S(z)$ which will give the energy balance equation,

$$\begin{aligned}\frac{dS(z)}{dz} &= \frac{1}{2\mu_0}\left(\frac{dE(z)}{dz}B(z)^* + E(z)\frac{dB(z)^*}{dz}\right)\\ &= \frac{1}{2\mu_0}\left(i\omega|B(z)|^2 - \frac{i\omega}{c^2}\left(n_b(z)^2(1-i\kappa_a(z))^2 + \chi_g(z)^*\right)|E(z)|^2\right).\end{aligned} \tag{4.19}$$

Using this idea of power flow will be important throughout this thesis, particularly when introducing dynamics using open boundaries with strongly coupled cavities. Moreover, the $q$-basis had been designed in the spirit of this energy balance equation.

### 4.1.3 $q$-basis

We will now assume we are dealing with a single section in some laser structure with constant refractive index $n_b$ and extinction coefficient $\kappa_a$. With this, we introduce real terms $q_A(z)$, $q_S(z)$, $q_R(z)$ and $q_I(z)$ which form the $q$-basis and is given by,

$$q_A(z) = |E(z)|^2 + \frac{c^2}{n_b^2}|B(z)|^2, \tag{4.20}$$

$$q_S(z) = |E(z)|^2 - \frac{c^2}{n_b^2}|B(z)|^2, \tag{4.21}$$

$$q_R(z) = \frac{c}{n_b}\left(E(z)B(z)^* + E(z)^*B(z)\right), \tag{4.22}$$

$$iq_I(z) = \frac{c}{n_b}\left(E(z)B(z)^* - E(z)^*B(z)\right). \tag{4.23}$$

Although there are four real quantities above, $q_A(z)$ can actually be represented in terms of the other quantities which is given by,

$$q_A(z) = \sqrt{q_S(z)^2 + q_R(z)^2 + q_I(z)^2}. \tag{4.24}$$

In physical terms, $q_A(z)$ can be thought of, up to a constant, as the energy density of the sum of the electromagnetic field intensities, $|E(z)|^2$ and $|B(z)|^2$ for a non-active medium. In contrast, $q_S(z)$ is linked to the difference between the electric field and magnetic induction energy densities. Moreover, $q_R(z)$ is related to the real part of the time-averaged complex Poynting vector, given by (4.18) while $q_I(z)$ is compared to the imaginary term of $S(z)$. We can reverse the $q$-basis to obtain the electromagnetic field amplitudes $|E(z)|^2$ and $|B(z)|^2$, and also the Poynting vector amplitude $S(z)$. They are as follows,

$$|E(z)|^2 = \frac{1}{2}(q_A(z) + q_S(z)), \tag{4.25}$$

$$|B(z)|^2 = \frac{n_b^2}{2c^2}(q_A(z) - q_S(z)), \tag{4.26}$$

$$S(z) = \frac{n_b}{4c\mu_0}(q_R(z) + iq_I(z)). \tag{4.27}$$

We can obtain spatial derivative equations for each of the terms in the $q$-basis

using Maxwell's equations by (4.13) and (4.14) for constant complex refractive index. In fact, taking the real and imaginary components of (4.19) will obtain differential equations for $q_R(z)$ and $q_I(z)$ respectively, up to a constant. The equation for $q_R(z)$ is given by,

$$\begin{aligned}\frac{dq_R(z)}{dz} =& \frac{c}{n_b}\left(\frac{dE(z)B(z)^*}{dz} + \frac{dE(z)^*B(z)}{dz}\right),\\ =& -\frac{\omega}{cn_b}(2n_b^2\kappa_a + \mathrm{Im}(\chi_g(z)))(q_A(z) + q_S(z)),\end{aligned} \tag{4.28}$$

and for $q_I(z)$,

$$\begin{aligned}\frac{dq_I(z)}{dz} =& -i\frac{c}{n_b}\left(\frac{dE(z)B(z)^*}{dz} - \frac{dE(z)^*B(z)}{dz}\right),\\ =& -\frac{2\omega n_b}{c}q_S(z) + \frac{\omega}{n_b c}(n_b^2\kappa_a^2 - \mathrm{Re}(\chi_g(z)))(q_A(z) + q_S(z)),\end{aligned} \tag{4.29}$$

where we used (4.25). Using (4.13) and (4.14), the differential equation for $q_S(z)$ is given by,

$$\begin{aligned}\frac{dq_S(z)}{dz} =& \frac{d|E(z)|^2}{dz} - \frac{c^2}{n_b^2}\frac{d|B(z)|^2}{dz},\\ =& \frac{2\omega n_b}{c}q_I(z) - \frac{\omega}{n_b c}(n_b^2\kappa_a^2 - \mathrm{Re}(\chi_g(z)))q_I(z)\\ &+ \frac{\omega}{cn_b}\left(2n_b^2\kappa_a + \mathrm{Im}(\chi_g(z))\right)q_R(z),\end{aligned} \tag{4.30}$$

and the equation for $q_A(z)$ is written as,

$$\begin{aligned}\frac{dq_A(z)}{dz} =& \frac{d|E(z)|^2}{dz} + \frac{c^2}{n_b^2}\frac{d|B(z)|^2}{dz},\\ =& \frac{\omega}{n_b c}(n_b^2\kappa_a^2 - \mathrm{Re}(\chi_g(z)))q_I(z) - \frac{\omega}{n_b c}(2n_b^2\kappa_a + \mathrm{Im}(\chi_g(z))q_R(z).\end{aligned} \tag{4.31}$$

Now we have obtained the above four differential equations which describe the electromagnetic field for an active medium without the need of using the phases of both field amplitudes $E(z)$ and $B(z)$ but just knowing their difference. In the next section, we will introduce SALT which has been used to model coupled-cavity lasers with open boundaries in the steady-state scenario. With what we will introduce, we can show the same can be obtained with less variables using the $q$-basis. Given the relation between $q_A(z)$ and the other variables, we essentially have three differential equations and even (4.31) can be represented in terms of the other equations and variables.

However, for the methods involved later in this chapter using the $q$-basis, it is in fact easier using (4.31) to generate a transfer matrix with linear equations. It is worthy to note that the same results are attainable using (4.24).

## 4.2 Steady-State *ab-initio* Laser Theory

We now introduce an overview of SALT which is the steady-state situation for the electromagnetic field for strongly coupled cavities with open boundaries where active medium is derived from quantum mechanics. When we use the term steady-state, this is the same way as we introduced in the beginning of the chapter. Luckily, to derive the equations used in SALT, we can use the electric field equation, the adiabatic elimination of gain polarisation and the dynamical equation for population inversion from Chapter 2. We will introduce the idea from SALT of Threshold Constant Flux (TCF) [19] states that will produce a nice modal picture close to threshold. With SALT, we introduce a unit change, known as SALT units where they relate to the electric field, gain polarisation and population inversion by [19] (Note that the authors use a convention different from ours by a factor 2),

$$E_S^+(z,t) = \frac{\wp}{\sqrt{\gamma_N \gamma_P}\hbar} E^+(z,t) \tag{4.32}$$

$$P_S^+(z,t) = \frac{\wp}{\sqrt{\gamma_N \gamma_P}\epsilon_0 \hbar} P_g^+(z,t) \tag{4.33}$$

$$N_S(z,t) = \frac{\wp^2}{\hbar \gamma_P \epsilon_0} N(z,t) \tag{4.34}$$

where $E^+(z,t)$, $P_g^+(z,t)$ and $N(z,t)$ are introduced in Chapter 2. Given we are considering this steady-state scenario, we now write the decomposition of the positive frequency electric field (2.67),

$$E_S^+(z,t) = \sum_n E_n(z) e^{-i\omega_n t}, \tag{4.35}$$

where for each mode, $E_n(z)$ is the electric field amplitude with SALT units for the steady-state solution of the electric field. As a result the gain polarisation term (2.78) can be written as,

$$P_S^+(z,t) \approx -N_S(z) \sum_n \mathscr{L}(\Delta_n)(\Delta_n + i) E_n(z) e^{-i\omega_n t}, \tag{4.36}$$

where $N_S(z)$ is the stationary population inversion and $\Delta_n = \frac{\omega_0 - \omega_n}{\gamma_P}$ is the detuning parameter for the $n^{\text{th}}$ mode. Like (2.79), $\mathscr{L}(\Delta_n) = (1 + \Delta_n^2)^{-1}$. (4.36) is valid in the case that $\gamma_P, |\omega_n - \omega_m| \ll |\omega_n + \omega_m|$ where $\omega_m$ and $\omega_n$ are two modal frequencies.

The stationary inversion approximation is used to obtain the stationary population inversion $N_S(z)$. To do this, we consider the stationary solutions of (2.83) which is given by,

$$N_S(z) = \frac{N_0^S(z)}{1 + \sum_{n=0}^{\infty} |E_n(z)|^2 \mathscr{L}(\Delta_n)}, \tag{4.37}$$

where $N_0^S(z)$ is the stationary pump term in SALT units and $\mathscr{L}(\Delta_n)$ is given by (2.79). The stationary inversion approximation is valid here provided that $\gamma_N \ll |\omega_n - \omega_m| \ll |\omega_m + \omega_n|$. Moreover, the denominator term for $N_S(z)$ with the electric field amplitude represents spatial hole burning and close to threshold is small. We will use this idea to introduce the TCF states.

### 4.2.1 Electric Field Equation Close to Threshold

We will consider a situation very similar to the derived electric field equation in terms of the positive frequency components given by (2.71). In our model, suppose that the cavities have no losses apart from the open boundaries and the absorption in the active medium and as a result, $\sigma = 0$ . To account for the absorption, we introduce the complex refractive index $\tilde{n}_b(z)$ in the same way as what was carried out when deriving the $q$-basis. Thus we can write (2.71) as,

$$\frac{\partial^2 E_S^+(z,t)}{\partial z^2} = \frac{\tilde{n}_b^2(z)}{c^2} \frac{\partial^2 E_S^+(z,t)}{\partial t^2} + \mu_0 \frac{\partial^2 P_S^+(z,t)}{\partial t^2}. \tag{4.38}$$

We can use the electric field decomposition (4.35), gain polarisation (4.36) and stationary inversion (4.37), with the electric field equation to find lasing modes $E_n(z)$ such that [19],

$$\begin{aligned} \left\{ \frac{d^2}{dz^2} + \frac{\omega_n^2}{c^2} \left( \tilde{n}_b^2(z) - (\Delta_n + i)\mathscr{L}(\Delta_n) \right.\right. \\ \left.\left. \times \frac{N_0^S(z)}{1 + \sum_{m=0}^{\infty} \mathscr{L}(\Delta_n) |E_m(z)|^2} \right) \right\} E_n(z) = 0. \end{aligned} \tag{4.39}$$

The interaction between modes arises via the spatial hole burning term [19] in the form $(1 + \sum_{m=0}^{\infty} \mathscr{L}(\Delta_n)|E_m(z)|^2)^{-1}$. However, we can neglect such a term close to

threshold as the magnitude of the electric field is small and thus the term with the intensity terms $|E_m(z)|^2$ can be neglected. The lasing modes which satisfy this condition are known as threshold lasing modes (TLMs) [19] with electric field $E_n^{TLM}(z)$. For these modes, (4.39) becomes,

$$\left\{\frac{d^2}{dz^2}+\frac{\omega_n^2}{c^2}\left(\tilde{n}^2(z)-(\Delta_n+i)\mathscr{L}(\Delta_n)N_0^S(z)\right)\right\}E_n^{TLM}(z)=0. \tag{4.40}$$

Moreover, we would like to connect these TLMs with open boundary conditions. To do this, we will suppose that these TLMs are constant flux states [19]. To be specific, suppose that $E_n^{CF}(z)$ is the constant flux state of the electric field for the $n^{th}$ mode. Inside the cavity, with some complex-valued permittivity $\epsilon(z)$ which includes gain and loss, the electric field inside the laser is given by,

$$\left\{\frac{d^2}{dz^2}+\frac{\omega_n^2}{c^2}\epsilon(z)\right\}E_n^{CF}(z)=0 \tag{4.41}$$

while outside the laser, for some real-valued refractive index $n_a$,

$$\left\{\frac{d^2}{dz^2}+\frac{\omega_n^2 n_a}{c^2}\right\}E_n^{CF}(z)=0 \tag{4.42}$$

For TLMs to be equivalent, although only at threshold, to the constant flux states, then the $E_n^{TLM}(z)$ satisfies the following equation outside the laser,

$$\left\{\frac{d^2}{dz^2}+\left(\frac{\omega_n n_a}{c}\right)^2\right\}E_n^{TLM}(z)=0. \tag{4.43}$$

We now are able to obtain the boundary conditions by solving for (4.43). Suppose that the laser structure we are considering starts at $z=z^-$ and finishes at $z=z^+$. This equation is equivalent to the Helmholtz equation given in (2.86). Solving (4.43) with only outgoing waves results the following boundary conditions,

$$\frac{d}{dz}\left(E_n^{TLM}(z^\pm)\right)=\pm i\frac{\omega_n}{c}E_n^{TLM}(z^\pm). \tag{4.44}$$

### 4.2.2 Threshold Constant Flux States (TCFs)

In this chapter, we have so far derived steady-state equations which describe the electromagnetic field distribution for a complex laser setup such as coupled-cavities with open boundaries. We want to see what the spatial variation of the electro-

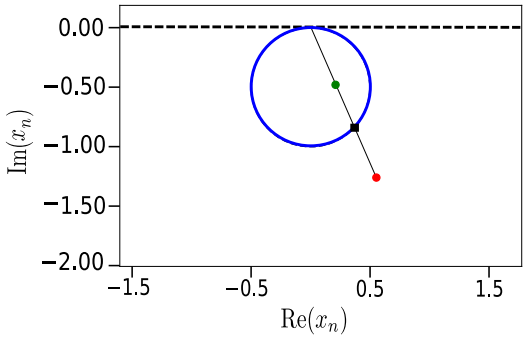



Figure 4.1: Mode picture in the $x_n$ complex plane where threshold is shown in blue while two modes above and below threshold are shown in green and red respectively. The projection of both modes at threshold is shown as a black square.

magnetic field looks like close to threshold. Thus we will introduce an electric field $E^{TCF}(z)$ which satisfies the constant flux condition (4.44). At threshold, $E_n^{TCF}(z)$ satisfies (4.40) inside the laser structure and the Helmholtz equation outside. We would like to further understand what occurs around the threshold region, such as slightly above or below threshold. To do this, we will look at the pre-factor of the population inversion, (4.40) which we will call $x_n(\omega_n)$ for each $\omega_n$,

$$x_n(\omega_n) = -\mathscr{L}\left(\Delta_n\right)\left(\Delta_n + i\right), \tag{4.45}$$

which also can be written in the form $x_n(\omega_n) = \frac{-1}{\Delta - i}$. All points for different $\Delta_n$ of $x_n(\omega_n)$ form a circle in the complex plane shown in Figure 4.1. In Figure 4.1, we see that the blue circle represents what we will call the threshold of the laser. Points along this circle are possible solutions for different $\Delta_n$ values where $x_n(\omega_n)$ satisfies (4.40). However we can also use $x_n(\omega_n)$ to approximate the electromagnetic field above and below threshold also. To consider such modes, we will seek solutions for eigenvalues $x_n(\omega_n)$ which corresponds to each electric field $E_n^{TCF}(z)$ for a particular pump profile $N_0^S(z)$ that satisfies [19],

$$\left\{\frac{d^2}{dz^2} + \frac{\omega_n^2}{c^2}\left(\tilde{n}^2(z) + x_n(\omega_n)N_0^S(z)\right)\right\}E_n^{TCF}(z) = 0. \tag{4.46}$$

The difference between (4.46) and (4.40) is that we find for every $N_0^S(z)$ and $E_n^{TCF}(z)$, an $x_n(\omega_n)$ which may not equal (4.45). As (4.45) represents $x_n(\omega_n)$ at threshold, then the solution for $x_n(\omega_n)$ obtained from solving (4.46) is thus an approximation of possible modes above or below threshold.

In Figure 4.1, we see a particular $x_n(\omega_n)$ as a black square at threshold. We see a line drawn between $x_n(\omega_n) = 0$ and this black square. We can approximate any mode away from the circle along this line by suitably scaling both $x_n(\omega_n)$ and the pump profile. For this scaling to work, we have to keep $x_n(\omega_n)N_0^S(z)$ constant to maintain the spatial profile approximation. Suppose that the amplitude for $x_n(\omega_n)$ is larger than if it was at threshold, for example the red dot in Figure 4.1. Then for $x_n(\omega_n)N_0^S(z)$ to be constant, we must have $N_0^S(z)$ be smaller than if the mode was at threshold. As a result of the inversion $N_0^S(z)$ being smaller, the mode in red is considered *below threshold*.

If we now suppose that the magnitude for $x_n(\omega_n)$ is lower than at threshold, then we have a similar situation as the green dot in Figure 4.1 which is inside the circle. For $x_n(\omega_n)N_0^S(z)$ to remain constant, this would require $N_0^S(z)$ to be higher than at threshold. This is what we will term as *above threshold*. Thus, to summarise, modes on the blue circle in Figure 4.1 are at threshold as they fulfil the electromagnetic field equation (4.46) with (4.45) being true. If a mode is located inside the circle, this is above threshold as this mode has typically higher $N_0^S(z)$. Finally, if a mode is located outside the circle, this is below threshold as the mode typically has lower $N_0^S(z)$.

We can determine whether a mode is below or above threshold mathematically by using (4.45) in a similar way as [20]. With (4.45), we derive a self-consistent equation for $x_n(\omega)$, that is the key to determining if a mode is above or below threshold. We can further write a second equation which relates back to the physics of the laser. These equations are given by,

$$|x_n(\omega_n)|^2 = -\mathrm{Im}(x_n(\omega_n)), \tag{4.47}$$

$$\omega_n = \omega_0 + \gamma_P \frac{\mathrm{Im}(x_n(\omega_n)) + 1}{\mathrm{Re}(x_n(\omega_n))}. \tag{4.48}$$

where (4.47) is still implicitly dependent on the modal frequencies $\omega_n$. Using (4.47), we can determine whether a laser is above, below or at threshold. We note three possibilities as explained above that $x_n(\omega_n)$ tells us about threshold which are,

$$\begin{aligned} |x_n(\omega_n)|^2 &< -\mathrm{Im}(x_n(\omega_n)) \;\rightarrow\; \text{Above threshold,} \\ |x_n(\omega_n)|^2 &= -\mathrm{Im}(x_n(\omega_n)) \;\rightarrow\; \text{At threshold,} \\ |x_n(\omega_n)|^2 &> -\mathrm{Im}(x_n(\omega_n)) \;\rightarrow\; \text{Below threshold.} \end{aligned} \tag{4.49}$$

We see that if $|x_n(\omega_n)|^2 < -\mathrm{Im}(x_n(\omega_n))$, this is inside the circle we have shown in Figure 4.1. This is above threshold. When $|x_n(\omega_n)|^2 = -\mathrm{Im}(x_n(\omega_n))$, this means that

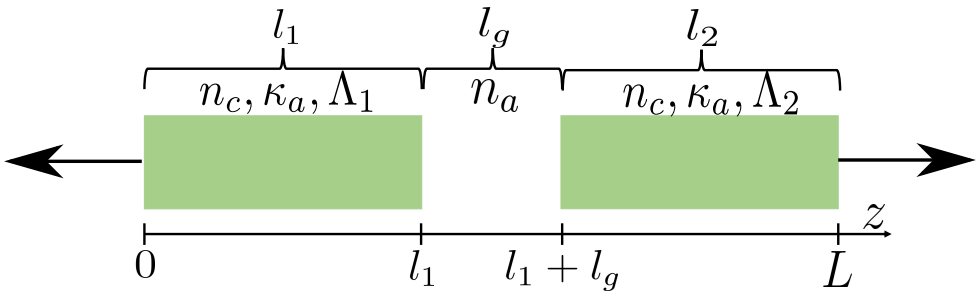



Figure 4.2: Open boundaries with a coupled-cavity laser system with two cavities of length $l_1$ and $l_2$ with pump profiles $\Lambda_1$ and $\Lambda_2$ respectively with a gap of length $l_g$ in between.

the mode is on the circle. This is threshold. Finally when $|x_n(\omega_n)|^2 > -\text{Im}(x_n(\omega_n))$, this means the mode is outside the circle. This is below threshold. We will use the self consistent equation, (4.47), along with (4.46) to determine the value of $x_n(\omega_n)$ for a given frequency $\omega_n$. For the first part of our analysis, we will explore the first condition, (4.47), and later will return to the second condition, (4.48) which modes can be relate back to physical characteristics $\omega_0$ and $\gamma_P$.

## 4.3 Coupled-Cavities and Exceptional Points using the $q$-basis

In this section, we would like to obtain modes of frequency $\omega$ that can be approximated above or below threshold by using the self-consistent equation for eigenvalues, (4.47). We will determine these modes by generating a transfer matrix which describes the spatial variation of the electromagnetic field throughout the laser using the $q$-basis. To do this, we will use the open boundary conditions and also determine interface conditions between all sections.

### 4.3.1 Transfer Matrix using the $q$-basis

In the same way as the previous section, we consider a coupled laser structure with open boundaries located at $z = 0$ and $z = L$. Taking Figure 4.2 into account, the

real refractive index for each section, $n_b(z)$ is given by,

$$n_b(z) = n_i = \begin{cases} n_c & \text{if } 0 < z < l_1 \\ n_a & \text{if } l_1 < z < l_1 + l_g \\ n_c & \text{if } l_1 + l_g < z < L \end{cases} \tag{4.50}$$

where the length of cavity 1 is $l_1$ (cavity 1), the gap between, $l_g$ (gap section) and the final cavity, $l_2$ (cavity 2). Outside the coupled system where $z < 0$ is the left section while $z > L$ is the right section. Note that outside the cavity has background refractive index the same as the gap, $n_a$. Note that we will take $n_i$ as the refractive index for each section.

To connect the gain susceptibility term in the $q$-basis with the active medium presented in SALT and SLT, we can use adiabatic elimination which can be obtained a relation between the gain polarisation, population inversion and electric field. For a single frequency $\omega$, we can relate the gain susceptibility from (4.35) to (4.36) and thus,

$$\chi_g(z) = -\mathscr{L}(\Delta)(\Delta + i)N_S(z) \tag{4.51}$$

where $\Delta$ is the detuning factor such that $\Delta = \frac{\omega_0 - \omega}{\gamma_P}$. the population inversion is constant in each cavity, given by,

$$N_0^S(z) = \begin{cases} \Lambda_1 & 0 \leq z \leq l_1 \\ 0 & l_1 \leq z \leq l_1 + l_g \\ \Lambda_2 & l_1 + l_g \leq z \leq L \end{cases},$$

where as a result of considering modes close to threshold, $N_0^S(z) = N_S(z)$. Like in the previous section, we will consider TCF states and thus the gain susceptibility for the $i^{\text{th}}$ section with gain, $\chi_g^{(i)}$, is written as follows,

$$\chi_g^{(i)} = x_n(\omega)\Lambda_i, \tag{4.52}$$

where $\Lambda_i$ is either $\Lambda_1$ and $\Lambda_2$. The complex refractive index $\tilde{n}_b(z)$ is made up of the real refractive index and the extinction coefficient given by (4.8). We note $\kappa_i$ as the extinction coefficient for the $i^{\text{th}}$ section which is $\kappa_a$ for both cavities or zero otherwise.

To use the $q$-basis, we consider the electric field which satisfies the TCF states, whose amplitude is $E^{TCF}(z)$. Moreover the magnetic induction will satisfy the TCF

condition too, denoted by $B^{TCF}(z)$. Inside the cavity, $E^{TCF}(z)$ and $B^{TCF}(z)$ satisfy the following equations for a single frequency $\omega$,

$$\frac{dE^{TCF}(z)}{dz} = i\omega B^{TCF}(z), \tag{4.53}$$

$$\frac{dB^{TCF}(z)}{dz} = \frac{i\omega}{c^2}\left(\tilde{n}_b(z)^2 + x_n(\omega)N(z)\right)E^{TCF}(z). \tag{4.54}$$

Outside the laser structure, $E^{TCF}(z)$ and $B^{TCF}(z)$ satisfy the following,

$$\frac{dE^{TCF}(z)}{dz} = i\omega B^{TCF}(z), \tag{4.55}$$

$$\frac{dB^{TCF}(z)}{dz} = \frac{i\omega n_a^2}{c^2}E^{TCF}(z). \tag{4.56}$$

We can use the $q$-basis to write $E^{TCF}(z)$ and $B^{TCF}(z)$ for each section. We define $\mathbf{q}^{(i)}$, which contains all elements of the $q$-basis for the $i^{th}$ section, as,

$$\mathbf{q}^{(i)} = \begin{pmatrix} q_A^{(i)} \\ q_S^{(i)} \\ q_R^{(i)} \\ q_I^{(i)} \end{pmatrix}. \tag{4.57}$$

Thus we have the following differential equation to solve:

$$\frac{d\mathbf{q}^{(i)}}{dz} = \mathcal{T}^{(i)}\mathbf{q}^{(i)}. \tag{4.58}$$

The matrix $\mathcal{T}^{(i)}$ for each section is obtained from the differential equations derived for each element of the $q$-basis, namely (4.29)-(4.31). Using these, we write,

$$\mathcal{T}^{(i)} = \begin{pmatrix} 0 & 0 & A^{(i)} & B^{(i)} \\ 0 & 0 & -A^{(i)} & \frac{2\omega n_i}{c} - B^{(i)} \\ A^{(i)} & A^{(i)} & 0 & 0 \\ B^{(i)} & -\frac{2\omega n_i}{c} + B^{(i)} & 0 & 0 \end{pmatrix} \tag{4.59}$$

where $A^{(i)}$ and $B^{(i)}$ are,

$$A^{(i)} = -\frac{\omega}{n_i c}(2n_i^2\kappa_i + \mathrm{Im}(x_n)\Lambda_i) \tag{4.60}$$

$$B^{(i)} = \frac{\omega}{n_i c}(n_i^2\kappa_i^2 - \mathrm{Re}(x_n)\Lambda_i) \tag{4.61}$$

As $\mathcal{T}^{(i)}$ is not dependent on position or $\mathbf{q}^{(i)}$ for each section, this is easily solved. Let this section be from $z = l_j$ to $z = l_i$. Thus,

$$\mathbf{q}^{(i)}(l_i) = \mathcal{M}^{(i)}(l_i - l_j)\mathbf{q}^{(i)}(l_j) \tag{4.62}$$

where $\mathcal{M}^{(i)}(l_i - l_j) = e^{(l_i - l_j)\mathcal{T}^{(i)}}$ and corresponds to the transfer matrix inside each section between $l_j$ and $l_i$.

### 4.3.2 Interface Conditions in terms of the $q$-Basis

We now would like to describe the $q$-basis accurately across different interfaces inside the laser. This is not possible without looking at the interface conditions at the boundaries of each section. While the electromagnetic field is continuous at each interface, this is not true with the $q$-basis as it is dependent on the refractive index which changes in each section. Suppose the equations governing the left side of the interface are $q_A^{(i)}$, $q_S^{(i)}$, $q_R^{(i)}$ and $q_I^{(i)}$ and on the right side, $q_A^{(j)}$, $q_S^{(j)}$, $q_R^{(j)}$ and $q_I^{(j)}$. Then the interface conditions are as follows,

$$q_A^{(j)}(l_i) = \frac{1}{2}\left(1 + \frac{n_i^2}{n_j^2}\right) q_A^{(i)}(l_i) + \frac{1}{2}\left(1 - \frac{n_i^2}{n_j^2}\right) q_S^{(i)}(l_i) \tag{4.63}$$

$$q_S^{(j)}(l_i) = \frac{1}{2}\left(1 - \frac{n_i^2}{n_j^2}\right) q_A^{(i)}(l_i) + \frac{1}{2}\left(1 + \frac{n_i^2}{n_j^2}\right) q_S^{(i)}(l_i) \tag{4.64}$$

$$q_R^{(j)}(l_i) = \frac{n_i}{n_j} q_R^{(i)}(l_i) \tag{4.65}$$

$$q_I^{(j)}(l_i) = \frac{n_i}{n_j} q_I^{(i)}(l_i) \tag{4.66}$$

The interface conditions for $\mathbf{q}^{(i)}$ and $\mathbf{q}^{(j)}$ with refractive indices $n_i$ and $n_j$ respectively, is given by the following matrix,

$$J(n_j, n_i) = \begin{pmatrix} \frac{1}{2}\left(1 + \frac{n_i^2}{n_j^2}\right) & \frac{1}{2}\left(1 - \frac{n_i^2}{n_j^2}\right) & 0 & 0 \\ \frac{1}{2}\left(1 - \frac{n_i^2}{n_j^2}\right) & \frac{1}{2}\left(1 + \frac{n_i^2}{n_j^2}\right) & 0 & 0 \\ 0 & 0 & \frac{n_i}{n_j} & 0 \\ 0 & 0 & 0 & \frac{n_i}{n_j} \end{pmatrix}. \tag{4.67}$$

Now we have assembled all the pieces together to create the transfer matrix to describe the $q$-basis from one end of the coupled-cavities to the other. Denoting the index for each section as $(l)$ for the left section outside the laser ($z < 0$), (1) will denote the first cavity ($0 < z < l_1$), $(g)$ will denote the gap length ($l_1 < z < l_1 + l_g$), (2) is the

second cavity ($l_1 + l_g < z < L$) and ($r$) is the right section outside the cavity ($z > L$). Thus for the coupled laser system is given by,

$$\mathbf{q}^{(r)}(L) = J(n_a, n_c)\mathcal{M}^{(2)}(l_2)J(n_c, n_a)\mathcal{M}^{(g)}(l_g)J(n_a, n_c)\mathcal{M}^{(1)}(l_1)J(n_c, n_a)\mathbf{q}^{(l)}(0) \tag{4.68}$$

### 4.3.3 Boundary Conditions in terms of the $q$-Basis

We have now obtained a transfer matrix which goes from the boundary at $z = 0$ to $z = L$. The next step is to obtain the boundary conditions for each term of the $q$-basis. Outside the laser, the electric field term $E^{TCF}(z)$ has left-going waves of the form $e^{-ikz}$ and right-going of the form $e^{ikz}$. We can thus write,

$$E^{TCF}(z) = \mathcal{E}_L e^{-in_a kz} + \mathcal{E}_R e^{in_a kz} \tag{4.69}$$

where $\mathcal{E}_L$ and $\mathcal{E}_R$ are complex constants for the left and right-moving waves respectively. Note $k = \frac{\omega}{c}$. These are valid solutions to the Helmholtz equation with refractive index $n_a$. Outside the laser, we can use both (4.53) and (4.69) while noting at $z = 0$ only has left-going waves and $z = L$ only has right-moving waves. Thus the boundary conditions for the TCF states for the electromagnetic field are given by,

$$B^{TCF}(0) = -\frac{n_a}{c}E^{TCF}(0), \tag{4.70}$$

$$B^{TCF}(L) = \frac{n_a}{c}E^{TCF}(L), \tag{4.71}$$

as at the boundaries, there are only outgoing waves. In terms of the $q$-basis and using (4.20)-(4.23), at $z = 0$, we have the following,

$$q_A^{(l)}(0) = 2|E^{TCF}(0)|^2, \tag{4.72}$$

$$q_S^{(l)}(0) = 0, \tag{4.73}$$

$$q_R^{(l)}(0) = -2|E^{TCF}(0)|^2, \tag{4.74}$$

$$q_I^{(l)}(0) = 0, \tag{4.75}$$

while at $z = L$,

$$q_A^{(r)}(L) = 2|E^{TCF}(L)|^2, \tag{4.76}$$
$$q_S^{(r)}(L) = 0, \tag{4.77}$$
$$q_R^{(r)}(L) = 2|E^{TCF}(L)|^2, \tag{4.78}$$
$$q_I^{(r)}(L) = 0. \tag{4.79}$$

We can also write these boundary conditions independent of the electric field as such that,

$$\frac{q_A^{(l)}(0)}{q_A^{(l)}(0)} = -\frac{q_A^{(r)}(L)}{q_A^{(r)}(L)} = -1, \tag{4.80}$$
$$q_S^{(l)}(0) = q_I^{(l)}(0) = q_S^{(r)}(L) = q_I^{(r)}(L) = 0. \tag{4.81}$$

### 4.3.4 Transfer Matrix Condition using the $q$-basis

So far, we have derived the general form of a transfer matrix which can describe the electromagnetic field throughout for each individual cavity and the gap between them. Then we were able to connect all sections together to use the interface conditions. We also discussed the open boundary conditions at each end of the laser. With all of these in mind, we can obtain a matrix condition that laser modes must satisfy. In particular, we can now obtain a condition for finding the eigenvalue $x_n(\omega)$ with the boundary conditions along with (4.68) and (4.47). Thus we have the following,

$$\frac{|E(L)|^2}{|E(0)|^2}\begin{pmatrix}1\\0\\1\\0\end{pmatrix} = J(n_a,n_c)\mathcal{M}^{(2)}(l_2)J(n_c,n_a)\mathcal{M}^{(g)}(l_g)J(n_a,n_c)\mathcal{M}^{(1)}(l_1)J(n_c,n_a)\begin{pmatrix}1\\0\\-1\\0\end{pmatrix} \tag{4.82}$$

where the complex $x_n$ can be solved while noting the boundary conditions. Solving this equation obtains numerous $x_n$'s for a single $\omega$ (with wavenumber $k$), albeit with different physical parameters $\omega_0$ and $\gamma_P$, as (4.82) is independent of these physical parameters. We can see for an individual $\omega$ a selection of modes which satisfy (4.82) as black dots in Figure 4.3. We see one mode inside the circle for this example which indicates that this mode is above threshold while the other modes are outside the circle, meaning they are below threshold. The choice of whether these modes are

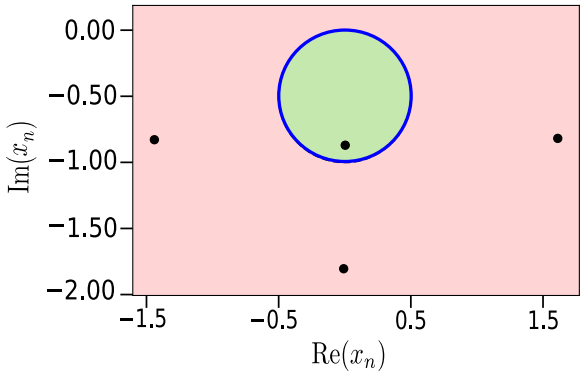



Figure 4.3: Modes of a system (in black) where $\Lambda_1 = 1.3$, $\Lambda_2 = 0.5$, $l_1 = l_2 = 0.1$ mm, $l_g = 0.01$ mm and $k = 95$ mm$^{-1}$. Modes at threshold would be located on the edge of the circle (in blue), while inside the circle, modes are above threshold (in green) and outside, below threshold (in red).

above or below threshold is determined using (4.47). Let $g = |x_n|^2 + \mathrm{Im}(x_n)$ and comparing this to (4.47), $g > 0$ indicates that a mode is below threshold, $g = 0$ means at threshold and finally, $g < 0$, which indicates a mode is above threshold. Thus we can obtain an EP when two of these $x_n$ terms coalesce. To see this, we will consider the EP when the two closest $x_n$ values to threshold meet. Moreover for the following discussion, the closest mode to threshold will be examined to determine the effect of an EP has on the lasing condition. Instead of using $\omega$, we will use wavenumber $k = \frac{\omega}{c}$. Examining the closest $x_n$, we obtain Figure 4.4 which shows the effect of EPs over a range of $k$ and $\Lambda_2$ while keeping $\Lambda_1$ fixed. For each EP shown in the figure, there appears to be different situations for the coupled system. In the $k = 70$-$80\text{mm}^{-1}$ range of Figure 4.4, we see an EP that moves the threshold region further up for similar $k$. A more interesting case appears between $k = 80$-$90\text{mm}^{-1}$ where two threshold regions are separated by an EP. Thus in this region, we see that with a fixed $k$, increasing $\Lambda_2$ will result in the closest mode to threshold going below threshold and thus go above threshold. The same phenomenon, albeit for less $k$ is seen in the $k = 90$-$100\text{mm}^{-1}$ range. This is a similar reproduction of what was obtained from SALT [20], albeit a different way of treating the pump parameters. For EPs in the ranges of $k = 100$-$110\text{mm}^{-1}$ and $k = 110$-$120\text{mm}^{-1}$, we see that the EP has little or no effect on whether a laser is above or below threshold. However, for these above threshold regions, $g$ close to the EPs is less negative or even above zero meaning the EP increases the value of $g$. Overall, this means that each EP is a local maximum for the function $g$ in each of the ranges in Figure 4.4. It is important to mention again that the determination of these modes above or below threshold

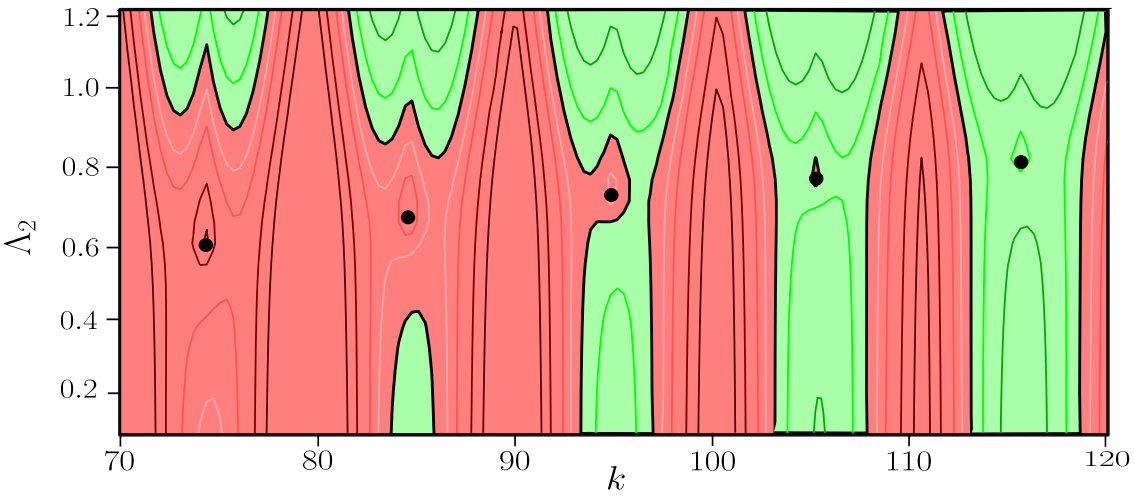



Figure 4.4: Plot of wavenumber ranges for a coupled laser system with $l_1 = .1\text{mm}$, $l_2 = .01\text{mm}$ and $l_3 = .1\text{mm}$. The laser sections have complex refractive index $\tilde{n}_b = 3(1 + .043i)$ and $\Lambda_1 = 1.2$. The $x$ axis represents the wavenumber, $k = \frac{\omega}{c}$ and $y$ axis the 2nd pump $\Lambda_2$. Green indicates above threshold region while red is below threshold. There are multiple EPs shown with black dots. The bold black line is threshold for the coupled system.

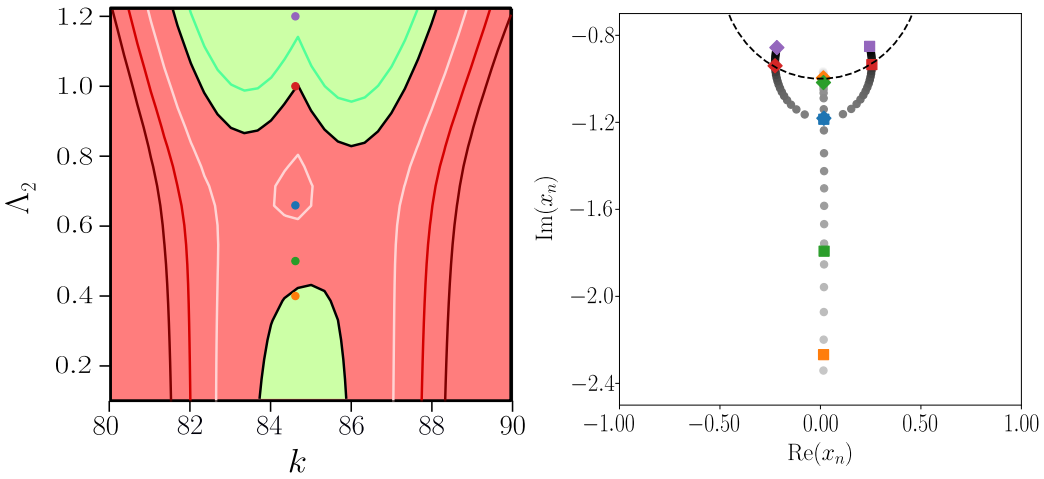
do not take into account the permissible values of $\omega_0$ and $\gamma_P$. For a fixed $k$, these will be different values of $\omega_0$ and $\gamma_P$ which can be determined using (4.48). We will explore the connection between these modes with constant $k$ in the next section with a change in $\Lambda_2$ in the next sections along with relating modes to $\omega_0$ and $\gamma_P$.

## 4.4 Analysis of Coupled-Cavity Laser Modes and Exceptional Points

In this section, we provide an analysis on coupled-cavity modes and EPs obtained using the $q$-basis for a variety of physical situations and perspectives. This will be done by focusing on the intensities of the modes, the power flow, the length of the gap between both cavities. We will also look into the second threshold condition given by (4.48), along with the first (4.47).

### 4.4.1 Intensity of Coupled Cavities at Exceptional Points

We have seen that in the previous section that for some fixed $k$ values that the closest mode to threshold results in the counter-intuitive phenomenon of with increasing $\Lambda_2$, modes go below threshold. We will investigate this result by considering the EP




(a) Mode lasing condition

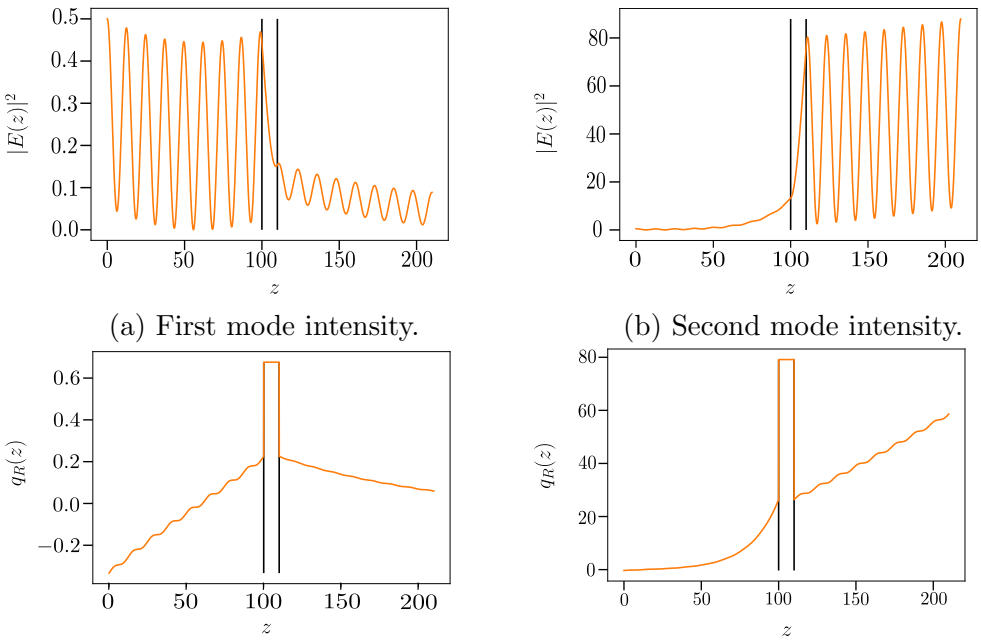
(b) Eigenvalue branches with varying $\Lambda_2$

Figure 4.5: A closer look at the region $k = 80\text{mm}^{-1}$ to $k = 90\text{mm}^{-1}$ where the relative intensity is shown for $\Lambda_2 = .4$ (orange), $\Lambda_2 = .5$ (green), $\Lambda_2 = 0.659265306122$ (blue), $\Lambda_2 = .1$ (red) and $\Lambda_2 = 1.2$ (purple) for $k = 84.5968367347\text{mm}^{-1}$, $\Lambda_1 = 1.2$ and the same lengths of the laser and gap and refractive index as Figure 4.4. (a) shows the lasing condition of the first lasing mode where light green region is above threshold and light red region is below threshold. (b) shows both modes with different $x_n(\omega)$ where inside the circle (dashed line), the mode is above threshold. At $\Lambda_2 = 0.659265306122$, there is an EP.

shown in Figure 4.5. In this case, as before, we vary the second pump from zero to when $\Lambda_1 = \Lambda_2$.

In Figure 4.5, we see that an EP is located at $k = 84.5968367347\text{mm}^{-1}$ and $\Lambda_2 = 0.659265306122$. We will study the effects of this EP to the threshold regions, to see what occurs to the intensity and power flow of the laser. Taking it step by step, we will consider the two closest modes to the threshold condition (4.47). In particular, Figure 4.5(b), we see a pictorial view of the changing two modes with increasing $\Lambda_2$. One mode starts above threshold and reduces below threshold to meet the second mode where the coalesce to form an EP and both deviate, one in positive $\mathrm{Re}(x_n)$ and the other with negative $\mathrm{Re}(x_n)$. What will determine the nature of the mode is the power flow which is related to $q_R(z)$. Note that if $q_R(z) < 0$, this indicates that the power is moving to the left while $q_R(z) = 0$ indicates there is no power flow. On the other hand, $q_R(z) > 0$ indicates the power is moving to the right.

Let us now take a step-by-step guide of what happens to both modes. We will start discussing $\Lambda_2 = 0.4$ for both modes. Looking at Figure 4.6, the closest mode




(a) First mode intensity.

(b) Second mode intensity.

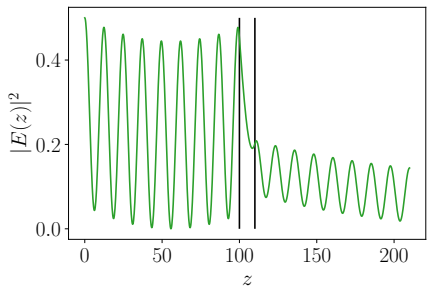
(c) First mode power flow.

(d) Second mode power flow.

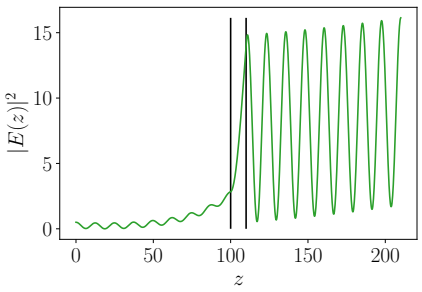
Figure 4.6: Plots of two modal relative intensities ((a) and (b)), with power flow ($q_R(z)$) shown for (a) and (b) in (c) and (d) respectively. Parameters are $k = 84.5968367347\text{mm}^{-1}$, $\Lambda_1 = 1.2$ and $\Lambda_2 = .4$. In reference to Figure 4.5.

to threshold, Figures 4.6(a) and 4.6(c), has more intensity in the first cavity than in the second. However, if we look at the power flow of the first mode, $q_R(z)$, we see that the power flows in both directions for the first cavity. This means some power is flowing from the first cavity into the second. Thus, even though the laser is above threshold, the first cavity compensates the low pump of the second by transferring power into it. Furthermore, we see that in the second cavity, with increasing $z$, $q_R(z)$ reduces which tells us the second cavity is absorbing. The second closest mode, seen in Figures 4.6(b) and (d) shows a mode well below threshold. This is still worthwhile to study as a mode similar to this can be seen at threshold for higher $\Lambda_1$ and $\Lambda_2$. We will discuss this in the next section. We see that the intensity of the second cavity is far higher than the first. This is due to the majority of the power flowing into the second cavity from the first.

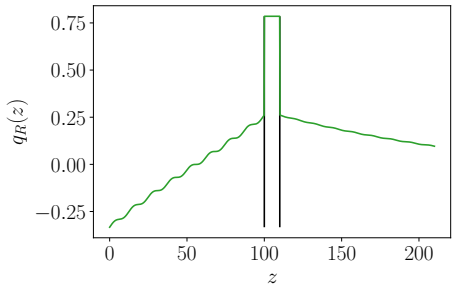
In fact, when we increase the pump to $\Lambda_2 = 0.5$, both modes shown in Figure 4.7 are below threshold, the first being just below the threshold level. This mode shown in Figures 4.7(a) and (c), more power flows into the second cavity from the first. This means less power is flowing outside the laser as the second cavity still has net absorption. As a result, the mode is below threshold. The second mode shown in



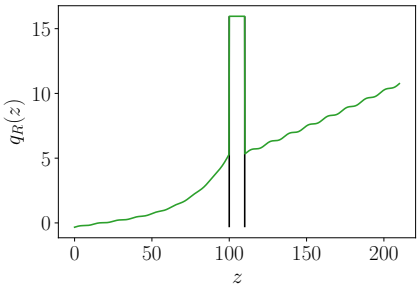

(a) First mode intensity.




(b) Second mode intensity.




(c) First mode power flow.



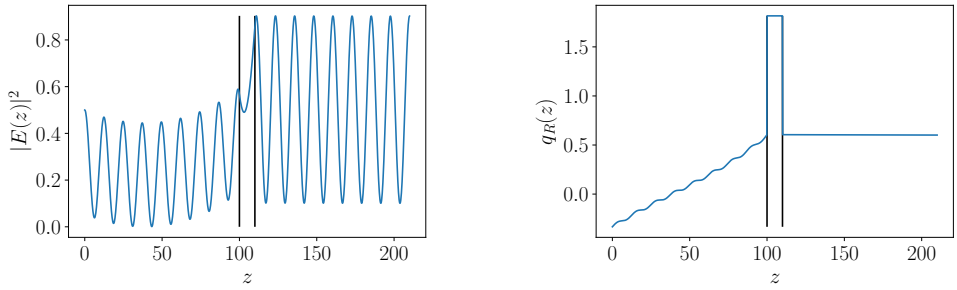

(d) Second mode power flow.

Figure 4.7: Plots of two modal relative intensities ((a) and (b)), with power flow ($q_R(z)$) shown for (a) and (b) in (c) and (d) respectively. Parameters are $k = 84.5968367347\text{mm}^{-1}$, $\Lambda_1 = 1.2$ and $\Lambda_2 = 0.5$. In reference to Figure 4.5.

Figures 4.7(b) and (d) is similar to the second shown in Figures 4.6(b) and (d) where the intensity of the first cavity is still smaller than the second, but the difference is not as dramatic as $\Lambda_2 = 0.4$.

The next pump level considered is given by Figure 4.8. This is the approximate location of the EP and both modes have coalesced into a single mode with the same relative intensity and power flow. The intensity of the coupled laser is now greater in the second cavity, even though the first still has a greater pump. This is the result of the power flow once again, as power flows mostly into the second cavity from the first. Notice that the second cavity has nearly constant power flow throughout which means the gain is approximately equal to absorption. In all cases for the first mode previously, the second cavity had net absorption while the second closest mode has net gain in the second cavity.

Focusing on $\Lambda_2 = 1$, Figure 4.9 shows both modal intensities just above threshold and the power flow. Both modes are equivalent a part from half a wavelength difference. This is the result of the real part of the eigenvalue which changes the refractive index. Consulting with Figure 4.5(b), we see that one mode has a positive $\text{Re}(x_n)$




(a) Mode intensity.

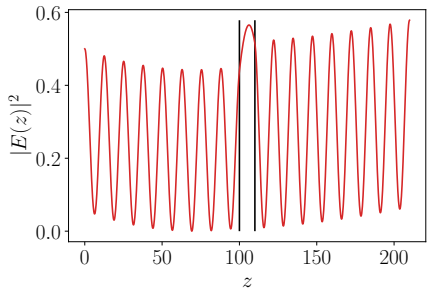
(b) Mode power flow.

Figure 4.8: Plot of modal relative intensity (a), located at the EP, below threshold and the power flow ($q_R(z)$) (b). Parameters are $k = 84.5968367347\text{mm}^{-1}$, $\Lambda_1 = 1.2$ and $\Lambda_2 = 0.659265306122$. In reference to Figure 4.5.

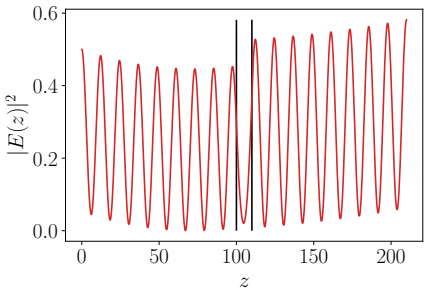
and the other has negative $\text{Re}(x_n)$. This results in the difference in the number of wavelengths permitted in the cavity between the two modes. This will be discussed further in later sections. In terms of intensity, the first cavity still has more pump, but the intensity is still less than the second cavity. This is still true because of the power flow. The first cavity, its power is moving in both directions while the second, as with all before, the power flow throughout its structure, moves to the right.

We now consider when both pumps are the same where $\Lambda_2 = 1.2$. In this instance, both modes are similar but as before differ by half a wavelength. However, because both pumps are the exact same, the power flow is only left moving for the first cavity and only right moving for the second. The relative intensity for both modes and both cavities are the same at the boundaries. Furthermore, we see that both modes have net gain in both cavities as seen in Figures 4.10 (c) and (d).

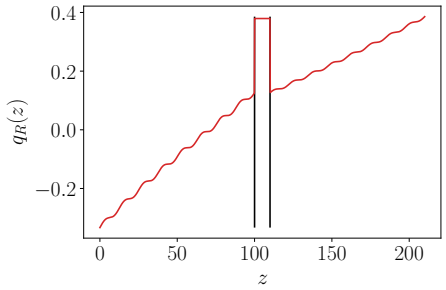
In this subsection, we have seen how the two closest modes to threshold change as they are in the region of the exceptional point. We see that the laser goes below threshold in Figure 4.5 as a result of the power of the first cavity flowing into the second where the second is a net absorbing cavity. We see this as the possible explanation for this phenomenon. However, as we have mentioned throughout, these modes assume constant $k$ and without relating to the physical parameters $\omega_0$ and $\gamma_P$. With increasing $\Lambda_2$, this means $x_n$ will change for both modes discussed. But, with a fixed $k$, like in Figures 4.5-4.10 where $k = 84.5968367347\text{mm}^{-1}$, when the mode passes two threshold regions, this means $\omega_0$ and $\gamma_P$ are different for when the modes hit threshold for different $\Lambda_2$. This means, we must have a varying $k$ such that the physical parameters $\omega_0$ and $\gamma_P$ can remain constant to study dynamics. This issue is addressed and solved in Chapter 6 when we introduce a dynamical description of the



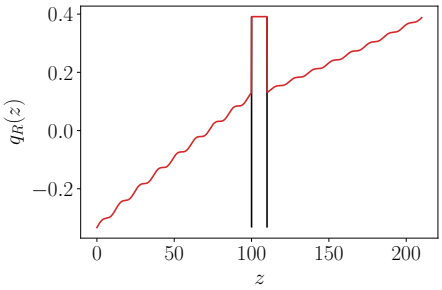

(a) First mode intensity.




(b) Second mode intensity.

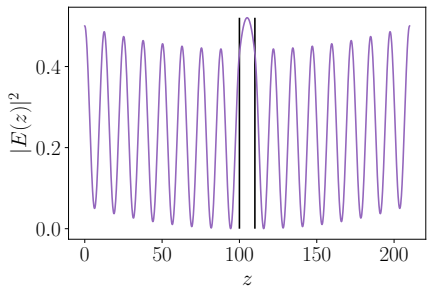



(c) First mode power flow.

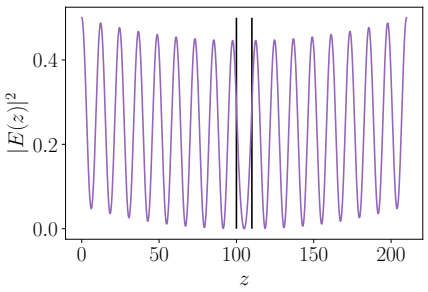



(d) Second mode power flow.

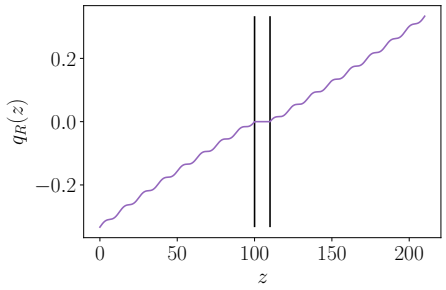
Figure 4.9: Plots of two modal relative intensities ((a) and (b)), with power flow ($q_R(z)$) shown for (a) and (b) in (c) and (d) respectively. Parameters are $k = 84.5968367347\text{mm}^{-1}$, $\Lambda_1 = 1.2$ and $\Lambda_2 = 1$. In reference to Figure 4.5.



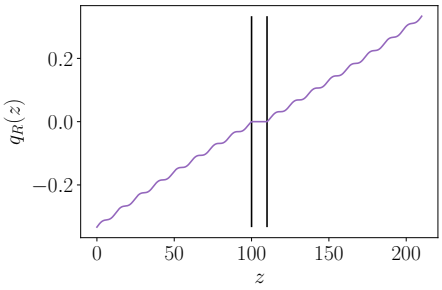

(a) First mode intensity.




(b) Second mode intensity.




(c) First mode power flow.




(d) Second mode power flow.

Figure 4.10: Plots of two modal relative intensities ((a) and (b)), with power flow ($q_R(z)$) shown for (a) and (b) in (c) and (d) respectively. Parameters are $k = 84.5968367347\text{mm}^{-1}$, $\Lambda_1 = 1.2$ and $\Lambda_2 = 1.2$. In reference to Figure 4.5.

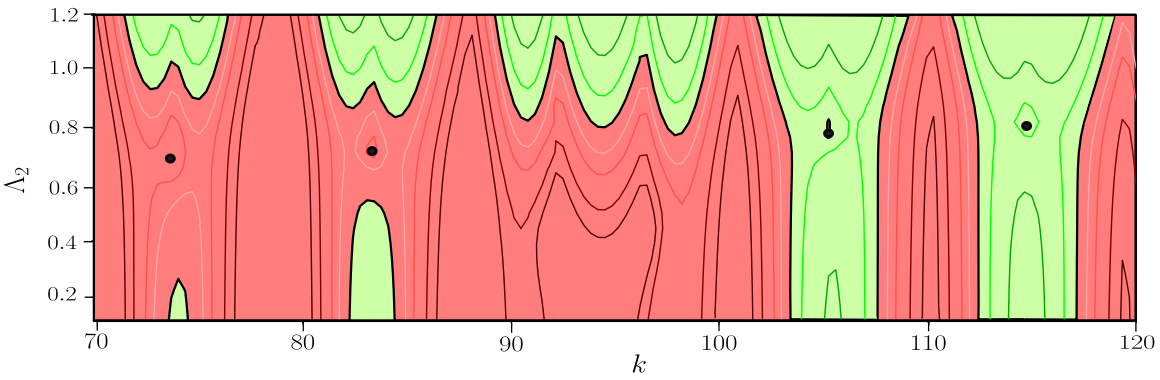



Figure 4.11: Range of wavenumbers which show various EPs (black dots) where $\Lambda_1 = 1.2$, $\tilde{n}_b = 3(1 + 0.043i)$ with $l_1 = 0.1$mm, $l_2 = 0.1$mm and $l_3 = 0.1$mm. Green indicates above threshold region while red is below threshold.

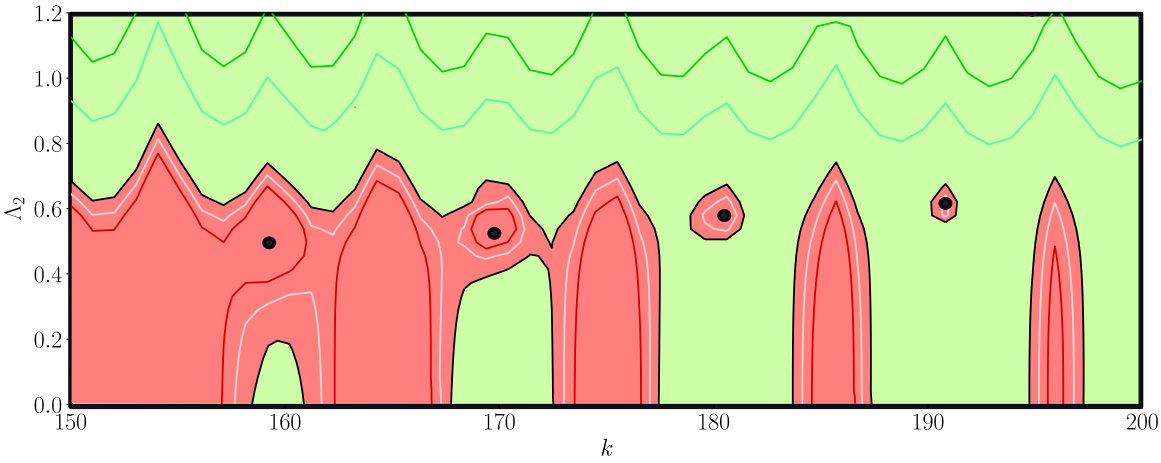



Figure 4.12: Range of wavenumbers which show various EPs (black dots) where $\Lambda_1 = 1.2$, $\tilde{n}_b = 3(1 + 0.43i)$ with $l_1 = 0.1$mm, $l_2 = 0.001$mm and $l_3 = 0.1$mm. Green indicates above threshold region while red is below threshold.

laser setup.

### 4.4.2 Exceptional Points with different Gap lengths

We have shown so far that where EPs are located, the laser goes below threshold with increasing pump and even without going below threshold, changes the intensity of each mode due to the power flow. In this case, we would like to investigate whether EPs exist if we increase or decrease the gap between both laser cavities and whether they cause the same effects shown in the previous subsection.

In Figure 4.11, it shows a coupled cavity system, where the only difference between this laser and before is the distance of the gap has increased to $l_g = 0.1$mm. Even with

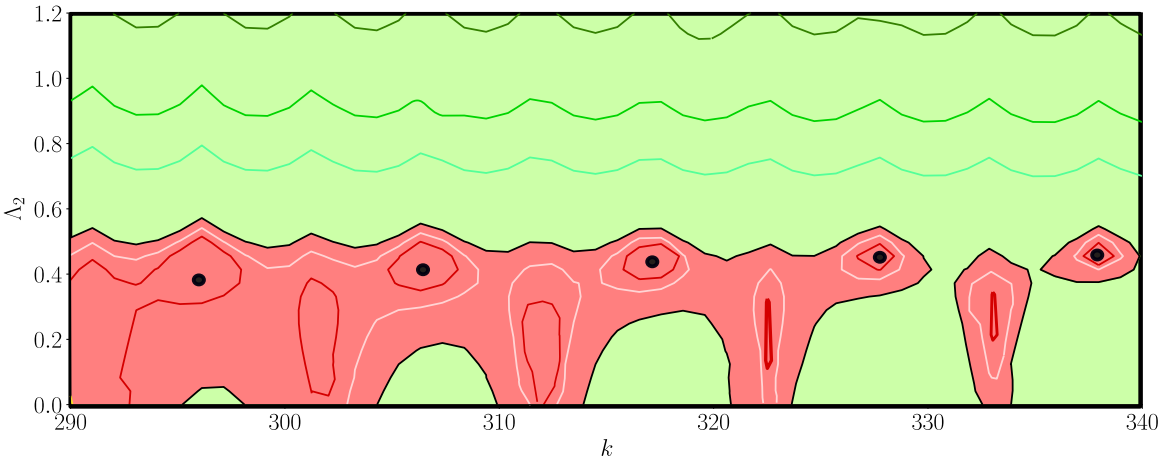



Figure 4.13: Range of wavenumbers which show various EPs (black dots) where $\Lambda_1 = 1.2$, $\tilde{n}_b = 3(1 + 0.043i)$ with $l_1 = 0.1$mm, $l_2 = 0$mm and $l_3 = 0.1$mm.Green indicates above threshold region while red is below threshold.

a greater length, albeit for different wavenumbers, EPs still have the same effect of causing the system to go below threshold with increasing pump. Although in Figure 4.11, we see an interesting result where between 90-100mm$^{-1}$, we see three branches meeting for higher pump where in all of figures for $l_g = 0.01$mm, we see two branches meet at higher $\Lambda_2$.

For smaller gap sizes such as in Figure 4.12, the length of the gap between both cavities has been decreased to $l_g = .001$mm, EPs still cause the lasers to go below threshold with increasing pump, although for larger $k$. In this case, we still see that there are instances where increasing pump will result in a lasing mode going below threshold around an EP. In Figure 4.12, we see two instances where this occurs. Finally we consider where there is no gap between both lasers, $l_g = 0$mm. Even with no gap, we consider two separate cavities with different pumps as before. Even here, we see the same idea happens where the lasing modes goes below threshold for increasing pump which happens for numerous $k$ as shown in Figure 4.13. In both of the cases with smaller gap size than the main laser studied in this chapter, i.e. Figures 4.12 and 4.13, we see that EPs occur at larger $k$. This interesting result is in fact answered in the next chapter with the use of the $\mathcal{Z}$-basis.

### 4.4.3 The second condition for Threshold

In the previous subsections, we have used (4.47) to determine whether a laser is above or below threshold using the idea of TCFs. However, we have neglected so far the

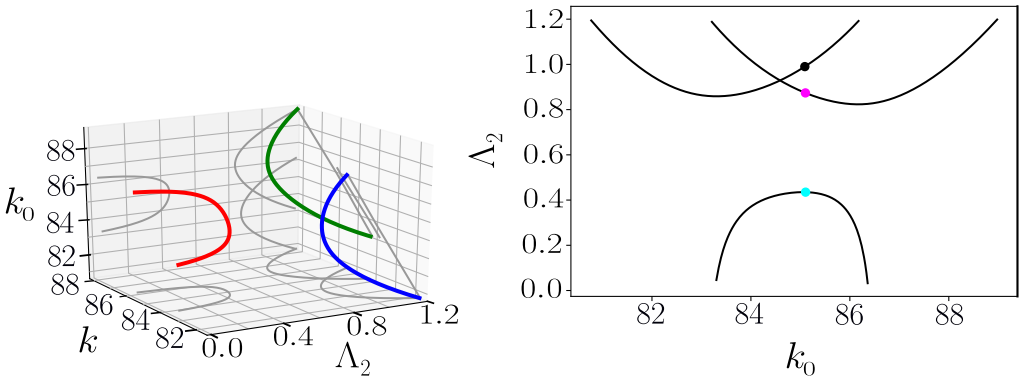



Figure 4.14: Plots where the points are using the conditions (4.47) and (4.48) showing first a three dimensional plot where the lines in green, blue and red is when the laser is at threshold for a given $k$, $k_0$ and $\Lambda_2$. In the background shows the view on each plane. The second plot shows the $k_0, \Lambda_2$ plane where the points are discussed.

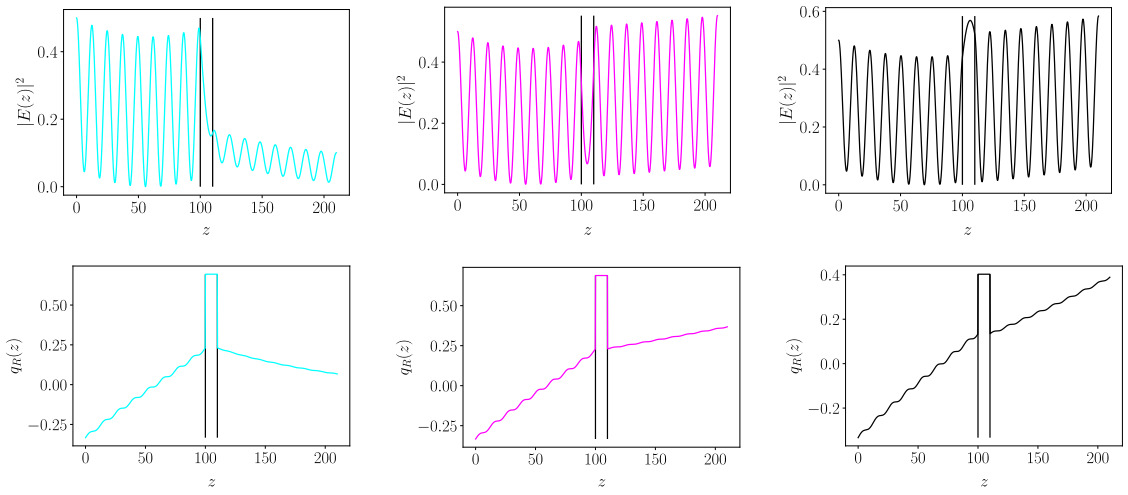



Figure 4.15: Intensity and power flow profile plots of coupled system where $\Lambda_2 = 0.43, k = 85.1$ (cyan) and $\Lambda_2 = .87, k = 85.3$ (magenta) and $\Lambda_2 = .99, k = 84.6$ (black). At these points, $\Lambda_1 = 1.2$ and $k_0 = 0.85$.

condition given in (4.48). Given a certain $\omega_0$ and $\gamma_P$, we can find suitable modes at $\omega$ with pump $\Lambda_2$ given $\Lambda_1 = 1.2$. Figure 4.14 shows the solutions using both conditions. We will deal with $k_0$ instead of $\omega_0$ such that $k_0 = \frac{\omega_0}{c}$. In previous work [20], the threshold was shown for when a single mode reaches it at a certain pump. However, increasing pump further results in another mode entering above threshold. But, both modes have different $k_0$, meaning the physical characteristics are not the same.

Instead of focusing on the $(k, \Lambda_2)$ plane, we will instead look at $(k_0, \Lambda_2)$. EPs exist still for constant $k_0$, in regions where suppression of laser output occurs and we can see what happens with increasing pump to the intensity and power flow. The only difference is that at constant $k_0$, we see that the frequencies change each time threshold is passed, as shown in Figure 4.15. The intensity at low $\Lambda_2$ (cyan) ($k = 85.1\text{mm}^{-1}$) is highest in the first laser with higher pump. However the power flow in the first laser is in both directions, and not just outgoing. In magenta ($k = 85.3\text{mm}^{-1}$), the plots show that intensity in the second laser is higher even with lower pump. This is most likely due to the result of the power flow in the first laser being in both directions and the second is only outgoing. The same description is true for the plots in black ($k = 84.6\text{mm}^{-1}$).

## 4.5 Unequal Pumping and the $q$-Basis

So far we have discussed SALT using the $q$-basis and the existence of EPs for different cavity structures and with absorption. We derived, with the $q$-basis, equations (4.28)-(4.31) are obtained assuming the modes are close to threshold. Clearly, with the $\Lambda_1$ and $\Lambda_2$ values used in the previous sections, some modes were considerably above or below threshold. One might think this makes these modes not worthy of being studied. However, this is not the case. If we change the pumps but keep the proportion between them the same, the gain susceptibility remains the same. As a result, electric field and $q$-basis spatial variations remain constant as long as the proportion between the pumps is constant. This is a result of the fact that changing the pumps this way, inversely changes the eigenvalues of $x_n$. Thus let $\eta$ be the proportional difference between both pumps such that,

$$\Lambda_2 = \eta\Lambda_1 \tag{4.83}$$

With this we can explore what the electric field and the $q$-basis look like and explain what happens to each mode around an EP with different scaling of each pump.

### 4.5.1 Power Outflow and Exceptional Points

As mentioned previously, $q_R(z)$ represents up to a constant the power flow (or Poynting's vector) inside the cavities. We will investigate the two closest modes with the same wavenumbers $k$, albeit different $k_0$. These modes we consider will reach threshold for sets of pump values $\Lambda_1$ and $\Lambda_2$. This is where $\eta$ becomes useful. For each of the modes studied, we will consider how the power flow at the boundaries at threshold changes for a given $\eta$. We can see in the previous sections, the two modes which satisfy (4.47) first, at low $\Lambda_2$ and increasing it will have power flowing into the second cavity which, for the closest mode result in $\mathrm{Im}(x_n)$ become more negative and reduces below threshold but then increases when the $\mathrm{Im}(x_n)$ becomes equal. For the second, increasing the pump will increase $\mathrm{Im}(x_n)$ and the power flow into the second cavity from the first will decrease with increasing pump. In the case of the pumps in both cavities equalling, this results zero power flow in the gap while the flow in both cavities is purely outgoing.

Let us focus on the boundaries and the power flow. Let $q_R^{(1)}(0)$ and $q_R^{(2)}(L)$ be that power flow at the left and right boundaries respectively, with the design of the coupled cavities the same as previous sections. We will look at the outflow proportion on each side i.e. $\frac{q_R^{(2)}(L)}{q_R^{(1)}(0)}$. Typically, one would expect the power flow to be greater at the edge of the first cavity when its pump is higher. However, close to an EP, the opposite occurs. That is, around an EP, $q_R^{(2)}(L) > q_R^{(1)}(0)$. However, away from the EP, $q_R^{(2)}(L) < q_R^{(1)}(0)$ as expected with increasing $\eta$.

Specifically talking about the first mode in Figure 4.16, $q_R^{(2)}(L) < q_R^{(1)}(0)$ for low $\eta$ while close to the EP, $q_R^{(2)}(L) > q_R^{(1)}(0)$ (red and green) while far away, we still have the case that $q_R^{(2)}(L) < q_R^{(1)}(0)$. Finally when both cavities have equal pumping, we see the case that the power flow at the boundaries are equal for all three wavenumbers. However the second mode is quite interesting. From very low $\eta$, the power flow at the right boundary is far greater than the left. With increasing $\eta$, $q_R^{(2)}(L)$ gets closer to $q_R^{(1)}(0)$ but at the EP, the modes coalesce, result in a sharp point seen in the first mode. Then both modes deviate again and become equal when the pumps are equivalent. For the second mode, away from the EP will always have $q_R^{(2)}(L) > q_R^{(1)}(0)$ until $\eta = 1$.

Consider what occurs to the power flow at the boundaries at various $k$ values shown in Figure 4.17. At the EP $k = 74.2\mathrm{mm}^{-1}$, we can see the sharp point when to modes coalesce. With varying $k$, the maximum instead of sharp becomes smooth as both modes do not meet. The maximum also decreases and moves to the right with increasing $\eta$ until far away from the EP, when the maximum occurs when the

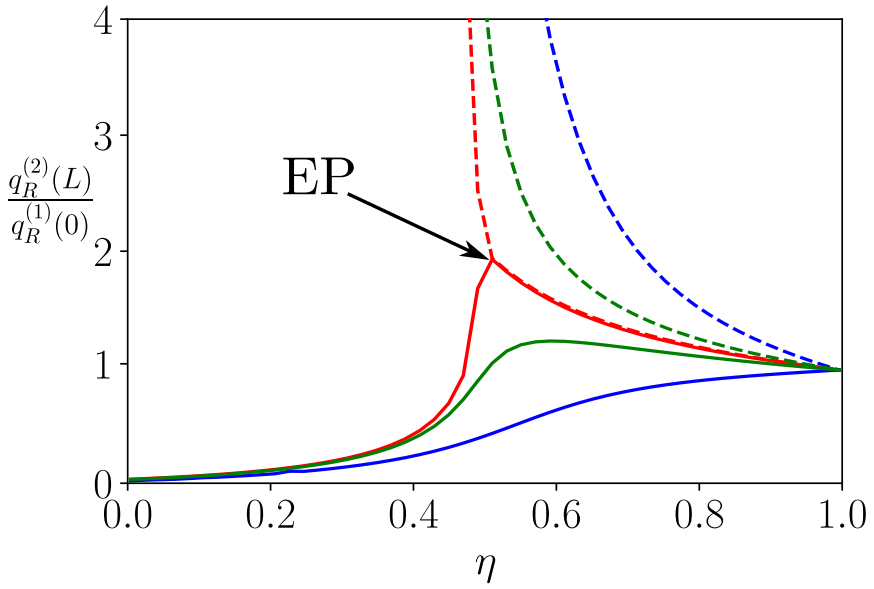



Figure 4.16: The scaling parameter is $\eta$ with varying wavenumber $k$ with $k = 84.6\text{mm}^{-1}$, $k = 86.6\text{mm}^{-1}$ and $k = 87.6\text{mm}^{-1}$ in red, green and blue respectively. The full line is the first mode while the dashed line is the second.

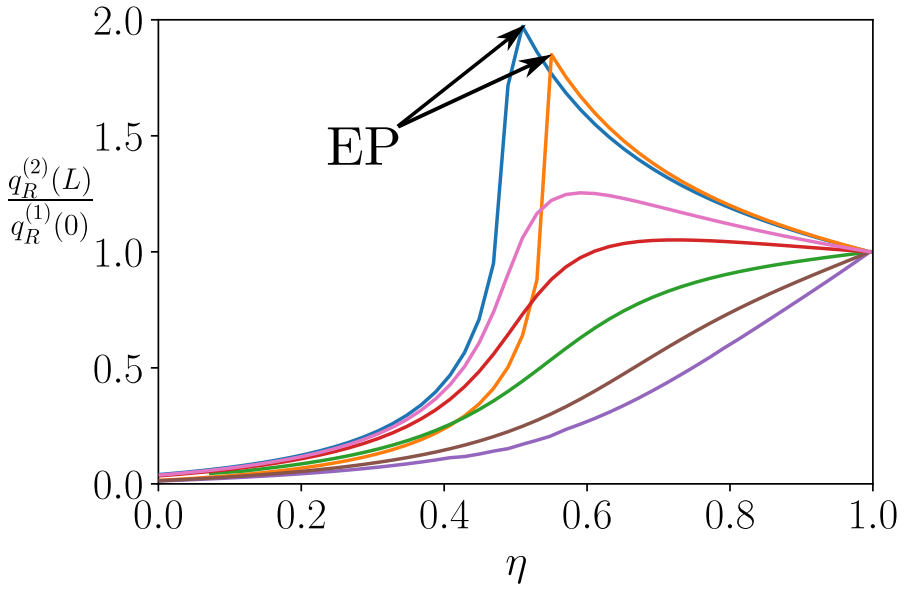



Figure 4.17: Power flow at the boundaries at varying $k$ for the first mode at (in $\text{mm}^{-1}$) $k = 74.2$ (blue,EP), $k = 75.2$ (pink), 76.2 (red), 77.2 (green), 79.2 (purple), 81 (brown) and 84.6 (orange,EP).

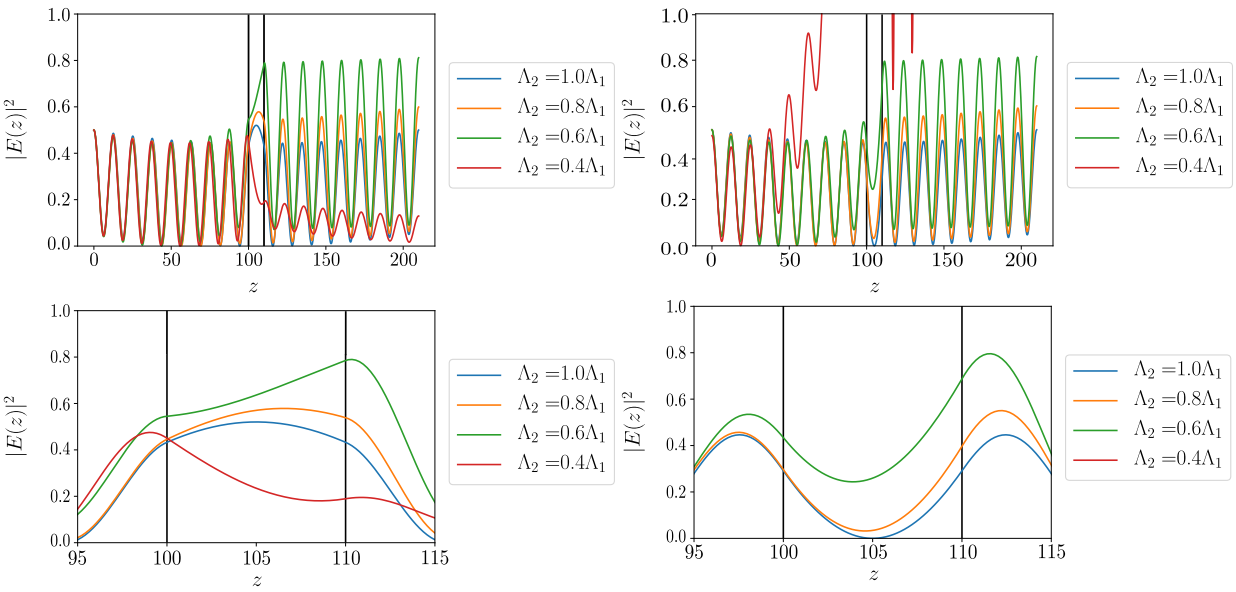



Figure 4.18: Both modes with the same $k = 84.5968367347\text{mm}^{-1}$ as an EP with varying $\eta$. The top left is the intensity for the closest mode while the bottom left is a zoomed in picture of the gap. The top right is the intensity for the second closest mode while the bottom right is a zoomed in picture of the gap.

pumps are equal. This means the highest power flow to the right only occurs when it is equivalent to the left. However, closer to the second EP, this maximum increases once more until it reaches the sharp maximum as shown.

### 4.5.2 Changes in Refractive Index at an EP

Now we turn our attention to the real part of the eigenvalues $x_n(\omega)$. While the imaginary part is related to gain of the medium, the real part changes the refractive index. Recall that $\text{Re}(\chi_g(z,t))$ results in a changing of the refractive index and as a result, $\text{Re}(x_n)$ reflects this too. When both modes coalesce, such as in figure 4.5, we see that after the modes meet, one increases in $\text{Re}(x_n)$ while the other decreases. As a result, the amount of wavelengths for one mode decreases while for the other increases. From what is seen in Figure 4.18, the first mode decreases in the number of wavelengths after the EP as two peaks coalesce into one in the gap. For the second mode, the two modes peaks closest to the gap move away from it and a trough develops in the gap.

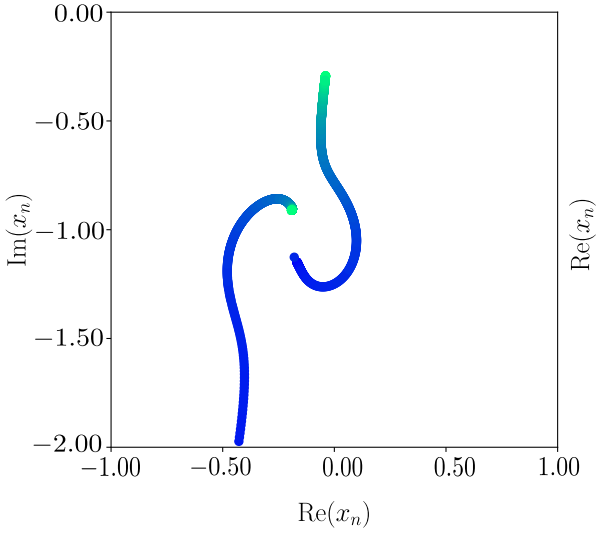
### 4.5.3 Eigenvalue Branches with varying $\eta$

In Chapter 3, we investigated the eigenvalues of coupled modes for weakly coupled oscillators. We have seen that by varying the detuning parameter, we got an idea of how the eigenvalues change. We seen three cases shown in Figures 3.2, 3.3 and 3.4 that, depending on various parameters, can result in the two eigenvalue branches meeting which results in an EP. While these results were obtained using a more basic description of coupled cavities, we can obtain similar effects using the $q$-basis for the two closest modes to threshold as we have used in previous sections. In Figures 4.19 and 4.20, we keep $k$ fixed and increase $\eta$ to determine how the two closest modes to threshold move. We will look at the first scenario seen in Figure 4.19. In Figure 4.19(a), starts just below $\mathrm{Im}(x_n) = -1$, and first gets more negative as the second mode comes from very negative $\mathrm{Im}(x_n)$. Then as the second mode continues to increase with in $\mathrm{Im}(x_n)$ and the first mode starts to increase towards zero. While this first mode moves towards zero, the second settles close to $\mathrm{Im}(x_n) = -1$. Looking at Figures 4.19(b) and (c), we see that for the $\eta$ we investigated, both modes never meet in terms of $\mathrm{Re}(x_n)$ but in fact meets for $\mathrm{Im}(x_n)$.Note that this is similar to Figures 3.2(b), 3.3(b) and 3.4(b).

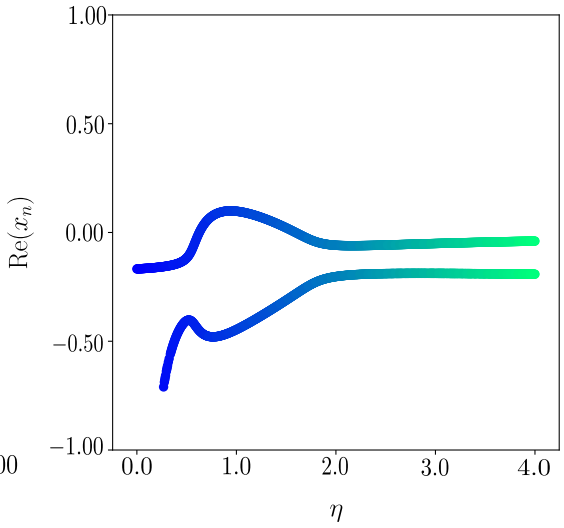
The more interesting scenario arises for in Figure 4.20. The only difference between Figures 4.20 and 4.19 is a different $k$. Looking at Figure 4.20(a), the one mode which we will call the first mode closest to threshold starts close to $\mathrm{Im}(x_n) = -1$. Then this mode decrease in $\mathrm{Im}(x_n)$ while the second closest mode from threshold increases in $\mathrm{Im}(x_n)$. Both coalesce to form an EP. This is confirmed by looking at Figures 4.20(b) and (c). After they both modes meet, we see one diverges to positive $\mathrm{Re}(x_n)$ and the other negative $\mathrm{Re}(x_n)$, both with increasing $\mathrm{Im}(x_n)$. Then both modes meet once again at higher $\mathrm{Im}(x_n)$ which is a second EP. Both modes thus diverge, one decreases in $\mathrm{Im}(x_n)$ while the other moves towards zero. This result is similar to Figures 3.2(c), 3.3(c) and 3.4(c).

## 4.6 Conclusions

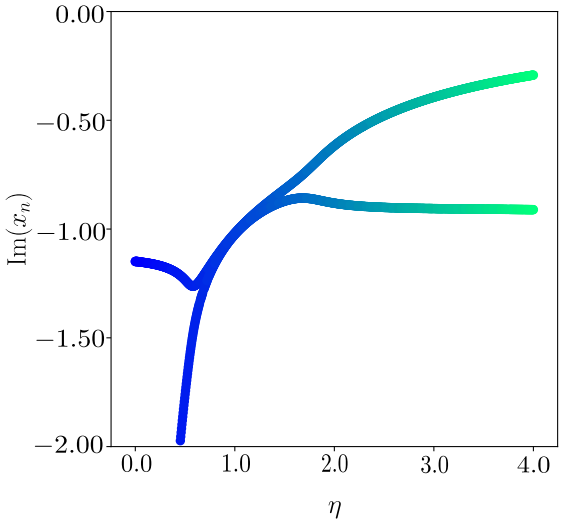
In this chapter, we have investigated in detail the EPs which occur due to unequal pumping in an open boundary, steady-state coupled-cavity laser using the $q$-basis. With the $q$-basis, we formulated spatial differential equations which include the complex geometrical nature of lasers with gain. With these equations, we were able to approximate modes above or below threshold by introducing the eigenvalue $x_n$.




(a) Real and imaginary parts of $x_n(\omega)$.

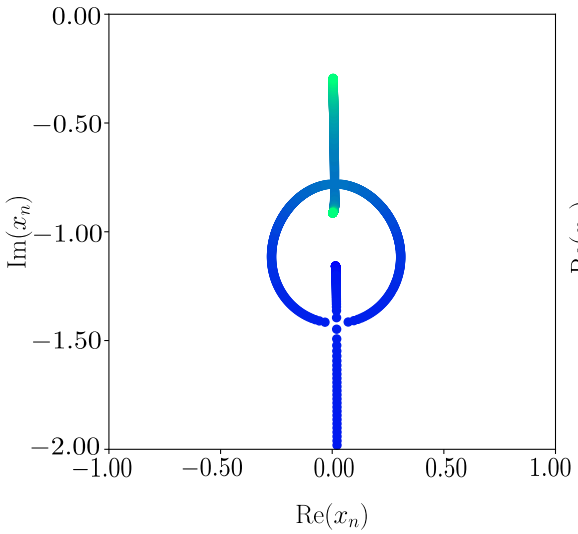



(b) Real part of $x_n(\omega)$ with varying $\eta$.

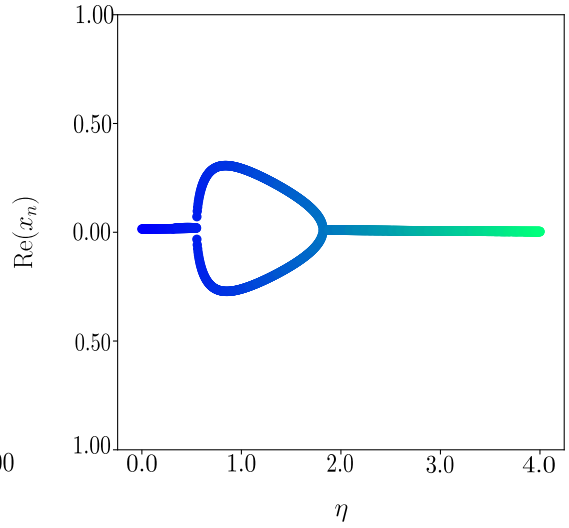



(c) Imaginary part of $x_n(\omega)$ with varying $\eta$.

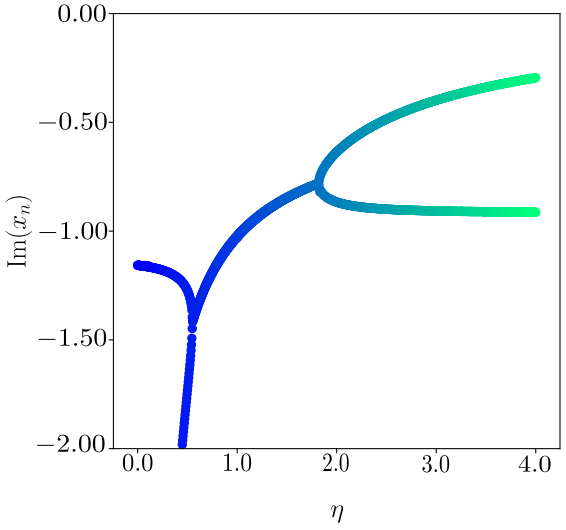
Figure 4.19: Two eigenvalue branches for varying $\eta$ for $k = 85.5\text{mm}^{-1}$ and in this case $\Lambda_1 = 1$




(a) Real and imaginary parts of $x_n(\omega)$.




(b) Real part of $x_n(\omega)$ with varying $\eta$.




(c) Imaginary part of $x_n(\omega)$ with varying $\eta$.

Figure 4.20: Two eigenvalue branches for varying $\eta$ for $k = 84.5968367347\text{mm}^{-1}$ and in this case $\Lambda_1 = 1$

Moreover, EPs are shown in various cases using the $q$-basis and also exist for different gap lengths. In particular, we have seen that even if there is no gap between two cavities, there is still the possibility for EPs to exist for some frequencies. One of the key elements of this chapter has been the physical description of how with unequal pumping, a lasing mode can go below threshold with increasing pump. We concluded that this is due to the power of one cavity transferring into the other to compensate the other cavity's low pump. We have related the determined modes using the $q$-basis to physical characteristics such as $\omega_0$ and $\gamma_P$. We have also seen the effects on the power output of coupled-cavities around an EP and how increasing pump changes the amount of wavelengths permissible inside the cavity. Finally, we have shown that we can obtain a similar profiles for varying two eigenvalues by a single parameter as we have done in Chapter 3.

# Chapter 5

# The $\mathcal{Z}$-Basis and Threshold EPs for Open Coupled Cavities

In this chapter, we will introduce another basis which we will title the $\mathcal{Z}$-basis. This basis provides a simple way to express the electic field equation as a first order complex differential equation which makes calculations far easier, with even less information required. As a result, we can present more complicated features in steady-state coupled-cavities using the $\mathcal{Z}$-basis. While the $q$-basis is extremely useful to describe physical ideas such as total energy and power flow, the equations are more complicated for what is required in this chapter, hence the introduction of the $\mathcal{Z}$-basis.

With the $\mathcal{Z}$-basis, we can solve the steady-state electric field equation analytically using the elegant approach of the Möbius transformation [93] which has been used in physics in such areas as in modelling electromagnetic waves using the finite difference time domain technique [94–96] and proves quite useful with Green's functions too [97]. These transformations can be adopted to understand interesting phenomenon that occurs in a coupled-cavity laser with open boundaries. We can show an interesting mathematical result which is that the $\mathcal{Z}$-basis can produce a loxodrome [93] which is spiral on a complex Riemann sphere that crosses all longitude lines at the same angle. This can be seen for both the Fabry-Perot cavity and the more complicated coupled-cavity laser. Loxodromes are also seen throughout physics such as relativity where they appear for different surfaces known as space-like and time-like loxodromes [98–100], in ray dynamics [101]and in domain wall fermions [102]. In particular, we see applications in optics and lasers such as a transfer matrix approach for an absorbing system [103] and polarisation dynamics in a semiconductor laser [104].

We apply this analytical approach of the Möbius transformation to both a simple Fabry-Perot laser and to more complex coupled-cavity lasers. We compare and con-

trast the analysis of both types of lasers to see how the threshold branches look and change depending on a number of parameters. We can even show that one cavity can have net gain while the other can have net absorption at threshold which depends heavily on the parameters used and also on EPs. Recall from the previous chapter, we investigated EPs with the use of threshold constant flux states and solving the eigenvalue problem given by (4.82). Moreover, these eigenvalues were a mathematical construct which is used to approximate the change in refractive index and the gain of the medium slightly away from threshold. However, in this chapter, we will introduce another type of EP, which we will call Threshold Exceptional Points (TEPs). The TEPs arise from the threshold constant flux states and are at threshold, which means for TEPs, we do not require the eigenvalues used in the previous chapter. As a result, these EPs use the semiclassical description of the laser medium at threshold which allows them to be more physically accurate. We will use the $\mathcal{Z}$-basis to show the existence of TEPs.

This chapter is structured as follows. In the first section, we will introduce the $\mathcal{Z}$-basis and connect it with the electric field equation while using a transfer matrix approach. From there, we will discuss the threshold constant flux states without the use of the eigenvalue approach of the previous chapter. This will lead to the TEPs which we will investigate in detail.

## 5.1 The $\mathcal{Z}$-basis

In this section we will introduce the $\mathcal{Z}$-basis which will allow us to write the steady-state electric field equation in terms of a first order differential equation, which is able to be solved analytically. Using the electric field composition in the SALT units, given by (4.3), we will write the electric field equation (4.38) with complex permittivity $\epsilon(z)$ as,

$$\left\{ \frac{d^2}{dz^2} + k^2\epsilon(z) \right\} E(z) = 0, \tag{5.1}$$

where $k = \frac{\omega}{c}$, the wavenumber is in terms of some frequency $\omega$. The complex permittivity includes both gain of the laser medium and changes to the refractive index which were both discussed in the previous chapter. Moreover it includes the steady-state term for the population inversion at threshold, and will satisfy the TCF states for a laser structure with open boundaries. However, for this section, when introducing the $\mathcal{Z}$-basis, we will keep it as general as possible. We now introduce the $\mathcal{Z}$-basis

which is made up of the complex term $\mathcal{Z}(z)$ which is a function on the Riemann Sphere in the complex space $\hat{\mathbb{C}} = \mathbb{C} \cup \{\infty\}$ which is defined as,

$$\mathcal{Z}(z) = \begin{cases} \frac{E'(z)}{kE(z)} & \text{for} \quad E(z) \neq 0, \\ \infty & \text{else.} \end{cases} \tag{5.2}$$

Moreover, we can obtain a differential equation for $\mathcal{Z}(z)$ independent of the electric field too which is given by,

$$\frac{d\mathcal{Z}(z)}{dz} = -k(\mathcal{Z}(z)^2 + \epsilon(z)). \tag{5.3}$$

We can turn our attention to the boundary conditions that will be used throughout this chapter. Like in Chapter 4, we will use the idea of constant flux states where at the boundary of the laser, we only have outgoing waves at each end like the conditions seen in (4.70) and (4.71) where $n_a = 1$. Using (4.13) with these boundary conditions, we can write these constant flux conditions in terms of $\mathcal{Z}(z)$ as,

$$\mathcal{Z}(0) = -i, \tag{5.4}$$

$$\mathcal{Z}(L) = i. \tag{5.5}$$

### 5.1.1 Permittivity of a Laser Medium

Now we will turn our attention to the electric field inside some laser structure to help us understand the permittivity of a laser medium that we will use throughout this chapter. As with the $q$-basis, we will consider each section of the laser separately. Let us write $\epsilon_c$ as the permittivity of some laser section. We write the electric field solution to (5.1) for $\epsilon(z) = \epsilon_c$ as,

$$E(z) = E_+ e^{ikz\mathrm{Re}(\sqrt{\epsilon_c})} e^{-kz\mathrm{Im}(\sqrt{\epsilon_c})} + E_- e^{-ikz\mathrm{Re}(\sqrt{\epsilon_c})} e^{kz\mathrm{Im}(\sqrt{\epsilon_c})}, \tag{5.6}$$

which is a valid solution to the wave equation given by (5.1) for an individual section with $E_+$ and $E_-$ being the right and left moving electric field constants respectively. In this case, we will take $\sqrt{\epsilon_c}$ as one of the two square roots of $\epsilon_c$. To be more specific, let us take the branch cut such that $\mathrm{Re}(\sqrt{\epsilon_c}) > 0$ for all values of $\epsilon_c$ which are not on the negative real axis and $\mathrm{Im}(\sqrt{\epsilon_c}) > 0$ for $\epsilon_c$ on the negative real axis. We can therefore identify the first (second) term in (5.6) with the right (left) moving component as before. On the other hand, the factor $e^{-kz\mathrm{Im}(\sqrt{\epsilon_c})}$ in the right moving

term means that for $\mathrm{Im}(\sqrt{\epsilon_c}) > 0$ the right moving term exponentially decays as we move to larger $z$. Physically this is associated with the effect of absorption of the right moving component. Similarly the left moving component also decays with decreasing $z$. On the other hand, the branch cut ensures that if $\mathrm{Im}(\sqrt{\epsilon_c}) > 0$, then $\mathrm{Im}(\epsilon_c) > 0$. As a result we see that for $\mathrm{Im}(\epsilon_c) > 0$, it represents absorption but for $\mathrm{Im}(\epsilon_c) < 0$, it represents gain.

### 5.1.2 $\mathcal{Z}$-Basis Spatial Fixed Points

We now obtain fixed points in a similar way to dynamical systems except these will be fixed points in space. To see this in action, consider a single permittivity $\epsilon_c$ once again. Then the fixed points are as follows,

$$\mathcal{Z}_1^F = -i\sqrt{\epsilon_c}, \tag{5.7}$$

$$\mathcal{Z}_2^F = i\sqrt{\epsilon_c}, \tag{5.8}$$

where $\mathcal{Z}_1^F$ and $\mathcal{Z}_2^F$ are the two fixed points. By our chosen convention that $\mathrm{Re}(\sqrt{\epsilon_c}) > 0$, we see that $\mathrm{Im}(\mathcal{Z}_1^F) < 0$ and $\mathrm{Im}(\mathcal{Z}_2^F) > 0$. Moreover if the imaginary part of the permittivity is negative, which is gain, then the $\mathrm{Re}(\mathcal{Z}_1^F) > 0$ while $\mathrm{Re}(\mathcal{Z}_2^F) < 0$. The stability of these fixed points is obtained from the complex Jacobian $J(\mathcal{Z})$ which is given by,

$$J(\mathcal{Z}) = -2k\mathcal{Z}(z). \tag{5.9}$$

Taking the first fixed point $\mathcal{Z}_1^F$, we see that $\mathrm{Re}(J(\mathcal{Z}_1^F)) = -2k\mathrm{Im}(\sqrt{\epsilon_c}) > 0$ which also means $\mathrm{Im}(\epsilon_c) < 0$. With this in mind, $\mathcal{Z}_1^F$ is an unstable fixed point. From this, we can also deduce that $\mathcal{Z}_2^F$ is an stable fixed point.

## 5.2 Analytical Solution and the $\mathcal{Z}$-basis

We can actually solve (5.3) analytically for constant permittivity $\epsilon_c$. With this, we will consider at an initial position $z_0$, $\mathcal{Z}(z_0) = \mathcal{Z}_0$. We will now change our co-ordinate system and introduce the variable $\mathcal{Y}(z)$, and this will allow us to solve for $\mathcal{Z}(z)$. $\mathcal{Y}(z)$ is written as,

$$\mathcal{Y}(z) = \frac{\mathcal{Z}(z) - \mathcal{Z}_1^F}{\mathcal{Z}(z) - \mathcal{Z}_2^F} = \frac{\mathcal{Z}(z) + i\sqrt{\epsilon_c}}{\mathcal{Z}(z) - i\sqrt{\epsilon_c}}. \tag{5.10}$$

With this composition, we obtain the following differential equation,

$$\frac{d\mathcal{Y}(z)}{dz} = \frac{-2i\sqrt{\epsilon_c}}{(\mathcal{Z}(z) - i\sqrt{\epsilon_c})^2}\frac{d\mathcal{Z}(z)}{dz} \tag{5.11}$$

This can be written without $\mathcal{Z}(z)$ if we use (5.3) and the fact that both $\mathcal{Z}(z) - i\sqrt{\epsilon_c} = i\sqrt{\epsilon_c}\frac{2}{\mathcal{Y}(z)-1}$ and $\mathcal{Z}(z)^2 + \epsilon_c = -\epsilon_c\frac{4\mathcal{Y}(z)}{(\mathcal{Y}(z)-1)^2}$, we get,

$$\frac{d\mathcal{Y}(z)}{dz} = 2ik\sqrt{\epsilon_c}\mathcal{Y}(z). \tag{5.12}$$

Thus we can obtain the explicit solution,

$$\mathcal{Y}(z) = \mathcal{Y}(z_0)e^{2ik\sqrt{\epsilon_c}(z-z_0)}. \tag{5.13}$$

By looking at the composition of $\mathcal{Y}(z)$, we see that this is a logarithmic spiral as $\sqrt{\epsilon_c}$ is a complex quantity. Turning our attention to $\mathcal{Z}(z)$ and without loss of generality, let $z_0 = 0$, where $\mathcal{Z}(0) = \mathcal{Z}_0$. With this, $\mathcal{Z}(z)$ is written as,

$$\mathcal{Z}(z) = i\sqrt{\epsilon_c}\frac{\mathcal{Y}(z)+1}{\mathcal{Y}(z)-1}, \tag{5.14}$$

$$= \sqrt{\epsilon_c}\frac{\mathcal{Z}_0\cos(k\sqrt{\epsilon_c}z) - \sqrt{\epsilon_c}\sin(k\sqrt{\epsilon_c}z)}{\mathcal{Z}_0\sin(k\sqrt{\epsilon_c}z) + \sqrt{\epsilon_c}\cos(k\sqrt{\epsilon_c}z)}, \tag{5.15}$$

$$= \sqrt{\epsilon_c}\frac{\mathcal{Z}_0 - \sqrt{\epsilon_c}\tan(k\sqrt{\epsilon_c}z)}{\mathcal{Z}_0\tan(k\sqrt{\epsilon_c}z) + \sqrt{\epsilon_c}}. \tag{5.16}$$

Thus $\mathcal{Z}(z)$ is a loxodrome as a Möbius transformation of a loxodrome is also a loxodrome [93]. Thus we have solved analytically an equation which represents a laser section with constant permittivity. Furthermore, for more than one section, we can still solve it analytically but we will do so in an elegant way by making use of Möbius transformations.

### 5.2.1 Möbius Transformation

The mathematics in the above derivation is quite arduaous and with multiple sections, can be quite cumbersome. This is why we will introduce the Möbius transformations and will result in a more elegant solution. We will use different notation to the standard formalism. Let $a_{11}, a_{12}, a_{21}$ and $a_{22}$ be complex constants. Then as long as

$a_{11}a_{22} - a_{12}a_{21} \neq 0$, the transformation is given by [93],

$$\begin{bmatrix} a_{11} & a_{12} \\ a_{21} & a_{22} \end{bmatrix} z_c = \frac{a_{11}z_c + a_{12}}{a_{21}z_c + a_{22}} \tag{5.17}$$

for some complex-valued $z_c$ where the right hand side of this equation is the standard formalism and the left hand side is the notation we will use to represent this. Although this is not a matrix, it has some characteristics of matrices.

With two Möbius transformations, we have a similar property to matrix multiplication. Introducing $b_{11}, b_{12}, b_{21}$ and $b_{22}$ as complex constants where $b_{11}b_{22} - b_{12}b_{21} \neq 0$, then,

$$\begin{bmatrix} b_{11} & b_{12} \\ b_{21} & b_{22} \end{bmatrix} \begin{bmatrix} a_{11} & a_{12} \\ a_{21} & a_{22} \end{bmatrix} z = \begin{bmatrix} b_{11} & b_{12} \\ b_{21} & b_{22} \end{bmatrix} \frac{a_{11}z_c + a_{12}}{a_{21}z_c + a_{22}}, \tag{5.18}$$

$$= \frac{b_{11}\frac{a_{11}z_c + a_{12}}{a_{21}z_c + a_{22}} + b_{12}}{b_{21}\frac{a_{11}z_c + a_{12}}{a_{21}z_c + a_{22}} + b_{22}}, \tag{5.19}$$

$$= \frac{(b_{11}a_{11} + b_{21}a_{21})z_c + b_{11}a_{12} + b_{21}a_{22}}{(b_{21}a_{11} + b_{22}a_{21})z_c + b_{21}a_{12} + b_{22}a_{22}}, \tag{5.20}$$

$$= \begin{bmatrix} b_{11}a_{11} + b_{12}a_{21} & b_{11}a_{12} + b_{12}a_{22} \\ b_{21}a_{11} + b_{22}a_{21} & b_{21}a_{12} + b_{22}a_{22} \end{bmatrix} z, \tag{5.21}$$

$$= \left[ \begin{pmatrix} b_{11} & b_{12} \\ b_{21} & b_{22} \end{pmatrix} \quad \begin{pmatrix} a_{11} & a_{12} \\ a_{21} & a_{22} \end{pmatrix} \right] z_c. \tag{5.22}$$

Thus applying a transformation to another transformation behaves in a similar way to matrix multiplication as shown. Moreover, a transformation has the following properties,

$$\begin{bmatrix} a_{11} & 0 \\ 0 & a_{22} \end{bmatrix} z_c = \frac{a_{11}}{a_{22}} z_c, \tag{5.23}$$

$$\begin{bmatrix} a_{11} & a_{12} \\ a_{21} & a_{22} \end{bmatrix}^{-1} = \begin{bmatrix} a_{22} & -a_{12} \\ -a_{21} & a_{11} \end{bmatrix}, \tag{5.24}$$

and for some complex constant $p$,

$$\begin{bmatrix} a_{11} & a_{12} \\ a_{21} & a_{22} \end{bmatrix} = \begin{bmatrix} pa_{11} & pa_{12} \\ pa_{21} & pa_{22} \end{bmatrix}, \tag{5.25}$$

$$p\begin{bmatrix} a_{11} & a_{12} \\ a_{21} & a_{22} \end{bmatrix} = \begin{bmatrix} pa_{11} & pa_{12} \\ a_{21} & a_{22} \end{bmatrix} = \begin{bmatrix} a_{11} & a_{12} \\ \frac{a_{21}}{p} & \frac{a_{22}}{p} \end{bmatrix}, \tag{5.26}$$

$$\begin{bmatrix} a_{11} & a_{12} \\ a_{21} & a_{22} \end{bmatrix} p = \begin{bmatrix} pa_{11} & a_{12} \\ pa_{21} & a_{22} \end{bmatrix} = \begin{bmatrix} a_{11} & \frac{a_{12}}{p} \\ a_{21} & \frac{a_{22}}{p} \end{bmatrix}. \tag{5.27}$$

Finally the derivative over $z$ of the Möbius transformation is given as follows,

$$\frac{d}{dz}\left\{\begin{bmatrix} a_{11} & a_{12} \\ a_{21} & a_{22} \end{bmatrix} z_c\right\} = \frac{a_{11}a_{22} - a_{12}a_{21}}{(a_{21}z_c + a_{22})^2}. \tag{5.28}$$

### 5.2.2 Solving $\mathcal{Z}(z)$ using the Möbius Transformation

Previously, we solved for $\mathcal{Z}(z)$ which will prove not as elegant of a solution in comparison to the use of our notation for the Möbius transformation. Firstly, we can use this transformation to write the equality between $\mathcal{Y}(z)$ and $\mathcal{Z}(z)$, given by (5.10), which can be written as,

$$\mathcal{Y}(z) = \begin{bmatrix} 1 & i\sqrt{\epsilon_c} \\ 1 & -i\sqrt{\epsilon_c} \end{bmatrix} \mathcal{Z}(z). \tag{5.29}$$

Moreover (5.13) can be written in terms of this transformation too by taking note of its properties (with $z_0 = 0$),

$$\mathcal{Y}(z) = \begin{bmatrix} e^{2ik\sqrt{\epsilon_c}z} & 0 \\ 0 & 1 \end{bmatrix} \mathcal{Y}(0). \tag{5.30}$$

Thus we can write $\mathcal{Z}(z)$ in terms of $\mathcal{Z}_0$ by using (5.29) and (5.30) to obtain,

$$\mathcal{Z}(z) = \begin{bmatrix} 1 & i\sqrt{\epsilon_c} \\ 1 & -i\sqrt{\epsilon_c} \end{bmatrix}^{-1} \begin{bmatrix} e^{2ik\sqrt{\epsilon_c}z} & 0 \\ 0 & 1 \end{bmatrix} \begin{bmatrix} 1 & i\sqrt{\epsilon_c} \\ 1 & -i\sqrt{\epsilon_c} \end{bmatrix} \mathcal{Z}_0 \tag{5.31}$$

$$= \begin{bmatrix} \cos(k\sqrt{\epsilon_c}z) & -\sqrt{\epsilon_c}\sin(k\sqrt{\epsilon_c}z) \\ \frac{\sin(k\sqrt{\epsilon_c}z)}{\sqrt{\epsilon_c}} & \cos(k\sqrt{\epsilon_c}z) \end{bmatrix} \mathcal{Z}_0. \tag{5.32}$$

While this solution is valid for a single section, we can use it in a similar way to the transfer matrix approach for coupled cavities.

### 5.2.3 Electric field Intensity

We will now introduce a method where results from the $\mathcal{Z}$-basis can be seen in terms of the electric field intensity, $|E(z)|^2$. Firstly, the differential equation for $|E(z)|^2$ is given by,

$$\begin{aligned}\frac{d|E(z)|^2}{dz} &= \frac{|E(z)|^2}{E(z)}\frac{dE(z)}{dz} + \frac{|E(z)|^2}{E(z)^*}\frac{dE(z)^*}{dz} \\ &= 2k|E(z)|^2\mathrm{Re}(\mathcal{Z}(z)),\end{aligned} \tag{5.33}$$

where we have used the composition of $\mathcal{Z}(z)$ in terms of $E(z)$ and its derivative. Thus, if we let the initial position for the electric field intensity to be $|E(0)|^2$,

$$|E(z)|^2 = |E(0)|^2 \exp\left(2k\int_0^z \mathrm{Re}(\mathcal{Z}(z'))dz'\right). \tag{5.34}$$

With this connection, we can provide greater understanding of the $\mathcal{Z}$-basis for Fabry-Perot cavities and also more complicated structures, all with open boundaries.

### 5.2.4 Power Flow with the $\mathcal{Z}$-basis

Another physical quantity we can relate the $\mathcal{Z}$-basis to is the power flow. The same equivalence was carried out in the previous chapter by matching the time averaged complex Poynting vector, $S(z)$ to the real quantities $q_R(z)$ and $q_I(z)$. Recall the definition of $S(z)$ given by (4.18), we can write this in terms of the electric field and its derivative by using (4.14). As a result we have the following equation,

$$S(z) = \frac{i}{2\mu_0\omega}E(z)E'(z)^*. \tag{5.35}$$

Comparing this with the composition of $\mathcal{Z}(z)$, we obtain the following relation,

$$S(z) = \frac{i}{2\mu_0 c}|E(z)|^2\mathcal{Z}(z)^* \tag{5.36}$$

The power flow is the real part of this quantity which is similar to the quantity which in the previous chapter we called $q_R(z)$. We thus introduce a new variable $\mathcal{Z}_P(z)$ which represents up to a constant the power flow and is related to $S(z)$ by,

$$\mathrm{Re}(S(z)) = \frac{1}{2\mu_0 c}\mathcal{Z}_P(z), \tag{5.37}$$

where $\mathcal{Z}_P(z)$ is given by,

$$\mathcal{Z}_P(z) = |E(z)|^2 \mathrm{Im}(\mathcal{Z}(z)). \tag{5.38}$$

Now we can use this quantity, along with $\mathcal{Z}(z)$ to investigate modes at threshold for a simple Fabry-Perot and coupled-cavity lasers.

## 5.3 Fabry-Perot with the $\mathcal{Z}$-Basis

Before we investigate more complicated structures, first we will use the $\mathcal{Z}$-basis to study the well known Fabry-Perot cavity. We will discuss the threshold branches using the threshold condition obtained with the Möbius transformation and the $\mathcal{Z}$-basis. Moreover, we will show that varying $\mathcal{Z}(z)$ will be a loxodrome on the complex Riemann sphere. We will also confirm that the cavity must have net gain to be at threshold, which is not always true for a cavity in the coupled-cavity system.

### 5.3.1 Threshold Condition for Fabry-Perot

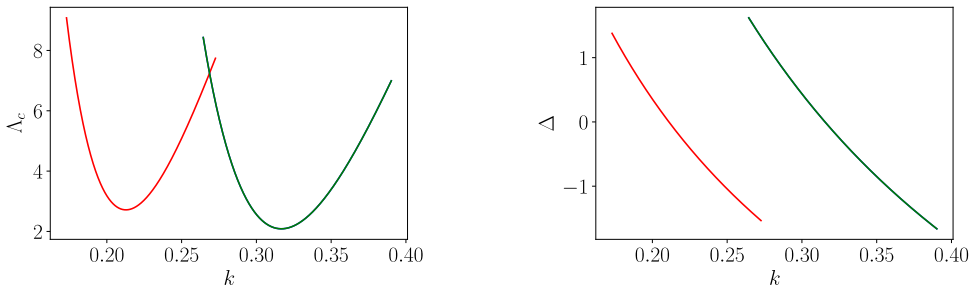
With this $\mathcal{Z}$-basis, we can obtain a good model for the Fabry-Perot cavity with open boundaries. Consider a simple single cavity structure of length $L$ from $z = 0$ to $z = L$ where we can use the boundary conditions given by (5.4) and (5.5). With constant permittivity $\epsilon_c$, along with the boundary conditions, we can write (5.32) as,

$$i = \begin{bmatrix} \cos(k\sqrt{\epsilon_c}L) & -\sqrt{\epsilon_c}\sin(k\sqrt{\epsilon_c}L) \\ \frac{\sin(k\sqrt{\epsilon_c}L)}{\sqrt{\epsilon_c}} & \cos(k\sqrt{\epsilon_c}L) \end{bmatrix} (-i). \tag{5.39}$$

In particular, we would like to analyse the situation for laser modes at threshold. We can thus use (5.39) along with the fact that $\mathcal{Z}(z)$ satisfies the threshold constant flux condition (4.47). Like the previous chapter in (4.40) and in Chapter 2 with (2.78), where close to threshold we can remove terms with spatial hole burning, we can write $\epsilon_c$ as,

$$\epsilon_c = \tilde{n}_b^2 - i\mathscr{L}(\Delta)(\Delta + i)\Lambda_c \tag{5.40}$$

where $\Lambda_c$ is the pump of the cavity and $\Delta$ is the frequency detuning factor. We will describe $\Delta > 0$ as positive detuning and $\Delta < 0$ as negative detuning. Before we treated $\epsilon_c$ as a complex quantity, we have thus related it to the complex background




(a) $\Lambda_c, k$ plane

(b) $\Delta, k$ plane

Figure 5.1: Two threshold branches for a range of $k$ from $k = 0.15$ to $k = 0.40$ shown in red and green for $L = 10$.

refractive index $\tilde{n}_b$ including absorption and the remaining terms form the gain in the medium.

With all of this, we can investigate the threshold branches for a single cavity laser. Consider Figure 5.1 for a simple Fabry-Perot cavity of length 10. We can see two distinct branches shown in green and red which do not meet which can be seen in the $\Delta, k$ plane. In 5.1(a), we see both branches decrease and increase once again, although the green threshold branch decreases even further than the red. In fact in 5.1(b), we see the same behaviour in both branches as they both go from positive detuning to negative detuning with increasing $k$. An important point to note also is that for a Fabry-Perot, there is no phenomenon where with increasing pump, you can go above or below threshold and this is shown here.

### 5.3.2 Loxodrome and the Fabry-Perot

We are now going to show that the $\mathcal{Z}$-basis produces a loxodrome when we vary position for a Fabry-Perot type laser with open boundaries. Noting the condition for a single cavity (5.39) along with the permittivity given by (5.40), we can see a loxodrome when looking at $\mathcal{Z}(z)$ from $z = 0$ to $z = L$.

Consider Figure 5.2, which corresponds to a value on the red threshold branch in Figure 5.1, where we see a loxodrome with boundary conditions $\mathcal{Z}(0) = -i$ and $\mathcal{Z}(L) = i$. Notice that ,with increasing $z$ starting at $\mathcal{Z}(0) = -i$ in the complex plane, that $\mathcal{Z}(z)$ orbits around the unstable fixed point. Then it is attracted by the second stable fixed point and as a result orbits around it before finishing at $\mathcal{Z}(L) = i$. We can actually obtain a condition that this orbit must satisfy mathematically. As $\mathcal{Z}(z)$ is a loxodrome and the boundary conditions are symmetric in terms of $\mathrm{Re}(\mathcal{Z}(z))$ axis,

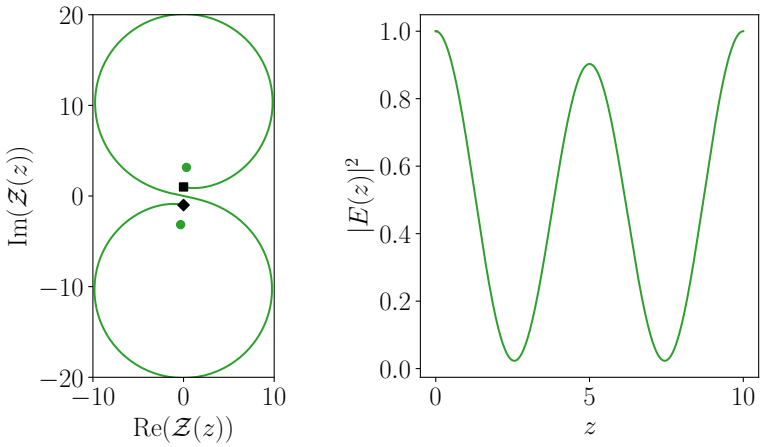



Figure 5.2: The left figure shows the variation of $\mathcal{Z}(z)$ from $z = 0$ to $z = L$ which shows a loxodrome. On the right is the corresponding electric field intensity. Parameters used are $k = 0.20124$, $\Lambda_c = 3.08992$, $\tilde{n}_b = 3 + 0.13i$, $\Delta = 0.313618$ and $L = 10$. The green dots are the fixed points. The black diamond and square are the boundary conditions.

then we have the case that $\mathcal{Z}(z)$ passes through the origin when $z = \frac{L}{2}$. To obtain this condition, we set $\mathcal{Z}_0 = \mathcal{Z}\left(\frac{L}{2}\right) = 0$, and thus choose the new origin to be at $\frac{L}{2}$. As a result we can obtain a condition for a single cavity open-boundaried laser which is easier than (5.39). Using (5.32),

$$i = -\sqrt{\epsilon_c}\tan\left(\frac{k\sqrt{\epsilon_c}L}{2}\right). \tag{5.41}$$

This condition is only valid for some modes where the electric field intensity is at a local maximum at $\frac{L}{2}$, as seen in Figure 5.2. However, there is a second situation where at the centre, $\frac{L}{2}$, there is the case that we have $|E(z)|^2 = 0$, which would be the absolute minimum. In this instance, we see that $\mathcal{Z}\left(\frac{L}{2}\right) = \infty$. In fact we can get a similar condition for these modes too. Letting $\mathcal{Z}_0 = \mathcal{Z}\left(\frac{L}{2}\right)$ with the new choice of origin to be $\frac{L}{2}$ as we have done for the other condition. As a result we can use (5.32) to obtain at $\mathcal{Z}(L)$,

$$i = \frac{\sqrt{\epsilon_c}}{\tan\left(\frac{k\sqrt{\epsilon_c}L}{2}\right)}. \tag{5.42}$$

As we can see in Figure 5.3, which corresponds to the green branch in Figure 5.1, we have a second scenario as $z$ increases from $z = 0$ to $z = L$ in this Fabry-

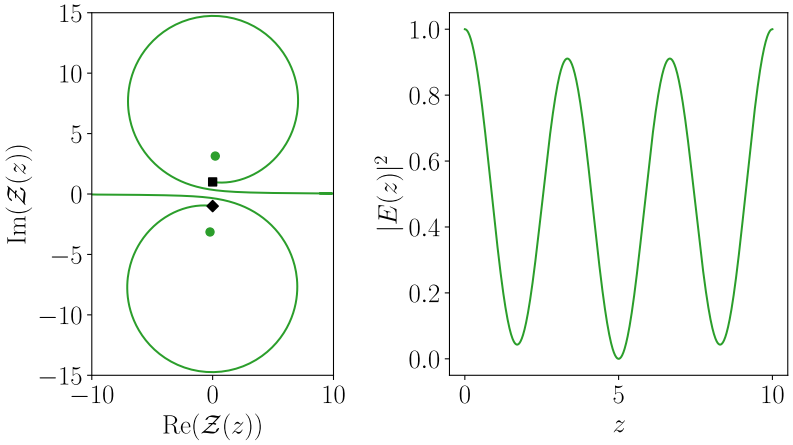
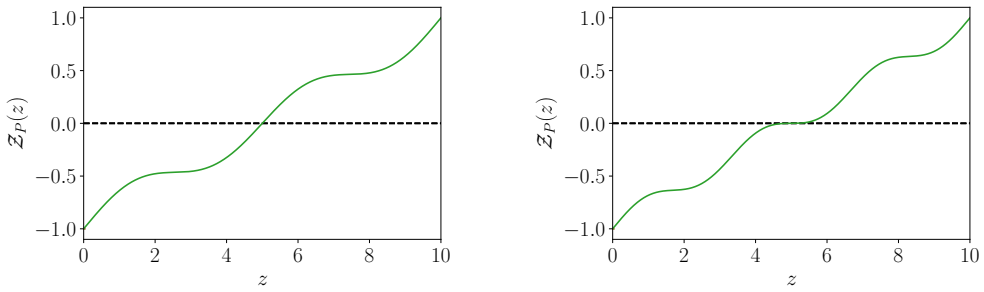



Figure 5.3: The left figure shows the variation of $\mathcal{Z}(z)$ from $z = 0$ to $z = L$. On the right is the corresponding electric field intensity. Parameters used are $k = 0.32339$, $\Lambda_c = 2.1513$, $\tilde{n}_b = 3 + 0.13i$, $\Delta = -0.21077$ and $L = 10$. The green dots are the fixed points. The black diamond and square are the boundary conditions.




(a) $\mathcal{Z}_P(z)$corresponding to Figure 5.2 (b) $\mathcal{Z}_P(z)$corresponding to Figure 5.3

Figure 5.4: Power flow represented by $\mathcal{Z}_P(z)$ for Fabry-Perot.

Perot type cavity. Given the initial condition is $\mathcal{Z}(0) = -i$, $\mathcal{Z}(z)$ orbits around the unstable fixed point and then goes towards minus infinity in the real of $\mathcal{Z}(z)$. It thus comes from infinity in the $\mathrm{Re}(\mathcal{Z}(z))$ and orbits around the attractive fixed point until it reaches the boundary condition $\mathcal{Z}(L) = i$. This behaviour corresponds to the absolute minimum at $\frac{L}{2}$ for the electric field intensity as shown in the figure.

### 5.3.3 Power Flow for Fabry-Perot

Now we will turn our attention to the power flow which we have derived in the previous section. Note that if $\mathcal{Z}(z) < 0$, this indicates power moves to the left and $\mathcal{Z}(z) > 0$ means power moves to the right. We have seen the existence of loxodromes

for the Fabry-Perot cavity with the $\mathcal{Z}$-basis which occurs when either $\mathcal{Z}\left(\frac{L}{2}\right) = 0$ or $\mathcal{Z}\left(\frac{L}{2}\right) = \infty$. In fact, when there is no power flow either side, $\mathcal{Z}_P(z) = 0$, this means that either $\mathrm{Im}(\mathcal{Z}(z)) = 0$ or $|E(z)|^2 = 0$. We see that in Figure 5.2, we see that $\mathcal{Z}(z)$ crosses the real axis only once at $\frac{L}{2}$ as at this point, $\mathrm{Im}(\mathcal{Z}(z)) = 0$. The power flow for this situation is shown in Figure 5.4(a). We see here that in the cavity, the power flow is to the left throughout the cavity until $z = \frac{L}{2}$. At $\frac{L}{2}$, the power flow is zero and greater than $\frac{L}{2}$, we see that $\mathcal{Z}_P(z)$ is positive and thus the power flow moves to the right and outward-going. This symmetric behaviour is the same as the symmetric behaviour shown by the loxodrome in Figure 5.2.

The second situation is when the electric field is zero. This is the case shown in Figure 5.3. Instead of $\mathcal{Z}(z)$ crossing the real axis at zero, we see instead that from below goes to negative infinity and above the real line goes to infinity. Both of these occur at $z = \frac{L}{2}$. This is when the power flow is zero at $\frac{L}{2}$, meaning $\mathcal{Z}_p\left(\frac{L}{2}\right) = 0$ because $\left|E\left(\frac{L}{2}\right)\right|^2 = 0$. Consider Figure 5.4(b). When $z < \frac{L}{2}$, we see the power flow moving outward from the left. At $z = \frac{L}{2}$, we see no power flow and then greater than $\frac{L}{2}$, we see that the power is flowing outward to the right.

### 5.3.4 Permittivity and the Fabry-Perot Laser

So far, we have investigated the active medium in terms of the absorption coefficient, frequency detuning and the population inversion. However, we can also develop interesting conclusions by looking at the permittivity of the medium as a whole such as whether the cavity is has more gain than absorption. We can also investigate the threshold branches in terms of the permittivity of the cavity. Recall that the imaginary component of the permittivity corresponds to the net gain of the medium if less than zero or net absorption if greater than zero. In a Fabry-Perot cavity, at threshold, one would expect that that the medium would have more gain than absorption or else it would not be lasing. This is in fact true if we look at Figure 5.5. We see that the red threshold branch starts at higher gain for lower $k$. With increasing $k$, the gain decreases. The same is true for the green branch, we see that it increases with increasing $k$. However, both branches are below zero which indicates that there is net gain in the medium. This is an expected result due to the fact the laser must have effective gain in the cavity to replenish the losses at the ends of the cavity as we have open boundary conditions. Thus using the $\mathcal{Z}$-basis, we have shown the standard behaviour that occurs in a Fabry-Perot cavity at threshold.

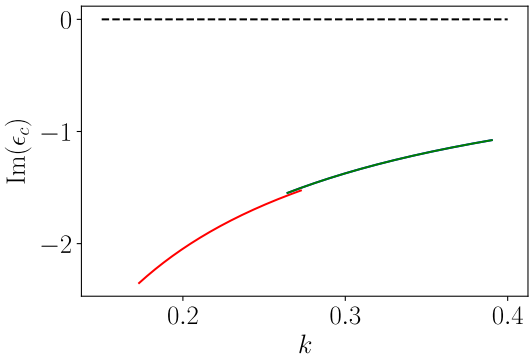



Figure 5.5: Threshold branches that correspond to the red and green branches seen in Figure 5.1 in the $\epsilon_c, k$ plane for $L = 10$.

## 5.4 Coupled-Cavities at Threshold and TEPs

Now that we have shown that the $\mathcal{Z}$-basis is a good model to replicate results in the steady-state situation for the Fabry-Perot cavity, we can turn our attention to a more complicated geometrical structure. As in the previous chapter, we consider a two cavity coupled laser with open boundaries where the electromagnetic field satisfies the threshold constant flux state condition when we investigate at threshold. In this section, the cavities are separated by the gap. With all this in mind, we can in fact show the existence of TEPs when two threshold branches coalesce. In addition to this, we can also show loxodromes in both cavities by varying $\mathcal{Z}(z)$. Finally, we are able to show a very important result which is that a laser can be at threshold if one cavity has net gain and the other net absorption and we discuss the conditions for this to happen.

### 5.4.1 Coupled-Cavity Lasers with the $\mathcal{Z}$-basis

In a similar way to the coordinate system used with SALT, we will take a separate co-ordinate system for each section of the laser. As a result, consider a laser of two cavities of lengths $l_1$ and $l_2$ with coordinates $z_1$ and $z_2$ respectively. Each cavity has a constant permittivity given by $\epsilon_1$ and $\epsilon_2$ respectively. The gap in between is of length $l_g$ with permittivity $\epsilon_g = 1$ with coordinate $z_g$. Moreover, let $\mathcal{Z}^{(1)}(z_1)$, $\mathcal{Z}^{(g)}(z_g)$ and $\mathcal{Z}^{(2)}(z_2)$ be the $\mathcal{Z}$-basis functions for the first cavity, gap and second cavity respectively. Another important idea to note is that $\mathcal{Z}^{(i)}(z_i)$ is continuous across the boundaries of each section such that $\mathcal{Z}^{(i)}(l_i) = \mathcal{Z}^{(j)}(0)$. Using the boundary conditions where $\mathcal{Z}^{(2)}(l_2) = -\mathcal{Z}^{(1)}(0) = i$, we can write the $\mathcal{Z}$-basis from one end to

the other of a laser as follows,

$$i = \begin{bmatrix} \cos(k\sqrt{\epsilon_2}l_2) & -\sqrt{\epsilon_2}\sin(k\sqrt{\epsilon_2}l_2) \\ \frac{\sin(k\sqrt{\epsilon_2}l_2)}{\sqrt{\epsilon_2}} & \cos(k\sqrt{\epsilon_2}l_2) \end{bmatrix} \begin{bmatrix} \cos(kl_g) & -\sin(kl_g) \\ \sin(kl_g) & \cos(kl_g) \end{bmatrix} \begin{bmatrix} \cos(k\sqrt{\epsilon_1}l_1) & -\sqrt{\epsilon_1}\sin(k\sqrt{\epsilon_1}l_1) \\ \frac{\sin(k\sqrt{\epsilon_1}l_1)}{\sqrt{\epsilon_1}} & \cos(k\sqrt{\epsilon_1}l_1) \end{bmatrix} (-i). \tag{5.43}$$

To do this, we calculated the $\mathcal{Z}$-basis for each section like (5.32). Thus, we have now obtained a condition which is like the transfer matrix equation with SALT and the $q$-basis equations.

### 5.4.2 Exceptional Points at Threshold

In the previous chapter, we have shown that EPs exist where the modes are close to threshold and are referred to as threshold constant flux states that satisfy the eigenvalue problem given by (4.82) for $x_n(\omega)$. However, a second type of EP occurs along what we will term the threshold branches which are the threshold lines shown in the the $\Lambda_2, k$ plane in the previous chapter. As we have also seen, these branches appear to meet, for example in Figure 4.5, however this is not the case when you consider Figure 4.14. In this figure, it is visible that there are three distinct branches. Here, we would like to see if it is possible that these branches can merge. In fact, if we define the permittivities $\epsilon_1$ and $\epsilon_2$ in the same way as in Chapter 4, we are able to use the $\mathcal{Z}$-basis to obtain the same threshold lines, and by tweaking the parameters, show when these branches merge.

Recall from chapters 3 and 4, that an EP is when eigenvalues coalesce with the variation of parameters, along with eigenvectors. In this subsection, we consider each of the branches to act like the eigenvalues seen in previous chapters in such a way that when two distinct branches coalesce, this corresponds to a TEP, a threshold exceptional point. This TEP specifically is the point where both of the branches coalesce, following the variation of parameters. To connect with the threshold lines in Chapter 4, we write the permittivities $\epsilon_1$ and $\epsilon_2$, while taking note of (2.78) and (4.40), as

$$\epsilon_1 = \tilde{n}_b^2 - \mathscr{L}(\Delta)(\Delta + i)\Lambda_1, \tag{5.44}$$

$$\epsilon_2 = \tilde{n}_b^2 - \mathscr{L}(\Delta)(\Delta + i)\Lambda_2, \tag{5.45}$$

where $\Lambda_1$ and $\Lambda_2$ are the pumps for the first and second cavities respectively. We note

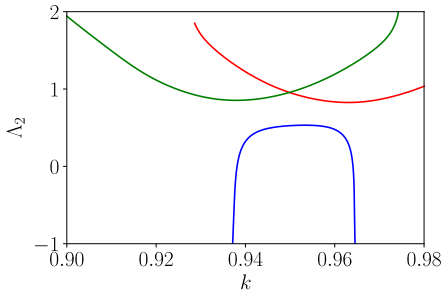
that both cavities have the same complex refractive index too. Therefore, the only difference we will consider between $\epsilon_1$ and $\epsilon_2$ are the different pumps.

Using (5.43), we can obtain the same threshold regions as in the previous chapter as shown in Figure 5.6. In these figures, we have taken length values of 10 for each cavity and 1 for the gap with $\tilde{n}_b = 3 + 0.13i$. Firstly, two examples are shown for TEPs with one TEP shown in Figures 5.6(c) and (d) where the blue and red branches meet and the second in Figures 5.7(a) and (b) where the blue and green branches meet. We will now go through the journey of how these TEPs effect the threshold branches. Moreover, in these figures, we have changed the first pump parameter, $\Lambda_1$. In Figure 5.6 (a) and in (b), we see three distinct branches. While two of these branches, green and red, in (a) cross, it is clear this is not the case and is the result of the projection. This is seen when we consider (b) which takes $\Delta$ into account and it is clear none of the branches cross. In Figure 5.6(c) and in (d), we see that with a higher pump in the first cavity, the blue and red threshold branches meet and we have a TEP as a result. Increasing further will result in two branches split to form new blue and red branches where we have three distinct branches shown in Figures 5.6(e) and (f).

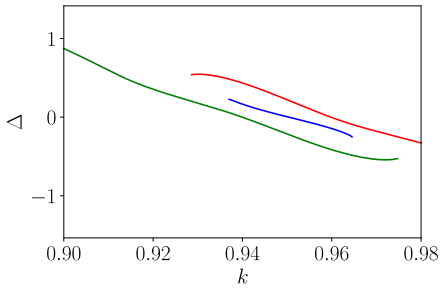
Moreover, we can also see a meeting between the green and blue branches by increasing $\Lambda_1$ even further which results in a second TEP. If we increase the pump for the first cavity from the situation shown in Figures 5.6(e) and (f), we arrive at the second TEP which is given Figures 5.7(a) and (b). What has happened here is the blue branch and green branch move closer together until they merge at a single point which is the TEP. From there, the two branches split which forms the new green and blue branches which are shown in Figures 5.7(c) and (d).

### 5.4.3 Loxodromes and Coupled-Cavity Lasers

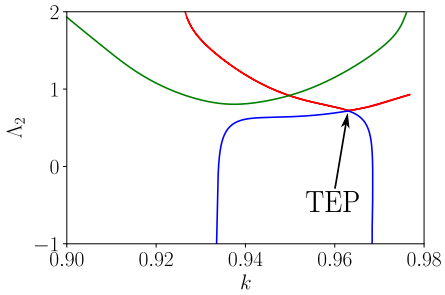
In the previous subsection, we have shown the existence of loxodromes for the steady-state scenario for modes at threshold for the Fabry-Perot laser. We now wish to extend this to coupled-cavities where we also see loxodromes. If we use the condition given by (5.43), we can see how a mode at threshold looks like with the $\mathcal{Z}$-basis and corresponding electric field intensity. Note that we will write $\mathcal{Z}_{j1}^F$ as the fixed point one below the real axis in the $\mathcal{Z}(z)$ complex plane and $\mathcal{Z}_{j2}^F$ fixed point is above the real axis. Note that $j$ is the index of which cavity we are considering. Recall that the fixed pints in each cavity are given by $\mathcal{Z}_{j1}^F = -i\sqrt{\epsilon_j}$ and $\mathcal{Z}_{j2}^F = i\sqrt{\epsilon_j}$ where $\epsilon_j$ is the permittivity of the section. Furthermore, the stability of each point was derived and



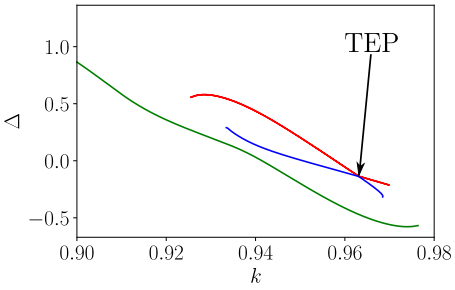

(a) $\Lambda_2, k$ plane with $\Lambda_1 = 1.15$.



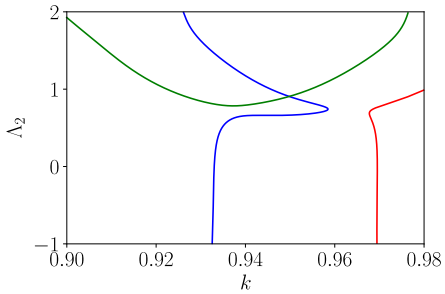

(b) $\Delta, k$ plane with $\Lambda_1 = 1.15$.



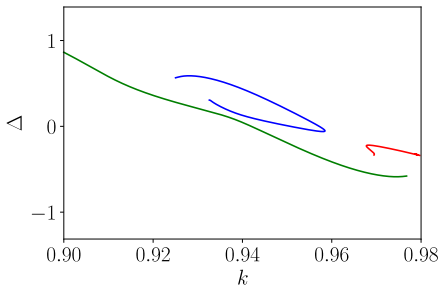

(c) $\Lambda_2, k$ plane with $\Lambda_1 = 1.189$.




(d) $\Delta, k$ plane with $\Lambda_1 = 1.189$.

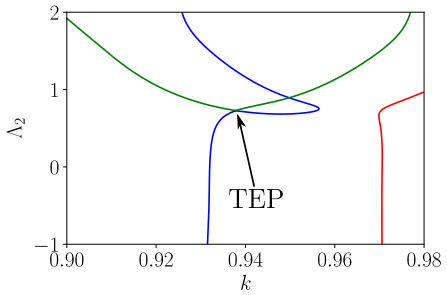



(e) $\Lambda_2, k$ plane with $\Lambda_1 = 1.2$.

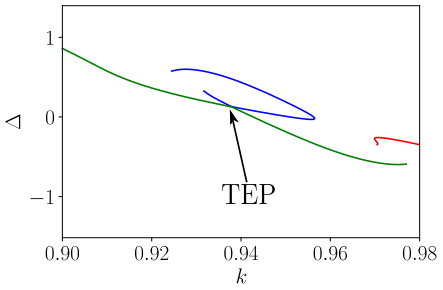



(f) $\Delta, k$ plane with $\Lambda_1 = 1.2$.

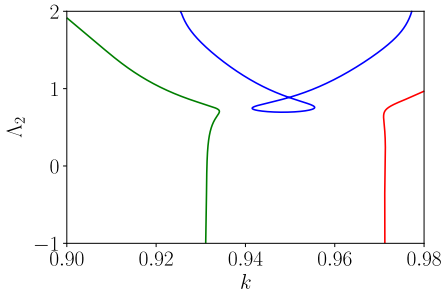
Figure 5.6: Threshold branches for a range of $k$ from $k = 0.90$ to $k = 0.98$. The three possible branches shown in green, blue and red for different $\Lambda_1$ where (a) and (b) have $\Lambda_1 = 1.18$, (c) and (d) have $\Lambda_1 = 1.189$ and (e) and (f) have $\Lambda_1 = 1.2$.



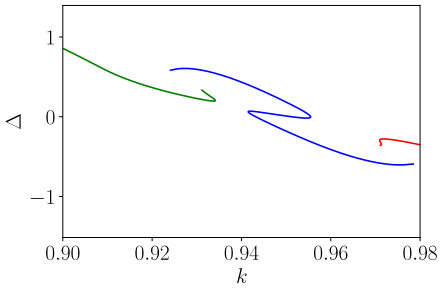

(a) $\Lambda_2, k$ plane with $\Lambda_1 = 1.2122$.




(b) $\Delta, k$ plane with $\Lambda_1 = 1.2122$.




(c) $\Lambda_2, k$ plane with $\Lambda_1 = 1.22$.




(d) $\Delta, k$ plane with $\Lambda_1 = 1.22$.

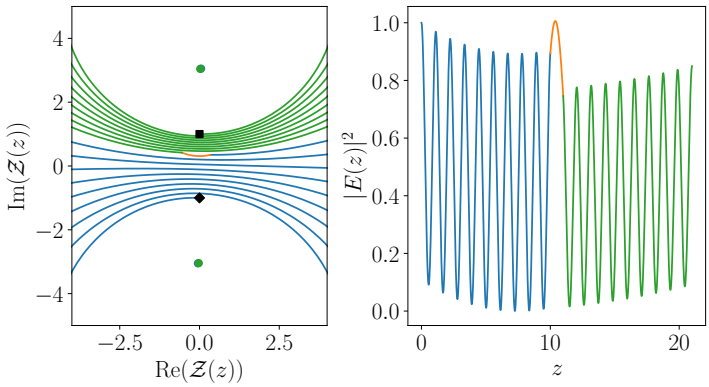
Figure 5.7: Threshold branches for a second TEP for the range of $k$ from $k = 0.90$ to $k = 0.98$. The three possible branches shown in green blue and red for different $\Lambda_1$ where (a) and (b) have $\Lambda_1 = 1.2122$, (c) and (d) have $\Lambda_1 = 1.22$

given by the Jacobian in (5.9).

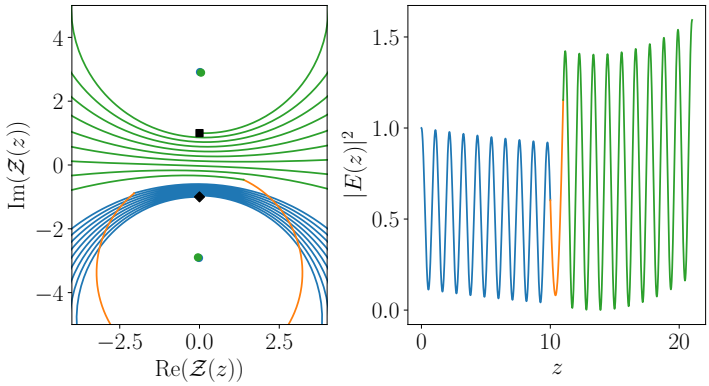
Consider Figure 5.8 which shows three pictures of the electric field intensity and $\mathcal{Z}(z)$ for coupled cavities. Each of the three parts of this figure correspond to the threshold branches shown in Figures 5.6(a) and (b). Firstly, let us look at Figure 5.8(a). We can see that the pump of the first cavity is higher than the second and as a result, the intensity is higher in the first section. Moreover in the first cavity, we have fixed points $\mathcal{Z}_{11}^F = -0.0454 - 3.0494i$ and $\mathcal{Z}_{12}^F = 0.0454 + 3.0494i$. In the second cavity, we have fixed points $\mathcal{Z}_{21}^F = -0.0279 - 3.044i$ and $\mathcal{Z}_{22}^F = 0.0279 + 3.044i$. Using the Jacobian, we see that $\mathcal{Z}_{11}^F$ and $\mathcal{Z}_{21}^F$ are unstable while $\mathcal{Z}_{12}^F$ and $\mathcal{Z}_{22}^F$ are stable. In terms of the $\mathcal{Z}$-basis, we see that loxodromes appear in a similar way as the Fabry-Perot laser. Starting with $z = 0$, we have the condition that $\mathcal{Z}^{(1)}(0) = -i$. From that point, $\mathcal{Z}^{(1)}(z)$ spirals out from the unstable fixed point and starts to spiral into the second stable fixed point for this first cavity. Then at the boundary, we move into the gap and we see that $\mathcal{Z}^{(g)}(z)$ moves slightly towards the second fixed point above the real axis in the complex $\mathcal{Z}$ plane. Then we move into the second cavity and $\mathcal{Z}^{(2)}(z)$ spirals towards the second fixed point and then finishes at the boundary $\mathcal{Z}^{(2)}(L) = i$. We see in this example that for both cavities, the fixed point stability is the same. This indicates that both cavities have more gain than absorption. Moreover, the left cavity, its loxodrome changes orbit of the fixed points before reaching the gap.

Let us move onto Figure 5.8(b). We see a similar situation as the previous discussion with a subtle difference. In this case we have a higher pump in the second cavity over the first. Note that in the first cavity, we have fixed points $\mathcal{Z}_{11}^F = -0.0154 - 2.914i$ and $\mathcal{Z}_{12}^F = 0.0154 + 2.914i$. Using the Jacobian, we see that $\mathcal{Z}_{11}^F$ and $\mathcal{Z}_{21}^F$ are unstable while $\mathcal{Z}_{12}^F$ and $\mathcal{Z}_{22}^F$ are stable. In the second cavity, we have fixed points $\mathcal{Z}_{21}^F = -0.0487 - 2.8953i$ and $\mathcal{Z}_{22}^F = 0.0487 + 2.8953i$. Starting as before at $\mathcal{Z}^{(1)}(0) = -i$, we see that $\mathcal{Z}^{(1)}(z)$ spirals away from the unstable fixed point. Then $\mathcal{Z}^{(g)}(z)$ spirals around the same fixed point before reaching the boundary of the second cavity. $\mathcal{Z}^{(2)}(z)$ starts orbiting away from the first unstable fixed point until the loxodrome goes around the second stable fixed point before reaching $\mathcal{Z}^{(2)}(L) = i$. In this case, we see again that both cavities have the same stability in terms of fixed points. However, as a result of the pump in the second cavity being higher, we see the orbit of fixed points changing for the second cavity, rather than the first.

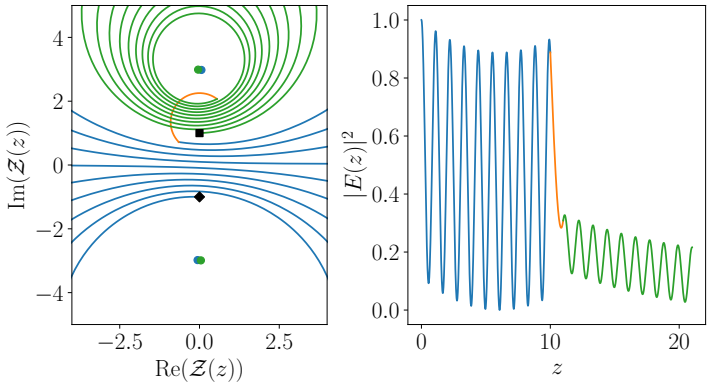
The most interesting case arises when we consider Figure 5.8(c). In this instance, the second pump is far lower than the first. Note that in the first cavity, we have fixed points $\mathcal{Z}_{11}^F = -0.0604 - 2.9799i$ and $\mathcal{Z}_{12}^F = 0.0604 + 2.9799i$. In the second cavity, we have fixed points $\mathcal{Z}_{21}^F = -0.0487 - 2.8953i$ and $\mathcal{Z}_{22}^F = 0.0487 + 2.8953i$. Using




(a) $\mathcal{Z}(z)$ and $|E(z)|^2$ where $k = 0.9231$, $\Lambda_2 = 1.0336$ and $\Delta = 0.29678$




(b) $\mathcal{Z}(z)$ and $|E(z)|^2$ where $k = 0.9925$, $\Lambda_2 = 1.4039$ and $\Delta = -0.5672$




(c) $\mathcal{Z}(z)$ and $|E(z)|^2$ where $k = 0.95687$, $\Lambda_2 = 0.5221$ and $\Delta = -0.09402$

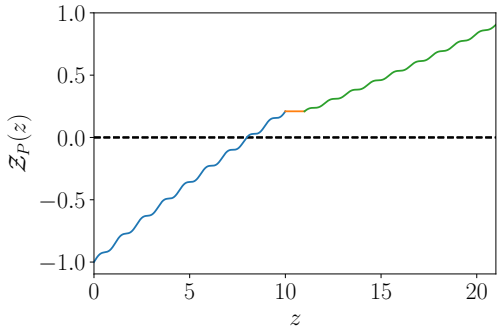
Figure 5.8: $\mathcal{Z}(z)$ and $|E(z)|^2$ plots for coupled-cavities where the first cavity is shown in blue, the gap in orange and the second cavity in green. (a) corresponds to the green branch of Figures 5.6(a) and (b), while (b) and (c) correspond to a mode profile on the red and blue branches respectively. Parameters used were $l_1 = l_2 = 10$, $l_g = 1$, $\Lambda_1 = 1.18$ and $\tilde{n}_b = 3 + 0.13i$. The blue and green dots are the fixed points for the first and second cavity respectively. The black diamond and square are the boundary conditions.

the Jacobian, we see that $\mathcal{Z}_{11}^F$ and $\mathcal{Z}_{22}^F$ are unstable while $\mathcal{Z}_{12}^F$ and $\mathcal{Z}_{21}^F$ are stable. Again, we start from $\mathcal{Z}^{(1)}(0) = -i$ and from there $\mathcal{Z}^{(1)}(z)$ spirals away from the first unstable fixed point and switches orbit towards the second which is a stable fixed point. Then across the gap boundary, $\mathcal{Z}^{(g)}(z)$ then pushes $\mathrm{Im}(\mathcal{Z}^{(g)}(z))$ above the final condition $\mathcal{Z}^{(2)}(L) = i$, the boundary of the second cavity. Then $\mathcal{Z}^{(2)}(z)$ spirals out to $\mathcal{Z}^{(2)}(L) = i$ which indicates the second fixed point is unstable for the second cavity. We see in this case that the stability changes for both fixed points depending on the cavity. This means that while the first cavity has more gain than absorption, the second has more absorption than gain.

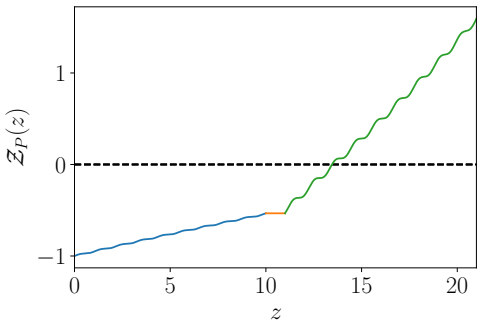
### 5.4.4 Power Flow for Coupled-Cavities

As we have seen in the case of the Fabry-Perot cavity, when the power flow crosses the real axis in the complex plane for $\mathcal{Z}(z)$, that the power flow is zero. In this easier case, it occurred at $z = \frac{L}{2}$. However, with coupled cavities, which were shown in the previous chapter, the power flow is far more complex. As we have also derived previously, we can write the Poynting vector in terms of the $\mathcal{Z}$-basis, namely $\mathcal{Z}_P(z)$. We can use this now to differentiate between the cases shown in Figure 5.8. Recall that in Figure 5.8(a), the loxodrome for the first cavity, labelled as $\mathcal{Z}^{(1)}(z)$, first orbited the stable fixed point and starts orbiting the unstable fixed point before reaching the gap. The same behaviour of the loxodrome is seen in Figure 5.8(c). In contrast, we see in Figure 5.8(b) that $\mathcal{Z}^{(1)}(z)$ only orbits one unstable fixed point while $\mathcal{Z}^{(2)}(z)$ orbits first this unstable fixed point then is attracted to the stable fixed point. This difference in behaviour can be seen by looking at when $\mathcal{Z}_P(z) = 0$. In all cases, unless with equal pumping, this does not occur at $\frac{L}{2}$.

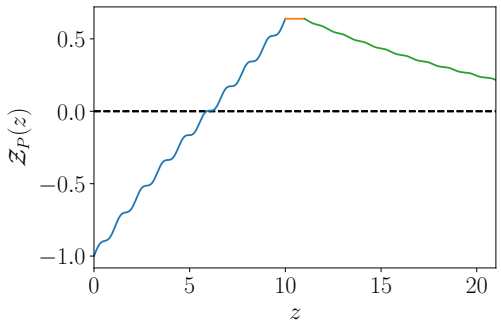
In Figure 5.9, we see three power flow diagrams which are in reference to the three different plots seen in Figure 5.8. If we first consider Figure 5.9(a) which is related to 5.8(a). We see that in the first cavity, we have the situation where there is power flow towards the boundary and towards the gap. As a result, in terms of the loxodrome, for $\mathcal{Z}^{(1)}(z)$, it passes the real axis in the first cavity such that $\mathcal{Z}_P(z) = 0$. This results in the orbit changing from one fixed point to the other in this cavity. In Figure 5.9(b), which relates to Figure 5.8(b), we see the opposite where the power flow is zero in the second cavity which means while the first cavity is purely outgoing, the second has power flowing out and towards the gap. This means that $\mathcal{Z}_P(z) = 0$ crosses zero in the second cavity, rather than the first. Finally in Figure 5.9(c), which is related to Figure 5.8(c), has the same behaviour as 5.9(a) meaning that $\mathcal{Z}_P(z) = 0$ occurs




(a) $\mathcal{Z}_P(z)$ corresponding to Figure 5.2(a).




(b) $\mathcal{Z}_P(z)$ corresponding to Figure 5.2(b).




(c) $\mathcal{Z}_P(z)$ corresponding to Figure 5.2(c).

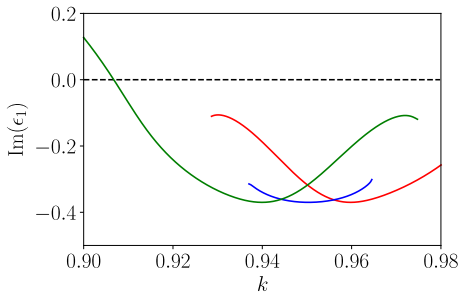
Figure 5.9: Various examples showing the power flow inside a coupled laser cavity with $\Lambda_1 = 1.18$, $l_1 = l_2 = 10$, $l_g = 1$ and $\tilde{n}_b = 3 + 0.13i$.

in the first cavity. However, there is a slight difference in the second cavity where the power outflow decreases closer to the boundary. This indicates a that this is an absorbing cavity due to the pump of the second cavity being far lower than the first. We will discuss this in terms of permittivities $\epsilon_1$ and $\epsilon_2$ in the next subsection.

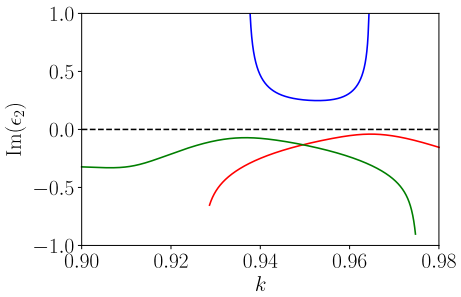
### 5.4.5 Permittivities of Coupled-Cavities with the $\mathcal{Z}$-basis

Like with the Fabry-Perot cavity, we can analyse the active mediums of both cavities just by focusing on the permittivities in the laser which are related to the refractive index, pump and absorption by (5.44) and (5.45). Using this formalisation, we can see whether a cavity is predominantly absorbing or not. As a result, we can determine if along any of the eigenvalue branches whether a cavity goes from gain to absorption by changing parameters. We can also see how the TEPs effect these threshold branches. In particular, we would like to focus on the imaginary component of the permittivities to determine whether each of these cavities are absorbing or have gain.

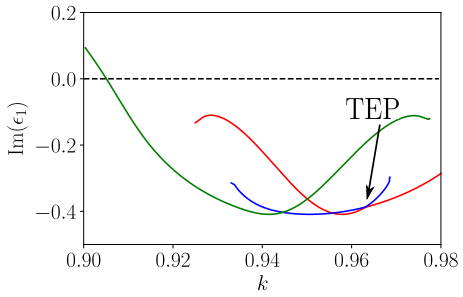
Let us consider each case in Figures 5.10 and 5.11 in detail. These figures are related to those shown in 5.6 and 5.7. We start off with Figures 5.10(a) and (b). We find that in the first cavity, the green branch as lower $k$ has $\mathrm{Im}(\epsilon_1) > 0$ which indicates



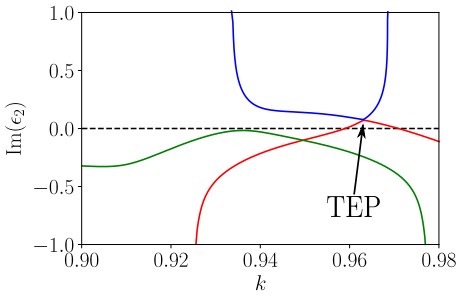

(a) $\Lambda_2, k$ plane with $\Lambda_1 = 1.15$.



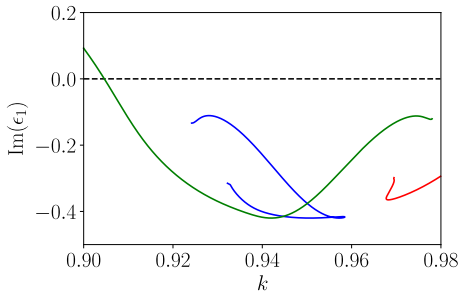

(b) $\Delta, k$ plane with $\Lambda_1 = 1.15$.



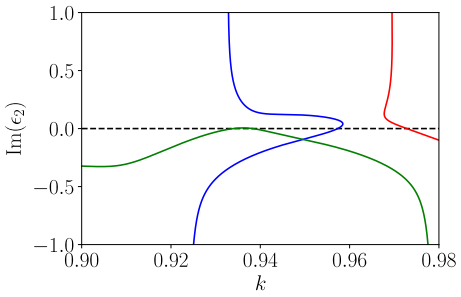

(c) $\Lambda_2, k$ plane with $\Lambda_1 = 1.189$.




(d) $\Delta, k$ plane with $\Lambda_1 = 1.189$.

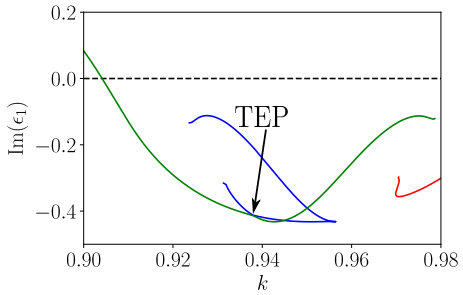



(e) $\Lambda_2, k$ plane with $\Lambda_1 = 1.2$.

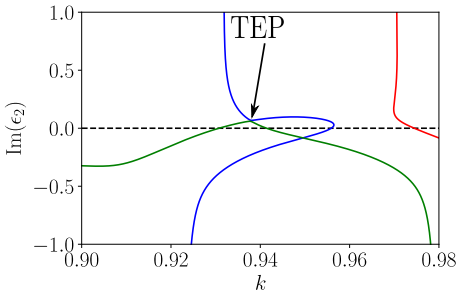



(f) $\Delta, k$ plane with $\Lambda_1 = 1.2$.

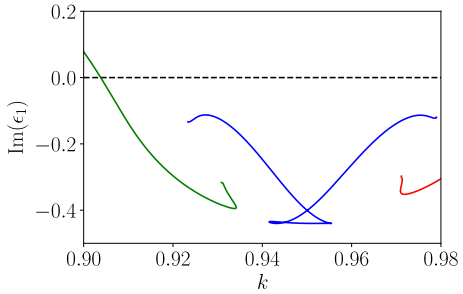
Figure 5.10: Threshold branches in terms of the permittivities for a range of $k$ from $k = 0.90$ to $k = 0.98$. The three possible branches shown in green, blue and red for different $\Lambda_1$ where (a) and (b) have $\Lambda_1 = 1.18$, (c) and (d) have $\Lambda_1 = 1.189$ and (e) and (f) have $\Lambda_1 = 1.2$.



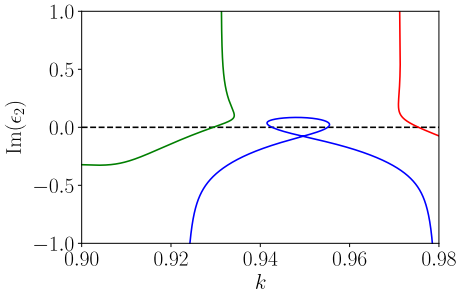

(a) $\Lambda_2, k$ plane with $\Lambda_1 = 1.2122$.




(b) $\Delta, k$ plane with $\Lambda_1 = 1.2122$.




(c) $\Lambda_2, k$ plane with $\Lambda_1 = 1.22$.




(d) $\Delta, k$ plane with $\Lambda_1 = 1.22$.

Figure 5.11: Threshold branches in terms of the permittivities for the range of $k$ from $k = 0.90$ to $k = 0.98$. The three possible branches shown in green blue and red for different $\Lambda_1$ where (a) and (b) have $\Lambda_1 = 1.2122$, (c) and (d) have $\Lambda_1 = 1.22$

that the cavity is absorbing. With increasing $k$, we see that the green branch has net gain in the first cavity. The other branches in the frequency range shown have net gain also. For the second cavity we see that both the green and red branches have net gain while the blue branch has net absorption. Thus we can conclude that for all modes shown on the blue branch, the second cavity is absorbing. We can also compare these results with the detuning in Figure 5.6(b), for all branches, the detuning can be both positive and negative. However, this is not always the case.

In Figures 5.10(c) and (d), we see the first instance of TEPs as discussed before. In this case we see again for low $k$, the green branch shows the first cavity is absorbing for the range shown and net gain otherwise. For higher $k$, and for both the red and blue branches, we have net gain in the first cavity. But the TEP effects the second cavity as the red branch moves to positive $\mathrm{Im}(\epsilon_2)$ for a small range of $k$ to meet the blue branch. The green branch for the range we are investigating, always has net gain. Looking at these branches in terms of detuning, in Figure 5.6(b), again all branches go from positive to negative detuning.

In Figures 5.10(e) and (f), we see the same situation as before with all branches having net gain apart from low $k$ where the green branch goes slightly above. In the second cavity the red and blue branches split with both, depending on the frequency, either has a net gain or absorption for the medium. The green branch has $\mathrm{Im}(\epsilon_2) < 0$ for all frequency values shown. Looking at the detuning in Figure 5.6(f), we see that on the green branch, the detuning goes from positive to negative. In contrast, the blue branch is mainly above zero in terms of detuning while the red branch is below zero.

The next TEP effects the green and blue branches of the second cavity in Figure 5.11(b). We see that the green branch has a small range of $k$ that indicates absorption to meet the blue branch at the TEP. The red branch for a small range of $k$ shown goes between net gain and absorption. In the first cavity, we have the same situation as mentioned previously which is shown in Figure 5.11(a). Looking at the detuning in Figure 5.7(b), only the green branch goes from negative detuning to positive detuning while the blue and red branches have positive and negative detuning respectively.

In the final set of diagrams, we see the effect of both TEPs with increasing pump shown in Figures 5.11(c) and (d). In this case we see again the same situation for the first cavity. In the second cavity the green and blue branches split as shown. In the case of the green and red branches, for a set of $k$, the cavity is either absorbing or has net gain. The blue branch has most threshold values that have net gain for most values of $k$ shown. In terms of the detuning as shown in Figure 5.7(d), the blue

branch goes between positive and negative detuning while the other two have either positive or negative detuning.

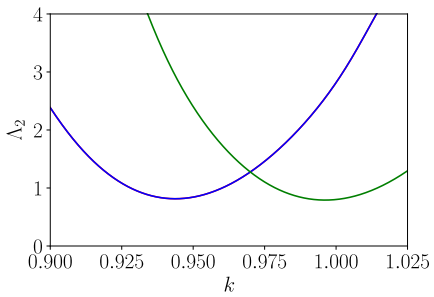
Thus we can summarise how the two TEPs have effected the three branches with increasing pump in the second cavity. Firstly, we see that these EPs have not much effect in changing whether the first cavity has net gain or is absorbing at threshold. However what it does effect is both the detuning and whether the second cavity has absorption or net gain. At first we see that all three branches have detuning going from positive and negative. After the two TEPs, this is only true for the blue branch and the green and red have positive and negative detuning respectively. In terms of gain and absorption, the second cavity has only absorption for the blue branch and for red and blue has only net gain for the range of $k$. After both TEPs, we green and red change from absorption to gain with changing $k$ and blue mostly remains as just gain.

### 5.4.6 Comparison to the Fabry-Perot Laser

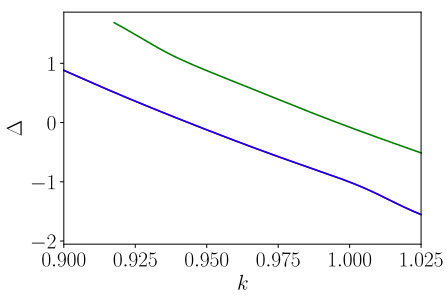
We can now compare the threshold branches above with the Fabry-Perot cavity and notice some similarities and differences between them. In Figure 5.6(a), we see that in this range of $k$, there are three distinct branches which we have talked about previously. By investigating the lower branch (blue) in terms of the permittivity of the second cavity, we saw that in all cases, the first cavity has net gain while the second has net absorption. This is the reason that the lower branch here is not possible in the Fabry-Perot case and this is why Figure 5.1 has only the upper branches. Moreover, for the most part in Figure 5.6(a), these branches are Fabry-Perot like except at high $\Lambda_2$ where the first cavity can have net adsorption. When increasing the first pump, we see that the two upper branches are no longer like the Fabry-Perot laser as these branches coalesce at a TEP and then splits and differ quite considerably from the single cavity laser, which can be seen Figure 5.7(c).

## 5.5 Analysis of Coupled-Cavities with no gap

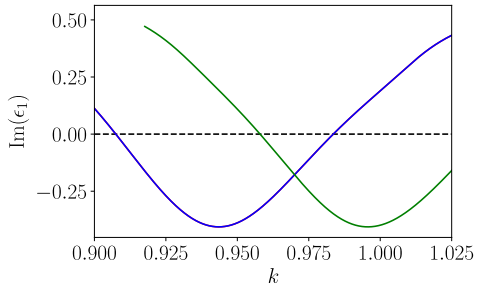
So far, we have discussed two geometrical types of lasers namely the Fabry-Perot laser and coupled-cavities with a gap between them. In between both of these lasers, is another type we would like to focus on, which are coupled-cavity lasers with no gap between them. We will see that there are differences from both Fabry-Perot lasers and coupled-cavity lasers with a gap. It turns out we see the phenomenon where one



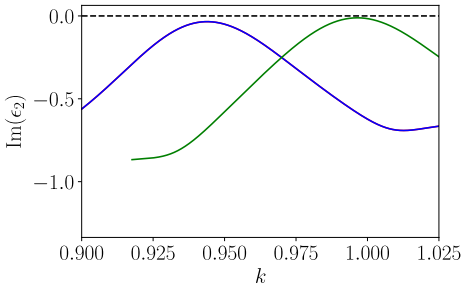

(a) $\Lambda_2, k$ plane with $\Lambda_1 = 1.1865$.




(b) $\Delta, k$ plane with $\Lambda_1 = 1.1865$.




(c) $\mathrm{Im}(\epsilon_1), k$ plane with $\Lambda_1 = 1.1865$.

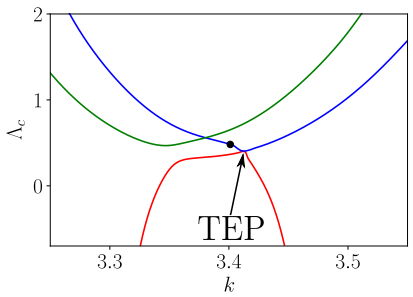



(d) $\mathrm{Im}(\epsilon_2), k$ plane with $\Lambda_1 = 1.1865$.

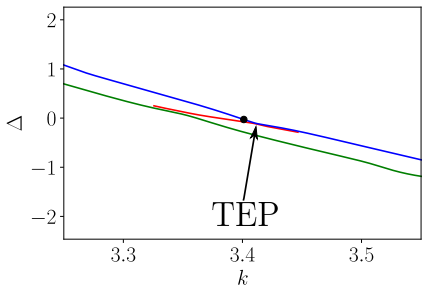
Figure 5.12: Threshold branches in terms of the pump, permittivities and $\Delta$ for the range of $k$ from $k = 0.90$ to $k = 1.025$. The two possible branches shown in green and blue with $l_1 = l_2 = 10$ and $l_g = 0$ with $\tilde{n}_b = 3 + 0.13i$.

cavity can have net gain and the other for net absorption except it occurs at higher $k$ and has similar characteristics as the coupled-cavity with a gap. Moreover, for lower $k$, we see similar behaviour as to the Fabry-Perot lasers. We will look into both of these connections in detail.

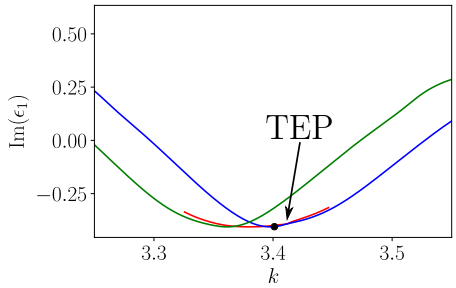
In the Fabry-Perot laser, we have seen that the threshold branches are given by Figure 5.1. In this figure, we have seen two branches as shown but in contrast to a coupled-cavity laser with a gap, there is no lower branch. The same is true for a suitable choice of $\Lambda_1$, which is close to ones chosen previously, that we also only have the situation which is similar as the Fabry-Perot laser. Consider Figure 5.12 where we have shown a range of diagrams which show the threshold branches in terms of the second pump, the frequency detuning and the permittivities of each cavity. In particular, Figure 5.12(a) shows two distinct threshold branches in green and blue. In contrast to the coupled-cavity situation with a gap, here we do not see the lower branch. At this particular $k$, the coupled-cavity without a gap is quite similar to the Fabry-Perot situation. However, at higher $\Lambda_2$, we see there are parts of the green branch where the first cavity can have net absorption. This is because the



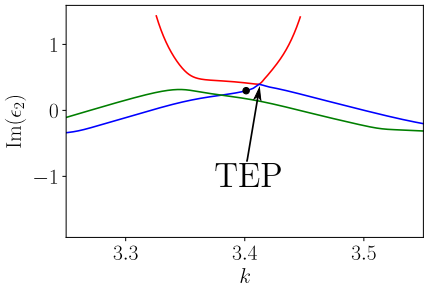

(a) $\Lambda_2, k$ plane with $\Lambda_1 = 1.1865$.




(b) $\Delta, k$ plane with $\Lambda_1 = 1.1865$.




(c) $\mathrm{Im}(\epsilon_1), k$ plane with $\Lambda_1 = 1.1865$.

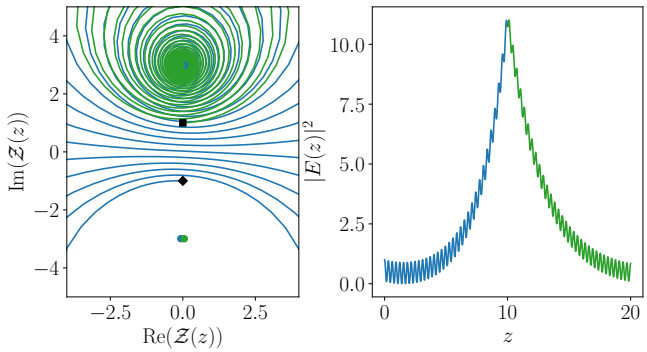



(d) $\mathrm{Im}(\epsilon_2), k$ plane with $\Lambda_1 = 1.1865$.

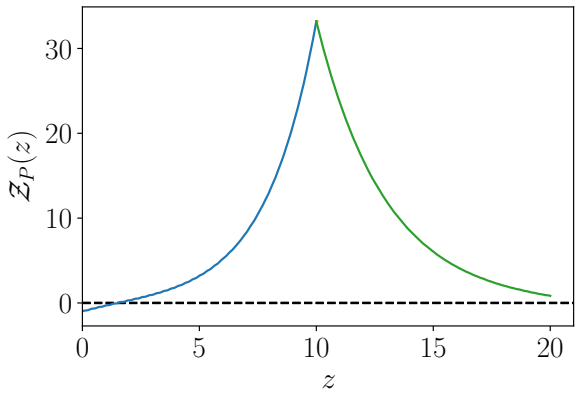
Figure 5.13: Threshold branches in terms of the pump, permittivities and $\Delta$ for the range of $k$ from $k = 3.2$ to $k = 3.6$. The three possible branches shown in red, green and blue with $l_1 = l_2 = 10$ and $l_g = 0$ with $\tilde{n}_b = 3 + 0.13i$.

second pump is far greater than the first and the gain in the second cavity is able to compensate the first for the laser to be at threshold.

In the previous chapter, we derived the eigenvalue transfer matrix equation using the $q$-basis, 4.82 which determined whether a laser is above or below threshold. We then used this to show that EPs exist in terms of these eigenvalues that create the three different threshold branches one below and two above the EP. From there, we investigated whether these EPs exist for smaller gaps including no gap at all. As a result, we obtained at a higher range of $k$, EPs which are shown in Figure 4.13. Although there is no TEP in this figure, if we reduce $\Lambda_1$ slightly, we can obtain a TEP as shown in Figure 5.13. We see here a very similar situation as the coupled-cavity laser with a gap as the red branch here has the situation where for all permissible values of $k$, $\mathrm{Im}(\epsilon_2) > 0$ meaning the second cavity has net absorption. As a result of the TEP, for the red branch to connect with the blue branch, the blue branch pushes up allowing some permissible values on this branch to have net absorption. It is also worthy to note that both the green and blue branches have parts of net absorption in the first cavity when the pump in the second cavity is large.




(a) $\mathcal{Z}(z)$ and $|E(z)|^2$ plots.




(b) $\mathcal{Z}_P(z)$ power flow plot.

Figure 5.14: $\mathcal{Z}(z)$, $|E(z)|^2$ and $\mathcal{Z}_P(z)$ plots for coupled-cavities where the first cavity is shown in blue, the gap in orange and the second cavity in green. They correspond to the black dot in Figure 5.13. Parameters used were $k = 3.401153$, $\Lambda_1 = 1.1865$, $\Lambda_2 = 0.48194$, $\Delta = -0.028204$, $l_1 = l_2 = 10$, $l_g = 0$ and $\tilde{n}_b = 3 + 0.13i$. The blue and green dots are the fixed points for the first and second cavity respectively. The black diamond and square are the boundary conditions.

There does remain a question from the previous chapter that why do these three branches occur for a much higher value of $k$, given that the only difference between the coupled-cavity systems is one has the gap and the other does not. We can see in Figure 4.4, which is a coupled-cavity system with a gap, that the threshold branch below the EPs is in a smaller range of $k$ than the ones shown in Figure 4.13, which is the coupled cavity system without the gap. This actually can be answered by looking at the loxodrome diagrams obtained from $\mathcal{Z}$-basis. Recall the example on the lower branch of Figure 5.6(a) shown in Figure 5.2(c). As discussed, this scenario is not possible in the Fabry-Perot type situation and the gap plays a central role in connecting the two cavity boundaries inside the laser in the figure. We thus consider the plots shown in Figure 5.14 which shows an example of the an upper threshold branch (the blue branch from Figure 5.13) where the second cavity has net absorption and the first having net gain. We see in this figure that the blue loxodrome for the first cavity orbits both fixed points. In particular, the blue orbit passes by the boundary condition of the outside of the second cavity so it can meet the boundary between both cavities. Recall that when $\mathcal{Z}_P(z) = 0$, the loxodrome, we have the case that for some $z$, $\mathrm{Im}(\mathcal{Z}(z)) = 0$ and the line shifts from the orbit of one fixed point to the other. As a result, Figure 5.14(b) shows that in the first cavity, the power flow to outside the laser is far less than the power flow to the other cavity. This means the orbit of $\mathcal{Z}^{(1)}(z)$ changes from one fixed point to the other for a small value of $z$. Also given the second cavity has decreasing power flow outside the laser to the right, this would indicate absorption in it. This is why $\mathrm{Im}(\mathcal{Z}^{(2)}(0)) > \mathrm{Im}(\mathcal{Z}^{(2)}(l_2)) = 1$. It is also worthy to note that the losses due to absorption in the second cavity are quite large given the decrease in $\mathcal{Z}_P(z)$ with increasing $z$ in the second cavity.

Thus we arrive at the difference between coupled-cavities with a gap and with out. In Figure 5.2(c), we see that the gap jumps from the end of the first cavity (blue) and the start of the second (green). For the cavities with no gap, the blue curve (first cavity) is expected to orbit until it meets the start of the green curve (second cavity). Given there are more orbits required for the blue and green curve to meet, this means we must have a higher $k$ as more wavelengths need to fit into the cavity. This is why we have the three branch situation for a higher $k$ where the coupled-cavities have no gap.

## 5.6 Conclusion

In this chapter we have introduced a new basis which we have titled as the $\mathcal{Z}$-basis. This allowed us to express the electric field and its derivative in terms of a single complex quantity given by $\mathcal{Z}(z)$. We were able to use this quantity to solve the stationary electromagnetic field equation analytically using the nice mathematical formalism known as the Möbius transformation. From there we used the $\mathcal{Z}$-basis to investigate the simplest open boundaried laser, the Fabry-Perot cavity. We have shown that $\mathcal{Z}(z)$ is in fact a loxodrome and have discussed this phenomenon with the power flow inside the cavity. We also showed with the $\mathcal{Z}$-basis that for the laser to be at threshold, we need to have net gain in the cavity. We thus extended this analysis to coupled cavities with a gap and introduced a new type of EP, which we called a TEP. We showed how TEPs effect the threshold branches and whether a single cavity of a coupled system has net absorption or has net gain. To add to this, we have also shown that there are loxodromes shown in each cavity too. We then compared this situation to when there is no gap between the cavities to show the three branch coupled-cavity phenomenon exits for higher $k$ than when there is a gap between the cavities.

# Chapter 6

# Open Coupled Cavity Dynamics

In this chapter, we would like to introduce dynamical equations for coupled cavity lasers with open boundary conditions. This is accomplished by combining the design of coupled open cavity modes from the time independent $q$-basis formalism while using the idea of energy balance within the modes. This will give rise to a complete set of dynamical equations for the amplitude and the population inversions in each cavity.

To introduce the dynamics, we will use the idea of energy balance. With the $q$-basis so far, there is no change in energy of the mode at threshold in time as it uses the steady-state condition. However, with the open boundary conditions from SALT [19] and the dynamics arising from the two level atom model [12] which results in the population inversion equation (2.83) and a scaling dynamical term for the electromagnetic field, via the power balance equation, we can obtain equations which effectively describe the dynamics of an open coupled-cavity laser.

This chapter is structured as follows. Firstly we introduce how dynamics will be included by scaling the electromagnetic field while using the $q$-basis to describe the spatial distribution in the coupled cavity system. Although some simplifications are made here, in terms of the relationship between the dynamics and spacial variation, it never the less introduces dynamics which is valid close to threshold. Then we consider a single cavity laser and we derive the dynamical equations for population inversion and the scaling variable of the electromagnetic field. We further introduce the eigenvalue problem from the previous chapter [20] which will aid the solving of the spatial distribution in the cavity off threshold. Finally, all of these concepts are collected together to derive dynamical equations for the open coupled cavity laser.

## 6.1 Scaling Dynamics for the Electromagnetic field

We will introduce the time dependence for the electromagnetic field by the following composition for the complex electric field and magnetic induction. Consider the ansatz for the electromagnetic field given by (4.3) and (4.4). These compositions, for the electric field and magnetic induction respectively represent the steady-state solution for the electromagnetic field. By scaling these electric field and stationary magnetic induction compositions for a single-mode, with frequency $\omega$, by a common time-dependent variable, $G(t)$, we thus make the following ansatz for the physical electric field and magnetic induction respectively,

$$E(z,t) = \frac{1}{2}G(t)E(z)e^{-i\omega t} + \text{c.c} \tag{6.1}$$

$$B(z,t) = \frac{1}{2}G(t)B(z)e^{-i\omega t} + \text{c.c} \tag{6.2}$$

where $G(t)$ is a real, slowly-varying quantity. We further note the assumption that the phases of $E(z)$ and $B(z)$ do not vary in time and are included in these complex spatially varying quantities. The electric displacement amplitude, $D(z,t)$ given by (4.10) is written with the scaling amplitude $G(t)$ as follows,

$$D(z,t) = \frac{1}{2}\epsilon_0(\tilde{n}(z)^2 + \chi_g(z,t))G(t)E(z)e^{-i\omega t} + \text{c.c} \tag{6.3}$$

where $\tilde{n}(z)$ is the complex refractive index defined the same way was the previous chapters, $\tilde{n}(z) = n(z)(1+i\kappa(z))$ where $n(z)$ is the real refractive index and $\kappa(z)$ is the extinction coefficient. $\chi_g(z,t)$ is the gain susceptibility which is now time dependent and given by the following noting (4.51),

$$\chi_g(z,t) = -\frac{N(z,t)}{1 - i\frac{\omega_0-\omega}{\gamma_p}} \tag{6.4}$$

$$= -\mathscr{L}(\Delta)(\Delta(\omega) + i)N(z,t) \tag{6.5}$$

where we have previously introduced the Lorentzian (2.79), $\mathscr{L}(\Delta) = \frac{1}{1+\Delta(\omega)^2}$ and detuning factor $\Delta(\omega) = \frac{\omega_0-\omega}{\gamma_P}$ with time-varying population inversion $N(z,t)$. We will describe $\Delta > 0$ as positive detuning and $\Delta < 0$ as negative detuning.

Note that we use the SALT units for $E(z)$, $B(z)$ and $N(z,t)$ [19] which are given

by,

$$E(z) = \frac{\wp}{\hbar\sqrt{\gamma_P\gamma_N}}E_{SI} \tag{6.6}$$

$$B(z) = \frac{\wp}{\hbar\sqrt{\gamma_P\gamma_N}}B_{SI} \tag{6.7}$$

$$N(z,t) = \frac{\wp^2}{\hbar\gamma_P\epsilon_0}N_{SI} \tag{6.8}$$

where $E_{SI}$, $B_{SI}$ and $N_{SI}$ are the SI unit variables for the electric field, magnetic induction and population inversion respectively. The same factor is used for $E(z)$ and $B(z)$. Note that $E(z)$ and $N(z,t)$ are dimensionless while $B(z)$ is unit time per unit distance. As we have done in the previous chapter, we will set the length of gaps used to be 1 and laser cavities of length 10. All other variables involving units of distance will be scaled accordingly.

### 6.1.1 Maxwell's Equations

We will consider the following Maxwell's equations (4.1) and (4.2),

$$\frac{\partial E(z,t)}{\partial z} = -\frac{\partial B(z,t)}{\partial t} \tag{6.9}$$

$$\frac{\partial B(z,t)}{\partial z} = -\mu_0\frac{\partial D(z,t)}{\partial t} \tag{6.10}$$

Here we will use the RWA. If we multiply (6.9) and (6.10) by $e^{i\omega_0 t}$, in a similar way to [12], after using the compositions of the electromagnetic field, (6.1), (6.2) and (6.3), we have exponential terms $e^{i(\omega_0-\omega)t}$ and $e^{i(\omega_0+\omega)t}$. We will only consider modes where frequencies are close to the atomic transition frequency which indicates $|\omega_0 - \omega| \ll |\omega_0 + \omega|$. Thus we can remove terms where the exponential is of the form $e^{i(\omega_0+\omega)t}$. This is all provided that $G(t)$ and $N(z,t)$ are slowly varying functions. This means the RWA can be used where (6.9) and (6.10) become,

$$G(t)\frac{dE(z)}{dz} = i\omega G(t)B(z) - B(z)\dot{G}(t) \tag{6.11}$$

$$\begin{aligned} G(t)\frac{dB(z)}{dz} =& \frac{1}{c^2}[(\tilde{n}(z)^2 - \mathscr{L}(\Delta)(\Delta(\omega)+i)N(z,t))(i\omega G(t) - \dot{G}(t)) \\ &+ \mathscr{L}(\Delta)(\Delta(\omega)+i)\dot{N}(z,t)G(t)]E(z) \end{aligned} \tag{6.12}$$

### 6.1.2 $Q$-time Basis

The goal is to obtain a power balance equation, and this can be done by using the $q$-basis from the previous chapter. We will use the same $q_A(z)$, $q_S(z)$, $q_R(z)$ and $q_I(z)$, given by (4.20)-(4.23), for the spatial variation. Moreover, the time dependence of the electromagnetic field will be accounted for by the scaling variable, $A(t)$. Thus we can define the $Q$-time Basis with variables $Q_A(z,t)$, $Q_S(z,t)$, $Q_R(z,t)$ and $Q_I(z,t)$ such that,

$$Q_A(z,t) = A(t)q_A(z) = A(t)\left(|E(z)|^2 + \frac{c^2}{n^2}|B(z)|^2\right) \tag{6.13}$$

$$Q_S(z,t) = A(t)q_S(z) = A(t)\left(|E(z)|^2 - \frac{c^2}{n^2}|B(z)|^2\right) \tag{6.14}$$

$$Q_R(z,t) = A(t)q_R(z) = A(t)\frac{c}{n}\left(E(z)B(z)^* + E(z)^*B(z)\right) \tag{6.15}$$

$$Q_I(z,t) = A(t)q_I(z) = -iA(t)\frac{c}{n}\left(E(z)B(z)^* - E(z)^*B(z)\right) \tag{6.16}$$

where the slowly varying real amplitude $A(t)$ is related to $G(t)$ by,

$$A(t) = G(t)^2. \tag{6.17}$$

As the $q$-basis are a set of discontinuous functions with changing refractive index, we will thus calculate the $Q$-time basis for each section. Note that $n$ is the refractive index of the given section. Recall in Chapter 4, the physical significance for all terms in the $q$-basis were explained. The same explanations can be used for the terms in the $Q$-time basis. Thus we can say that up to a constant that $Q_A(z,t)$ represents up to a constant the sum of the electromagnetic intensities, which represents the energy density for a non-active medium, scaled by a factor $A(t)$. Similarly scaled with $A(t)$, $Q_S(z,t)$ represents the difference in the electric field and magnetic induction energy densities. $Q_R(z,t)$ is related to the real part of the time-averaged Poynting vector scaled with $A(t)$. Finally $Q_I(z,t)$ is related to the imaginary part of this complex-valued Poynting vector.

### 6.1.3 Dynamics for Scaling and Population Inversion

In this chapter, the main aim is to introduce a set of self-consistent equations which describe the dynamical effects of the electromagnetic field and population inversion of open-boundary lasers. We will derive these equations with the following format. For a single-cavity laser, we can write two equations, one for the scaling amplitude

$A(t)$ and global population inversion over the entire cavity, $N_c(t)$ where we use all of the assumptions made already in this section. Thus, these equations are written in the following form,

$$\dot{A} = cF_c(N_c)N_cA \tag{6.18}$$

$$\dot{N}_c = -\gamma_N \left(N_c - \Lambda_c + H_c(N_c)N_cA\right), \tag{6.19}$$

where $\Lambda_c$ is the pump of the cavity. In the next section, we will derive the functions $F_c(N_c)$ and $H_c(N_c)$. The $A(t)$ equation will be derived from the idea of power balance we have seen throughout this thesis. This will arise from computing $\frac{\partial Q_R(z,t)}{\partial z}$ along with using some steady-state properties from the $q$-basis in Chapter 4. The population inversion equation $N_c(t)$ comes from (2.83) which we will use to derive the above equation.

For the coupled-cavity laser with open boundaries, we will derive three self-consistent equations for the global scaling amplitude $A(t)$, along with global population inversion terms $N_1(t)$ and $N_2(t)$ which correspond to the first and second cavities respectively. Similar to the single-cavity equations, we will use the assumptions in this section to write the following equations,

$$\dot{A} = cF_{12}(N_1, N_2)A, \tag{6.20}$$

$$\dot{N}_1 = -\gamma_N \left[N_1 - \Lambda_1 + H_1(N_1, N_2)AN_1\right], \tag{6.21}$$

$$\dot{N}_2 = -\gamma_N \left[N_2 - \Lambda_2 + H_2(N_1, N_2)AN_2\right]. \tag{6.22}$$

where $\Lambda_1$ and $\Lambda_2$ are the pumps of the first and second cavities respectively. In later sections, we will determine values for $F_{12}(N_1, N_2)$, $H_1(N_1, N_2)$ and $H_2(N_1, N_2)$. These equations will be derived with the same principles as the single-cavity case but with the added complexity of multiple sections and population inversions.

## 6.2 Power Flow Dynamics for a Single Cavity Open Laser

### 6.2.1 Power Flow Equation

In this subsection, we will derive the power flow equation in terms of the dynamical scaling term $A(t)$ which has a similar composition to the steady-state condition given by (4.19) but for a single cavity and in terms of the $Q$-time basis. It is worthy to

note that in the simple case of a single cavity, Fabry-Perot type cavity, there is not a distinct advantage over other models. However, when it comes to more than one inversion, we will show this power balance equation method has an advantage over other models. But first, let us look into the Fabry-Perot case as a start.

To discuss the dynamics here, we will consider a single cavity laser with length $L$ from $z = 0$ and $z = L$. The refractive index is $n_c$ , constant population inversion in space, $N_c(t)$ and extinction coefficient $\kappa_c$. Rather than dealing with the local $N(z,t)$, we characterise the $N_c(t)$ term as the global population inversion or the spatially-averaged inversion over the entire cavity which are related by,

$$N_c(t) = \frac{1}{L}\int_0^L N(z,t)dz. \tag{6.23}$$

To use the spatial averaged inversion instead of $N(z,t)$, we consider the local variation in the population in version as either small enough to have a negligible effect or that if these variations occur, they will level out quite fast in comparison to the remaining dynamics.

If we calculate the spatial derivative of $Q_R(z,t)$, we are able to obtain a power balance equation. Using (6.11)-(6.15) to calculate this, we obtain,

$$\begin{aligned}\frac{\partial Q_R(z,t)}{\partial z} =& A(t)\frac{c}{n_c}\left(\frac{d}{dz}(E(z)B(z)^*) + \text{c.c}\right).\\ =& -\frac{n_c}{c}\dot{Q}_A(z,t) + \frac{1}{2n_c c}(n_c^2\kappa_c^2 + \mathscr{L}(\Delta)\Delta(\omega)N_c(t))(\dot{Q}_A(z,t)\\ &+ \dot{Q}_S(z,t)) - \frac{\omega}{n_c c}(2n_c^2\kappa_c - \mathscr{L}(\Delta)N_c(t))(Q_A(z,t) + Q_S(z,t))\\ &+ \frac{\mathscr{L}(\Delta)\Delta(\omega)}{n_c c}\dot{N}_c(t)(Q_A(z,t) + Q_S(z,t))\end{aligned} \tag{6.24}$$

We will make a couple of assumptions to simplify our equation. First, we assume that $\kappa_c$ and $\Delta(\omega)$ are small such that terms with $(n_c^2\kappa_c^2 + \mathscr{L}(\Delta)\Delta(\omega)N_c(t))(\dot{Q}_A(z,t) + \dot{Q}_S(z,t)) \ll (2n_c^2\kappa_c - \mathscr{L}(\Delta)N_c(t))(Q_A(z,t) + Q_S(z,t))$ are negligible. Secondly, we further note $\Delta(\omega)\dot{N}_c(t) \ll \omega N_c(t)$ as the detuning between the modal frequency and transition frequency is small. Taking these assumptions into account, (6.24) becomes,

$$\dot{Q}_A(z,t) = -\frac{c}{n_c}\frac{\partial Q_R(z,t)}{\partial z} - \frac{\omega}{n_c^2}(2n_c^2\kappa_c - \mathscr{L}(\Delta)N_c(t))(Q_A(z,t) + Q_S(z,t)). \tag{6.25}$$

Taking the integral over the cavity, we obtain,

$$\begin{aligned}\int_0^L \dot{Q}_A(z,t)dz = &-\frac{c}{n_c}(Q_R(L,t)-Q_R(0,t)) - \frac{\omega}{n_c^2}(2n_c^2\kappa_c \\ &- \mathscr{L}(\Delta)N_c(t))\int_0^L (Q_A(z,t)+Q_S(z,t))dz,\end{aligned} \tag{6.26}$$

which is the power balance equation. The term of the left hand side is the change in energy density of the mode, $Q_A(z,t)$, which decreases due to absorption, $2\omega\kappa_c\int_0^L(Q_A(z,t)+Q_S(z,t))dz$ and leakage from the boundaries of the cavity, $\frac{c}{n_c}(Q_R(L,t)-Q_R(0,t))$. However the energy of the mode increases due to the population inversion from $\mathscr{L}(\Delta)N_c(t)\int_0^L(Q_A(z,t)+Q_S(z,t))dz$. Using (6.13)-(6.15), in terms of $A(t)$, this power balance equation becomes,

$$\dot{A}(t) = -\frac{A(t)}{\zeta_{LI}}\left(\frac{c}{n_c}(q_R(L)-q_R(0)) + \frac{\omega}{n_c^2}(2n_c^2\kappa_c - \mathscr{L}(\Delta)N_c(t))\zeta_{AM}\right), \tag{6.27}$$

where

$$\zeta_{LI} = \int_0^L q_A(z)dz, \tag{6.28}$$

and

$$\zeta_{AM} = \int_0^L (q_A(z)+q_S(z))dz. \tag{6.29}$$

This equation is analogous to the derivation of Poynting's theorem where the energy density equation of the electromagnetic field is obtained in [22].

### 6.2.2 Population Inversion Dynamical Equation

There are two dynamical variables we are considering, one for the amplitude which corresponds to the scaling of the electromagnetic field, $A(t)$ and the population inversion. We can now introduce the dynamical equation for local $N(z,t)$ which comes from the Maxwell-Bloch equations (2.83). In the $Q$-time basis,

$$\dot{N}(z,t) = -\gamma_N\left(N(z,t) - \Lambda_c + \frac{1}{2}\mathscr{L}(\Delta)N(z,t)(Q_A(z,t)+Q_S(z,t))\right), \tag{6.30}$$

where $\Lambda_c$ is the constant pump and using the relation $|E(z)|^2 = \frac{q_A(z)+q_S(z)}{2}$. As discussed previously, we will replace $N(z,t)$ with the global population inversion,

due to the small or negligible local variations or the variations are fast and level out quickly in terms of the population inversion dynamics. As a result, we instead consider the spatially averaged, or global population inversion, denoted as $N_c(t)$ for the entire cavity. We thus write the dynamical equation of $N_c(t)$ with reference to (6.30), as,

$$\dot{N}_c(t) = -\gamma_N \left( N_c(t) - \Lambda_c + \frac{1}{2L} \mathscr{L}(\Delta) N_c(t) A(t) \zeta_{AM} \right), \tag{6.31}$$

where, we have integrated over the entire cavity of length $L$ which results in $\zeta_{AM}$.

## 6.3 Spatial Variation of Cavity and the $q$-basis

So far we have discussed the composition of dynamical equations for both $A(t)$ and $N_c(t)$. However, this does not take into account the spatial dependence of the mode which would satisfy the open boundary conditions. First let us discuss what happens at threshold. As mentioned throughout, we have a steady-state solution for this situation. Thus (6.25) becomes,

$$\frac{dq_R(z)}{dz} = -\frac{\omega}{n_c c}(2n_c^2\kappa_c - \mathscr{L}(\Delta)\Lambda_c)(q_A(z) + q_S(z)), \tag{6.32}$$

where $\Lambda_c$ is a constant pump rate that is calculated by using the stationary inversion approximation. This is assuming the electric field intensity is small and thus spatial hole burning can be neglected. The electric field satisfying this is known as TCF states [19], as used in the previous chapter.

Now let us consider (6.32) in terms of the eigenvalues $x_n$ calculated in the previous chapter and let $\chi_g = x_n(N_c(t))N_c(t)$. In this instance $N_c(t)$ becomes time dependent and for each $N_c(t)$, there exists an $x_n(N_c(t))$ which satisfies the following equation,

$$\frac{dq_R(z)}{dz} = -\frac{\omega}{n_c c}(2n_c^2\kappa_c + \mathrm{Im}(x_n)N_c(t))(q_A(z) + q_S(z)). \tag{6.33}$$

To maintain (6.33) in the steady-state form in the same way as (6.32), the gain susceptibility $\chi_g$ must remain constant. As a result, if $N_c(t) > \Lambda_c$, then $-\mathrm{Im}(x_n) < \mathscr{L}(\Delta)$ and vice versa. This indicates that as $N_c(t)$ scales, $\mathrm{Im}(x_n)$ must counteract the scaling of the population inversion to still allow the gain susceptibility to be constant, thus maintaining (6.33). This discussion of is analogous to Chapter 4, in particular Figure 4.1.

The fact that the mode no longer is in the stationary situation is accounted for by the amplitude $A(t)$. Although this is an assumption, it is still valid close to threshold. We similarly obtain the spatial profiles for the remaining variables $q_A(z)$, $q_S(z)$ and $q_I(z)$ which are given by (4.31), (4.30) and (4.29) respectively,

$$\begin{aligned}\frac{dq_A(z)}{dz} =&\frac{\omega}{n_c c}\Big((n_c^2\kappa^2 - \mathrm{Re}(x_n)N_c(t))q_I(z) \\ &- (2n_c^2\kappa + \mathrm{Im}(x_n)N_c(t))q_R(z)\Big),\end{aligned} \tag{6.34}$$

$$\begin{aligned}\frac{dq_S(z)}{dz} =&\frac{2\omega n_c}{c}q_I(z) - \frac{\omega}{n_c c}(n_c^2\kappa_c^2 - \mathrm{Re}(x_n)N_c(t))q_I(z) \\ &+ \frac{\omega}{cn_c}\left(2n_c^2\kappa_c + \mathrm{Im}(x_n)N_c(t)\right)q_R(z),\end{aligned} \tag{6.35}$$

$$\frac{dq_I(z)}{dz} = -\frac{2\omega n_c}{c}q_S(z) + \frac{\omega}{n_c c}(n_c^2\kappa_c^2 - \mathrm{Re}(x_n)N_c(t))(q_A(z) + q_S(z)). \tag{6.36}$$

We can determine the value of $x_n$ by using the transfer matrix method from Chapter 4. Then we are able to determine if a mode is above or below threshold as follows, if $\mathscr{L} < -\mathrm{Im}(x_n)$, a mode described by (6.33) is below threshold and $\mathscr{L} > -\mathrm{Im}(x_n)$ signifies a mode above threshold. Moreover, when $\mathscr{L} = -\mathrm{Im}(x_n)$, (6.33) is the same as (6.32). This is because if this arises, the laser is at threshold.

### 6.3.1 Dynamics of $A(t)$ with $x_n$

It is quite simple to relate the dynamics of $A(t)$ to the eigenvalue $x_n$ by using (6.33). Integrating it over the laser cavity, one obtains,

$$q_R(L) - q_R(0) = -\frac{\omega}{n_c c}(2n_c^2\kappa_c + \mathrm{Im}(x_n)N_c(t))\zeta_{AM}. \tag{6.37}$$

Rearranging yields,

$$-\frac{\omega}{n_c^2}\mathrm{Im}(x_n)N_c(t)\zeta_{AM} = \frac{c}{n_c}(q_R(L) - q_R(0)) + \frac{\omega}{n_c^2}2n_c^2\kappa_c\zeta_{AM}. \tag{6.38}$$

With this and (6.27), we obtain the following dynamical equation for $A(t)$,

$$\dot{A}(t) = \frac{\omega}{n_c^2}(\mathrm{Im}(x_n) + \mathscr{L}(\Delta))A(t)N_c(t)\frac{\zeta_{AM}}{\zeta_{LI}}. \tag{6.39}$$

Since $\text{Im}(x_n) < 0$, (6.39) acts like a gain and loss dynamical equation. To explain the significance of the eigenvalue consider Figure 4.3. Recall that the circle in this figure refers to whether you are at, above or below threshold. Suppose $-\text{Im}(x_n) > \mathscr{L}(\Delta)$, this indicates the laser is below threshold as mentioned, then $\dot{A}(t) < 0$ and as a result, will decay. In the figure, this is when the mode outside the circle. Conversely, $-\text{Im}(x_n) < \mathscr{L}(\Delta)$ indicates the mode above threshold and amplitude increases as $\dot{A} > 0$, or in the circle. The steady-state solution occurs when the mode is at threshold as $\dot{A}(t) = 0$, or on the circle. Thus (6.39) physically makes sense using the idea of the eigenvalue problem in the previous chapter. This means that we now have dynamical equations for a time-dependent electromagnetic field and population inversion where a single cavity laser satisfies with open boundaries. If we look at the integral terms which were defined previously which were $\zeta_{AM}$ and $\zeta_{LI}$, we see that with a single population inversion varying in time, these terms will remain constant. This will only be true in the case of a single population inversion. This will be discussed in further detail in later sections. For the coupled-cavity case, these will vary and as a result, we can see interesting spatial changes as a result of the dynamics.

### 6.3.2 Single-Cavity Dynamical Equations

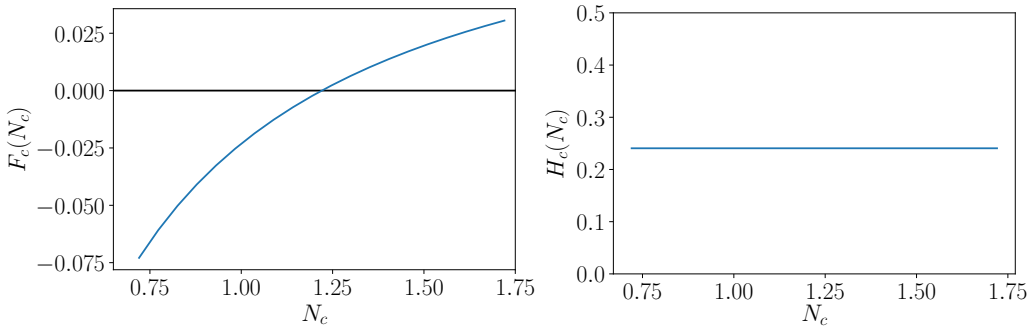
In this subsection and for the Fabry-Perot cavity, we will write $A(t)$ and $N_c(t)$ as $A$ and $N_c$. We will also write $\Delta$ as,

$$\Delta = \frac{k_0 - k}{\tilde{\gamma}_P}, \tag{6.40}$$

where $k_0 = \frac{\omega_0}{c}$ and $\tilde{\gamma}_P = \frac{\gamma_P}{c}$. We will now consider the single cavity laser equations which we derived earlier and are given by (6.27) and (6.31). We can write these equations in a self-consistent way as follows. We first define two functions $F_c(N_c)$ and $H_c(N_c)$ which relates to the dynamical equations for $A$ and $N_c$ respectively. They are given by,

$$F_c(N_c) = \frac{k(N_c)}{n_c^2}(\text{Im}(x_n(N_c)) + \mathscr{L}(\Delta))\frac{\zeta_{AM}(N_c)}{\zeta_{LI}(N_c)}, \tag{6.41}$$

$$H_c(N_c) = \frac{1}{2L}\mathscr{L}(\Delta)\zeta_{AM}(N_c). \tag{6.42}$$




(a) $F_c(N_c)$ varying around threshold.

(b) $H_c(N_c)$ varying around threshold.

Figure 6.1: Variation of $N_c$ for $F_c(N_c)$ and $H_c(N_c)$. For both plots, $k_0 = 0.95$, $\tilde{\gamma}_P = 1$ and $k = 0.94407$. Note the laser structure has $L = 10$ with $\tilde{n}_b = 3 + 0.13i$.

With these functions in mind, we can write the dynamical equations (6.39) and (6.30) for $A$ and $N_c$ as,

$$\dot{A} = cF_c(N_c)N_cA, \tag{6.43}$$

$$\dot{N}_c = -\gamma_N \left(N_c - \Lambda_c + H_c(N_c)N_cA\right). \tag{6.44}$$

Thus we have arrived at a set of self-consistent dynamical equations for variables $A$ and $N_c$. It is worthy to investigate the behaviour of the newly defined functions $F_c(N_c)$ and $H_c(N_c)$ close to threshold by varying $N_c$. To do this, we first fix the atomic transition wave number $k_0 = 0.95$, and for simplicity choose $\tilde{\gamma}_P = 1$, and using the $q$-basis, with (4.82), (4.47) and (4.48), we can determine when $F_c(N_c) = 0$, to find when (6.43) is zero. We can see Figure 6.1(a) shows the variation of $F_c(N_c)$ close to the lasing threshold. In the case of Figure 6.1(b), we see that close to threshold, $H_c(N_c)$ does not change with respect to a changing $N_c$. As a result of this, the dynamical equations for both $A$ and $N_c$ become easier to solve.

## 6.4 Coupled-Cavity Open Laser

So far, we have derived the dynamical equations for an open single-cavity laser. Now we can turn our attention to a more complicated structure, namely a coupled cavity open laser system given by Figure 6.2. For this example, we will take the refractive index and extinction to be equivalent in both cavities, $n_b$ and $\kappa_b$ respectively. Cavity 1 is of length $L_1$ with time-varying population inversion $N_1(t)$, which is spatially constant. The second cavity is of length $L_2$ with time varying population inversion

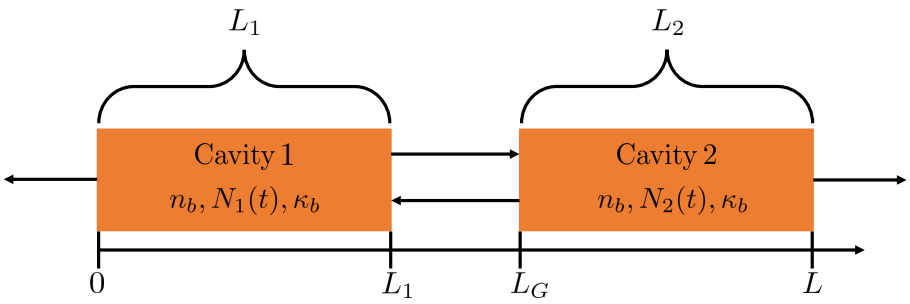



Figure 6.2: A single open laser with coupled cavities of length $L$ where each cavity has refractive index $n_b$ and extinction coefficient $\kappa_b$. The population inversions for cavity 1 and cavity 2 are $N_1(t)$ and $N_2(t)$ respectively. The gap and outside the laser have refractive index $n_a$.

$N_2(t)$. In between there is the "Gap" region which has length $L_G - L_1$ and refractive index $n_1$. We make the assumption that there is no loss in the gap or absorption.

Let $A(t)$, as discussed in the previous sections be the scaling amplitude over the entire laser. In terms of the $Q$-time basis, we will denote (6.13)-(6.16) as $Q_A^{(s)}(z,t)$, $Q_S^{(s)}(z,t)$,$Q_R^{(s)}(z,t)$ and $Q_I^{(s)}(z,t)$ where the index denotes each section. $s$ is either 1, $G$ or 2 and the first cavity, the gap and the second cavity respectively. The same applies to the $q$-basis denoted by $q_A^{(s)}(z)$, $q_S^{(s)}(z)$, $q_R^{(s)}(z)$ and $q_I^{(s)}(z)$. Furthermore, $A(t)$ describes the scaling of the mode over the entire coupled laser structure. Although there exist separate changes to the mode in time in each cavity, we assume they are small in comparison to changes of the entire mode.

### 6.4.1 Dynamics of Population Inversion

For each cavity, we can obtain the the population inversion the same way as (6.31). For the first/second cavity with $N_{1/2}(t)$, its dynamical equation is given by,

$$\dot{N}_{1/2}(t) = -\gamma_N \left( N_{1/2}(t) - \Lambda_{1/2} + \frac{A(t)}{2L_{1/2}} \mathscr{L}(\Delta) N_{1/2}(t) \zeta_{AM}^{(1/2)} \right), \tag{6.45}$$

where $\Lambda_1$ and $\Lambda_2$ are the pumps of the first and second cavities. The integral over the intensity of the electric field in the first and second cavities respectively are

$$\zeta_{AM}^{(1)} = \int_0^{L_1} (q_A^{(1)}(z) + q_S^{(1)}(z)) dz, \tag{6.46}$$

and

$$\zeta_{AM}^{(2)} = \int_{L_G}^{L} (q_A^{(2)}(z) + q_S^{(2)}(z))dz. \tag{6.47}$$

### 6.4.2 Power Balance Equation

The power balance equation for each section of the laser is obtained from the results of the one cavity laser. For $0 < z < L_1$, (6.27) with some reordering becomes,

$$A(t)(q_R^{(1)}(L_1) - q_R^{(1)}(0)) = -\frac{n_b}{c}\zeta_{LI}^{(1)}\dot{A}(t) - A(t)\frac{\omega}{n_b c}(2n_b^2\kappa_b - \mathscr{L}(\Delta)N_1(t))\zeta_{AM}^{(1)}, \tag{6.48}$$

where

$$\zeta_{LI}^{(1)} = \int_0^{L_1} q_A^{(1)}(z)dz. \tag{6.49}$$

For $L_A < z < L_G$, since there is no absorption or gain, (6.48) for the gap can be written as,

$$A(t)(q_R^{(G)}(L_G) - q_R^{(G)}(L_1)) = -\frac{n_a}{c}\zeta_{LI}^{(G)}\dot{A}(t) \tag{6.50}$$

where

$$\zeta_{LI}^{(G)} = \int_{L_1}^{L_G} q_A^{(G)}(z)dz. \tag{6.51}$$

Finally the same equation can be written for the final section, cavity 2,

$$A(t)(q_R^{(2)}(L) - q_R^{(2)}(L_G)) = -\frac{n_b}{c}\zeta_{LI}^{(2)}\dot{A}(t) - A(t)\frac{\omega}{n_b c}(2n_b^2\kappa_b - \mathscr{L}(\Delta)N_2(t))\zeta_{AM}^{(2)}, \tag{6.52}$$

where

$$\zeta_{LI}^{(2)} = \int_{L_G}^{L} q_A^{(2)}(z)dz. \tag{6.53}$$

Due to the fact each function from the $q$-basis is dependent on the refractive index, the boundaries are discontinuous. For example $q^{(1)}(L_1) \neq q^{(G)}(L_1)$. However, we have already calculated the boundary conditions in the previous chapter namely (4.63)-(4.66). As a result, we can relate $q_R$ terms at the boundary. We see that $q_R^{(1)}(L_1) = \frac{n_a}{n_b}q_R^{(G)}(L_1)$ and $q_R^{(G)}(L_G) = \frac{n_b}{n_a}q_R^{(2)}(L_G)$. Using these conditions, we can relate (6.48)-

(6.52) to obtain,

$$\begin{aligned}\dot{A}(t) = -\frac{A(t)c}{\zeta_M}\Bigg(& q_R^{(2)}(L) - q_R^{(1)}(0) + \frac{2n_b\kappa_b\omega}{c}[\zeta_{AM}^{(1)} + \zeta_{AM}^{(2)}] \\ & - \frac{\omega}{n_b c}\mathscr{L}(\Delta)[N_1(t)\zeta_{AM}^{(1)} + N_2(t)\zeta_{AM}^{(2)}]\Bigg)\end{aligned} \tag{6.54}$$

where $\zeta_M = n_b\zeta_{LI}^{(1)} + \frac{n_a^2}{n_b}\zeta_{LI}^{(G)} + n_b\zeta_{LI}^{(2)}$.

### 6.4.3 Steady-state solution and scaling with $x_n$

As in the previous section with a single cavity laser, we will introduce the $x_n$ term the same way however it scales to satisfy the change in both population inversion terms $N_1(t)$ and $N_2(t)$. We will use the same formalisation here. Firstly, (6.54) is the following at threshold,

$$\frac{\omega}{n_b c}\mathscr{L}(\Delta)[\Lambda_1\zeta_{AM}^{(1)} + \Lambda_2\zeta_{AM}^{(2)}] = q_R^{(2)}(L) - q_R^{(1)}(0) + \frac{2n_b\kappa_b\omega}{c}[\zeta_{AM}^{(1)} + \zeta_{AM}^{(2)}], \tag{6.55}$$

where the population inversion is equal to the pumps $\Lambda_1$ and $\Lambda_2$ in the first and second cavities respectively. The $q$-basis satisfies the conditions for TCF states in the equation above. However, this no longer applies off threshold where the population inversions are no longer pumps and with eigenvalue $x_n$ satisfy the following equation,

$$-\frac{\omega}{n_b c}\mathrm{Im}(x_n)[N_1(t)\zeta_{AM}^{(1)} + N_2(t)\zeta_{AM}^{(2)}] = q_R^{(2)}(L) - q_R^{(1)}(0) + \frac{2n_b\kappa_b\omega}{c}[\zeta_{AM}^{(1)} + \zeta_{AM}^{(2)}], \tag{6.56}$$

which is equivalent to (6.38).

With all this in mind, we can write the dynamical equation for $A(t)$ as,

$$\begin{aligned}\dot{A}(t) = \frac{A(t)\omega}{\zeta_M n_b}(\mathrm{Im}(x_n(N_1(t), N_2(t))) + \mathscr{L}(\Delta))[N_1(t)\zeta_{AM}^{(1)}(N_1(t), N_2(t)) \\ + N_2(t)\zeta_{AM}^{(2)}(N_1(t), N_2(t))].\end{aligned} \tag{6.57}$$

Using the fact that $\zeta_M$ and both $\zeta_{AM}^{(1)}$ and $\zeta_{AM}^{(2)}$ are positive, we see the same explanation for the effect of the term $(\mathrm{Im}(x_n) + \mathscr{L}(\Delta))$ as the single cavity Fabry-Perot laser. We see that at threshold, $-\mathrm{Im}(x_n) = \mathscr{L}(\Delta)$ and as a result $\dot{A}(t) = 0$. We see that the scaling factor for the electromagnetic field decreases over time if $-\mathrm{Im}(x_n) > \mathscr{L}(\Delta)$. Finally, $A(t)$ will increase if $-\mathrm{Im}(x_n) < \mathscr{L}(\Delta)$. With all this in mind, we have now

obtained a full set of dynamical equations which can be used to describe complex phenomenon involving dynamics close to threshold. Moreover, we can also provide further insight into the behaviour of the spatially integrated terms $\zeta_M(N_1(t), N_2(t))$ and $\zeta^{(i)}_{AM}(N_1(t), N_2(t))$. We can determine $x_n$ for $N_1(t)$ and $N_2(t)$ for a particular $\omega$ by using the transfer matrix condition from Chapter 4, namely (4.82). In Chapter 4, we took constant $\omega$ (or $k$) to determine modes above and below threshold and varied the pump. This time, we would like to be more accurate and change $\omega$ with the changing of dynamical variables $N_1(t)$ and $N_2(t)$. To do this, we will determine $\omega$ by finding the closest mode at threshold with the same proportion for $N_1(t)$ and $N_2(t)$. Thus this $\omega$ can be used with (4.82) along with $N_1(t)$ and $N_2(t)$. To be more specific, recall from Chapter 4 when we introduced the term $\eta$ such that,

$$\Lambda_2 = \eta\Lambda_1, \tag{6.58}$$

that all elements of the $q$-basis spatial distribution. will be the same for all combinations of $\Lambda_1$ and $\Lambda_2$ as long as $\eta$ is the same. Thus we will approximate modes above and below threshold to have the same $\omega$ as modes at threshold with the same $\eta$. Thus we can say that for some positive real constant $\vartheta$, we can write,

$$\zeta_M(N_1(t), N_2(t)) = \zeta_M(\vartheta N_1(t), \vartheta N_2(t)), \tag{6.59}$$

$$\zeta^{(i)}_{AM}(N_1(t), N_2(t)) = \zeta^{(i)}_{AM}(\vartheta N_1(t), \vartheta N_2(t)). \tag{6.60}$$

However, for changing $\eta$, we see that $\zeta_M(N_1(t), N_2(t))$ and $\zeta^{(i)}_{AM}(N_1(t), N_2(t))$ are not constant when $N_1(t)$ and $N_2(t)$ varies. We will see this in the next section.

## 6.5 Coupled-Cavity Dynamical Equations

For this section,we will write the time-dependent quantities for the coupled cavities $A(t)$, $N_1(t)$ and $N_2(t)$ as $A$, $N_1$ and $N_2$ respectively. In a similar way to the single cavity regime, we can write the dynamical equations for $A$, $N_1$ and $N_2$ as a set of three self consistent set of equations. Firstly we define the function $F_{12}(N_1, N_2)$ such that,

$$\begin{aligned} F_{12}(N_1, N_2) = \frac{k(N_1, N_2)}{\zeta_M(N_1, N_2) n_b} &(\mathrm{Im}(x_n(N_1, N_2)) + \mathscr{L}(\Delta)) \\ &\times [N_1 \zeta^{(1)}_{AM}(N_1, N_2) + N_2 \zeta^{(2)}_{AM}(N_1, N_2)] \end{aligned} \tag{6.61}$$

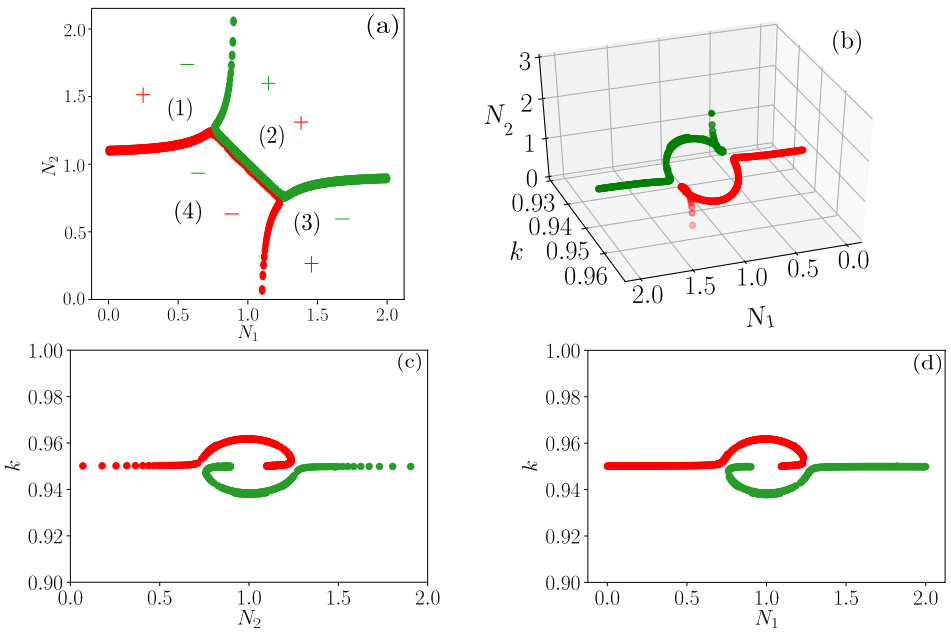



Figure 6.3: Zero branches for $F_{12}(N_1, N_2)$ for varying $N_1$, $N_2$ and $k$ for a fixed $k_0 = .95$ and $\tilde{\gamma}_P = 1$ for a coupled cavity laser with $l_1 = l_2 = 10$, $l_g = 1$ and $\tilde{n}_b = 3 + 0.13i$.

which corresponds to the dynamical equation for $A$ where we have written the frequency in terms of the wavenumber $k$. We further define two functions $H_1(N_1, N_2)$ and $H_2(N_1, N_2)$ which correspond to the dynamical equations for $N_1$ and $N_2$ respectively. They are given by,

$$H_1(N_1, N_2) = \frac{1}{2L_1}\mathscr{L}(\Delta)\zeta^{(1)}_{AM}(N_1, N_2), \tag{6.62}$$

$$H_2(N_1, N_2) = \frac{1}{2L_2}\mathscr{L}(\Delta)\zeta^{(2)}_{AM}(N_1, N_2). \tag{6.63}$$

Thus we arrive at the three self-consistent equations which are written as,

$$\dot{A} = cF_{12}(N_1, N_2)A, \tag{6.64}$$

$$\dot{N}_1 = -\gamma_N \left[N_1 - \Lambda_1 + H_1(N_1, N_2)AN_1\right], \tag{6.65}$$

$$\dot{N}_2 = -\gamma_N \left[N_2 - \Lambda_2 + H_2(N_1, N_2)AN_2\right]. \tag{6.66}$$

To provide greater understanding for these equations, we will discuss some behaviour given by the functions $F_{12}(N_1, N_2)$, $H_1(N_1, N_2)$ and $H_2(N_1, N_2)$.

### 6.5.1 Dynamics of $N_1$ and $N_2$ when $\dot{A} = 0$

Firstly, let us consider the situation such that $F_{21}(N_1, N_2) = 0$. This means that for certain values of the population inversion in each cavity and $k$, we can determine when $\dot{A} = 0$. We can investigate this by using the $q$-basis to determine for which combination of $N_1$, $N_2$ and $k$, we have $F_{21}(N_1, N_2) = 0$ for a fixed $k_0 = \frac{\omega_0}{c}$ and $\tilde{\gamma}_P = \frac{\gamma_P}{c}$. For modes located in the range $k = 0.92$ to $k = 0.97$ for a fixed $k_0 = 0.95$ and for simplicity take $\tilde{\gamma}_P = 1$. We then use the transfer matrix condition (4.82) along with (4.47) and (4.48) to determine when $F_{21}(N_1, N_2) = 0$. The results are shown in Figure 6.3 for modes located in the $k$ region we are considering. We can see that in Figure 6.3(a), that there are two branches for values of $N_2$ with varying $N_1$ that meets another branch which appear to coalesce where multiple modes exist in this straight line region and these to branches separate again for higher $N_1$. In fact, we can see this picture has similar characteristics as the figures shown with the simple CMT, Figure 3.2(c) and the eigenvalue branches shown in 4.20(c). However, the idea of these branches coalescing is not true, as seen in Figure 6.3(b). We can clearly see that there are two distinct branches and they do not coalesce because of the $k$. This is also confirmed by looking at Figures 6.3(c) and (d). We also note that the two branches created in Figure 6.3(c) and 6.3(d) are also similar to the shapes seen in when we discussed CMT, such as Figure 3.4(b) and 4.20(a) for the eigenvalue branches using the $q$-basis. These figures show clearly how $k$ changes on both branches with $k_0 = 0.95$. Taking Figure 6.3(d), we see that the green branch has almost the $k$ as the atomic transition wavenumber at high $N_1$. Then it decreases in $k$ when approaching the red branch and reaches about $N_1 = 0.75$, where the inversion in the first cavity starts increasing at $k$ close to $k_0$. A similar situation occurs for the red branch where at low $N_1$, $k \approx k_0$ but when it approaches the green branch $k > k_0$. At about $N_1 = 1.2$, we see $k$ being close to $k_0$ once again as $N_1$ slightly decreases.

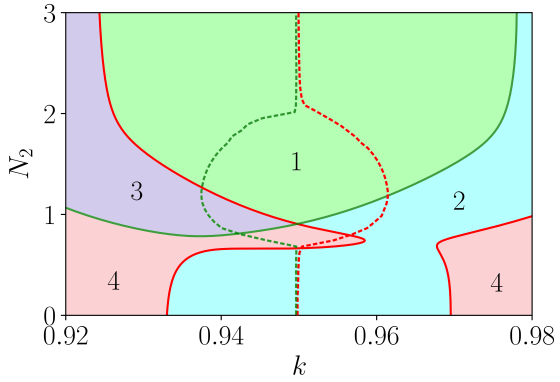
Let us focus in on what can happen for the dynamics of $N_1$ and $N_2$ by assuming a stationary electromagnetic field which means $F_{21}(N_1, N_2) = 0$. Let us consider now the effect of a changing of $N_1$ and $N_2$ by looking at Figure 6.3(b). We can see that the dynamics of $N_1$ and $N_2$ can only stay on either the green or red branch when $\dot{A} = 0$. For the red branch, it starts at low $N_1$ and increases while $N_2$ varies little until about $N_1 = 1.2$, then $N_2$ goes towards zero. Thus the red branch goes from zero $N_1$ to zero $N_2$. The other branch is quite the opposite. We can see that on the green branch, we first come from large $N_1$ for with fairly constant $N_2$ until about $N_1 = 0.75$ where $N_1$ starts to slightly increase once more but $N_2$ increases more dramatically.

The next question that Figure 6.3(a) can answer is how will the population inversion change in each cavity with a slight deviation from $F_{12}(N_1, N_2) = 0$. First let us consider what happens moving slightly away from the red branch. If we consider moving away from the red branch to region (1), we will see an increasing $A$ along with regions (2) and (3). We only see a deceasing $A$ in region (4) and this is because both inversions are too low to maintain the overall laser to be above threshold. However, the green branch proves more interesting. If we slightly deviate from the green branch into region (1), we see that even for high $N_2$, we have the case that $A$ will decrease over time. This is because for these particular modes, a high $N_2$ is not sufficient for the laser to be above threshold because of low $N_1$. The same is true for region (3) except for low $N_2$ and high $N_1$. For regions (2) and (4), we see the same outcome as the red branch.

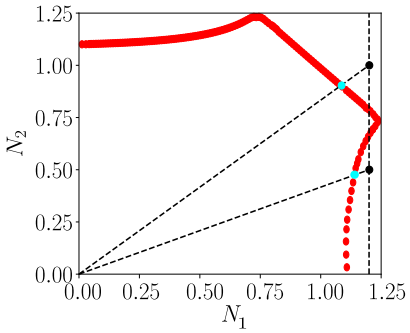
### 6.5.2 Approximation of modes above and below threshold

We will call the red and green modes, those which correspond to the red and green threshold branches respectively in Figure 6.4. We will investigate how the the green and red modes shown in Figure 6.4 vary around their threshold branches. We use the following method to determine modes around threshold for both the green and red modes. Firstly, we fix the $k_0$ and $\gamma_P$, along with the remaining physical constants we have done in previous chapters. Then for each mode (green or red), we determine the $k$ from the threshold branch (green or red depending on mode) that has the same ratio $\eta$ as the relation between $N_1$ and $N_2$ for the mode away from threshold. Examples of these modes mapped from the threshold branches to above and below threshold are shown for the red branch in Figure 6.4(b) and for the green branch in Figure 6.4(c).

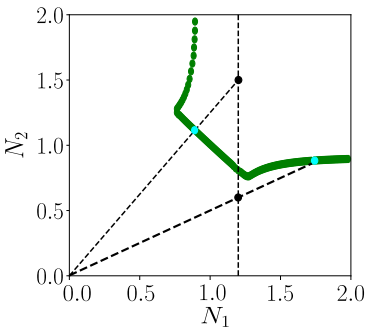
With this method for choosing $k$, we can now get our first idea of how $k$ changes with moving $N_1$ and $N_2$. To relate to work completed in previous chapters, we will fix $N_1 = 1.2$ and vary $N_2$ for both the green and red modes. This corresponds to the dashed vertical line in both Figures 6.4(b) and (c). These corresponding modes can be seen varying in $k$ as the dashed green and red lines in Figure 6.4(a) for green and red modes respectively. We can thus relate the threshold lines obtained in Chapters 4 and 5 to these green and red dashed lines in this figure. The green full line is the threshold line for the green mode while the red full line is the threshold line for the red mode. These are the same same threshold lines as those seen in Figures 5.6(e) and 4.4. For the chosen $k$ we are exploring, we can divide Figure 6.4(a) into four distinct regions. We see that for region 1, both the green and red modes are above threshold,




(a) Threshold region from Chapter 4 with the variation of $F_{12}(N_1, N_2)$ along the red dashed line (red mode) and green dashed line (green mode). The four different regions are as follows: 1 is above threshold for both the green and red modes, 2 is above threshold for the red mode only, 3 is above threshold for the green mode only and 4 is below threshold for both modes.




(b) Threshold modes along the red branch where the modes off-threshold (vertical black line) are mapped to threshold (black dots mapped to cyan dots)




(c) Threshold modes along the green branch where the modes off-threshold (vertical black line) are mapped to threshold (black dots mapped to cyan dots)

Figure 6.4: Variation of $N_2$ and $k$ with fixed $N_1 = 1.2$. For all plots, $k_0 = 0.95$, $\tilde{\gamma}_P = 1$. Note the laser structure has $l_1 = l_2 = 10$ and $l_g = 1$ with $\tilde{n}_b = 3 + 0.13i$.

regions 2 and 3 correspond to the red and green modes only above threshold. Finally in region 4, we see both modes are below threshold.

With all of this in mind, we can predict how the sample modes shown as green and red dashed lines behave around threshold. Taking the green mode first, we see that for low $N_2$, $k$ is close $k_0 = 0.95$ and is below threshold. However with increasing $N_2$, the green mode goes from region 2 to region 4 but is still below threshold. At the same time, $k$ decreases. Then the green mode enters region 3 and is above threshold, still with decreasing $k$. After this, the mode remains above threshold in region 1 where $k$ returns to approximately the same value as $k_0$. For the red mode, it starts at approximately at the same $k$ as the green, close to $k_0$. In contrast, the red mode is above threshold in region 2. With increasing $N_2$, we see $k$ starts to increase also but more importantly, the red mode goes below threshold as it is in region 4. Then the red mode continually increases in $k$ as it enters region 2 and thus goes above threshold again. Finally, $k$ reduces close to $k_0$ once again with increasing $N_2$ and goes into region 1.

We can already draw a few conclusions from the analysis presented here. In terms of both modes, we see that both modes act differently with increasing $N_2$. The green mode is below threshold until a higher $N_2$ than the red mode which was already above threshold due to a sufficiently high $N_1$. Moreover, for the red mode, we see the same counter-intuitive effect of an increasing $N_2$ where the red mode goes below threshold and above once again. The green mode does not show the same effect as the red, as it started below threshold.

### 6.5.3 Variation of $F_{12}(N_1, N_2)$, $H_1(N_1, N_2)$ and $H_2(N_1, N_2)$

The next avenue we would like to explore is investigating how $F_{12}(N_1, N_2)$, $H_1(N_1, N_2)$ and $H_2(N_1, N_2)$ change when we vary $N_1$ and $N_2$ close to threshold. With the $k$ from the previous subsection, we use it, along with $N_1$, $N_2$ and the transfer matrix condition (4.82) from Chapter 4, to find $x_n(N_1, N_2)$ for both the red and green modes. $F_{12}(N_1, N_2)$ is an important function for an analysis into the dynamics of the scaling term of the electromagnetic field, $A$. As mentioned previously, if $F_{12}(N_1, N_2) > 0$, this indicates that the intensity of the mode increases in time, $\dot{A} > 0$. If $F_{12}(N_1, N_2) < 0$, this indicates that the intensity of the mode decreases in time, $\dot{A} < 0$. We have already discussed in detail the threshold condition which is $F_{12}(N_1, N_2) = 0$. With the determination of $x_n(N_1, N_2)$, we use the $q$-basis equations in matrix form, (4.68), to determine (6.61), (6.62) and (6.63).

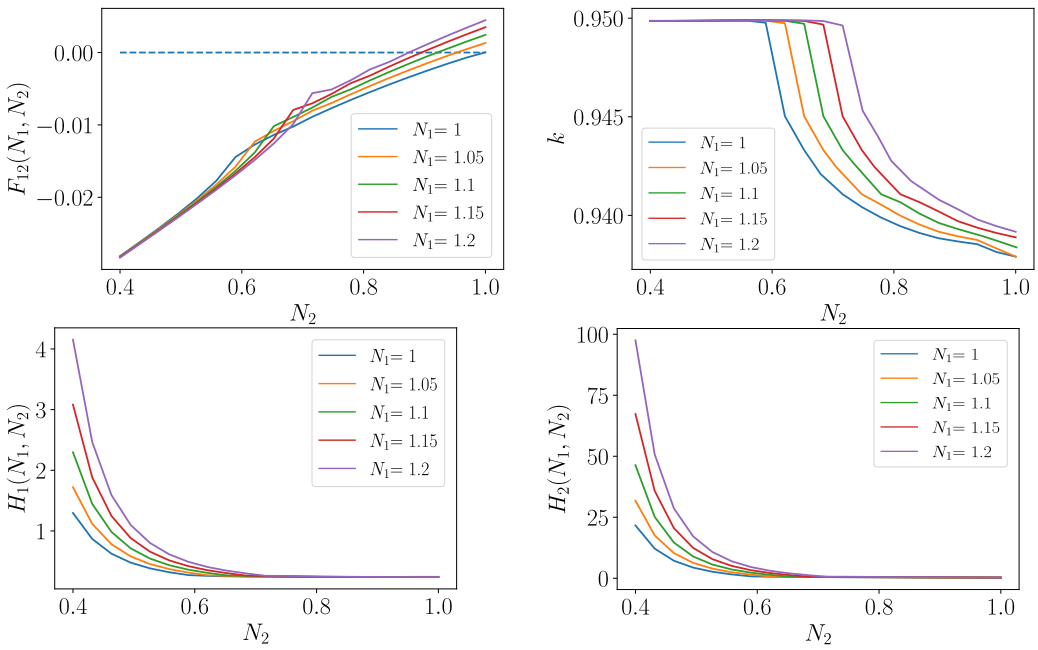



Figure 6.5: Variation of $N_2$ with fixed $N_1$ for $F_{12}(N_1, N_2)$, $k$, $H_1(N_1, N_2)$ and $H_2(N_1, N_2)$ for the green mode. For all plots, $k_0 = 0.95$, $\tilde{\gamma}_P = 1$. Note the laser structure has $l_1 = l_2 = 10$ and $l_g = 1$ with $\tilde{n}_b = 3 + 0.13i$.

We will now discuss how, for both the green and red mode, $F_{12}(N_1, N_2)$, $H_1(N_1, N_2)$ and $H_2(N_1, N_2)$ vary with a changing population inversion. Like in the previous subsections and chapters, we will fix multiple $N_1$ values and increase $N_2$ from $N_2 = 0.4$ to $N_2 = 1$. We see how the green mode varies in Figure 6.5. In the case of $F_{12}(N_1, N_2)$, this is below zero for all $N_1$ values investigated for low $N_2$ which means a decaying mode as $\dot{A} < 0$. Only at later values of $N_2$, these $F_{12}(N_1, N_2)$ go above threshold. In terms of $k$, this decreases from $k_0$ with increasing $N_2$ for the interval we are considering. In the case of $H_1(N_1, N_2)$ and $H_2(N_1, N_2)$, there is a significant decrease in these as $N_2$ increases, for all $N_1$ values shown. It seems for the green mode here, both $H_1(N_1, N_2)$ and $H_2(N_1, N_2)$ are quite large below threshold than above. Finally in terms of $k$, we see that the value of it increases with increasing $N_2$.

The red mode for various $N_1$ with increasing $N_2$ is shown in Figure 6.6 for $F_{12}(N_1, N_2)$, $H_1(N_1, N_2)$ and $H_1(N_1, N_2)$. We see that for $F_{12}(N_1, N_2)$, at low $N_2$, $F_{12}(N_1, N_2) > 0$ which indicates an increasing mode and would equate to a mode above threshold for $N_1 = 1.15$ and $N_2 = 1.2$. For the other $N_1$ values, there is a decrease in $F_{12}(N_1, N_2)$ but both are less than zero already. However, as $N_2$ increases, we see that for $N_1 = 1.15, 1.2$, $F_{12}(N_1, N_2)$ becomes negative which is a decaying mode and would be considered below threshold. For all values of $N_1$, $F_{12}(N_1, N_2)$ increases

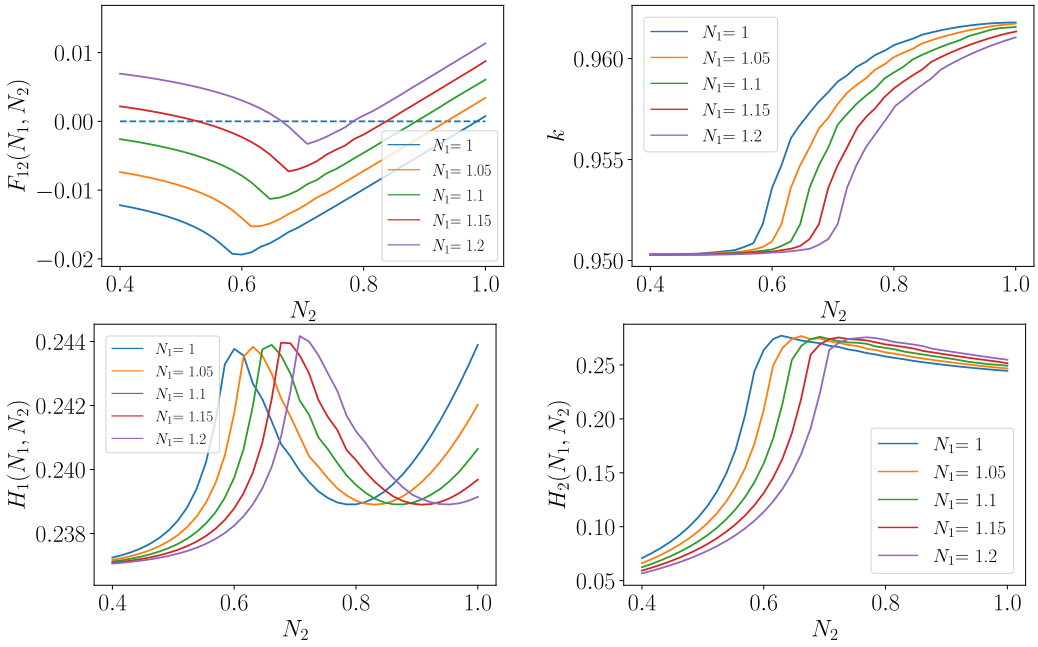



Figure 6.6: Variation of $N_2$ with fixed $N_1$ for $F_{12}(N_1, N_2)$, $k$, $H_1(N_1, N_2)$ and $H_2(N_1, N_2)$ for the red mode. For all plots, $k_0 = 0.95$, $\tilde{\gamma}_P = 1$. Note the laser structure has $l_1 = l_2 = 10$ and $l_g = 1$ with $\tilde{n}_b = 3 + 0.13i$.

until it it positive and above threshold for a higher $N_2$. In terms of the remaining diagrams in this figure, we see that $k$ increases for all $N_1$ values for the interval of $N_2$ shown. For $H_1(N_1, N_2)$, we see an increase function the larger the $N_2$ until the same $N_2$ as the minimum of $F_{12}(N_1, N_2)$. From there, the function acts like a parabola for the $N_2$ range shown. For $H_2(H_1, H_2)$, it behaves like $H_1(N_1, N_2)$ until the $N_2$ point where $F_{12}(N_1, N_2)$ is at a minimum. Then there is a slight decrease from there for the $N_2$ range shown. It is worthy to note that $H_2(H_1, H_2)$ varies quite significantly in comparison to $H_1(N_1, N_2)$.

Overall, we can get an idea of what happens when we vary these functions with a changing $N_1$ and $N_2$. As we have seen in Chapter 4, where it is possible to go below threshold with increasing pump, the same is seen here for the red branch and confirms the analysis completed in the previous subsection. In region 4 of Figure 6.4(a), that the red branch goes below threshold when $F_{12}(N_1, N_2) < 0$. Then when the red mode is in regions 1 and 2, we see that $F_{12}(N_1, N_2) > 0$. In terms of the green mode, when this mode is in regions 2 and 4, $F_{12}(N_1, N_2) < 0$ and is below threshold. Thus we can say that the analysis of $F_{12}(N_1, N_2)$ matches the results obtained in Chapters 4, 5 and in previous subsections in this chapter.

## 6.6 Conclusion

In this chapter, the aim was to derive a set of dynamical equations for both the electromagnetic field and the gain medium while satisfying the open boundary conditions for complex laser structures such as coupled cavities with a gap. To do this, we used the $q$-basis which can describe the spatial distribution of the electromagnetic field inside a laser. We introduced dynamics along with this $q$-basis by $G$ which scales the electric field and magnetic induction equally. With this idea, we were able to derive a dynamical equations for $A$ which is the square of $G$ by using energy conservation and Poynting's theorem. We were able to connect this with the two-level model description of the laser medium where we derived for a single cavity laser an equation for the population inversion $N_c$. We derived the single-cavity self-consistent equations for the scaling variable $A$ and inversion $N_c$. For the coupled-cavity scenario, we derived to separate equations for the population inversion in both cavities, $N_1$ and $N_2$. Moreover, instead of writing the dynamical equations in both types of cavities in terms of absorption and power flow, we were able to derive all of the dynamical equations mentioned in terms of the eigenvalues $x_n$ seen in Chapter 4. We have also shown the self-consistency equations for $A$, $N_1$ and $N_2$. We discussed the dynamics of $N_1$ and $N_2$ under the condition that the mode is a threshold, which is $\dot{A} = 0$. We showed under this analysis the existence of two separate modes at $\dot{A} = 0$ and how they vary along these branches with a changing population inversion. This lead to a discussion in determining modes above and below threshold which were based on the scaling parameter $\eta$ seen in Chapter 4. The final element of this chapter showed these modes agree with previous work in this thesis where the counter-intuitive phenomenon is observed, that with increasing inversion, the mode can go below threshold.

# Chapter 7

# Conclusion and Future Work

In this thesis, we have explored various aspects of laser physics and different models that describe the physics behind such devices. In particular, the focus of this work was to expand on existing knowledge of two laser cavities which are strongly-coupled which has open boundary conditions. This is important to analyse as modern devices like photonic integrated circuits require closely interacting laser cavities. In the case of the boundary conditions, we need open boundary conditions to accurately describe the loss of light due to leakage. While previous models have been designed that describe these strongly coupled-cavities, such as lasers that use composite-cavity modes, they use closed boundary conditions. In other models, such as those involving delay differential equations (DDEs), we see that these cannot describe lasers which are strongly-coupled as we have discussed in Chapter 2. However, models like the steady-state *ab-intio* laser theory (SALT) have addressed the idea of open boundaries for strongly coupled-cavities but in the steady-state case. Thus we arrive at what this thesis has aimed to achieve, which was to understand the steady-state scenario for strongly-coupled laser cavities with this open boundaries at threshold while also designing a dynamical model that can describe these laser modes off-threshold.

To further understand the steady-state scenario, we needed to get an intuition of a phenomenon obtained using SALT which were exceptional points (EPs). We have seen that EPs, which are the coalescing of two eigenvalues, occur in a variety of physical models, such as those seen in SALT and in a more simplistic model like Coupled Mode Theory (CMT). In Chapter 3, we looked into CMT to develop a greater understanding of this model, along with uncovering the behaviour of EPs. We first showed the existence of these EPs for the coupled modes and how they behave with the variation of parameters. Interestingly, it turns out the movement of these EPs in CMT with changing a parameter also occurs in Chapters 4 and 6 in the same way.

Thus with this preliminary analysis we undertook with a more simplistic model as CMT, we obtain the same behaviour as with more complicated models like SALT. Moreover, we also were able to show the limitations of this model in the context of weakly-coupled resonators.

We then moved on from this model to further investigate the openness of strongly coupled-cavities in the steady-state scenario, which was SALT. In Chapter 4, we first found a more elegant approach to represent the steady-state electromagnetic field, which we titled the $q$-basis, an inspiration from the idea of power balance and Poynting's theorem. Instead of using the complex representation of the electric field and magnetic induction, which is four variables, we instead wrote them in terms of this $q$-basis, which is three. With this new basis, we then explored the idea of EPs which were already calculated through SALT. In pervious work, SALT showed a counter-intuitive phenomenon, which was that around an EP, it was possible with increasing the pump, that a laser had the potential to go from above threshold to below. This was replicated and explained in Chapter 4. Interestingly, it turns out this effect was due to the power flow, where the power from a cavity in one pump flows into the second which is absorbing. This results in the mode reducing below threshold. We further completed a detailed analysis of coupled cavities including introducing new questions which included how EPs occur for a higher frequency with no gap between the cavities. This in fact was answered by developing a new and more efficient method for calculating these threshold branches in Chapter 5.

The $q$-basis was extremely useful to gain some physical insight into how the electromagnetic field behaves in a coupled-cavity laser with open boundaries. However, in Chapter 5, we developed another mathematical method to represent the electromagnetic field which was used to gain insight into the threshold branches of each laser while also uncovering a new type of EP at threshold, which we titled the threshold exceptional point. We called it the $\mathcal{Z}$-basis. The main function in the $\mathcal{Z}$-basis was given by $\mathcal{Z}(z)$ which was the projection of the electromagnetic field onto a complex Riemann sphere. In fact this basis is a Möbius transformation and the projection of this transformation onto a complex Riemann sphere is a loxodromic logarithmic spiral. This spiral led to explain why there are three distinct threshold branches, separated by an EP in the previous chapter, for higher frequencies when there is no gap. Moreover, what proved fascinating was the fact that the the lower branch (for high pump in one cavity and low pump in the other) can only exist for more than one cavity. This was due to one cavity absorbing while the other cavity has enough gain to result in the laser to be at threshold. With this detailed analysis of the steady-state,

this could be used to introduce dynamics into the situation.

In Chapter 6, the aim is to use the previous work in this thesis on the steady-state regime, to design a dynamical set of equations to describe the coupled-cavity laser with open boundaries. The key element to do this was to introduce a scaling term which scales the electromagnetic field with the variation of the population inversion of both cavities. This was carried out using the same principle of power balance and Poynting's theorem, with this scaling term to derive these dynamical equations. We calculated modes by comparing those at threshold with the same proportion of population inversion in both cavities. This resulted in a nice description of modes above and below threshold dynamically. for these coupled cavities with an accurate spatial description by connecting the dynamics with the $q$-basis. We analysed the regions around threshold and our model also confirmed the threshold branches showed in Chapters 4 and 5. One of the most interesting parts of this thesis was that in theory, with increasing population inversion, it is possible to go from above threshold to below threshold, confirming the work done with SALT in the literature and the phenomenon showing up in Chapter 4 with the $q$-basis.

In this thesis, we have added to the research of coupled-cavities where we explored the steady-state of the electromagnetic field at threshold and derived multiple mathematical representations to aid us to describe and solve some of the intriguing mysteries that surrounds how these coupled-cavities behave at threshold. Using this knowledge, we fulfilled the task from the outset of the thesis to derive a set of self consistent dynamical equations to describe this strongly coupled-cavity lasers with open boundaries. With all this in mind, the question is where can we go from here. The first possible avenue to take is trying to develop further understanding of complex laser structures with the dynamical equations derived in the previous chapter. With them, one can uncover the dynamical effects and intriguing complexities that are possible close to threshold for coupled cavities with outward flowing open boundaries. While there has been previous work such as with composite cavity modes which can already show many types of dynamical effects, they do not treat the boundary correctly as mentioned.

Another area that could be investigated is how to describe the gain medium more accurately such as for semiconductor gain material. This was beyond the scope of what we were concerned about in this thesis, as we formulated the dynamics of the electromagnetic field where we used the idea of the two-level atom or two level semiconductor as discussed in Chapter 2. Instead of using the two-level atom or the two level semiconductor model where we derived the population inversion from, one

could connect the dynamics with the electromagnetic field from the previous chapter to dynamical equations for electrons and holes. This could lead to a more accurate understanding of the gain medium dynamics that can be connected with the scaling dynamics for the electromagnetic field we have derived.

# List of Abbreviations

The following is a list of abbreviations used throughout this thesis:

| | |
|---|---|
| CMT | Coupled Mode Theory |
| DDE | Delay Differential Equation |
| EP | Exceptional Point |
| FP | Fixed Point |
| GaAs | Gallium Arsenide |
| InP | Indium Phosphide |
| PIC | Photonic Integrated Circuit |
| RWA | Rotating Wave Approximation |
| SALT | Steady-state *ab-initio* Laser Theory |
| SLT | Semiclassical Laser Theory |
| SVAA | Slowly Varying Amplitude Approximation |
| TCF | Threshold Constant Flux (states) |
| TEP | Threshold Exceptional Point |
| TLM | Threshold Lasing Mode |

# List of Symbols

This list of symbols is a compilation of symbols used in this thesis with their physical meaning. The following are a list of symbols in alphabetical order:

| | |
|---|---|
| $a_i(t), \hat{a}_i(t), A_i(\tau)$ | Complex-valued $i^{th}$ electric field mode amplitude from CMT |
| $A(t)$ | Scaling term for the electromagnetic field |
| $A(z,t), A(z)$ | Population of semiconductor levels |
| $A_i^{FP}$ | Fixed point solution for the $i^{th}$ CMT mode |
| $B(z)$ | Complex-valued magnetic induction amplitude |
| $B^{TCF}(z)$ | TCF state complex-valued magnetic induction amplitude |
| $\mathbf{B}(\mathbf{r},t)/B(z,t)$ | Magnetic induction vector/amplitude |
| $c$ | Speed of light |
| $c_n(t)$ | Probability amplitude corresponding the $n^{th}$ eigenstate |
| $C_p$ | Coupling phase (Mutually Coupled lasers) |
| $\mathbf{D}(\mathbf{r},t)/D(z,t)$ | Electric displacement vector/amplitude |
| $e$ | Charge of the electron ($e > 0$) |
| $\mathcal{E}_{L/R}, E_{-/+}$ | Left/right moving complex-valued electric field amplitude |
| $E(z)$ | complex-valued electric field amplitude |
| $\mathcal{E}_n(t)$ | Time-dependent complex-valued electric field amplitude for the $n^{th}$ mode |
| $\tilde{E}(t)$ | Time-dependent complex-valued electric field amplitude for optical injection |
| $\tilde{E}_i(t)$ | Time-dependent complex-valued electric field amplitude injection signal for optical injection |

| | |
|---|---|
| $E_n(z)$ | Spatially-varying complex-valued electric field in SALT units |
| $E_n^{TLM}(z)$ | TLM complex-valued electric field amplitude for $n^{th}$ mode |
| $E^{TCF}(z), E_n^{TCF}(z)$ | TCF state complex-valued electric field amplitude |
| $E_n^{CF}(z)$ | Constant flux complex-valued electric field amplitude for $n^{th}$ mode |
| $E_S^+(z,t)$ | Electric field amplitude in SALT units |
| $\mathbf{E}_\mathbf{r}(t)/E_z(t)$ | Time-dependent spatially-constant electric field vector/amplitude |
| $\mathbf{E}(\mathbf{r},t)/E(z,t)$ | Electric field vector/amplitude |
| $\mathscr{E}_{1/2}/\mathscr{E}_{1/2}^s$ | Electric field amplitides (mutually-coupled lasers) |
| $F_c, F_{12}$ | Functions in their respective scaling amplitude dynamical equations $A(t)/A$ |
| $g$ | Self-consistent threshold laser condition in terms of $x_n$ |
| $G(t)$ | Scaling amplitude for electric field and magnetic induction |
| $\hbar$ | Plank's reduced constant |
| $\mathcal{H}$ | Classical Hamiltonian |
| $\hat{H}(t)$ | Time-dependent Hamiltonian |
| $\hat{H}_0$ | Time-independent Hamiltonian |
| $H_{mn}$ | Time-dependent Hamiltonian where $\langle\phi_m\vert\,\hat{H}\,\vert\phi_n\rangle$ |
| $\mathbf{H}(\mathbf{r},t)/H(z,t)$ | Magnetic field vector/amplitude |
| $H_1, H_2, H_c$ | Functions in their respective population inversion dynamical equations |
| $J$ | Pump (Optical injection laser, mutually-coupled lasers) |
| $\mathbf{J}(\mathbf{r},t)/J(z,t)$ | Current density vector/amplitude |
| $\mathcal{J}^{(i)}(n_1,n_2)$ | Interface matrix between refractive indices $n_1$ and $n_2$ be the $i^{th}$ section |
| $k$ | Wavenumber |
| $k_0$ | Transition wavenumber |
| $K$ | Injection field rate |

| | |
|---|---|
| $\mathcal{K}$ | Classical kinetic energy |
| $\tilde{\mathcal{K}}$ | Coupling strength (Mutually coupled lasers) |
| $l_i, L_i$ | Length of $i^{th}$ section |
| $L$ | Total length of laser |
| $\mathscr{L}$ | Lorentzian distribution |
| $m_e$ | Mass of electron |
| $M(z,t)$ | Magnetisation amplitude |
| $\mathcal{M}^{(i)}$ | Transfer matrix be the $i^{th}$ section |
| $n_b(z), n_s, n_c, n_a$ | Background refractive index |
| $\tilde{n}_b(z)$ | Complex-valued background refractive index |
| $N_0(z,t), N_0(z)$ | Local population inversion pump profile |
| $N(z,t)$ | Time-dependent local population inversion |
| $N_i(t)$ | Global population inversion for $i^{th}$ section/single cavity |
| $\bar{N}(t)$ | Spatially-averaged population inversion |
| $\tilde{N}(t)$ | Time-dependent population inversion amplitude for optical injection |
| $N_{thr}$ | Carrier density at threshold (Optical injection) |
| $\mathscr{N}_{1/2}, \mathscr{N}^s_{1/2}$ | Population inversion (mutually-coupled lasers) |
| $N_S(z,t), N_S(z)$ | Population inversion amplitude in SALT units |
| $N_0^S(z)$ | Population inversion stationary pump term in SALT units |
| $\wp$ | Electric dipole constant |
| $p_i$ | Probability of $i^{th}$ state vector for a mixed density operator |
| $\mathcal{P}_n(z,t), \tilde{\mathcal{P}}_n(t)$ | Time-dependent complex-valued gain polarisation amplitude for the $n^{th}$ mode |
| $P_S^+(z,t)$ | Gain polarisation amplitude in SALT units |
| $\mathbf{P}_g^+(\mathbf{r},t)/P_g^+(z,t)$ | Positive frequency complex-valued gain polarisation amplitude |
| $\mathbf{P}(\mathbf{r},t)/P(z,t)$ | Total polarisation vector/amplitude |

| | |
|---|---|
| $\mathbf{P}_b(\mathbf{r},t)/P_b(z,t)$ | Background polarisation vector/amplitude |
| $\mathbf{P}_g(\mathbf{r},t)/P_g(z,t)$ | Gain polarisation vector/amplitude |
| $\mathbf{P}_g(z,t)$ | Gain polarisation vector |
| $q_A(z)/q_A^{(i)}$ | $q$-basis element, energy density of electromagnetic field amplitudes |
| $q_I(z)/q_I^{(i)}$ | $q$-basis element, imaginary component of complex-valued Poynting's vector $S(z)$ |
| $q_R(z)/q_R^{(i)}$ | $q$-basis element, real component of complex-valued Poynting's vector $S(z)$, power flow |
| $q_S(z)/q_S^{(i)}$ | $q$-basis element, difference in electromagnetic field amplitudes |
| $\mathbf{q}^{(i)}$ | $q$-basis vector |
| $Q_A(z,t)$ | $Q$-time basis element, energy density of electromagnetic field amplitudes |
| $Q_I(z,t)$ | $Q$-time basis element, imaginary component of complex-valued Poynting's vector $S(z)$ |
| $Q_R(z,t)$ | $Q$-time basis, real component of complex-valued Poynting's vector $S(z)$, power flow |
| $Q_S(z,t)$ | $Q$-time basis element, difference in electromagnetic field amplitudes |
| $\mathbf{r}$ | Laboratory co-ordinate system |
| $r(z,t_0)$ | Rate of pumped atoms, two-level atom model |
| $\mathbf{R}, X, Y, Z$ | Atomic scale displacement of electron from nucleus |
| $\hat{\mathbf{R}}, \hat{X}, \hat{Y}, \hat{Z}$ | Atomic position operator |
| $\mathbf{R}_{mn}, X_{mn}$ | Position where $\langle\phi_m\vert\,\hat{\mathbf{R}}\,\vert\phi_n\rangle$ |
| $S(z)$ | Complex-valued Poynting's vector amplitude |
| $\langle\mathcal{S}(z)\rangle$ | Time-averaged real-valued Poynting's vector amplitude |
| $\mathcal{S}(z,t)$ | Real-valued Poynting's vector amplitude |
| $t_0$ | Time of atomic excitation |

| | |
|---|---|
| $U_n(z)$ | Complex-valued electric field spatial distribution for the $n^{th}$ mode |
| $\mathcal{V}$ | Classical potential energy |
| $\hat{W}(t)$ | Light-Matter interaction Operator |
| $W_{mn}$ | Light-Matter interaction where $\langle\phi_m\vert\,\hat{W}\,\vert\phi_n\rangle$ |
| $x_n$ | Above/Below threshold approximation eigenvalue |
| $\mathcal{Y}(z)$ | Logarithmic spiral function in complex plane |
| $\mathcal{Z}_0$ | Initial condition of $\mathcal{Z}(z)$ |
| $\mathcal{Z}(z), \mathcal{Z}^{(i)}(z)$ | $\mathcal{Z}$-basis function |
| $\mathcal{Z}_i^F$ | $\mathcal{Z}$-basis $i^{th}$ fixed point |
| $\mathcal{Z}_P(z)$ | Power flow in terms of the $\mathcal{Z}$-basis. |

The following are a list of symbols from the greek alphabet:

| | |
|---|---|
| $\alpha$ | Linewidth enhancement factor |
| $\gamma_i$ | Decay terms for atoms and modes |
| $\gamma_{ph}$ | Decay due to elastic atomic collisions |
| $\gamma_a, \gamma_P$ | Gain polarisation decay rate |
| $\gamma_N$ | Population inversion decay rate |
| $\gamma_E$ | Cavity losses |
| $\tilde{\gamma}$ | Decay term for modes in CMT |
| $\Gamma$ | Loss term from the excited atom level |
| $\Gamma_\pm$ | Decay term of eigenvalues in CMT |
| $\delta_{mn}$ | Kronecker's delta |
| $\Delta\tilde{\omega}$ | Detuning between two modes in CMT |
| $\Delta, \Delta_n$ | Detuning of a single mode/$n^{th}$ mode |
| $\epsilon_0$ | Permittivity of free space |
| $\epsilon(z)$ | Complex-valued permittivity profile |
| $\epsilon_i, \epsilon_c$ | Complex-valued permittivity profile for $i^{th}$ section/cavity |
| $\zeta_{LI}, \zeta_{AM}$ | Integral functions over the $q$-basis for a single cavity |
| $\zeta_M, \zeta_{AM}^{(i)}, \zeta_{LI}^{(i)}$ | Integral functions over the $q$-basis for coupled cavities for each section |
| $\eta$ | Scaling parameter between pumps in coupled cavity |
| $\theta$ | complex argument of coupling between two modes in CMT |
| $\kappa_{nm}, \kappa, \tilde{\kappa}$ | Coupling constant between modes in CMT |
| $\kappa_a, \kappa(z), \kappa_i$ | Extinction coefficient in cavity |
| $\lambda_i(z,t)$ | Pumping term for the $i^{th}$ atomic level |
| $\lambda_\pm, \lambda_\pm^{EP}$ | Eigenvalues of CMT |
| $\Lambda$ | Pumping term to excited atomic state |
| $\Lambda_i, \Lambda_c$ | Pump profile for the $i^{th}$ cavity/single cavity |

| | |
|---|---|
| $\mu_0$ | Permeability of free space |
| $\xi$ | Gain coefficient (Optical injection) |
| $\hat{\rho}(t)$ | Density operator |
| $\rho_{nm}(t)$ | Density matrix elements |
| $\rho(z,t)$ | Population matrix |
| $\rho_{nm}(z,t)$ | Population matrix elements |
| $\rho_c(\mathbf{r},t)$ | Charge density |
| $\sigma$ | Electrical conductivity of the medium |
| $\hat{\sigma}$ | Phase shift between lasers (Mutually-coupled lasers) |
| $\tau$ | Redefined timescale for CMT |
| $\|\phi_n\rangle$ | $n^{th}$ eigenstate decomposition of state vector $\|\psi(t)\rangle$. |
| $\phi_n(\mathbf{R})$ | Eigenfunction for the $n^{th}$ mode that is part of the decomposition of the state function $\psi(\mathbf{R},t)$. |
| $\chi_b(z)$ | Background susceptibility |
| $\tilde{\chi}_b(z)$ | Complex-valued background susceptibility |
| $\chi_g(z), \chi_g(z,t), \chi_g^{(i)}$ | Complex-valued gain susceptibility |
| $\psi(\mathbf{R},t)$ | Complex-valued probability function |
| $\|\psi(t)\rangle$ | Electron state vector |
| $\omega_A$ | Natural frequency |
| $\omega, \omega_n$ | Frequency of mode/$n^{th}$ mode |
| $\omega_0$ | Atomic transition frequency |
| $\Omega_n$ | Passive cavity frequency for the $n^{th}$ mode |
| $\Omega_\pm$ | Frequency term of eigenvalues in CMT |

# List of Figures


1.1 Setup of a simplistic single-cavity laser with an external pump, and excited atoms (blue) in an active medium (green). This example has a fully reflective mirror on the left and a partially reflective one on the right which allows photons to escape. . . . . 2

1.2 Setup of the coupled cavity system with open boundaries separated by a gap. . . . . 4

2.1 Classical constant in time electric field amplitude in the $x$ direction, $E(z)$ (red line) with atoms (in blue) along the $z$ axis. Each atom contains a separate co-ordinate system with position vector $\mathbf{R}$ which measures the distance from the nucleus to electrons of an atom (subset of figure). . . . . 11

2.2 Two-level atom with the excited state $|1\rangle$ and lower state $|2\rangle$. Both decay to a level $|3\rangle$ at decay rates $\gamma_1$ and $\gamma_2$ from levels $|1\rangle$ and $|2\rangle$ respectively. . . . . 12

2.3 Open boundaries of a coupled-cavity laser system with two cavities with a gap in between. . . . . 25

3.1 Two resonators coupled via the complex term $\kappa$ with decays present in each. . . . . 35

3.2 Frequency terms from eigenvalues $\lambda_\pm$ over the detuning $\Delta\tilde{\omega}$ where for all cases $|\tilde{\kappa}| = .5$. . . . . 39

3.3 Loss terms from eigenvalues $\lambda_\pm$ over the detuning $\Delta\tilde{\omega}$ where for all cases $|\tilde{\kappa}| = .5$. . . . . 40

3.4 Real and imaginary parts of eigenvalues $\lambda_\pm$ over the detuning range $(-3, 3)$ for $\Delta\tilde{\omega}$ where for all cases $|\tilde{\kappa}| = .5$. . . . . 41

3.5 Illustration of allowed values (green) of coupling $\tilde{\kappa}$ where both $\Gamma_\pm \leq 0$. (a):$\tilde{\gamma} = 1, \Delta\tilde{\omega} = 0$, (b):$\tilde{\gamma} = 1, \Delta\tilde{\omega} = 4$, (c):$\tilde{\gamma} = 4, \Delta\tilde{\omega} = 4$, (d):$\tilde{\gamma} = 4, \Delta\tilde{\omega} = -4$, (e):$\tilde{\gamma} = \frac{1}{2}, \Delta\tilde{\omega} = 4$ and (f):$\tilde{\gamma} = 4, \Delta\tilde{\omega} = 0$. . . . . 43
3.6 Dynamical picture where both $\Gamma_\pm < 0$ such that $\mathrm{Re}(\tilde{\kappa}) = 1$, $\mathrm{Im}(\tilde{\kappa}) = .7$, $\Delta\tilde{\omega} = 4$ and $\tilde{\gamma} = 1$. . . . . 45
3.7 Dynamical picture where both $\Gamma_\pm < 0$ such that $\mathrm{Re}(\tilde{\kappa}) = .5$, $\mathrm{Im}(\tilde{\kappa}) = 1.8$, $\Delta\tilde{\omega} = 4$ and $\tilde{\gamma} = 1$. . . . . 46
3.8 Dynamical picture where one of $\Gamma_\pm > 0$ such that $\mathrm{Re}(\tilde{\kappa}) = 0$, $\mathrm{Im}(\tilde{\kappa}) = 2.3$, $\Delta\tilde{\omega} = 4$ and $\tilde{\gamma} = 1$. . . . . 46

4.1 Mode picture in the $x_n$ complex plane where threshold is shown in blue while two modes above and below threshold are shown in green and red respectively. The projection of both modes at threshold is shown as a black square. . . . . 58
4.2 Open boundaries with a coupled-cavity laser system with two cavities of length $l_1$ and $l_2$ with pump profiles $\Lambda_1$ and $\Lambda_2$ respectively with a gap of length $l_g$ in between. . . . . 60
4.3 Modes of a system (in black) where $\Lambda_1 = 1.3$, $\Lambda_2 = 0.5$, $l_1 = l_2 = 0.1$ mm, $l_g = 0.01$ mm and $k = 95$ mm$^{-1}$. Modes at threshold would be located on the edge of the circle (in blue), while inside the circle, modes are above threshold (in green) and outside, below threshold (in red). . 66
4.4 Plot of wavenumber ranges for a coupled laser system with $l_1 = .1$mm, $l_2 = .01$mm and $l_3 = .1$mm. The laser sections have complex refractive index $\tilde{n}_b = 3(1 + .043i)$ and $\Lambda_1 = 1.2$. The $x$ axis represents the wavenumber, $k = \frac{\omega}{c}$ and $y$ axis the 2nd pump $\Lambda_2$. Green indicates above threshold region while red is below threshold. There are multiple EPs shown with black dots. The bold black line is threshold for the coupled system. . . . . 67

4.5 A closer look at the region $k = 80\text{mm}^{-1}$ to $k = 90\text{mm}^{-1}$ where the relative intensity is shown for $\Lambda_2 = .4$ (orange), $\Lambda_2 = .5$ (green), $\Lambda_2 = 0.659265306122$ (blue), $\Lambda_2 = .1$ (red) and $\Lambda_2 = 1.2$ (purple) for $k = 84.5968367347\text{mm}^{-1}$, $\Lambda_1 = 1.2$ and the same lengths of the laser and gap and refractive index as Figure 4.4. (a) shows the lasing condition of the first lasing mode where light green region is above threshold and light red region is below threshold. (b) shows both modes with different $x_n(\omega)$ where inside the circle (dashed line), the mode is above threshold. At $\Lambda_2 = 0.659265306122$, there is an EP. . . . . 68

4.6 Plots of two modal relative intensities ((a) and (b)), with power flow ($q_R(z)$) shown for (a) and (b) in (c) and (d) respectively. Parameters are $k = 84.5968367347\text{mm}^{-1}$, $\Lambda_1 = 1.2$ and $\Lambda_2 = .4$. In reference to Figure 4.5. . . . . 69

4.7 Plots of two modal relative intensities ((a) and (b)), with power flow ($q_R(z)$) shown for (a) and (b) in (c) and (d) respectively. Parameters are $k = 84.5968367347\text{mm}^{-1}$, $\Lambda_1 = 1.2$ and $\Lambda_2 = 0.5$. In reference to Figure 4.5. . . . . 70

4.8 Plot of modal relative intensity (a), located at the EP, below threshold and the power flow ($q_R(z)$) (b). Parameters are $k = 84.5968367347\text{mm}^{-1}$, $\Lambda_1 = 1.2$ and $\Lambda_2 = 0.659265306122$. In reference to Figure 4.5. . . . . 71

4.9 Plots of two modal relative intensities ((a) and (b)), with power flow ($q_R(z)$) shown for (a) and (b) in (c) and (d) respectively. Parameters are $k = 84.5968367347\text{mm}^{-1}$, $\Lambda_1 = 1.2$ and $\Lambda_2 = 1$. In reference to Figure 4.5. . . . . 72

4.10 Plots of two modal relative intensities ((a) and (b)), with power flow ($q_R(z)$) shown for (a) and (b) in (c) and (d) respectively. Parameters are $k = 84.5968367347\text{mm}^{-1}$, $\Lambda_1 = 1.2$ and $\Lambda_2 = 1.2$. In reference to Figure 4.5. . . . . 73

4.11 Range of wavenumbers which show various EPs (black dots) where $\Lambda_1 = 1.2$, $\tilde{n}_b = 3(1 + 0.043i)$ with $l_1 = 0.1\text{mm}$, $l_2 = 0.1\text{mm}$ and $l_3 = 0.1\text{mm}$. Green indicates above threshold region while red is below threshold. . . . . 74

4.12 Range of wavenumbers which show various EPs (black dots) where $\Lambda_1 = 1.2$, $\tilde{n}_b = 3(1 + 0.43i)$ with $l_1 = 0.1\text{mm}$, $l_2 = 0.001\text{mm}$ and $l_3 = 0.1\text{mm}$. Green indicates above threshold region while red is below threshold. . . . . 74

4.13 Range of wavenumbers which show various EPs (black dots) where $\Lambda_1 = 1.2$, $\tilde{n}_b = 3(1 + 0.043i)$ with $l_1 = 0.1$mm, $l_2 = 0$mm and $l_3 = 0.1$mm.Green indicates above threshold region while red is below threshold. . . . . 75

4.14 Plots where the points are using the conditions (4.47) and (4.48) showing first a three dimensional plot where the lines in green, blue and red is when the laser is at threshold for a given $k$, $k_0$ and $\Lambda_2$. In the background shows the view on each plane. The second plot shows the $k_0, \Lambda_2$ plane where the points are discussed. . . . . 76

4.15 Intensity and power flow profile plots of coupled system where $\Lambda_2 = 0.43, k = 85.1$ (cyan) and $\Lambda_2 = .87, k = 85.3$ (magenta) and $\Lambda_2 = .99, k = 84.6$ (black). At these points, $\Lambda_1 = 1.2$ and $k_0 = 0.85$. . . . . 76

4.16 The scaling parameter is $\eta$ with varying wavenumber $k$ with $k = 84.6\text{mm}^{-1}$, $k = 86.6\text{mm}^{-1}$ and $k = 87.6\text{mm}^{-1}$ in red, green and blue respectively. The full line is the first mode while the dashed line is the second. . . . . 79

4.17 Power flow at the boundaries at varying $k$ for the first mode at (in $\text{mm}^{-1}$) $k = 74.2$ (blue,EP), $k = 75.2$ (pink), 76.2 (red), 77.2 (green), 79.2 (purple), 81 (brown) and 84.6 (orange,EP). . . . . 79

4.18 Both modes with the same $k = 84.5968367347\text{mm}^{-1}$ as an EP with varying $\eta$. The top left is the intensity for the closest mode while the bottom left is a zoomed in picture of the gap. The top right is the intensity for the second closest mode while the bottom right is a zoomed in picture of the gap. . . . . 80

4.19 Two eigenvalue branches for varying $\eta$ for $k = 85.5\text{mm}^{-1}$ and in this case $\Lambda_1 = 1$ . . . . . 82

4.20 Two eigenvalue branches for varying $\eta$ for $k = 84.5968367347\text{mm}^{-1}$ and in this case $\Lambda_1 = 1$ . . . . . 83

5.1 Two threshold branches for a range of $k$ from $k = 0.15$ to $k = 0.40$ shown in red and green for $L = 10$. . . . . 94

5.2 The left figure shows the variation of $\mathcal{Z}(z)$ from $z = 0$ to $z = L$ which shows a loxodrome. On the right is the corresponding electric field intensity. Parameters used are $k = 0.20124$, $\Lambda_c = 3.08992$, $\tilde{n}_b = 3 + 0.13i$, $\Delta = 0.313618$ and $L = 10$. The green dots are the fixed points. The black diamond and square are the boundary conditions. . 95

5.3 The left figure shows the variation of $\mathcal{Z}(z)$ from $z = 0$ to $z = L$. On the right is the corresponding electric field intensity. Parameters used are $k = 0.32339$, $\Lambda_c = 2.1513$, $\tilde{n}_b = 3 + 0.13i$, $\Delta = -0.21077$ and $L = 10$. The green dots are the fixed points. The black diamond and square are the boundary conditions. . . . . 96
5.4 Power flow represented by $\mathcal{Z}_P(z)$ for Fabry-Perot. . . . . 96
5.5 Threshold branches that correspond to the red and green branches seen in Figure 5.1 in the $\epsilon_c, k$ plane for $L = 10$. . . . . 98
5.6 Threshold branches for a range of $k$ from $k = 0.90$ to $k = 0.98$. The three possible branches shown in green, blue and red for different $\Lambda_1$ where (a) and (b) have $\Lambda_1 = 1.18$, (c) and (d) have $\Lambda_1 = 1.189$ and (e) and (f) have $\Lambda_1 = 1.2$. . . . . 101
5.7 Threshold branches for a second TEP for the range of $k$ from $k = 0.90$ to $k = 0.98$. The three possible branches shown in green blue and red for different $\Lambda_1$ where (a) and (b) have $\Lambda_1 = 1.2122$, (c) and (d) have $\Lambda_1 = 1.22$ . . . . . 102
5.8 $\mathcal{Z}(z)$ and $|E(z)|^2$ plots for coupled-cavities where the first cavity is shown in blue, the gap in orange and the second cavity in green. (a) corresponds to the green branch of Figures 5.6(a) and (b), while (b) and (c) correspond to a mode profile on the red and blue branches respectively. Parameters used were $l_1 = l_2 = 10$, $l_g = 1$, $\Lambda_1 = 1.18$ and $\tilde{n}_b = 3 + 0.13i$. The blue and green dots are the fixed points for the first and second cavity respectively. The black diamond and square are the boundary conditions. . . . . 104
5.9 Various examples showing the power flow inside a coupled laser cavity with $\Lambda_1 = 1.18$, $l_1 = l_2 = 10$, $l_g = 1$ and $\tilde{n}_b = 3 + 0.13i$. . . . . 106
5.10 Threshold branches in terms of the permittivities for a range of $k$ from $k = 0.90$ to $k = 0.98$. The three possible branches shown in green, blue and red for different $\Lambda_1$ where (a) and (b) have $\Lambda_1 = 1.18$, (c) and (d) have $\Lambda_1 = 1.189$ and (e) and (f) have $\Lambda_1 = 1.2$. . . . . 107
5.11 Threshold branches in terms of the permittivities for the range of $k$ from $k = 0.90$ to $k = 0.98$. The three possible branches shown in green blue and red for different $\Lambda_1$ where (a) and (b) have $\Lambda_1 = 1.2122$, (c) and (d) have $\Lambda_1 = 1.22$ . . . . . 108

5.12 Threshold branches in terms of the pump, permittivities and $\Delta$ for the range of $k$ from $k = 0.90$ to $k = 1.025$. The two possible branches shown in green and blue with $l_1 = l_2 = 10$ and $l_g = 0$ with $\tilde{n}_b = 3 + 0.13i$. 111

5.13 Threshold branches in terms of the pump, permittivities and $\Delta$ for the range of $k$ from $k = 3.2$ to $k = 3.6$. The three possible branches shown in red, green and blue with $l_1 = l_2 = 10$ and $l_g = 0$ with $\tilde{n}_b = 3 + 0.13i$. 112

5.14 $\mathcal{Z}(z)$, $|E(z)|^2$ and $\mathcal{Z}_P(z)$ plots for coupled-cavities where the first cavity is shown in blue, the gap in orange and the second cavity in green. They correspond to the black dot in Figure 5.13. Parameters used were $k = 3.401153$, $\Lambda_1 = 1.1865$, $\Lambda_2 = 0.48194$, $\Delta = -0.028204$, $l_1 = l_2 = 10$, $l_g = 0$ and $\tilde{n}_b = 3 + 0.13i$. The blue and green dots are the fixed points for the first and second cavity respectively. The black diamond and square are the boundary conditions. . . . . 113

6.1 Variation of $N_c$ for $F_c(N_c)$ and $H_c(N_c)$. For both plots, $k_0 = 0.95$, $\tilde{\gamma}_P = 1$ and $k = 0.94407$. Note the laser structure has $L = 10$ with $\tilde{n}_b = 3 + 0.13i$. . . . . 126

6.2 A single open laser with coupled cavities of length $L$ where each cavity has refractive index $n_b$ and extinction coefficient $\kappa_b$. The population inversions for cavity 1 and cavity 2 are $N_1(t)$ and $N_2(t)$ respectively. The gap and outside the laser have refractive index $n_a$. . . . . 127

6.3 Zero branches for $F_{12}(N_1, N_2)$ for varying $N_1$, $N_2$ and $k$ for a fixed $k_0 = .95$ and $\tilde{\gamma}_P = 1$ for a coupled cavity laser with $l_1 = l_2 = 10$, $l_g = 1$ and $\tilde{n}_b = 3 + 0.13i$. . . . . 131

6.4 Variation of $N_2$ and $k$ with fixed $N_1 = 1.2$. For all plots, $k_0 = 0.95$, $\tilde{\gamma}_P = 1$. Note the laser structure has $l_1 = l_2 = 10$ and $l_g = 1$ with $\tilde{n}_b = 3 + 0.13i$. . . . . 134

6.5 Variation of $N_2$ with fixed $N_1$ for $F_{12}(N_1, N_2)$, $k$, $H_1(N_1, N_2)$ and $H_2(N_1, N_2)$ for the green mode. For all plots, $k_0 = 0.95$, $\tilde{\gamma}_P = 1$. Note the laser structure has $l_1 = l_2 = 10$ and $l_g = 1$ with $\tilde{n}_b = 3 + 0.13i$. 136

6.6 Variation of $N_2$ with fixed $N_1$ for $F_{12}(N_1, N_2)$, $k$, $H_1(N_1, N_2)$ and $H_2(N_1, N_2)$ for the red mode. For all plots, $k_0 = 0.95$, $\tilde{\gamma}_P = 1$. Note the laser structure has $l_1 = l_2 = 10$ and $l_g = 1$ with $\tilde{n}_b = 3 + 0.13i$. . . 137

# Bibliography


[1] K. Shimoda, *Introduction to laser physics*, vol. 44. Springer, 2013.

[2] Q. Peng, A. Juzeniene, J. Chen, L. O. Svaasand, T. Warloe, K.-E. Giercksky, and J. Moan, "Lasers in medicine," *Reports on Progress in Physics*, vol. 71, p. 056701, 2008.

[3] L. A. Coldren, S. W. Corzine, and M. L. Mashanovitch, *Diode lasers and photonic integrated circuits*, vol. 218. John Wiley & Sons, 2012.

[4] A. Einstein, "Zur Quantentheorie der Strahlung," *Phys. Z.*, vol. 18, p. 121, 1917.

[5] J. P. Gordon, H. J. Zeiger, and C. H. Townes, "The maser—new type of microwave amplifier, frequency standard, and spectrometer," *Physical review*, vol. 99, p. 1264, 1955.

[6] A. L. Schawlow and C. H. Townes, "Infrared and optical masers," *Physical Review*, vol. 112, p. 1940, 1958.

[7] T. H. Maiman, "Stimulated optical radiation in ruby," *nature*, vol. 187, p. 493, 1960.

[8] A. Javan, W. R. Bennett Jr, and D. R. Herriott, "Population inversion and continuous optical maser oscillation in a gas discharge containing a he-ne mixture," *Physical Review Letters*, vol. 6, p. 106, 1961.

[9] P. P. Sorokin and J. Lankard, "Stimulated emission observed from an organic dye, chloro-aluminum phthalocyanine," *IBM Journal of Research and Development*, vol. 10, p. 162, 1966.

[10] F. P. Schäfer, W. Schmidt, and J. Volze, "Organic dye solution laser," *Applied Physics Letters*, vol. 9, p. 306, 1966.

[11] W. E. Lamb Jr, "Theory of an optical maser," *Physical Review*, vol. 134, p. A1429, 1964.

[12] H. Haken, *Laser light dynamics*, vol. 1. North-Holland Amsterdam, 1985.

[13] T. L. Koch and U. Koren, "Semiconductor photonic integrated circuits," *IEEE Journal of Quantum Electronics*, vol. 27, p. 641, 1991.

[14] H. A. Haus and W. Huang, "Coupled-mode theory," *Proceedings of the IEEE*, vol. 79, p. 1505, 1991.

[15] H. Erzgraber, D. Lenstra, B. Krauskopf, and I. Fischer, "Dynamical properties of mutually delayed coupled semiconductor lasers," in *Semiconductor Lasers and Laser Dynamics*, vol. 5452, p. 352, International Society for Optics and Photonics, 2004.

[16] S. Wieczorek, B. Krauskopf, T. B. Simpson, and D. Lenstra, "The dynamical complexity of optically injected semiconductor lasers," *Physics Reports*, vol. 416, p. 1, 2005.

[17] H. Erzgräber, S. Wieczorek, and B. Krauskopf, "Dynamics of two laterally coupled semiconductor lasers: Strong-and weak-coupling theory," *Physical Review E*, vol. 78, p. 066201, 2008.

[18] H. E. Türeci, A. D. Stone, L. Ge, S. Rotter, and R. J. Tandy, "Ab initio self-consistent laser theory and random lasers," *Nonlinearity*, vol. 22, p. C1, 2008.

[19] L. Ge, Y. Chong, and A. D. Stone, "Steady-state ab initio laser theory: generalizations and analytic results," *Physical Review A*, vol. 82, p. 063824, 2010.

[20] M. Liertzer, L. Ge, A. Cerjan, A. Stone, H. E. Türeci, and S. Rotter, "Pump-induced exceptional points in lasers," *Physical Review Letters*, vol. 108, p. 173901, 2012.

[21] W. Heiss, "The physics of exceptional points," *Journal of Physics A: Mathematical and Theoretical*, vol. 45, p. 444016, 2012.

[22] J. D. Jackson, *Classical electrodynamics*. John Wiley & Sons, 2007.

[23] J. H. Poynting, "Xv. on the transfer of energy in the electromagnetic field," *Philosophical Transactions of the Royal Society of London*, p. 343, 1884.

[24] G. G. Stokes, "On the composition and resolution of streams of polarized light from different sources," *TCaPS*, vol. 9, p. 399, 1851.

[25] H. Haken and H. Sauermann, "Nonlinear interaction of laser modes," *Zeitschrift für Physik*, vol. 173, p. 261, 1963.

[26] H. Haken and H. Sauermann, "Frequency shifts of laser modes in solid state and gaseous systems," *Zeitschrift für Physik*, vol. 176, p. 47, 1963.

[27] M. Sargent III, M. Scully, and W. Lamb, *Laser Physics*. Addison-Wesley, 1974.

[28] M. O. Scully and W. E. Lamb Jr, "Quantum theory of an optical maser. i. general theory," *Physical Review*, vol. 159, p. 208, 1967.

[29] A. Icsevgi and W. Lamb Jr, "Propagation of light pulses in a laser amplifier," *Physical Review*, vol. 185, p. 517, 1969.

[30] C. Cohen-Tannoudji, B. Diu, F. Laloe, and B. Dui, "Quantum mechanics (2 vol. set)," 2006.

[31] P. Meystre and M. Sargent, *Elements of quantum optics*. Springer Science & Business Media, 2013.

[32] M. O. Scully and M. S. Zubairy, "Quantum optics," 1999.

[33] W. W. Chow, S. W. Koch, and M. Sargent III, *Semiconductor-laser physics*. Springer-Verlag, 1994.

[34] S. Stenholm and W. E. Lamb Jr, "Semiclassical theory of a high-intensity laser," *Physical Review*, vol. 181, p. 618, 1969.

[35] S. Wieczorek and W. W. Chow, "Stabilising and destabilising effects of polarization dynamics in class c lasers with optical external injection or time-delayed feedback," 2014.

[36] S. A. Shakir and W. W. Chow, "Semiclassical theory of coupled lasers," *Optics letters*, vol. 9, p. 202, 1984.

[37] S. A. Shakir and W. W. Chow, "Semiclassical theory of coupled lasers," *Physical Review A*, vol. 32, p. 983, 1985.

[38] M. Rose, M. Lindberg, W. Chow, S. W. Koch, and M. Sargent III, "Composite-cavity-mode approach to single-mode semiconductor-laser feedback instabilities," *Physical Review A*, vol. 46, p. 603, 1992.

[39] S. Wieczorek and W. W. Chow, "Bifurcations and interacting modes in coupled lasers: A strong-coupling theory," *Physical Review A*, vol. 69, p. 033811, 2004.

[40] S. Wieczorek and W. W. Chow, "Global view of nonlinear dynamics in coupled-cavity lasers–a bifurcation study," *Optics communications*, vol. 246, p. 471, 2005.

[41] H. Erzgräber, S. Wieczorek, and B. Krauskopf, "Bifurcations of composite-cavity modes in multi-stripe laser arrays," in *Semiconductor Lasers and Laser Dynamics III*, vol. 6997, p. 69971L, International Society for Optics and Photonics, 2008.

[42] H. Erzgräber, S. Wieczorek, and B. Krauskopf, "Locking behavior of three coupled laser oscillators," *Physical Review E*, vol. 80, p. 026212, 2009.

[43] H. Erzgräber, S. Wieczorek, and B. Krauskopf, "Dynamics of two semiconductor lasers coupled by a passive resonator," *Physical Review E*, vol. 81, p. 056201, 2010.

[44] G. Van Tartwijk and D. Lenstra, "Semiconductor lasers with optical injection and feedback," *Quantum and Semiclassical Optics: Journal of the European Optical Society Part B*, vol. 7, p. 87, 1995.

[45] T. Simpson, J. Liu, K.-F. Huang, and K. Tai, "Nonlinear dynamics induced by external optical injection in semiconductor lasers," *Quantum and Semiclassical Optics: Journal of the European Optical Society Part B*, vol. 9, p. 765, 1997.

[46] Y. Hong, P. S. Spencer, P. Rees, and K. A. Shore, "Optical injection dynamics of two-mode vertical cavity surface-emitting semiconductor lasers," *IEEE journal of quantum electronics*, vol. 38, p. 274, 2002.

[47] F. Mogensen, H. Olesen, and G. Jacobsen, "Locking conditions and stability properties for a semiconductor laser with external light injection," *IEEE Journal of Quantum Electronics*, vol. 21, p. 784, 1985.

[48] C. Henry, "Theory of the linewidth of semiconductor lasers," *IEEE Journal of Quantum Electronics*, vol. 18, p. 259, 1982.

[49] B. Krauskopf, N. Tollenaar, and D. Lenstra, "Tori and their bifurcations in an optically injected semiconductor laser," *Optics communications*, vol. 156, p. 158, 1998.

[50] S. Wieczorek, B. Krauskopf, and D. Lenstra, "A unifying view of bifurcations in a semiconductor laser subject to optical injection," *Optics communications*, vol. 172, p. 279, 1999.

[51] S. Wieczorek, T. B. Simpson, B. Krauskopf, and D. Lenstra, "Global quantitative predictions of complex laser dynamics," *Physical Review E*, vol. 65, p. 045207, 2002.

[52] S. Wieczorek, B. Krauskopf, and D. Lenstra, "Multipulse excitability in a semiconductor laser with optical injection," *Physical review letters*, vol. 88, p. 063901, 2002.

[53] T. Simpson, "Mapping the nonlinear dynamics of a distributed feedback semiconductor laser subject to external optical injection," *Optics Communications*, vol. 215, p. 135, 2003.

[54] R. Lang and K. Kobayashi, "External optical feedback effects on semiconductor injection laser properties," *IEEE journal of Quantum Electronics*, vol. 16, p. 347, 1980.

[55] H. Erzgräber, B. Krauskopf, and D. Lenstra, "Compound laser modes of mutually delay-coupled lasers," *SIAM Journal on Applied Dynamical Systems*, vol. 5, p. 30, 2006.

[56] F. Rogister and M. Blondel, "Dynamics of two mutually delay-coupled semiconductor lasers," *Optics communications*, vol. 239, p. 173, 2004.

[57] S. Yanchuk, K. R. Schneider, and L. Recke, "Dynamics of two mutually coupled semiconductor lasers: instantaneous coupling limit," *Physical Review E*, vol. 69, p. 056221, 2004.

[58] H. Erzgräber, B. Krauskopf, and D. Lenstra, "Mode structure of delay-coupled semiconductor lasers: influence of the pump current," *Journal of Optics B: Quantum and Semiclassical Optics*, vol. 7, p. 361, 2005.

[59] H. Erzgräber, E. Wille, B. Krauskopf, and I. Fischer, "Amplitude–phase dynamics near the locking region of two delay-coupled semiconductor lasers," *Nonlinearity*, vol. 22, p. 585, 2009.

[60] E. Clerkin, S. O'Brien, and A. Amann, "Multistabilities and symmetry-broken one-color and two-color states in closely coupled single-mode lasers," *Physical Review E*, vol. 89, p. 032919, 2014.

[61] M. Seifikar, A. Amann, and F. H. Peters, "Dynamics of two identical mutually delay-coupled semiconductor lasers in photonic integrated circuits," *Applied optics*, vol. 57, p. E37, 2018.

[62] F. M. Dubois, M. Seifikar, A. H. Perrott, and F. H. Peters, "Modeling mutually coupled non-identical semiconductor lasers on photonic integrated circuits," *Applied optics*, vol. 57, p. E154, 2018.

[63] S. Miller, "Coupled wave theory and waveguide applications," *Bell System Technical Journal*, vol. 33, p. 661, 1954.

[64] J. R. Pierce, "Coupling of modes of propagation," *Journal of Applied Physics*, vol. 25, p. 179, 1954.

[65] A. Yariv, "Coupled-mode theory for guided-wave optics," *IEEE Journal of Quantum Electronics*, vol. 9, p. 919, 1973.

[66] W.-P. Huang, "Coupled-mode theory for optical waveguides: an overview," *JOSA A*, vol. 11, p. 963, 1994.

[67] S. Fan, W. Suh, and J. D. Joannopoulos, "Temporal coupled-mode theory for the fano resonance in optical resonators," *JOSA A*, vol. 20, p. 569, 2003.

[68] W. Suh, Z. Wang, and S. Fan, "Temporal coupled-mode theory and the presence of non-orthogonal modes in lossless multimode cavities," *IEEE Journal of Quantum Electronics*, vol. 40, p. 1511, 2004.

[69] S. Wang, B. Hou, W. Lu, Y. Chen, Z. Zhang, and C. Chan, "Arbitrary order exceptional point induced by photonic spin–orbit interaction in coupled resonators," *Nature communications*, vol. 10, p. 1, 2019.

[70] M.-A. Miri and A. Alu, "Exceptional points in optics and photonics," *Science*, vol. 363, 2019.

[71] M. V. Berry, "Physics of nonhermitian degeneracies," *Czechoslovak journal of physics*, vol. 54, p. 1039, 2004.

[72] Ş. Özdemir, S. Rotter, F. Nori, and L. Yang, "Parity–time symmetry and exceptional points in photonics," *Nature materials*, vol. 18, p. 783, 2019.

[73] M. Brandstetter, M. Liertzer, C. Deutsch, P. Klang, J. Schöberl, H. E. Türeci, G. Strasser, K. Unterrainer, and S. Rotter, "Reversing the pump dependence of a laser at an exceptional point," *Nature communications*, vol. 5, p. 1, 2014.

[74] T. Goldzak, A. A. Mailybaev, and N. Moiseyev, "Light stops at exceptional points," *Physical review letters*, vol. 120, p. 013901, 2018.

[75] H. Lü, S. Özdemir, L.-M. Kuang, F. Nori, and H. Jing, "Exceptional points in random-defect phonon lasers," *Physical Review Applied*, vol. 8, p. 044020, 2017.

[76] J. Zhang, B. Peng, Ş. K. Özdemir, K. Pichler, D. O. Krimer, G. Zhao, F. Nori, Y.-x. Liu, S. Rotter, and L. Yang, "A phonon laser operating at an exceptional point," *Nature Photonics*, vol. 12, p. 479, 2018.

[77] I. I. Arkhipov, A. Miranowicz, F. Minganti, and F. Nori, "Quantum and semiclassical exceptional points of a linear system of coupled cavities with losses and gain within the scully-lamb laser theory," *Physical Review A*, vol. 101, p. 013812, 2020.

[78] R. El-Ganainy, M. Khajavikhan, and L. Ge, "Exceptional points and lasing self-termination in photonic molecules," *Physical Review A*, vol. 90, p. 013802, 2014.

[79] H. A. Haus, *Waves and fields in optoelectronics*. Prentice-Hall,, 1984.

[80] R. L. Cooke, *Classical algebra: its nature, origins, and uses*. John Wiley & Sons, 2008.

[81] U. Fano, "A stokes-parameter technique for the treatment of polarization in quantum mechanics," *Physical Review*, vol. 93, p. 121, 1954.

[82] W. H. McMaster, "Polarization and the stokes parameters," *American Journal of Physics*, vol. 22, p. 351, 1954.

[83] R. P. Feynman, F. L. Vernon Jr, and R. W. Hellwarth, "Geometrical representation of the schrödinger equation for solving maser problems," *Journal of applied physics*, vol. 28, p. 49, 1957.

[84] A. Cerjan, Y. Chong, L. Ge, and A. D. Stone, "Steady-state ab initio laser theory for n-level lasers," *Optics express*, vol. 20, p. 474, 2012.

[85] L. Ge, Y. Chong, S. Rotter, H. Türeci, and A. D. Stone, "Unconventional modes in lasers with spatially varying gain and loss," *Physical Review A*, vol. 84, p. 023820, 2011.

[86] S. Esterhazy, D. Liu, M. Liertzer, A. Cerjan, L. Ge, K. Makris, A. Stone, J. Melenk, S. Johnson, and S. Rotter, "Scalable numerical approach for the steady-state ab initio laser theory," *Physical Review A*, vol. 90, p. 023816, 2014.

[87] D. Gagnon, J. Dumont, J.-L. Déziel, and L. J. Dubé, "Ab initio investigation of lasing thresholds in photonic molecules," *JOSA B*, vol. 31, p. 1867, 2014.

[88] S. Burkhardt, M. Liertzer, D. O. Krimer, and S. Rotter, "Steady-state ab initio laser theory for fully or nearly degenerate cavity modes," *Physical Review A*, vol. 92, p. 013847, 2015.

[89] L. Ge, "Selective excitation of lasing modes by controlling modal interactions," *Optics Express*, vol. 23, p. 30049, 2015.

[90] L. Ge, H. Cao, and A. D. Stone, "Condensation of thresholds in multimode microlasers," *Physical Review A*, vol. 95, p. 023842, 2017.

[91] A. Cerjan, S. Bittner, M. Constantin, M. Guy, Y. Zeng, Q. J. Wang, H. Cao, and A. D. Stone, "Multimode lasing in wave-chaotic semiconductor microlasers," *Physical Review A*, vol. 100, p. 063814, 2019.

[92] G. R. Fowles, *Introduction to modern optics*. Courier Corporation, 1989.

[93] V. V. Kisil and J. Reid, "Conformal parametrisation of loxodromes by triples of circles," in *Topics in Clifford Analysis*, p. 313, Springer, 2019.

[94] J. A. Pereda, Á. Vegas, and A. Prieto, "Fdtd modeling of wave propagation in dispersive media by using the mobius transformation technique," *IEEE Transactions on Microwave Theory and Techniques*, vol. 50, p. 1689, 2002.

[95] J. A. Pereda, A. Grande, O. Gonzales, and Á. Vegas, "Fdtd modeling of chiral media by using the mobius transformation technique," *IEEE Antennas and Wireless Propagation Letters*, vol. 5, p. 327, 2006.

[96] O. González, J. A. Pereda, A. Herrera, and Á. Vegas, "An extension of the lumped-network fdtd method to linear two-port lumped circuits," *IEEE transactions on Microwave Theory and Techniques*, vol. 54, p. 3045, 2006.

[97] A. Umerski, "Closed-form solutions to surface green's functions," *Physical Review B*, vol. 55, p. 5266, 1997.

[98] M. Babaarslan and Y. Yayli, "Space-like loxodromes on rotational surfaces in minkowski 3-space," *Journal of Mathematical Analysis and Applications*, vol. 409, p. 288, 2014.

[99] M. Babaarslan and M. I. Munteanu, "Time-like loxodromes on rotational surfaces in minkowski 3-space," *Annals of the Alexandru Ioan Cuza University-Mathematics, doi*, vol. 10, 2015.

[100] M. Babaarslan and M. Kayacik, "Differential equations of the space-like loxodromes on the helicoidal surfaces in minkowski 3-space," *Differential Equations and Dynamical Systems*, vol. 28, p. 495, 2020.

[101] S. Cornbleet, "Ray paths in a nonuniform axially symmetric medium," *IEE Journal on Microwaves, Optics and Acoustics*, vol. 2, p. 194, 1978.

[102] R. C. Brower, H. Neff, and K. Orginos, "Möbius fermions: Improved domain wall chiral fermions," *Nuclear Physics B-Proceedings Supplements*, vol. 140, p. 686, 2005.

[103] J. Monzón, A. Barriuso, L. Sánchez-Soto, and J. Montesinos-Amilibia, "Geometrical interpretation of optical absorption," *Physical Review A*, vol. 84, p. 023830, 2011.

[104] M. Willemsen, M. Van Exter, and J. Woerdman, "Polarization loxodrome of a vertical-cavity semiconductor laser," *Optics communications*, vol. 199, p. 167, 2001.